Development of Ti-Fe-based powders for laser additive manufacturing of ultrafine lamellar eutectics

by

Akshya Kumar Pandey

A dissertation submitted in partial fulfilment of the requirements for the degree of Doctor of Philosophy in

Materials Science and Engineering

Universidad Carlos III de Madrid

Advisors:

Dr. Federico Sket
Dr. Srdjan Milenkovic

Tutor:

Dr. Srdjan Milenkovic

Leganés, June 2023

To my parents.
To Shiva.
To my younger self.

ACKNOWLEDGEMENTS

I express my heartfelt gratitude towards two great institutions, IMDEA Materials and Universidad Carlos III de Madrid, that hosted me on this transformative journey of almost 5 years. They allowed me to learn and grow among the best of peers to become a trained professional in science. Time spent in these establishments will be forever imprinted in my memory and I will keep drawing fruitful lessons from them.

I would like to express my sincerest gratitude towards my supervisors Dr. Federico Sket and Dr. Srdjan Milenkovic. They inspired me and made sure I received proper guidance whenever necessary. They introduced me to the field and provided access to all resources used to carry out this work. They trained me to think critically, plan objectively and observe diligently. There were several setbacks in our project, often due to the pandemic situation. They always cooperated to find the best solution and helped me within their capacity. I owe special thanks to Dr. Paula Alvaredo for always helping me with her valuable experience in powder metallurgy. She taught me several practical and theoretical lessons from the field, without which this work would have been impossible. She acted as a reliable connecting point between me and the university. I had to often use equipment at the campus on short notice and she tried her best to accommodate me.

Further, I thank all my colleagues from IMDEA (especially Amalia, Arturo, Jonathan, Javier Garcia, Marcos Angelo and Miguel Monclus) who worked with me patiently since day one to make this study possible. There was a strong comradery among the students and staff of IMDEA which I will always cherish. I will remember coffee and snack breaks with my delightful colleagues as the best work moments during these years. They made experimental work run smoother and life easier. They stayed in touch with me and provided necessary help whenever I asked, until I finished writing this thesis.

Last but the most, I would like to thank my family and friends for their constant support and motivation. My parents are pillars of my strength, something which I realised more and more during this journey, especially during stressful pandemic times. It was not easy to carry on research work and keep writing while experiencing fear and anxiety in a foreign land, but constant communication with a family of pure souls which I have been blessed with, kept me going. The values they instilled in me are the only reasons I came this far. My younger brother Aju and my beloved sister Gudli always cheered me up whenever I needed it. My close friends Abhinav, Akash and Marine always believed in me (more than I did) and inspired me to stay positive in every situation. They gave me the confidence to turn every challenge into an opportunity for my own growth.

PUBLISHED AND SUBMITTED CONTENT

- "Development of powders of Ti-Fe-Sn ultrafine eutectics for laser additive manufacturing"
  Akshya K. Pandey, Paula Alvaredo, Srdjan Milenkovic, Federico Sket
  Published by: Powder Technology, Volume 404, p. 117416, May 2022,
  DOI: https://doi.org/10.1016/j.powtec.2022.117416
  (This item is wholly included in the thesis (in Chapter 4). The material from this source included in this thesis is not singled out with typographic means and references.)

OTHER RESEARCH MERITS

Oral contributions to the following congresses

.

- "Developing Ti- and Fe-based powders for laser additive manufacturing of ultrafine eutectics" (Oral presentation)
  Akshya K. Pandey, P. Alvaredo, S. Milenkovic and F. Sket

  VII Congreso Español de Pulvimetalurgia y II Congreso Iberoamericano de Pulvimetalurgia, 24 – 26 June, 2019, Campus Madrid-Puerta de Toledo, Universidad Carlos III de Madrid, Spain

- "Pre-alloyed powders of Ti-Fe ultrafine eutectics for laser additive manufacturing" (Oral presentation)
  Akshya K. Pandey, P. Alvaredo, S. Milenkovic and F. Sket

  9th World Congress on Particle Technology, 18 – 22 September 2022, Asociación Nacional De Químicos E Ingenieros Químicos De España, Madrid, Spain

Abstract

Years of academic research has gone into developing Ti-Fe-based ultrafine eutectic and near-eutectic alloys with remarkable mechanical properties. Cast ingots (few mm in dimensions) have demonstrated high compressive strengths (> 2 GPa) similar to bulk metallic glasses (BMGs), while retaining more than 15 % plasticity at room temperature [1–3]. However, conventional casting methods are incapable of providing uniform and high cooling rates necessary for growing such ultrafine microstructures over large dimensions without introducing significant heterogeneities. On the other hand, laser-based Additive Manufacturing (AM) techniques with inherently very high cooling rates like Selective Laser Melting (SLM) (ranging 10^6 K/s) or Laser Metal Deposition (LMD) (ranging 10^4 – 10^5 K/s) are appropriate for such microstructural growth and their track and layer-wise building approach maintains an almost constant cooling rate throughout bulk. This strongly motivates the development of high-quality powders for SLM and LMD trials.

In this work, pre-alloyed powder of Fe-rich near-eutectic composition $Fe_{82.4}Ti_{17.6}$ (at %) was developed for LMD, while powders of two Ti-rich compositions: near-eutectic $Ti_{66}Fe_{27}Nb_3Sn_4$ (at %) and off-eutectic $Ti_{73.5}Fe_{23}Nb_{1.5}Sn_2$ (at %) were explored for SLM trials. Three gas atomisation methods, namely Crucible-based Gas atomisation (CGA), Crucible-Free atomisation (CFA) and Arc-melting Atomisation (AMA) were investigated for optimising powder production. In addition to conventional techniques, a novel methodology was proposed for one-step screening of powders' key features based on advanced image analysis of X-Ray Computed Tomography (XCT) data. The methodology generated volume-weighted particle size distributions (which were validated against conventional laser diffraction), provided accurate estimations of internal porosity and quantitatively evaluated the 3D morphology of powders. In order to create a solidification knowledge dataset and further optimise the processing of powders under high cooling rates, in-depth microstructural studies were performed on these powders sieved into different particle size ranges (experiencing different solidification rates during atomisation). Results revealed that powder particle size is clearly related to, and can possibly predict, the solidification pathway followed during gas atomisation as well as its degree of completion. The ultrafine interlamellar spacing λ (< 190 µm) of lamellar eutectics observed in powders of near-eutectic compostitions increased almost linearly with particle size and revealed solidification rates similar to those encountered during SLM/LMD processing of the same or similar compositions. Therefore, this work highlights the potential of gas atomisation as a method to study rapid solidification and Laser-AM processing.

Finally, two alloys were consolidated by AM using pre-alloyed powders and characterised mechanically, i.e. LMD-built $Fe_{82.4}Ti_{17.6}$ with lamellar eutectic microstructure and SLM-built $Ti_{73.5}Fe_{23}Nb_{1.5}Sn_2$ (off-eutectic) showing a unique "composite" microstructure of α-Ti and β-Ti grains strengthened by FeTi dispersoids that partially arranged themeselves as fine

lamellas. Both alloys showed high compressive yield strengths (≈ 1.8 GPa and ≈ 1.9 GPa) at room temperature, with $Ti_{73.5}Fe_{23}Nb_{1.5}Sn_2$ showing high plasticity up to 20 %. The alloy showed higher tensile yield strength and elongation at intermediate temperatures (450 °C to 600 °C) than popular (α+β) aerospace alloys, like Ti-6Al-4V built by laser-AM [4–6]. LMD-built $Fe_{82.4}Ti_{17.6}$ largely remained brittle below 500 °C, but out-performed similar induction cast [7] and sintered alloys in compressive yield strength, thus proving an impressive candidate for compression-based applications (like tools) in the intermediate temperature range.

REFERENCES

[1] J. Das and T. Maity, "A few aspects on the processing and deformation behavior of advanced eutectic alloys," *Trans. Indian Inst. Met.*, vol. 65, no. 6, pp. 571–576, 2012, doi: 10.1007/s12666-012-0185-y.

[2] D. A. T. A. J. Louzguine-Luzgin, "High-strength ti-based alloys containing fe as one of the main alloying elements," *Mater. Trans.*, vol. 59, no. 10, pp. 1537–1544, 2018, doi: 10.2320/matertrans.M2018114.

[3] J. Das, K. B. Kim, F. Baier, W. Löser, and J. Eckert, "High-strength Ti-base ultrafine eutectic with enhanced ductility," *Appl. Phys. Lett.*, vol. 87, no. 16, pp. 1–3, 2005, doi: 10.1063/1.2105998.

[4] A. Popovich, V. Sufiiarov, E. Borisov, and I. Polozov, "Microstructure and mechanical properties of Ti-6AL-4V manufactured by SLM," *Key Eng. Mater.*, vol. 651–653, no. February, pp. 677–682, 2015, doi: 10.4028/www.scientific.net/KEM.651-653.677.

[5] S. Ivanov, M. Gushchina, A. Artinov, M. Khomutov, and E. Zemlyakov, "Effect of Elevated Temperatures on the Mechanical Properties of a Direct Laser Deposited Ti-6Al-4V," *Materials (Basel).*, vol. 14, no. 21, Nov. 2021, doi: 10.3390/MA14216432.

[6] J. Song *et al.*, "Temperature sensitivity of mechanical properties and microstructure during moderate temperature deformation of selective laser melted Ti-6Al-4V alloy," 2020, doi: 10.1016/j.matchar.2020.110342.

[7] D. Barbier, M. X. Huang, and O. Bouaziz, "A novel eutectic Fe-15 wt.% Ti alloy with an ultrafine lamellar structure for high temperature applications," *Intermetallics*, vol. 35, pp. 41–44, 2013, doi: 10.1016/j.intermet.2012.11.016.

Table of Contents

List of Figures

List of Tables

Chapter 1

Introduction

1 Introduction

This chapter provides a state-of-the-art literature review of all topics related to this thesis. It consists of three main sections. The first one introduces the fundamental aspects of binary eutectic alloys and their growth, common eutectics used in industry and eutectics in the Ti-Fe binary system. The second section provides an overview of the reported literature on Ti-Fe-based ultrafine eutectics in terms of common processing methods, used alloying elements, hierarchically structured eutectic microstructures (with embedded primary dendrite or another eutectic of different length scale), microstructure evolution in Ti-Fe-Sn near-eutectic cast alloys and laser-additive manufacturing (AM) trials of similar alloys. The last section discusses powder production techniques and the desirable powder characteristics for AM. It explains the role of each relevant powder characteristic on the overall AM process and also describes the conventionally used techniques for characterising them.

1.1 Eutectic alloys: in-situ composites

1.1.1 Fundamental aspects

Eutectics grow as multi-phase materials directly from the melt because of a miscibility gap in the solid state. Such a transition is called a 'eutectic reaction' and it occurs at a particular 'eutectic temperature' and 'eutectic composition', thus, defining the invariant 'eutectic point' on a conventional phase diagram (fixed Pressure and Volume). The schematic in Figure 1.1 represents a eutectic point (marked as E) in a binary system where the reaction 'L→ α + β' takes place directly forming two solids α (A-rich) and β (B-rich) from the liquid. Equilibrium compositions of the two solidified phases in the alloy are given by their respective solvus lines, while their relative volume fractions can be determined by lever rule.

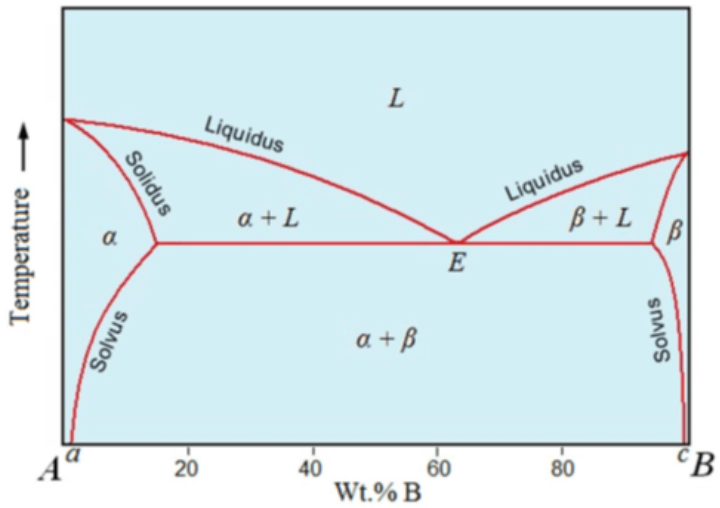

Figure 1.1: A typical binary eutectic phase diagram showing the eutectic point E [1]

The two solids in a binary eutectic can exhibit several morphologies or geometrical arrangements as they grow, which are broadly grouped as regular or irregular. A regular eutectic is formed when both phases have a low entropy of fusion or a low anisotropy in the solid-liquid interfacial energy making them non-faceted. If one or both of them are faceted, it results in irregular structures. When the two solid phases tend to grow side-by-side along a common interface with the liquid, it is termed as coupled growth and results in lamellar or rod-like/fibrous morphologies. The schematic in Figure 1.2(a) represents the traverse cross-sections of binary eutectics in coupled growth assuming a non-faceted α phase (denoted as white). The eutectic is regular or irregular depending on whether the minor β phase is faceted or not, while its volume fraction determines if it is lamellar or rod-like/fibrous. It tends to be lamellar for a volume fraction between ≈ 0.25 to 0.5 and fibrous for lower volume fractions [2].

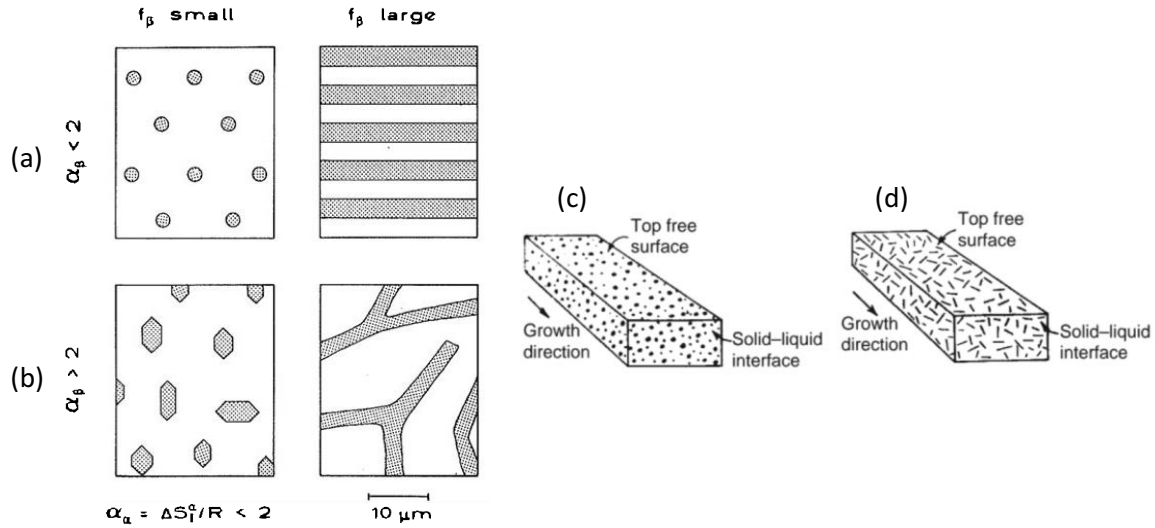

Figure 1.2: Traverse cross-sections of binary eutectics showing coupled growth with (a) regular rod-like and lamellar morphologies when both α and β phases are non-faceted, and (b) irregular rod-like and lamellar morphologies when β phase is faceted [2]; Binary eutectics showing independent growth (when both α and β phases are faceted) with (c) globular and (d) acicular or needle-like morphology [3]

Both phases being faceted is unfavourable for coupled growth and results in them growing independently to form irregular microstructures. In such cases, eutectics exhibit randomly growing needle-like phases, namely acicular morphology, or a globular morphology with spheroidal particles as shown in Figure 1.2(b) [3]. Some common regular eutectic systems are Al-Au, Pb-Sn and Al-Zn. Irregular eutectics usually contain a non-metal component, such as Fe-C (graphite) and Al-Si [4].

The spacing between two consecutive lamellas of a phase in a regular lamellar eutectic is referred to as ‘inter-lamellar spacing’ or ‘λ’. According to Jackson-Hunt´s model for binary eutectic growth, ‘λ’ and solidification rate or growth velocity ‘v’ are related to each other by the following relation

$$\lambda^2 v = K$$

Equation 1.1

where K is a constant for a material and 'v' is the solidification front velocity [5]
Alloys are often designed with near-eutectic compositions to obtain microstructures with a eutectic matrix containing embedded primary phase dendrites. Such materials are called 'hierarchically structured eutectics' or 'bimodal in situ composites' [6] as they feature two distinct length scales, namely, dendrite size 'D' and inter-lamellar spacing 'λ' where D is much larger than λ. However, both of these parameters depend strongly on solidification conditions and tend to decrease with increasing growth velocity.

1.1.2 Common eutectics in industry

As shown in Figure 1.3, eutectic alloys show a remarkable balance between yield strength and plastic strain due to their periodic nature. The most widely used eutectic alloys are Al-Si and grey iron or Fe-C (graphite) as structural materials [2].

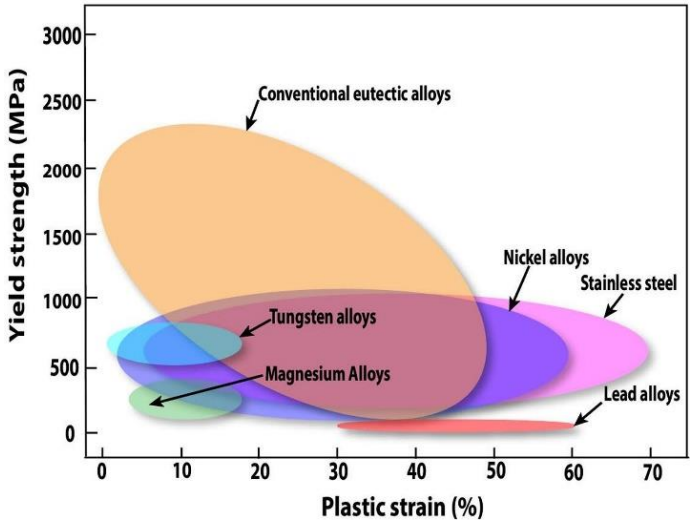

Figure 1.3: Yield strength vs plastic strain map of conventional eutectic alloys and various structural alloys

Several conventional eutectic alloys used in electronics, automotive, aerospace, casting and related industries can be broadly classified according to the temperature range of their applications: low-temperature alloys (Aluminium-based structural eutectics like Al-Cu, Al-Ni-Fe, Al-Ni-Si), mid-temperature range (Titanium and Copper alloys) and the high-temperature domain (Nickel-based superalloys like Ni-Al-Cr, Ni-Al-Co and similar alloys) [7]. Since eutectic alloys melt at lower temperatures than their pure components, they are quite popular as soldering alloys, like Au80-Sn20, Sn63-Pb37 and more recent Pb-free alternatives like Sn-Ag-Cu [8, 9]. Cu-Mg and Cu-La eutectic alloys are becoming popular for high strength and high conductivity applications previously dominated by age-hardened Cu-Be alloys [10, 11]. Ti-based eutectic alloys with ultrafine (λ < 1 μm) lamellar microstructures are being developed over the last few decades, mostly with Fe as well as in some ternary and quaternary systems

like Ti-Fe-Sn-Nb, Ti-Fe-Co, Fe-Ti-Si and Fe-Ti-Zr [12] . They demonstrate excellent and balanced mechanical properties, as discussed in the following sections, however, conventional casting techniques have failed so far to produce them in dimensions large enough for industrial use.

1.1.3 Ti-Fe eutectics

As seen in Figure 1.4, two eutectic points exist in the Ti-Fe equilibrium phase diagram (marked by arrows).

i. L→ β-Ti + FeTi at 29.5 at % or 32.5 wt % Fe and 1085 °C (Ti-rich eutectic)

ii. L→ α-Fe + Fe_2Ti at 84 at % or 86 wt % Fe and 1289 °C (Fe-rich eutectic)

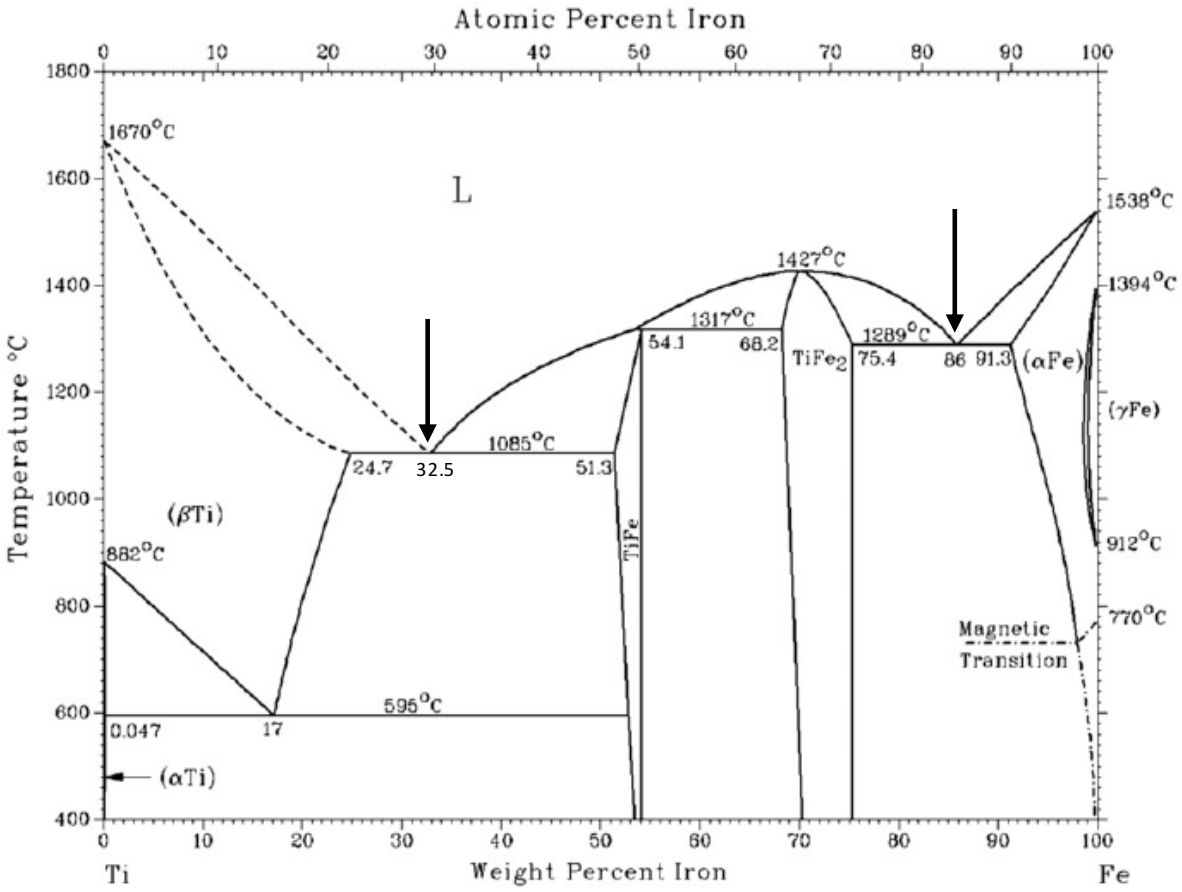

Figure 1.4: The Ti-Fe equilibrium phase diagram (eutectic points are marked by arrows) [13]

Eutectic Ti-32.5 wt % Fe ($Ti_{70.5}Fe_{29.5}$) produced by arc-melting directional solidification showed a eutectic microstructure of β-Ti (cubic A2 structure) and FeTi (ordered B2 intermetallic) phases in rod-like and lamellar morphologies [13]. Contieri et al. [13] further confirmed that the inter-lamellar spacing 'λ' decreases with increasing growth velocity or solidification rate in agreement with the Jackson-Hunt relation [5] for binary eutectic growth. They determined K to be 22.27 x 10^{-15} m^3/h in this case. Decreasing λ causes a size hardening effect that

increased the compressive strength (σ_{max}) and plasticity (ε_f), until 3 GPa and 25.2 % respectively for the highest v = 60 mm/h, while maintaining yield strengths above 1.5 GPa (see Figure 1.5). This inspired studies on rapidly solidified eutectics produced by arc-melting on cold copper crucibles and suction casting of thin specimens.

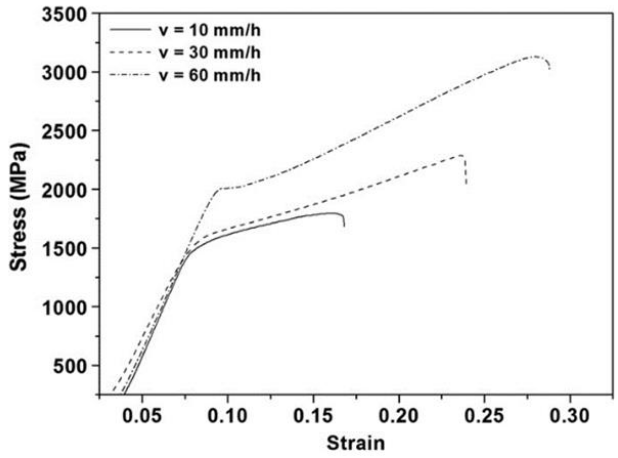

Figure 1.5: Room temperature compressive engineering stress–strain curve of the directionally solidified Ti–Fe eutectic alloy [13]

1.2 Ti-Fe-based ultrafine eutectics: overview of processing methods, microstructures and properties

1.2.1 Processing methods

Most common processing methods that have been used to cast and study specimens of ultrafine Ti-Fe eutectics are Suction casting and Arc-melting.

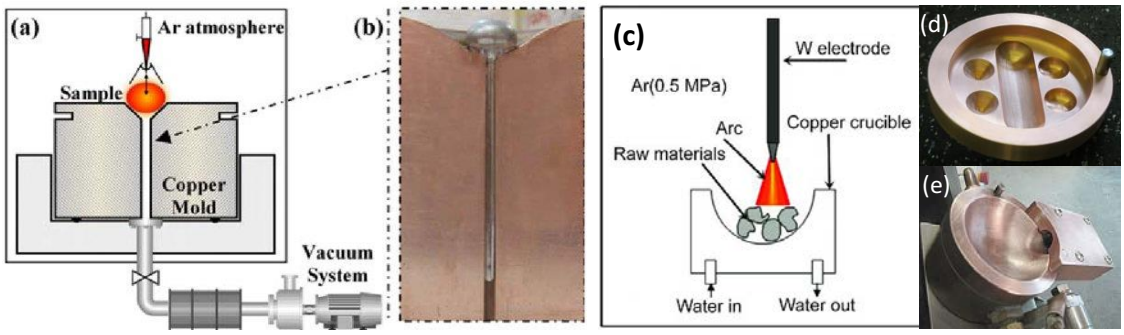

Figure 1.6: (a) Schematic of a suction casting process along with (b) a typical suction-cast cylindrical sample in a split copper mould [14], (c) schematic of an arc-melting process [15] along with commonly used water-cooled copper crucibles for producing (d) small button-like samples or (e) cylindrical samples by tilt casting into a split mould [16]

In both cases, an electric arc created between a Tungsten electrode and water-cooled copper crucible is used for melting raw materials in an inert atmosphere. It can reach temperatures over 3000 °C [16]. In suction casting, the molten material is pulled into a split copper mould

using vacuum, as shown in Figure 1.6(a), where it is cooled rapidly to produce thin cylindrical specimens. Samples with variable diameters of 1 to 6 mm are commonly produced. This method is sometimes used to cast amorphous and glassy materials because of the high cooling rates achievable. Although typically cooling rates are in the order of 100 K/s, suction cast cylindrical specimens of Fe-25 wt % Ni which were 1 mm in diameter have been reported to experience cooling rates as high as ≈ 10^4 K/s [17]. Meanwhile, thicker specimens (up to 4 mm in diameter) of the alloy experienced lower cooling rates in the order of 10^2 – 10^3 K/s. The cooling rates are higher near the alloy surface as compared to the interior [17, 18].

In arc-melting, the melt is solidified on the water-cooled copper crucible itself which often has surface features, as shown in Figure 1.6(d), to produce small samples of different shapes. The crucible can further be connected to a split copper mould in order to tilt and pour the melt for casting rods, as in Figure 1.6(e) [16]. High cooling rates of 2 × 10^3 K/s have been reported for arc-melted ingots of $Al_{95.5}Cu_{4.5}$ alloy [19]. Sections 1.2.2 to 1.2.5 discuss the existing literature on Ti-Fe-based eutectics produced primarily by arc-melting and suction casting.

More unconventional processing methods offering high cooling rates that have been recently investigated to produce such ultrafine eutectics are laser additive manufacturing techniques like Selective Laser Melting (SLM) and Laser Metal Deposition (LMD).

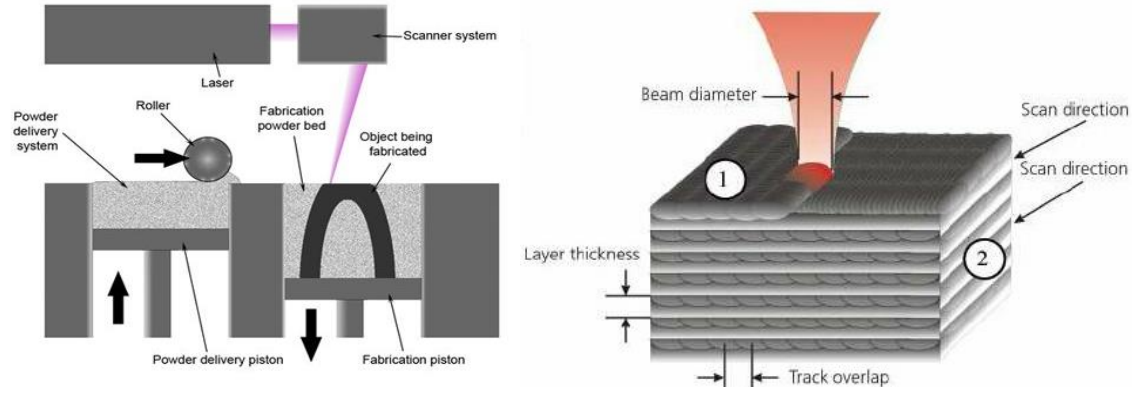

Figure 1.7: Schematics showing basic set up and building process of Selective Laser Melting (SLM) [20]

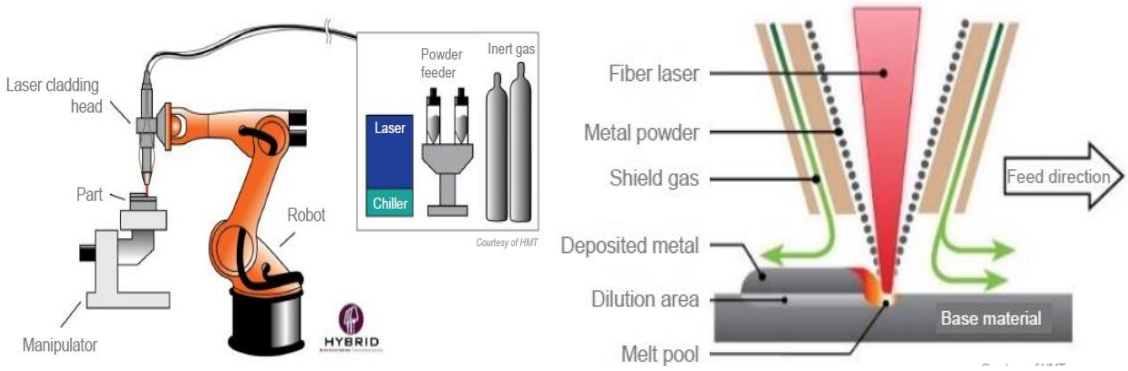

Figure 1.8: Schematics showing basic set up and building process of Laser Metal Deposition (LMD) [21]

Powder bed fusion technique SLM uses lasers to fuse specific locations on a powder layer. As shown in Figure 1.7, a roller keeps adding a new powder layer to the building area that moves downwards after each melting, until the part is complete. One or several lasers with powers in the order of 10^2 W are used that can focus the beam on a small spot up to 70 µm in diameter, thus offering a very high build resolution [22].

In LMD, metal powder is supplied laterally via a carrier gas into a laser-clad nozzle that fuses the material simultaneously while moving above desired locations, as shown in Figure 1.8. A minimum track width up to 0.7 mm can be achieved in a typical LMD setup [23]. Very high cooling rates in the order of 10^6 K/s are observed during SLM, while they lie between 10^4 – 10^5 K/s for LMD.

The current limited number of studies involving AM, which are discussed in section 1.2.6, have only used elemental powders or mechanically alloyed pure powders as raw materials for producing small specimens of Ti-Fe-based eutectics.

1.2.2 Role of alloying elements

Fe, Nb and Ta are known to act as β-Ti phase stabilizers in this alloy system [24]. Studies by Cao et al. [25] on arc-cast bulk $(Ti_{70.5}Fe_{29.5})_{100-x}Nb_x$ (x = 0, 3, 5 and 7 at %) alloys revealed that Nb addition to the eutectic composition creates a bimodal structure or hierarchically structured eutectic with µm-scale primary β-Ti dendrites embedded in an ultrafine eutectic matrix. Further, Nb was seen to reduce λ (from 500 nm to 200 nm at 7 at %) by decreasing the β-Ti/FeTi interface energy. All Nb-containing compositions in their studies showed minimum compressive strengths and plasticity values of 2.29 GPa and 13.5 % respectively (3 at % Nb being at the highest with 2.53 GPa strength and 15 % plasticity) as opposed to 2.14 GPa strength and 7% plasticity for the cast eutectic alloy.

Upon addition of Sn to arc-cast eutectic $(Ti_{70.5}Fe_{29.5})_{100-x}Sn_x$ (x = 0, 1, 2, 3 and 4), Das et al. [26] concluded that Sn also causes refinement of the lamellar microstructure and an increase in density (5.61 g/cm^3 to 5.81 g/cm^3 for 4 at %) by promoting the heavier FeTi phase. However, Sn preferentially dissolved in the β-Ti phase and lowered the bulk and Young's moduli by ≈ 5 %. Through Transmission Electron Microscopy (TEM) studies, they confirmed that slip lines formed during plastic deformation are mostly accommodated by the ductile β-Ti phase, while very fine slip transfer happens to the FeTi lamellae across β-Ti/FeTi interface leading to strain hardening. Han et al. [27] went further to add Sn up to x = 5, 7 and 9 at % in suction cast Ti-Fe eutectic alloys and reported the formation of hexagonal Ti_3Sn phase for x ≥ 5 at % in the form of µm-scale dendrites embedded in a bimodal eutectic. Increasing Sn content until x = 3 at % reduced λ and modified eutectic colony morphology leading to better properties. Figure 1.9(a) shows spherical eutectic colonies observed for x = 3 at % that enhanced plasticity under compression up to 4.3 % (as compared to 0.7 % for x = 0 prepared by same method) by controlling shear band propagation and multiplication through colony rotation.

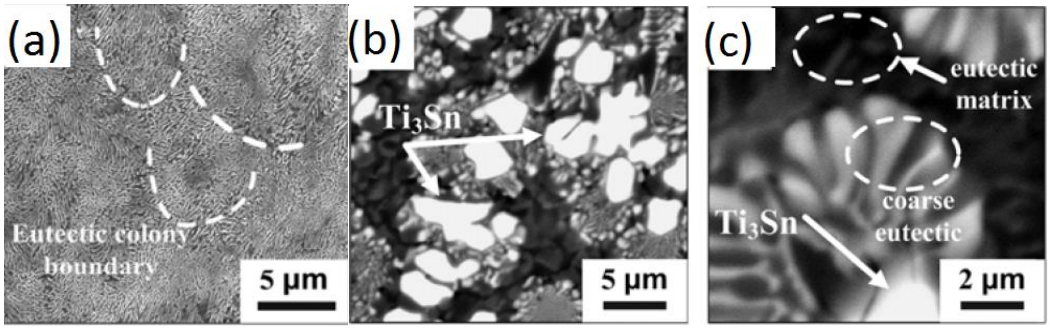

Figure 1.9: SEM micrographs of as-cast $(Ti_{70.5}Fe_{29.5})_{100-x}Sn_x$ alloys with (a) x = 3 at %, (b) and (c) x = 9 at % [27]

A bimodal eutectic structure around Ti_3Sn is seen in Figure 1.9(b) and (c) for x = 9 at %, where a coarse spherical eutectic colony (λ = 300 – 500 nm) is developed within a finer eutectic matrix (λ = 100 – 300 nm). This unique structure enhanced the plasticity to 6.3 % and 11.8 % for x = 7 and 9 respectively while maintaining their compressive strengths around 2 GPa.

Cao et al. [28] proved that lamellar morphology of eutectic $Ti_{70.5}Fe_{29.5}$ (produced by cold crucible levitation melting) can be modified into globular by alloying with Sn and Nb. Figure 1.10(b) shows that an addition of 3.85 at % Sn leads to a finer lamellar morphology surrounded by μm-scale FeTi. Further addition of 3 at % Nb led to almost completely globular and even finer morphology, as shown in Figure 1.10(c). The latter two alloys showed higher plasticity under compression of 10 % and 15 % respectively as compared to 5 % for the original eutectic. Globular morphology seemed to enhance plasticity as well as compressive strength (by ≈ 18 % to 2.36 GPa).

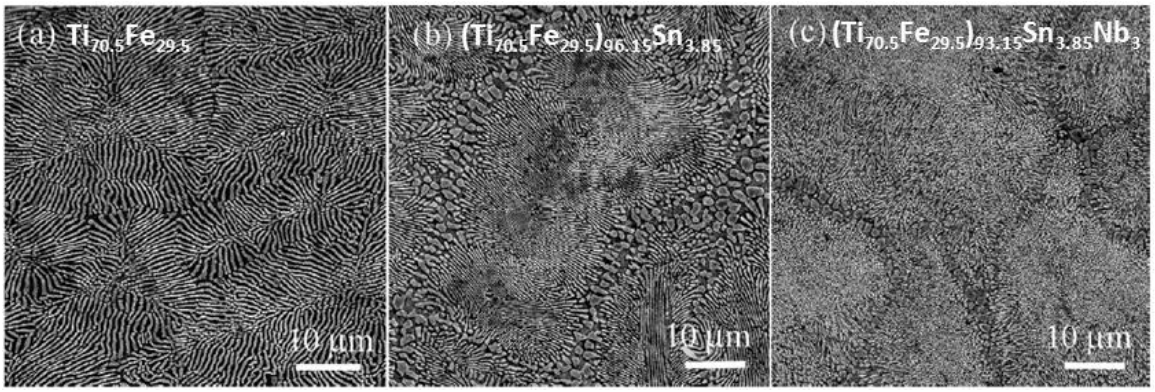

Figure 1.10: SEM BSE micrographs of (a) $Ti_{70.5}Fe_{29.5}$, (b) $(Ti_{70.5}Fe_{29.5})_{96.15}Sn_{3.85}$, and (c) $(Ti_{70.5}Fe_{29.5})_{93.15}Sn_{3.85}Nb_3$ alloys [28]

However, in another work, Zhao et al. [29] obtained lamellar eutectic morphology with embedded β-Ti primary dendrites upon (Sn, Nb) addition in a hypoeutectic alloy $Ti_{67}Fe_{27}Sn_3Nb_3$. This bimodal composite demonstrated a high 13.6 % plasticity under compression. Further, hard FeTi lamellas, ultrafine eutectic morphology and solution hardening of β-Ti by alloying elements contributed to a remarkable compressive strength of 2.9 GPa.

1.2.3 Role of primary dendrites in eutectic matrix

Zhao et al. [29] attributed the enhanced plasticity of bimodal eutectic $Ti_{67}Fe_{27}Sn_3Nb_3$ to dislocation-induced slip bands and shear band formation in primary β-Ti dendrites accompanied by continuous strain hardening. Dendrite/eutectic interfaces were found to act as strong barriers to shear band propagation.

Lee et al. [30] succeeded in selectively growing µm-scale primary dendrites in bimodal eutectics, namely β-Ti, FeTi and Ti_3Sn dendrites in suction cast $Ti_{72}Fe_{22}Sn_6$, $Ti_{64}Fe_{32}Sn_4$ and $Ti_{68}Fe_{23}Sn_9$ alloys respectively. β-Ti dendrites exhibited a high concentration of shear bands (and uniformly distributed thin and dense slip bands) that created multiples steps on fracture surfaces. FeTi dendrites also formed several shear bands during deformation that underwent shear bands bypass and extinction at the dendrite/eutectic interface, thus causing strain hardening. However, Ti_3Sn dendrites deformed by forming slips bands which were densely arranged to induce strain hardening in the alloy. All three alloys demonstrated high yield strength (≈ 1.65 GPa), compressive strength (≈ 2 GPa) and plasticity (6 – 9 %) under compression. Length scale, distribution and chemistry of primary dendrites play important roles in plastic deformation of these alloys besides eutectic morphology, colony shape and λ.

1.2.4 Bimodal Nanoeutectic composites

A unique microstructure where two ultrafine eutectics of different length-scales and morphologies: lamellar (TiFe + Ti_3Sn) with λ = 150 – 250 nm and rod-like (β-Ti + FeTi) with λ = 900 – 1500 nm, coexist as a 'bimodal nanoeutetic composite', was achieved by Song et al. [31] in suction cast alloy $Ti_{63.5}Fe_{30.5}Sn_6$.

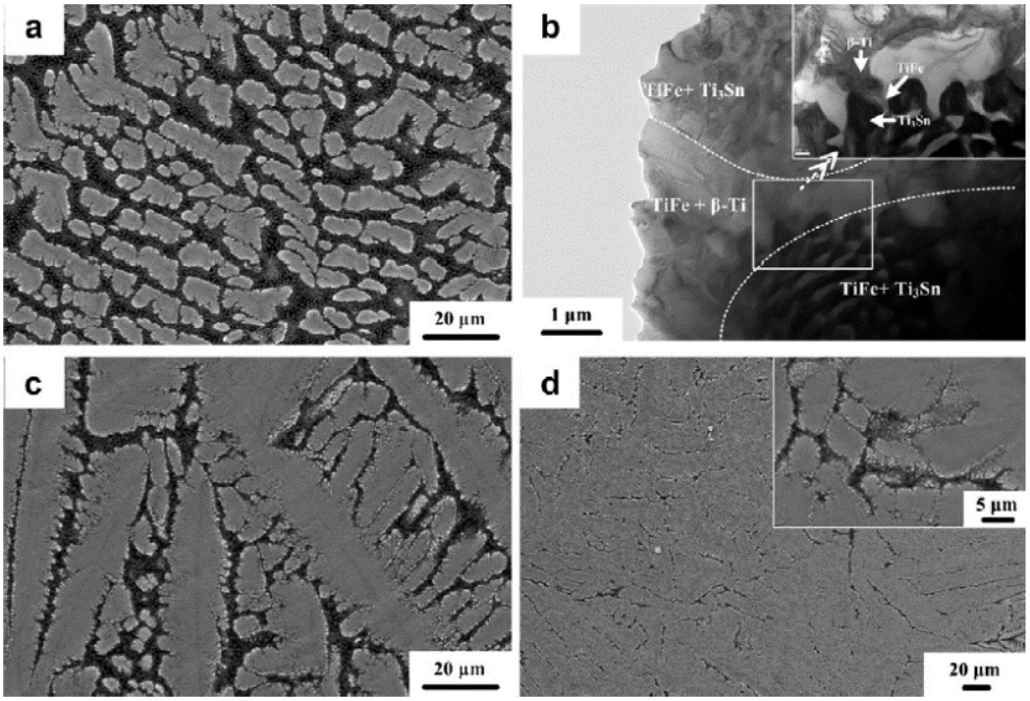

Figure 1.11: SEM [(a), (c) and (d)] and TEM bright field images (b) of the as-cast Ti-Fe-Sn alloys bimodal eutectic composites (a) and (b) $Ti_{63.5}Fe_{30.5}Sn_6$, (c) $Ti_{61}Fe_{32}Sn_7$ and (d) $Ti_{59}Fe_{33}Sn_8$, respectively [32]

As shown in Figure 1.11, no µm-scale primary dendrites were formed here. They further managed to increase the volume fraction of the visibly bright (FeTi + Ti_3Sn) eutectic, as is apparent by the SEM images, by compositional tuning in $Ti_{61}Fe_{32}Sn_7$ and $Ti_{59}Fe_{33}Sn_8$ alloys [32]. This composite structure showed yield strength (1.8 GPa), compressive strength (2.1 GPa) and plasticity (8.4 %) at par with bimodal 'eutectic + dendrite' structures we discussed earlier. The mechanical behaviour is found to be directly influenced by the relative volume fractions of the eutectics. Increasing (TiFe + Ti_3Sn) volume fraction in $Ti_{61}Fe_{32}Sn_7$ and $Ti_{59}Fe_{33}Sn_8$ led to decreasing strengths and plasticity, with plasticity falling to 4 % for $Ti_{59}Fe_{33}Sn_8$. This composite deformed mainly by shear bands propagating along the interfaces between the bimodal eutectic structures with (TiFe + Ti_3Sn) phases acting as barriers. High volume fraction of this eutectic reduced the interface, increased colony size and modified colony morphology making it unfavorable for band propagation and colony rotations.

1.2.5 Microstructure evolution in Ti-Fe-Sn system

Based on previous discussions, it can be inferred that microstructure of Ti-Fe-based Ti-rich eutectics depends mainly on composition (especially alloying elements), casting method and solidification/cooling rate. Hypoeutectic compositions (Fe < 29.5 at %) result in bimodal (β-Ti + FeTi) eutectics with embedded primary β-Ti dendrites, while hypereutectic ones grow with primary FeTi dendrites. Upon Sn addition, Ti_3Sn dendrites in a bimodal eutectic, or in a 'bimodal nanoeutectic composite' with two types of eutectic colonies for certain compositions, can be obtained. Unfortunately, no equilibrium Ti-Fe-Sn ternary phase diagram was found in literature and very little is known regarding phase selection and microstructure evolution in these alloys.

Samal et al. [33] performed extensive microscopy studies on suction cast hypoeutectic alloys $Ti_{71}Fe_{29-x}Sn_x$ (x=0, 2, 2.5, 3, 3.85, 4.5, 6 and 10 at %) to identify various phase-forming reactions and reported a Gibbs ternary plot for Ti-rich end of Ti-Fe-Sn alloys (see Figure 1.12). Several alloys discussed in the previous section and their references are marked on it. The liquidus projections marked as dotted lines A-P, E1-P and E2-P separate the liquidus surfaces for FeTi, Ti_3Sn and β-Ti. They were determined by Song et al. [31].

Samal et al. [33] determined the average composition of P to be $Ti_{69.2\pm0.8}Fe_{27.4\pm0.7}Sn_{3.4\pm0.2}$, marked by the pink diamond in Figure 1.12, and approximately the same as projected by Song et al. [31].

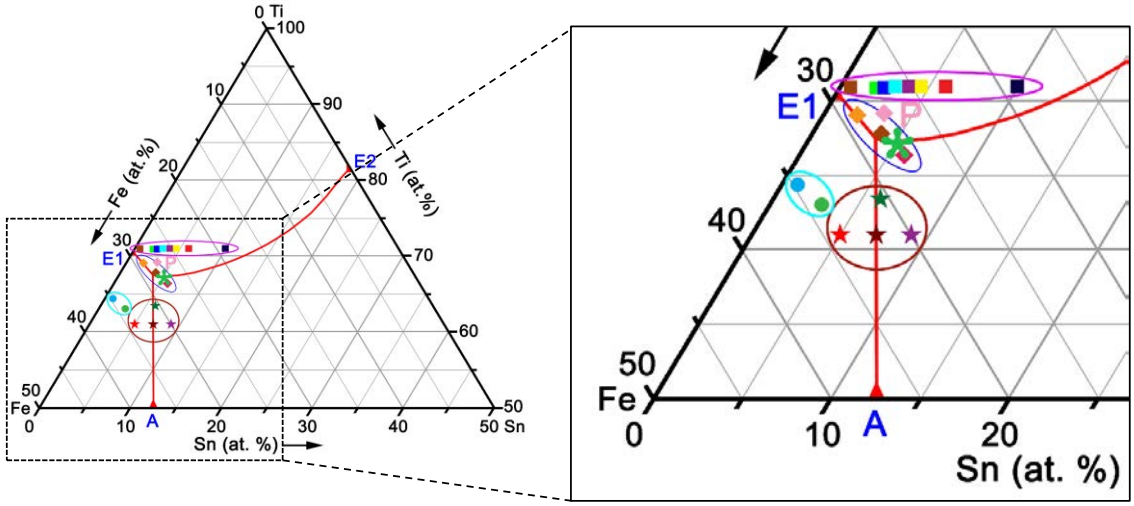

Figure 1.12: *(for colour version please refer to the online version of the figure)* Gibbs ternary plot of Ti-Fe-Sn alloys. Green star "*" approximately denotes the studied alloy $Ti_{66}Fe_{27}Nb_3Sn_4$ while neglecting the Nb content. Closed loops in different colours show the alloys studied by different groups. Closed loop in pink (alloys studied by Samal et al. [33] $Ti_{71}Fe_{29-x}Sn_x$ (x = 2, 2.5, 3, 3.85, 4.5, 6, and 10 at %) denoted by squares), red closed loop (alloy studied by Song et al. [32] denoted by stars), cyan closed loop (alloy studied by Han et al. [27] denoted by dots), and blue closed loop (alloy studied by Das et al. [26] denoted by diamonds). Point P (filled diamond in pink): $Ti_{69.2\pm0.8}Fe_{27.4\pm0.7}Sn_{3.4\pm0.2}$ determined by Samal et al. [33]. Liquidus projections drawn according to Song et al. [31]. Reproduced and adapted from Samal et al. [33]

The microstructure evolution in all studied alloys occurred in three main steps or reactions during cooling, namely, the formation of Ti_3Sn, formation of FeTi and lastly the eutectic reaction [33]. These steps are elaborated in the following paragraphs which mention their proceedings based on alloy compositions and cast specimen dimensions, as reported by Samal et al. [33].

1. Formation of Ti_3Sn:

For alloys with low Sn-content (x = 2, 2.5, 3, 4.5 at %, see inside the pink circle above the invariant point P in Figure 1.12), Ti_3Sn started forming as a result of the peritectic reaction**: L + β-Ti → Ti_3Sn**. Signs of the peritectic reaction were somewhat visible under SEM and TEM (see Figure 1.13 (a-c)). However, high cooling rates during suction casting did not allow the reaction to complete leaving some β-Ti unreacted. This β-Ti was found to undergo a eutectoid transformation: **β-Ti → α-Ti + FeTi** during solid state cooling, leaving behind clearly visible α-Ti and FeTi phases around Ti_3Sn dendrites as shown in Figure 1.13(a-c).

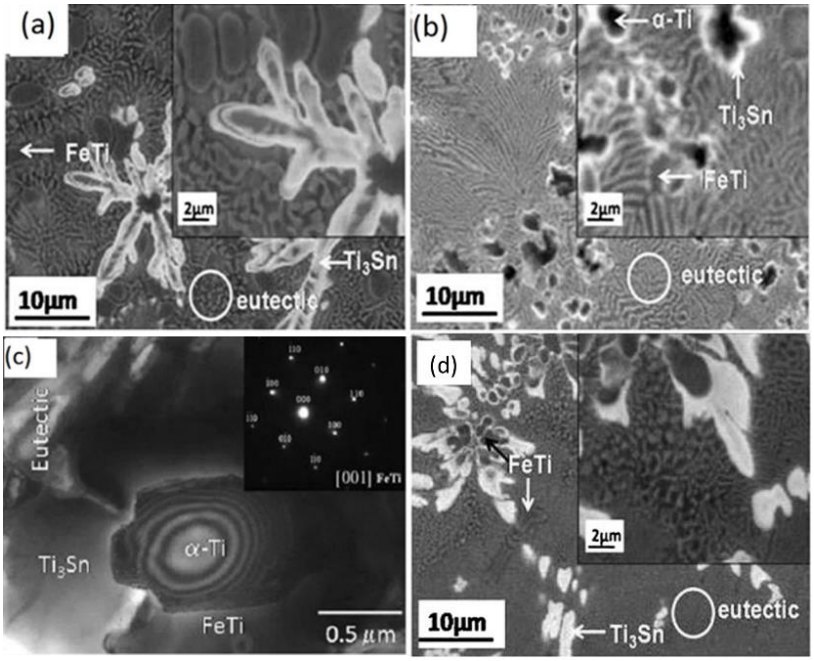

Figure 1.13: SEM backscattered electron micrographs of suction cast (diameter = 3 mm) cylinders of alloys: (a) $Ti_{71}Fe_{25.15}Sn_{3.85}$ and (b) $Ti_{71}Fe_{25.15}Sn_{4.5}$, (d) $Ti_{71}Fe_{23}Sn_{6}$. (c) Bright field TEM micrograph of $Ti_{71}Fe_{25.15}Sn_{4.5}$ showing the presence of different phases in the microstructure [33]

On the other hand, two alloys with the highest Sn content (i.e. x = 6 and 10 at %) grew Ti_3Sn by undergoing a univariant reaction: **L + FeTi → Ti_3Sn**. As shown in SEM micrograph of $Ti_{71}Fe_{23}Sn_6$ in Figure 1.13(d), Sn content beyond 4.5 at % resulted in extensive Ti_3Sn phase and reduction of FeTi phase. Ti_3Sn morphologies further indicated formation from liquid and FeTi.

Ti_3Sn, along with FeTi, can form directly from the liquid (**L → Ti_3Sn**) which was observed in $Ti_{71}Fe_{25.15}Sn_{3.85}$ cylindrical specimens of 1 mm diameter. This was characterised by free dendritic growth morphology of Ti_3Sn with six arms, as shown in Figure 1.14. However, 3 mm diameter cylindrical specimens of the same alloy were found to proceed through the peritectic reaction (see Figure 1.13(a)), evidencing the strong influence of the solidification rate on microstructure evolution, since thicker samples cool down slower.

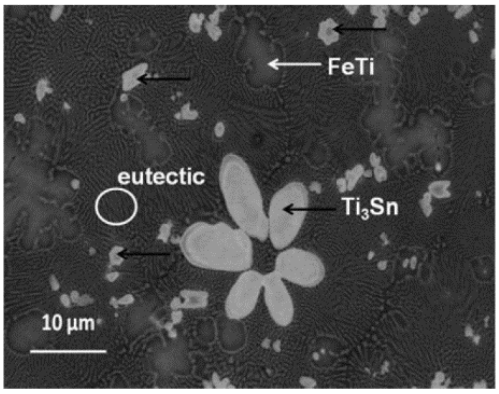

Figure 1.14: SEM backscattered electron micrograph of suction cast (diameter = 1 mm) cylinder of $Ti_{71}Fe_{25.15}Sn_{3.85}$ alloy showing free growth of Ti_3Sn (marked as black arrow) [33]

2. Formation of FeTi:

Ti_3Sn growth makes the remaining liquid rich in Fe and all melt compositions move towards the invariant quasi-peritectic point P (see Figure 1.12). At P, FeTi phase started forming via the ternary quasi-peritectic reaction: **L + Ti_3Sn → β-Ti + FeTi**.

3. Eutectic reaction:
The last step involves the co-precipitation of β-Ti and FeTi (eutectic reaction**: L → β-Ti + FeTi**) from the residual melt proceeding along the univariant valley P-E1.
Meanwhile, the 1 mm thin specimens of $Ti_{71}Fe_{25.15}Sn_{3.85}$ proceeded directly to the eutectic reaction after free dendritic growth of Ti_3Sn from the liquid, thus completing the solidification in two steps.

Song et al. [31, 32], suggested the same reaction pathway as that of alloy $Ti_{71}Fe_{25.15}Sn_{3.85}$ behind the formation of bimodal nanoeutectic structures containing (TiFe + Ti_3Sn) and (β-Ti + FeTi) eutectics as discussed in section 1.2.4. In addition, they had found that $Ti_{61}Fe_{34}Sn_5$ and $Ti_{59}Fe_{33}Sn_9$ also featured primary dendrites of FeTi and Ti_3Sn (alloys are marked by red circle in Figure 1.12) respectively which makes sense looking at the ternary phase diagram. They concluded that the evolution of such bimodal composites started with the univariant reaction: **L → FeTi + Ti_3Sn** which proceeds along the univariant valley A-P. This led to the formation of ultrafine (FeTi + Ti_3Sn) binary eutectic. When the melt compositions reach the invariant point P, the quasi-peritectic reaction**: L + Ti_3Sn → β-Ti + FeTi** starts occurring. As in the case of hypoeutectic alloys studied by Samal et al. [33], this was followed by the eutectic reaction: **L → β-Ti + FeTi** which forms the coarser secondary eutectic.

1.2.6 Laser additive manufacturing of Ti-Fe ultrafine eutectics

Wang et al. [36] produced $Ti_{70.5}Fe_{29.5}$ by laser-induced synthesis of a powder blend consisting of elemental Ti and Fe powders mixed in a eutectic composition. They reported a microstructure containing eutectic (β-Ti + FeTi) with inter-lamellar spacing (λ) below 600 nm. However, the high cooling rates and Oxygen content resulted in grains of Fe_2Ti_4O or Oxygen stabilised $FeTi_2$ between the eutectic cells. Later, Han and Wang [37] produced an alloy $Ti_{64.5}Fe_{26.40}Zr_{5.86}Sn_{2.93}Y_{0.30}$ where they managed to get rid of this oxide by adding small quantities of Zr and Y which act as Oxygen-getters. In this case, elemental powders were ball-milled and used to deposit layers by laser-melting. An ultrafine eutectic structure (mean λ = 450 nm) and a high compressive strength of 2.2 GPa along with 14 % plasticity were reported. Although the alloy showed a low elastic modulus of 87.5 GPa, they argued that the comprehensive performance was better than commercial Ti-6Al-4V alloy. Figure 1.15 compares the microstructure of the alloy $Ti_{64.5}Fe_{26.40}Zr_{5.86}Sn_{2.93}Y_{0.30}$ to that of $Ti_{70.5}Fe_{29.5}$ produced by Wang et al. [36].

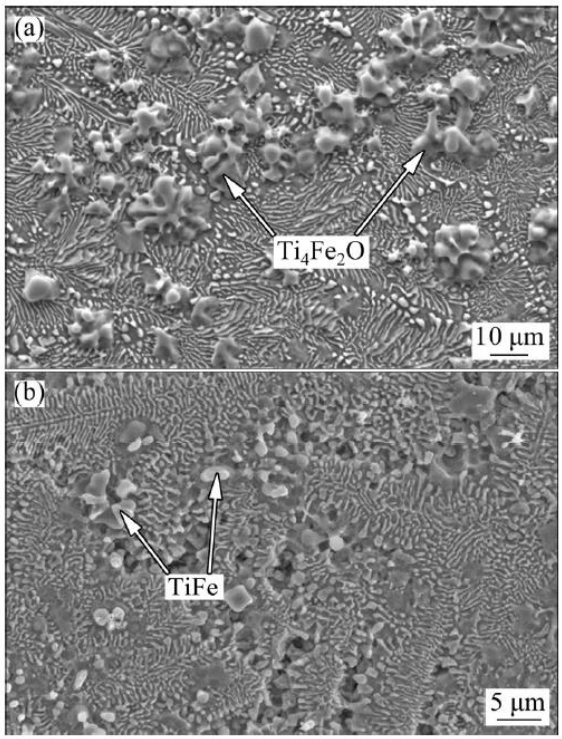

Figure 1.15: SEM micrographs showing microstructures of (a) $Ti_{70.5}Fe_{29.5}$ and (b) $Ti_{64.5}Fe_{26.40}Zr_{5.86}Sn_{2.93}Y_{0.30}$ prepared by laser-melting [37]

Afonso et al. [38] used ball-milled elemental (and a few binary alloyed) powders to produce laser-clad coatings of $Ti_{66}Fe_{20}Nb_8Sn_6$ on a Ti substrate. The alloy microstructure and properties depended strongly on the laser parameters (laser power and scanning speed) used. Figure 1.16 shows SEM micrographs of the laser-cladded alloy coating for various sets of processing parameters, as reported by Afonso et al. [38]. Although they failed to obtain a completely homogenous melt pool using mechanically alloyed powders, they still managed to grow an ultrafine eutectic matrix at low laser power (200 W) and scanning speed (16.7 mm/s), which also featured Ti_3Sn and β-Ti dendrites growing in several locations depending on the local composition (see Figure 1.16(d)). Further, a cellular morphology was observed near the boundaries, occurring due to relatively higher cooling rates, which transitioned into a finer eutectic matrix towards the interior. Higher laser powers resulted in coatings consisting almost entirely of β-Ti with segregated alloying elements, very distinctly visible in Figure 1.16(a) as grayscale contrasts. The laser-clad coatings demonstrated nano-hardnesss of 4.8 – 8 GPa and elastic modulus of 98 – 150 GPa depending on the laser parameters used.

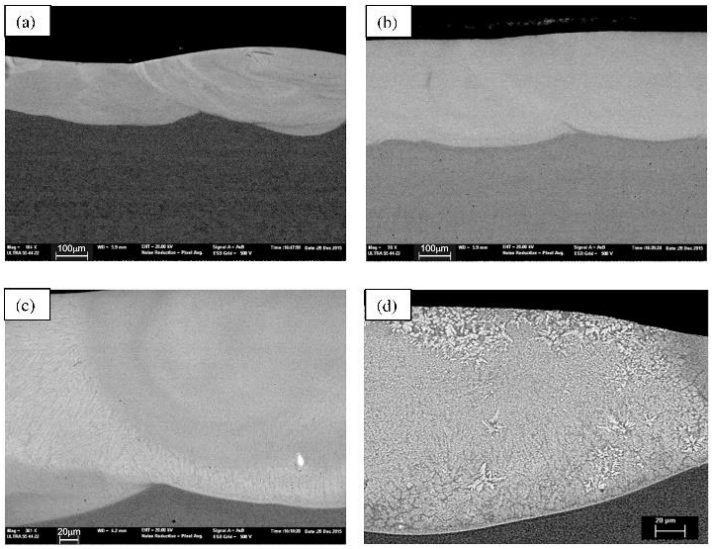

Figure 1.16: SEM micrographs of typical coating profiles obtained by laser cladding of pre-alloyed powders of $Ti_{66}Fe_{20}Nb_8Sn_6$ alloy for combinations of laser parameters: (a) 800 W (33.3 mm/s); (b) 600 W (16.7 mm/s); (c) 400 W (16.7 mm/s); and (d) 200 W (16.7 mm/s) [38]

Our collaborators Gussone et al. [39] fabricated a bulk eutectic alloy Ti-32.5 Fe (wt %) by SLM using elemental powders. Using process energy densities between 160 J/mm^2 and 180 J/mm^2 resulted in a dense crack-free material with an ultrafine microstructure. The mean λ values of the (β-Ti + FeTi) eutectic colonies varied from ≈ 160 nm to ≈ 50 nm with values as low as 30 – 50 nm. This is finer than conventional casting techniques and results from the high cooling rates of SLM. However, an Oxygen content of ≈ 0.45 wt % led to µm-size η-$Fe_2Ti_4O_x$ dendrites which were embedded in a (β-Ti + FeTi) matrix, thus forming a hierarchically structured eutectic. It further demonstrated a compressive strength of ≈ 800 MPa with a high strain ≈ 30 % without damage at 600 °C. Figure 1.17 shows the microstructure of the SLM-built alloy along with marked phases.

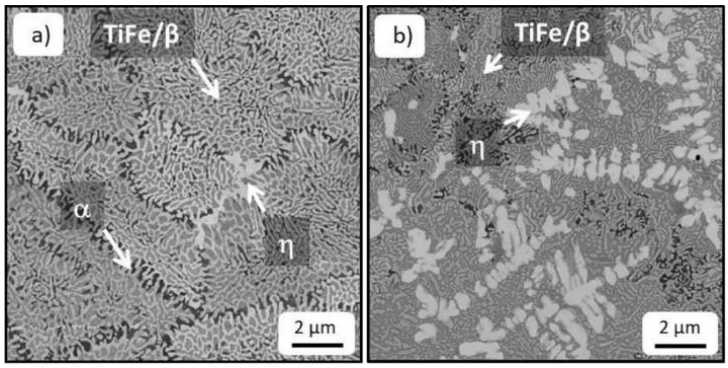

Figure 1.17: (a and b) SEM micrographs of SLM-built Ti-32.5Fe (wt %) produced on a substrate preheated to 790 °C with energy density 178 J/mm^3

Other collaborators Requena et al. [40] investigated the additive manufacturing of Fe-rich near-eutectic composition Fe-17.6 at % Ti using elemental powders with a maximum laser output of 2 kW. They used Directed Energy Deposition (DED) to obtain an ultrafine lamellar

microstructure consisting of Fe_2Ti and α-Fe lamellas with λ ranging 190 ± 25 nm. However, the inter-layer boundaries (thickness 12 ± 5 µm) displayed a globular morphology with primary Fe_2Ti phase surrounded by α-Fe layers, as shown in Figure 1.18. Further investigation suggested that partially remelted and spheroidized particles of eutectic lamellae from previous layers acted as nucleus for the growth of the globular phases in the inter-layer. Using experimental data, they further managed to develop a phase-field simulation of the melt pool, which successfully predicts the coupled growth of binary eutectics. Figure 1.19 shows the simulation results for the solidification of a new layer during laser melting occurring via the nucleation of a globular inter-layer on remelted particles, very much resembling the experimentally observed microstructures.

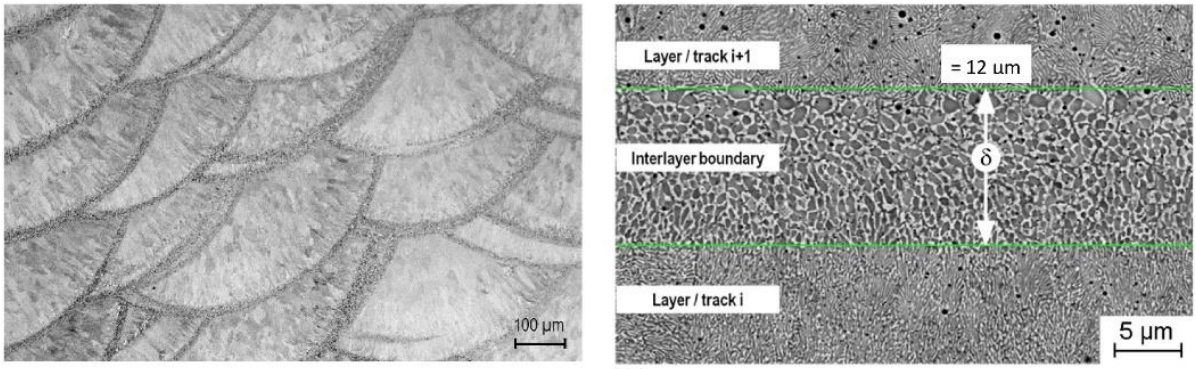

Figure 1.18: Microstructures of DED-built Fe-17.6 at % Ti alloy showing elongated eutectic grains in the layers and inter-layer boundaries with distinct globular morphology as observed by (a) optical microscopy and (b) backscatter electron microscopy(SEM-BSE) [40]

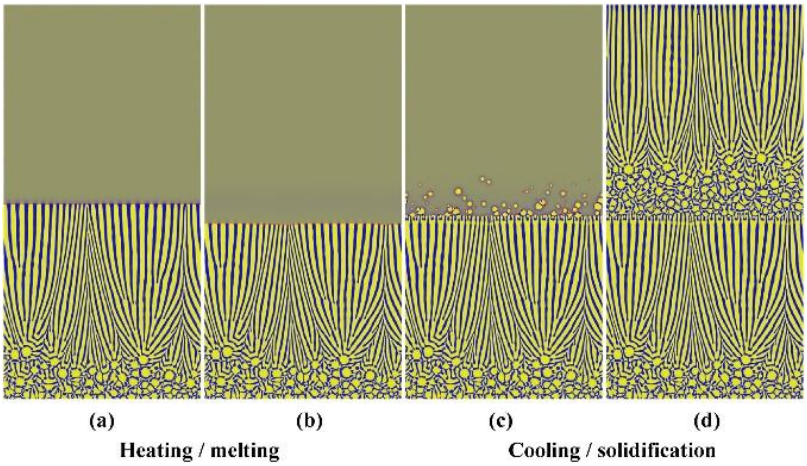

Figure 1.19: Snapshots of the composition map from the phase-field simulation of melting and solidification during a full heating/cooling cycle of laser additive manufacturing, as presented by Requena et al. [40]. Time elapses from left to right showing (a) the lamellar eutectic structure from the previous cycle and freshly melted powder on the top, (b) the remelting of the topmost part of the lamellar structure during heating, (c) the epitaxial growth of the lamellae and the nucleation of the primary phase ahead and (d) the subsequent growth of elongated eutectic grains during cooling.

1.3 Raw materials for laser additive manufacturing: metallic powders

1.3.1 Atomisation techniques for powder production

Powders for AM, as well as for conventional Powder Metallurgy (PM) and Metal Injection Moulding (MIM) processes, are mostly mass-produced by atomisation. Several powder atomisation techniques are used today such as gas, water, plasma, plasma rotating electrode and centrifugal processes [41]. The atomisation method and atmospheric conditions used, determine the properties of produced powders. Gas and water atomisation are the most common for producing AM feedstock.

In gas atomisation, a low-velocity liquid metal stream is introduced suddenly to a relatively very high-velocity gas (usually inert) stream that breaks it into small droplets cooled rapidly by convection. Water atomisation uses a high-pressure water stream instead of gas as the cooling medium. Although it is cheaper than other atomisation processes, it can lead to oxidation in reactive metals and alloys. The morphology of solidified particles is defined by the spheroidisation and solidification time [42]. Higher specific heat of water leads to higher quenching rates during water atomisation as compared to gas, thus resulting in lower solidification times than what it is required for spheroidisation of droplets. This produces irregularly shaped particles. Powders produced by gas atomisation have high sphericity, high cleanliness and a homogeneous microstructure. Figure 1.20 compares the morphology of 316L stainless steel powders produces by gas and water atomisation [43].

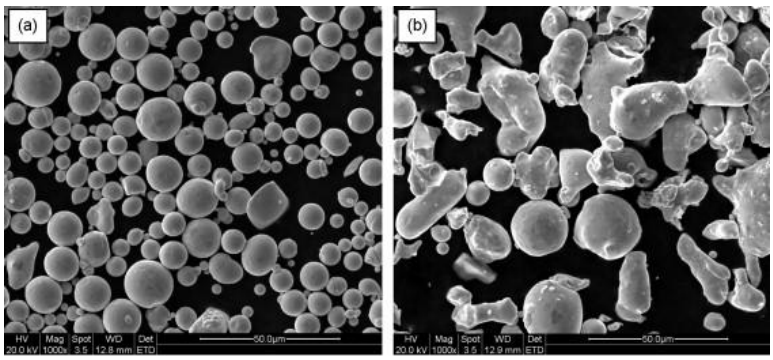

Figure 1.20: SEM micrographs showing powders of 316L stainless steel produced by (a) gas and (b) water atomisation [43]

In gas atomisation, the shape of powders can be controlled during production stage by choosing the gas and controlling the gas temperature and pressure used [42, 44–46]. Argon is known to produce more spherical powders than Nitrogen [44]. A slightly heated gas can increase the solidification time leading to higher sphericity and less irregularly shaped powder [42]. However, the gas pressure and flow parameters have to be optimised depending on the nozzle and chamber geometry. Inappropriate gas pressure and circulation can result in formation of flakes/needle-shaped particles and cause collisions between particles creating satellites and deformed particles [46].

Powder size distribution and yield depend on the gas and pressure used, melt temperature (viscosity) and melt flow rate [44–47]. Particles becomes coarser and show more size dispersion with increasing flow rate, while Helium is known to produce finer particles than Nitrogen or Argon. Higher melt temperature or low melt viscosity results in lower average size of produced powder. These parameters have to be optimised during powder production stage considering the alloy and atomisation set up used.

Cooling rates involved in gas atomisation are typically very high, ranging from 10^4 to 10^6 K/s depending on the particle size. This often leads to metastable phases forming in the powder [48, 49]. Higher surface-to-volume ratio and more efficient heat exchange with the gas results in higher cooling rates in smaller particles, thus making crystallisation kinetics dependent on powder particle size [45, 48, 49].

Plasma-based atomisation methods have been known to produce powders with higher sphericity and uniform size distribution as compared to gas-atomised ones [50], but their relatively high cost makes gas atomised powders the most popular choice for SLM.

As shown in Figure 1.21, mainly three types of gas atomisation set-ups exist: Vacuum induction melting inert gas atomisation (VIGA), Electrode induction melting gas atomisation (EIGA) and Arc melting atomisation (AMA).

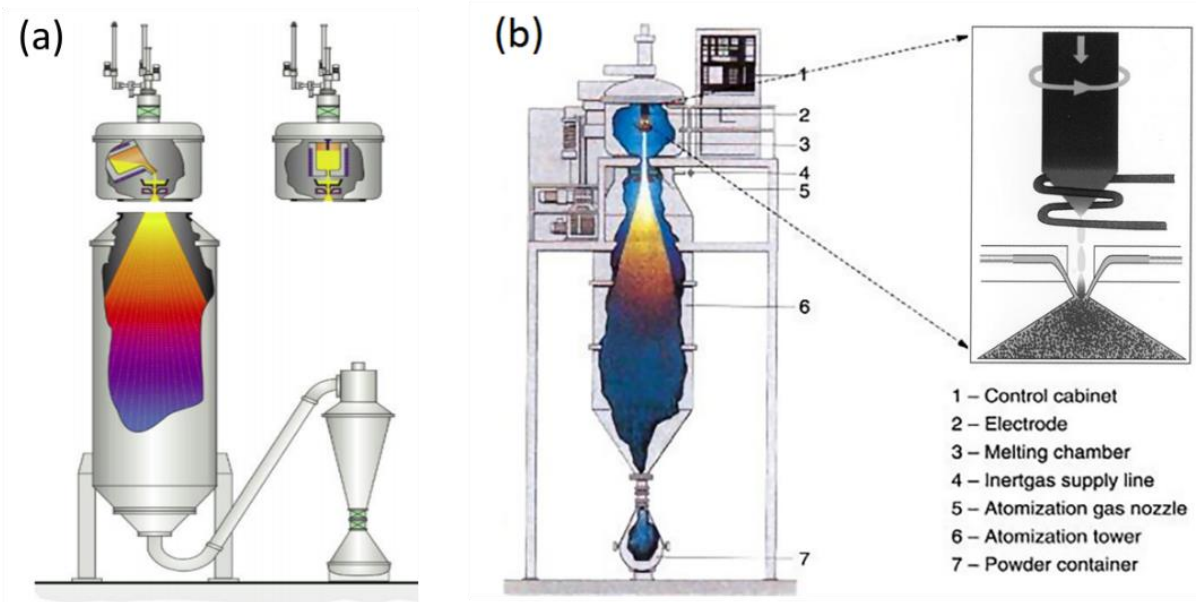

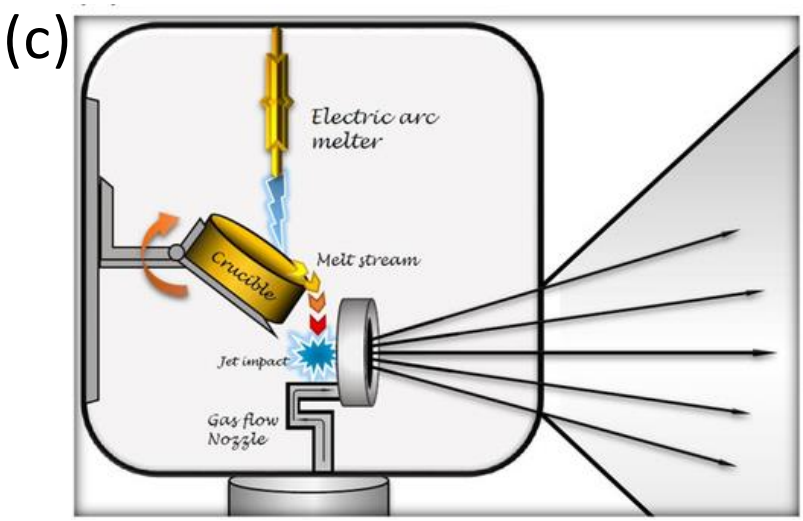

Figure 1.21: Schematics showing the basics of gas atomisation processes: (a) Vacuum induction melting inert gas atomisation (VIGA) [51], (b) Electrode induction melting gas atomisation (EIGA) [52] and (c) Arc melting atomisation [53]

In VIGA, materials are molten in a crucible (usually ceramic or graphite) using induction coils and poured into a conical funnel-like ceramic nozzle fixed above a concentric vertical gas stream (see Figure 1.21(a)). ´Free-fall´ atomisation setups also exist that don't use such confined nozzles to direct the melt. The melt is dropped for about 50 – 200 mm in an inert atmosphere before encountering a gas stream [3].

However, EIGA is a crucible-less atomisation technique where rods of material are passed through induction coils, gradually melting and atomising the falling melt (see Figure 1.21(b)). These rods are long and cylindrical with a conical tip where the melting happens while the rod is rotated at a low frequency to ensure symmetric heating. Passing velocity of the rod and the induction power are used to control the melt flow rate [54]. It avoids any direct contamination from crucible, but requires casting and machining of materials into rods of a specific geometry, which can be expensive and very difficult to achieve for some materials.

Arc-melting atomisation technique melts material in a water-cooled copper crucible using an electric arc which is capable of achieving very high melt temperatures (over 3000 ˚C) without any crucible reaction [55]. It has a 'free-fall' setup where the melt is poured from the cold crucible onto a vertical or horizontal gas stream, as shown in Figure 1.21(c). This technique suffers very low material loss and is favourable for reactive and high melting point materials since they easily get contaminated while melting in ceramic crucibles or casting into rods for EIGA.

1.3.2 Powder properties for AM

SLM and LMD processes require powders to firstly have good flowability and packing density for achieving good part densification and avoid clogging issues [56]. These properties further depend on particle morphology (spherical, spherical with satellites, irregular, etc.), size distribution and surface chemistry of powders, which are again inter-linked. The following sections discuss the importance and inter-dependence of these powder characteristics, along with the common characterisation techniques associated with them.

1.3.2.1 Flowability

Flowability is not an inherent powder property and is specific to the equipment and measurement technique used. It is the overall result of a complex combination of measurable bulk properties that affect powder flow under stress. Schematic in Figure 1.22 shows the classification of various measurable powder parameters into four main groups which are further inter-related [57, 58].

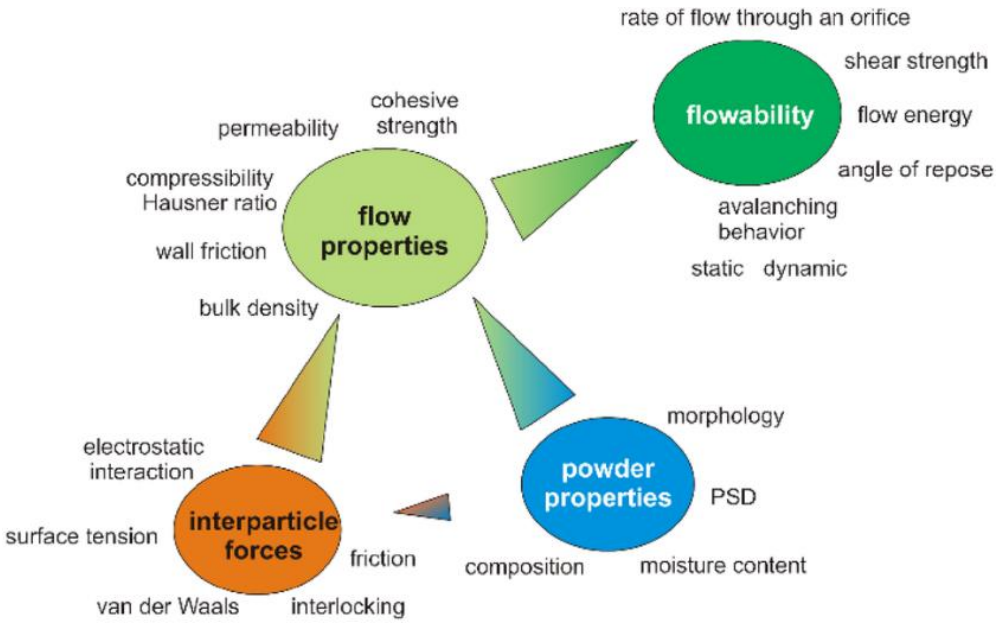

Figure 1.22: Schematic showing the relations between powder properties, inter-particle forces, flow properties and flowability along with their respective measurable parameters [57, 58]

Flowability is usually higher for spherical coarser particles and increases as the particle size distribution becomes narrower [59–65]. Humidity or powder moisture content is a crucial parameter. High humidity leads to water absorption and powder agglomeration, while over-drying of powders can generate static electricity, deteriorating the flowability in both cases [42, 59, 66].

The common parameters used to comparatively assess flow properties and flowability of AM powders are Hausner ratio (HR), angle of repose (AOR) and flow rate through an orifice. Hausner ratio is defined as the ratio between powder tap density (ρ_{tap}) and apparent density

($\rho_{apparent}$) determined as per ASTM D7481 [67]. A ratio ≤ 1.25 usually means a free-flowing powder, while HR > 1.4 represents high powder compressibility and poor flowability [68]. AOR and flow rate through an orifice are commonly measured using a Hall flowmeter as per ASTM B213 [69]. The angle made by the slope of the deposited powder heap with the base plate, after flowing through a Hall funnel is known as AOR. Lower AOR means better flowability and well-flowing powders usually have a AOR < 30 ° [70]. The flow rate is estimated by measuring the discharge time for 50 g of powder. Lower discharge time means higher flow rate and higher flowability. Ti-6Al-4V powders produced by gas atomisation techniques for SLM have been reported to show flowrates between 26.2 to 35.3 s/50 g when measured at 23 °C and 38 % relative humidity [42].

A more advanced and recent technique characterises rheological properties of powders by measuring the avalanche angle while it is continuously moved sideways inside a rotating drum, as shown in the schematic in Figure 1.23. The purpose is to simulate the deposition of multiple powder layers during PBF processes like SLM. The avalanche angle usually lies between 49° to 54° for well-flowing powders with a Gaussian size distribution. Further, rheometers like Freeman FT4 Rheometer [71] are also used to measure the flow resistance of powders (in terms of basic flow energy) under low stresses similar to SLM conditions.

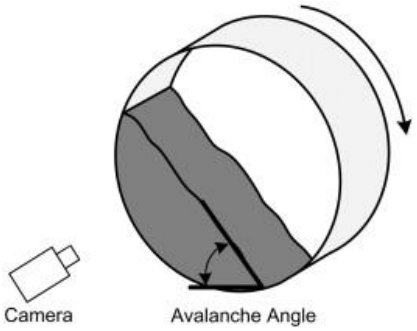

Figure 1.23: Schematic showing avalanche angle measurement in a revolution powder analyser [72]

1.3.2.2 Morphology

Powder particles are classified into different shapes, such as spherical, rounded, irregular, dendritic, flake, etc., as per the geometries described in ASTM B243 [73]. Particle morphology with high sphericity or an aspect ratio close to 1 is ideal for SLM feedstock as it is associated with increased apparent density and mass flow rate, as shown in Figure 1.24. Irregularly shaped and rough powders produced by water atomisation have been reported to produce higher porosity in AM parts as compared to those fabricated using spherical and smoother gas atomised powders [43].

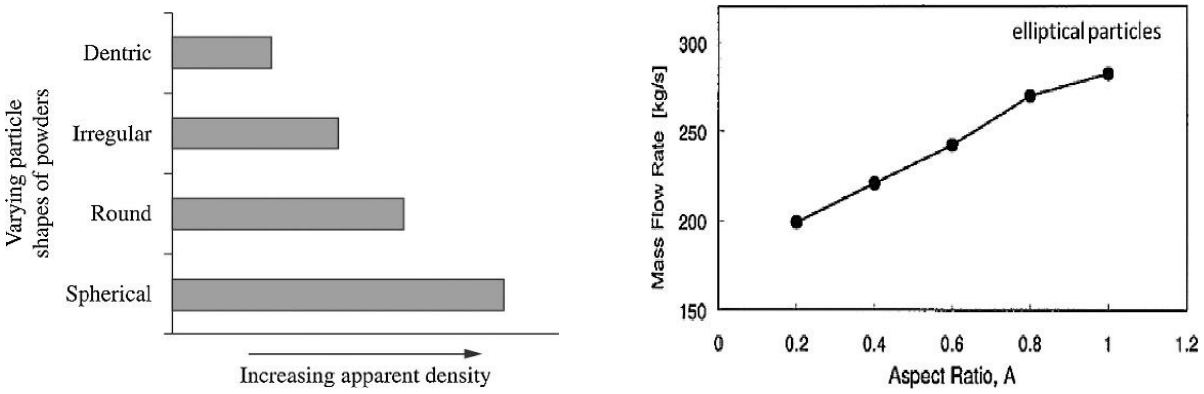

Figure 1.24: (left) Variation of apparent density with powder shape [74], (right) Variation of mass flow rate with aspect ratio of particles [75]

Although gas atomised powders generally show a spherical morphology, some undesirable shapes and defects, as shown in Figure 1.25, are often encountered. They can form as a result of incomplete spheroidisation and collisions between particles during atomisation leading to fusion, damages and deformations. All defects, especially the presence of satellites, adversely affect the aspect ratio of particles, their flow and the powder-packing ability [76, 77]. However, smooth and spherical particles can still suffer from less apparent defects like internal porosity, formed as a result of gas entrapment during solidification (see Figure 1.26). For all atomisation techniques and alloys, porosity content usually increases with increasing particle size up to a certain size and then remains fairly constant [78]. Beside gas entrapment, interdendritic solidification shrinkage can also create fine pores inside particles [79]. Closed porosities with trapped gases are detrimental to AM as their content and distribution in powders is known to be directly linked to the content and distribution of spherical gas pores in the final AM parts [80]. Further, they can coalesce into macropores at elevated temperatures, thus requiring proper post-processing treatments of the parts under high external pressures like hot isostatic pressing (HIP) [80, 81].

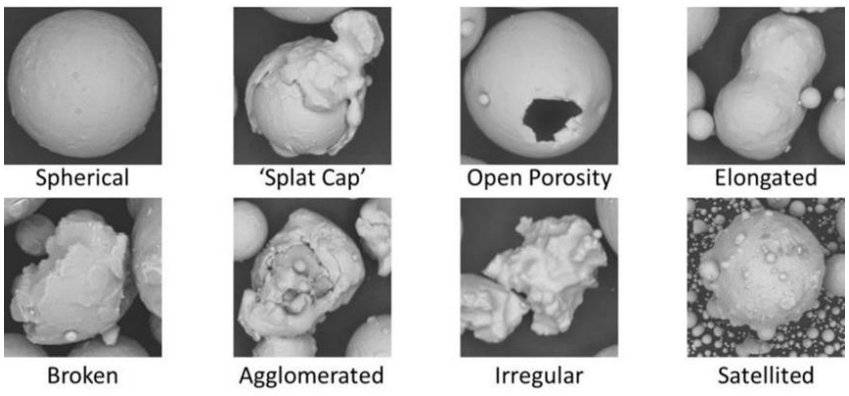

Figure 1.25: Various particle shapes typically observed in gas atomised powders [82]

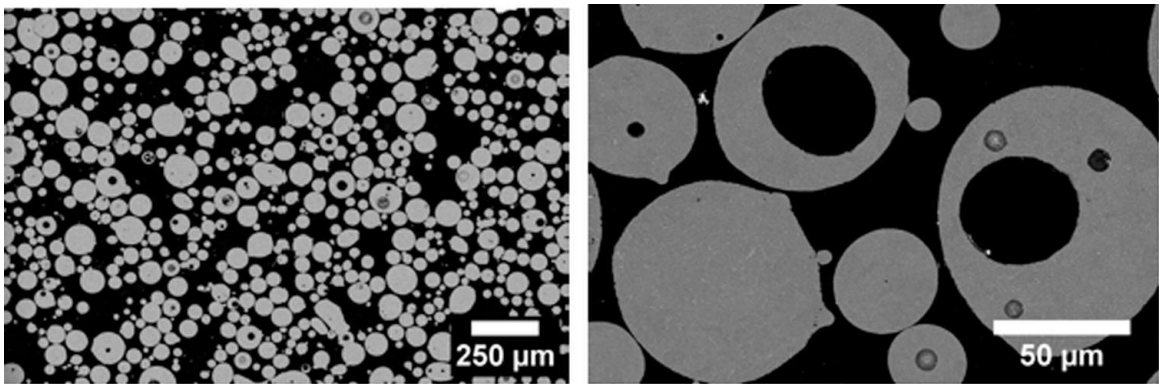

Figure 1.26: SEM micrographs showing internal porosity in the cross-sections of gas atomised MAR-M-247 powder (size range 45 – 106 µm) at low and high magnifications [83]

Powder morphology, as well as internal porosity, are most commonly characterised by visual inspection of particles and their cross-sections using optical microscopy, Scanning Electron Microscopy (SEM) or X-ray Computed Tomography (XCT). High resolution static image analysis tools (like Morphologi G3, Camsizer M1) can be used to quantify geometrical features like Feret´s diameter, aspect ratio and circularity based on 2D projections of captured optical images of particles. Feret´s diameter is the distance between two parallel tangents drawn on the contour of the particle projection. This is measured repeatedly by rotating the projection a number of times. These projections are also used to determine the area equivalent diameter and the perimeter equivalent diameters, which are the diameters of theoretical circles with the same area and perimeter as the projection respectively. Based on these values the aspect ratio (denoted by B/L) and circularity of the projected shape (denoted by C) are estimated using the following equations [84]:

$$\boldsymbol{Aspect\ ratio}\ \frac{B}{L} = \frac{F_{min}}{F_{max}}$$

Equation 1.2

$$\boldsymbol{Circularity}\ C = \sqrt{\frac{4 \cdot \pi \cdot Area}{Perimeter^2}} = \frac{x_{area}}{x_P}$$

Equation 1.3

$$\boldsymbol{Sphericity}\ S = C^2$$

Equation 1.4

Where F_{min} and F_{max} represent the minimum and maximum ferret´s diameters measured while rotating the projection, x_{area} is the area equivalent diameter and x_P is the perimeter equivalent diameter.

A high circularity represents high sphericity and is equal to 1 for a perfect circle. Commercial Ti-6Al-4V powders have a circularity ≥ 0.95 [85, 86].

1.3.2.3 Particle size distribution

Most of the powders produced commercially for SLM possess a Gaussian size distribution. Based on the available literature, the appropriate feedstock should have a granulometry with $D_{90}/D_{10} \leq 19$ and D_{90} << layer thickness [73, 87]. A narrower PSD has been reported to result in better ultimate tensile strength and hardness in fabricated steel parts, while a wider PSD was observed to produce better powder bed density, part density and surface quality (face parallel to build direction) [88]. Other studies [64, 89–91] have concluded that a PSD biased towards fine particles leads to better packing of voids and thus, better part density and surface quality, but, a bias towards coarse particles results in better mechanical properties. Sometimes a bimodal distribution containing a mix of fine and coarse powders can result in better packing density through effective size mixing and percolation. However, smaller particles, especially below 30 µm tend to agglomerate easily due to dominating adhesive forces like Van der Waals [92]. This adversely affects powder flowability and apparent density [93], as shown in Figure 1.27.

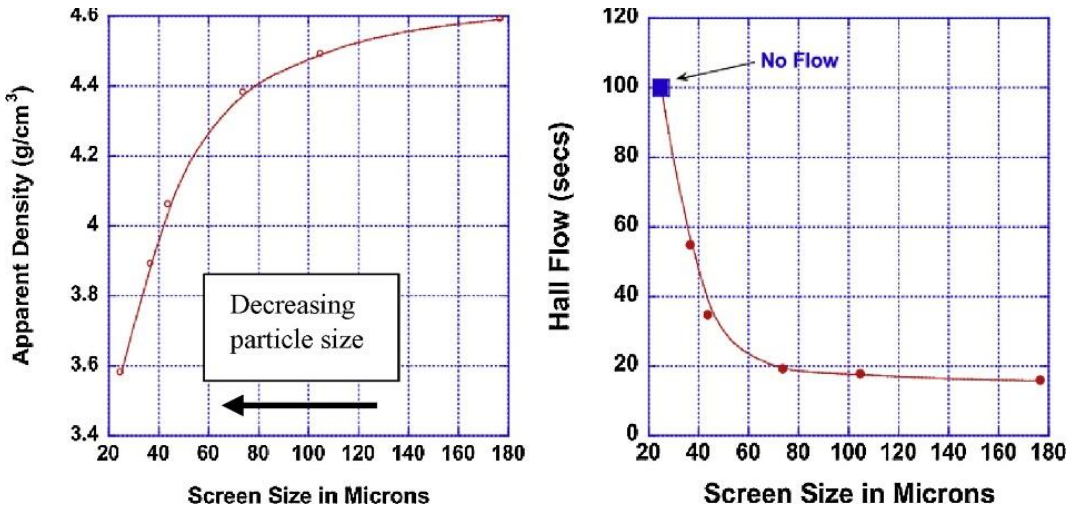

Figure 1.27: Effect of powder size on apparent density (left) and hall flow time (right) [93]

For SLM of most materials, the used powder size range is 20 – 63 µm. LMD uses slightly larger particles between 45 – 90 µm to maintain a consistent flow through the carrier gas [23]. Using smaller particles, especially below 20 µm, can lead to very inconsistent flow and significantly increases the risk of clogging the nozzle and dispersing powder particles into the surrounding [94].

Common techniques used to characterise size distribution of powders are sieve analysis, laser diffraction, static and dynamic image analysis. The disadvantage of using sieve analysis is that it is quite expensive and time-consuming to obtain a distribution with a narrow bin size. Laser diffraction is a quick technique that generates size related information of particles by measuring angle and intensity changes in light scattered by them [95]. Larger particles scatter light more intensely and at smaller angles. However, it is not reliable for non-spherical shapes and requires knowledge of the particle refractive index. Static image analysis techniques, in

addition to quantifying shape-related features as described in section 1.3.2.2, can also generate size and volume related information from 2D projections. For the purpose of volume calculations, the particles are assumed to be spheres with diameters equal to their area equivalent diameter x_{area}. A volume-based distribution of size, sphericity, aspect ratio, etc. can thus be obtained from 2D projections. Dynamic image analysis instruments (like Camsizer X2) use two cameras to observe large and small particles separately at different magnifications while the powder particles are passed through a pulsed light source [96]. This improves the accuracy much further than static image analysis methods, especially for particles with irregular shapes and satellites.

1.3.2.4 Surface chemistry

It is desirable for powders to have a low Oxygen and Hydrogen content since such interstitial contamination can adversely affect layer adhesion during SLM. Presence of Oxygen also can lead to formation of surface oxides on powder particles reducing their flowability [74], as well as create porosity and inclusions during the AM processes [97, 98]. High concentration of oxides can cause embrittlement in fabricated structural alloys and degradation of mechanical properties in general [99]. Exposure to moisture or high humidity can result in contamination by hydroxides on powder surfaces [100]. They form a viscous adsorbate film and hinder powder flow [101]. Also, they can crystallise to produce oxides in build chamber conditions at high temperatures. Laser interaction with adsorbed water molecules on the powder surface can dissociate Hydrogen atoms and lead to trapped gases in the melt pool [102]. Some powders need to be pre-heated until a low relative humidity (< 0.01 %) is obtained before using in SLM. Moisture content analysis is performed using the weight differences of the powder before and after drying. Humidity and Oxygen sensors are usually used in powder processing and storage facilities. Inert gas fusion is a common technique used to calculate the content of undesirable elements like Oxygen, Hydrogen, Nitrogen and Carbon in metal powders destructively [103]. Some powder is fused in a furnace and an inert gas carrier takes the produced gases through a serious of infrared and thermal conductivity sensors that quantify the respective elements in them. Contaminating elements on the powder particle surface are often characterised using X-ray Photoelectron Spectroscopy (XPS). It uses the kinetic energy signatures of irradiated electrons on the surface to identify elements. Powder surface chemistry can also be characterised by measuring changes in surface free energy by the sessile drop method [104] or by observing the adhesion forces using Atomic Force microscopy (AFM) [105]. Commercial Ti-6Al-4V powders produced by gas atomisation for AM have Oxygen content < 2000 ppm and Hydrogen content < 150 ppm [85, 86].

REFERENCES

[1] "Eutectic Systems - Materials Science Questions and Answers - Sanfoundry." https://www.sanfoundry.com/materials-science-questions-answers-eutectic-systems/ (accessed May 22, 2022).

[2] W. Kurz and D. J. Fisher, *Fundamentals of Solidification*. Trans Tech Publications Limited, 1998. [Online]. Available: https://books.google.es/books?id=bFaxDwAAQBAJ

[3] W. C. Winegard, *An Introduction to the Solidification of Metals*. Institute of Metals, 1964. [Online]. Available: https://books.google.es/books?id=YjN8AAAAIAAJ

[4] J. A. Dantzig and M. Rappaz, *Solidification: 2nd Edition - Revised & Expanded*. CRC Press LLC, 2016. [Online]. Available: https://books.google.es/books?id=k1Q-DgAAQBAJ

[5] K. A. Jackson and J. D. Hunt, "Lamellar and Rod Eutectic Growth," *Trans. Met. Soc. AIME*, vol. 236, no. 8, pp. 1129–1142, 1966.

[6] J. H. Han *et al.*, "Influence of a bimodal eutectic structure on the plasticity of a (Ti 70.5 Fe29.5)91 Sn9 ultrafine composite," *Appl. Phys. Lett.*, vol. 93, no. 20, pp. 91–94, 2008, doi: 10.1063/1.3029745.

[7] C. S. Tiwary *et al.*, "Five decades of research on the development of eutectic as engineering materials," *Prog. Mater. Sci.*, vol. 123, p. 100793, Jan. 2022, doi: 10.1016/J.PMATSCI.2021.100793.

[8] "Index." https://princeizant.com/news/eutectic-alloys (accessed May 23, 2022).

[9] C. M. Miller, I. E. Anderson, and J. F. Smith, "A viable tin-lead solder substitute: Sn-Ag-Cu," *J. Electron. Mater. 1994 237*, vol. 23, no. 7, pp. 595–601, Jul. 1994, doi: 10.1007/BF02653344.

[10] S. Gorsse, B. Ouvrard, M. Gouné, and A. Poulon-Quintin, "Microstructural design of new high conductivity – high strength Cu-based alloy," *J. Alloys Compd.*, vol. 633, pp. 42–47, Jun. 2015, doi: 10.1016/J.JALLCOM.2015.01.234.

[11] B. S. Senturk, Y. Liu, J. V. Mantese, S. P. Alpay, and M. Aindow, "Effects of microstructure on native oxide scale development and electrical characteristics of eutectic Cu–Cu6La alloys," *Acta Mater.*, vol. 60, no. 3, pp. 851–859, Feb. 2012, doi: 10.1016/J.ACTAMAT.2011.11.013.

[12] L. M. Kang and C. Yang, "A Review on High-Strength Titanium Alloys: Microstructure, Strengthening, and Properties," *Adv. Eng. Mater.*, vol. 21, no. 8, pp. 1–27, 2019, doi: 10.1002/adem.201801359.

[13] R. J. Contieri, E. S. N. Lopes, M. Taquire De La Cruz, A. M. Costa, C. R. M. Afonso, and R. Caram, "Microstructure of directionally solidified TiFe eutectic alloy with low

interstitial and high mechanical strength," *J. Cryst. Growth*, vol. 333, no. 1, pp. 40–47, 2011, doi: 10.1016/j.jcrysgro.2011.07.007.

[14] Z. O. Yazici, A. Hitit, Y. Yalcin, and M. Ozgul, "Effects of minor Cu and Si additions on glass forming ability and mechanical properties of Co-Fe-Ta-B Bulk metallic glass," *Met. Mater. Int.*, vol. 22, no. 1, pp. 50–57, 2016, doi: 10.1007/s12540-016-5220-9.

[15] S. Fashu *et al.*, "A review on crucibles for induction melting of titanium alloys," *Mater. Des.*, vol. 186, no. November, 2020, doi: 10.1016/j.matdes.2019.108295.

[16] "Arcast Products - Arc 200 Cold Crucible Arc Melting Furnace." http://www.arcastinc.com/arc200.htm (accessed Apr. 26, 2022).

[17] P. Pawlik, K. Pawlik, and A. Przybył, "Investigation of the cooling rate in the suction casting process," *Rev. Adv. Mater. Sci.*, vol. 18, no. 1, pp. 81–84, 2008.

[18] T. Kozieł, "Estimation Of Cooling Rates In Suction Casting And Copper-Mould Casting Processes," *Arch. Metall. Mater.*, no. No 2 June, 2015, doi: 10.1515/amm-2015-0204.

[19] T. Nagase, M. Matsumoto, and Y. Fujii, "Microstructure of Ti-Ag immiscible alloys with liquid phase separation," *J. Alloys Compd.*, vol. 738, pp. 440–447, 2018, doi: 10.1016/j.jallcom.2017.12.138.

[20] "Figure 4. Basic principle of selective laser melting (Vilaro, 2008) | Scientific Diagram." https://www.researchgate.net/figure/Basic-principle-of-selective-laser-melting-Vilaro-2008_fig4_275533064/actions#reference (accessed May 17, 2019).

[21] "Laser metal deposition illustration_v3_with logo - Advanced Manufacturing." https://advancedmanufacturing.org/pluses-minuses-combining-additive-subtractive-machining/laser-metal-deposition-illustration_v3_with-logo/ (accessed May 20, 2019).

[22] "SLM Solutions Group AG: SLM® Machines." https://www.slm-solutions.com/products/machines/selectivelasermeltingmachines/ (accessed Apr. 23, 2019).

[23] "Laser Material Deposition - Fraunhofer ILT." https://www.ilt.fraunhofer.de/en/technology-focus/laser-material-processing/laser-metal-deposition.html (accessed Apr. 23, 2019).

[24] D. V. Louzguine, H. Kato, and A. Inoue, "High strength and ductile binary Ti-Fe composite alloy," *J. Alloys Compd.*, vol. 384, no. 1–2, pp. 10–12, 2004, doi: 10.1016/j.jallcom.2004.03.114.

[25] G. H. Cao *et al.*, "Formation of a bimodal structure in ultrafine Ti-Fe-Nb alloys with high-strength and enhanced ductility," *Mater. Sci. Eng. A*, vol. 609, pp. 60–64, 2014, doi: 10.1016/j.msea.2014.04.088.

[26] J. Das and T. Maity, “A few aspects on the processing and deformation behavior of advanced eutectic alloys,” *Trans. Indian Inst. Met.*, vol. 65, no. 6, pp. 571–576, 2012, doi: 10.1007/s12666-012-0185-y.

[27] J. H. Han *et al.*, “Effect of microstructure modulation on mechanical properties of Ti-Fe-Sn ultrafine eutectic composites,” *Met. Mater. Int.*, vol. 17, no. 6, pp. 873–877, 2011, doi: 10.1007/s12540-011-6002-z.

[28] G. H. Cao *et al.*, “Sn and Nb modified ultrafine Ti-based bulk alloys with high-strength and enhanced ductility,” *Appl. Phys. Lett.*, vol. 102, no. 6, pp. 1–5, 2013, doi: 10.1063/1.4792592.

[29] G.-H. Zhao, S. V Ketov, H. Mao, A. Borgenstam, and D. V. Louzguine-Luzgin, *Ti-Fe-Sn-Nb hypoeutectic alloys with superb yield strength and significant strain-hardening*, vol. 135. 2017. doi: 10.1016/j.scriptamat.2017.03.033.

[30] C. H. Lee *et al.*, “Investigation of the mechanical properties of Ti-Fe-Sn ultrafine eutectic composites by dendrite phase selection,” *Met. Mater. Int.*, vol. 20, no. 3, pp. 417–421, 2014, doi: 10.1007/s12540-014-3003-8.

[31] G. Song *et al.*, *Heterogeneous eutectic structure in Ti–Fe–Sn alloys*, vol. 19. 2011. doi: 10.1016/j.intermet.2010.11.030.

[32] G. A. Song *et al.*, “Optimization of mechanical properties of Ti-Fe-Sn alloys by controlling heterogeneous eutectic structure,” *Intermetallics*, vol. 23, pp. 27–31, 2012, doi: 10.1016/j.intermet.2011.12.005.

[33] S. Samal, B. Mondal, K. Biswas, and Govind, “Electron microscopic study on the suction cast in situ Ti-Fe-Sn ultrafine composites,” *Metall. Mater. Trans. A Phys. Metall. Mater. Sci.*, vol. 44, no. 1, pp. 427–439, 2013, doi: 10.1007/s11661-012-1404-1.

[34] G. A. Song *et al.*, “Heterogeneous eutectic structure in Ti-Fe-Sn alloys,” *Intermetallics*, vol. 19, no. 4, pp. 536–540, 2011, doi: 10.1016/j.intermet.2010.11.030.

[35] J. H. Han *et al.*, “Effect of microstructure modulation on mechanical properties of Ti-Fe-Sn ultrafine eutectic composites,” *Met. Mater. Int.*, vol. 17, no. 6, pp. 873–877, 2011, doi: 10.1007/s12540-011-6002-z.

[36] C. S. Wang, K. S. Zhang, H. J. Pang, Y. Z. Chen, and C. Dong, “Laser-induced self-propagating reaction synthesis of Ti-Fe alloys,” *J. Mater. Sci.*, vol. 43, no. 1, pp. 218–221, 2008, doi: 10.1007/s10853-007-2146-0.

[37] L. ying HAN and C. shan WANG, “Microstructure and properties of Ti64.51Fe26.40Zr5.86Sn2.93Y0.30 biomedical alloy fabricated by laser additive manufacturing,” *Trans. Nonferrous Met. Soc. China (English Ed.*, vol. 30, no. 12, pp. 3274–3286, 2020, doi: 10.1016/S1003-6326(20)65460-7.

[38] C. R. M. Afonso, A. L. Vidilli, J. E. Spinelli, R. Riva, V. Amigó, and C. S. Kiminami, "An assessment of microstructure and properties of laser clad coatings of ultrafine eutectic β Ti-Fe-Nb-Sn composite for implants," *Surf. Coatings Technol.*, vol. 328, pp. 161–171, 2017, doi: 10.1016/j.surfcoat.2017.08.035.

[39] J. Gussone *et al.*, "Ultrafine eutectic Ti-Fe-based alloys processed by additive manufacturing – A new candidate for high temperature applications," *Appl. Mater. Today*, vol. 20, pp. 1–11, 2020, doi: 10.1016/j.apmt.2020.100767.

[40] G. Requena *et al.*, "Ultrafine Fe-Fe2Ti eutectics by directed energy deposition: Insights into microstructure formation based on experimental techniques and phase field modelling," *Addit. Manuf.*, vol. 33, no. August 2019, p. 101133, 2020, doi: 10.1016/j.addma.2020.101133.

[41] A. Popovich and V. Sufiiarov, "Metal Powder Additive Manufacturing," *New Trends 3D Print.*, 2016, doi: 10.5772/63337.

[42] B. Xie, Y. Fan, and S. Zhao, "Characterization of Ti6Al4V powders produced by different methods for selective laser melting," *Mater. Res. Express*, vol. 8, no. 7, p. 076510, Jul. 2021, doi: 10.1088/2053-1591/AC10D1.

[43] R. Li, Y. Shi, Z. Wang, L. Wang, J. Liu, and W. Jiang, "Densification behavior of gas and water atomized 316L stainless steel powder during selective laser melting," *Appl. Surf. Sci.*, vol. 256, no. 13, pp. 4350–4356, 2010, doi: 10.1016/j.apsusc.2010.02.030.

[44] M. Z. Gao, B. Ludwig, and T. A. Palmer, "Impact of atomization gas on characteristics of austenitic stainless steel powder feedstocks for additive manufacturing," *Powder Technol.*, vol. 383, pp. 30–42, 2021, doi: 10.1016/j.powtec.2020.12.005.

[45] A. Ünal, "Effect of processing variables on particle size in gas atomization of rapidly solidified aluminium powders," *Mater. Sci. Technol.*, vol. 3, no. 12, pp. 1029–1039, Dec. 1987, doi: 10.1179/mst.1987.3.12.1029.

[46] D. Beckers, N. Ellendt, U. Fritsching, and V. Uhlenwinkel, "Impact of process flow conditions on particle morphology in metal powder production via gas atomization," *Adv. Powder Technol.*, vol. 31, no. 1, pp. 300–311, 2020, doi: 10.1016/j.apt.2019.10.022.

[47] M. Wei, S. Chen, M. Sun, J. Liang, C. Liu, and M. Wang, "Atomization simulation and preparation of 24CrNiMoY alloy steel powder using VIGA technology at high gas pressure," *Powder Technol.*, vol. 367, pp. 724–739, 2020, doi: 10.1016/j.powtec.2020.04.030.

[48] D. Tourret *et al.*, "Gas atomization of Al-Ni powders: Solidification modeling and neutron diffraction analysis," *Acta Mater.*, vol. 59, no. 17, pp. 6658–6669, 2011, doi: 10.1016/j.actamat.2011.07.023.

[49] L. Sang, Y. Xu, P. Fang, H. Zhang, Y. Cai, and X. Liu, “The influence of cooling rate on the microstructure and phase fraction of gas atomized NiAl3alloy powders during rapid solidification,” *Vacuum*, vol. 157, no. June, pp. 354–360, 2018, doi: 10.1016/j.vacuum.2018.08.057.

[50] B. Engel and D. L. Bourell, “Titanium alloy powder preparation for selective laser sintering,” *Rapid Prototyp. J.*, vol. 6, no. 2, pp. 97–106, 2000, doi: 10.1108/13552540010323574.

[51] “Powder Metallurgy.” http://www.ald-dynatech.com/index.php/product-2/powder-metallurgy (accessed May 18, 2019).

[52] F. H. (Sam) Froes, “Additive manufacturing of titanium components: An up-date,” *Met. Powder Rep.*, vol. 73, no. 6, pp. 329–337, 2018, doi: 10.1016/j.mprp.2018.10.001.

[53] A. Martín, C. M. Cepeda-Jiménez, and M. T. Pérez-Prado, “Gas atomization of γ-TiAl Alloy Powder for Additive Manufacturing,” *Adv. Eng. Mater.*, vol. 22, no. 1, pp. 1–9, 2020, doi: 10.1002/adem.201900594.

[54] R. Gerling, H. Clemens, and F. P. Schimansky, “Powder metallurgical processing of intermetallic gamma titanium aluminides,” *Adv. Eng. Mater.*, vol. 6, no. 1–2, pp. 23–38, 2004, doi: 10.1002/adem.200310559.

[55] “Arcast Products.” http://www.arcastinc.com/products.htm (accessed Jan. 12, 2022).

[56] D. D. Gu, W. Meiners, K. Wissenbach, and R. Poprawe, “Laser additive manufacturing of metallic components: materials, processes and mechanisms,” *Int. Mater. Rev.*, vol. 57, no. 3, pp. 133–164, 2012.

[57] J. K. Prescott and R. A. Barnum, “On powder flowability,” *Pharm. Technol.*, vol. 24, no. 10, p. 60, 2000.

[58] S. Vock, B. Klöden, · Alexander Kirchner, T. Weißgärber, and · Bernd Kieback, “Powders for powder bed fusion: a review,” *Prog. Addit. Manuf.*, vol. 4, pp. 383–397, 2019, doi: 10.1007/s40964-019-00078-6.

[59] D. Schulze, J. Schwedes, and J. W. Carson, “Powders and bulk solids: Behavior, characterization, storage and flow,” *Powders Bulk Solids Behav. Charact. Storage Flow*, pp. 1–511, 2008, doi: 10.1007/978-3-540-73768-1.

[60] P. Karapatis, “A sub-process approach of selective laser sintering,” 2002, doi: 10.5075/EPFL-THESIS-2506.

[61] N. A. Pohlman, J. A. Roberts, and M. J. Gonser, “Characterization of titanium powder: Microscopic views and macroscopic flow,” *Powder Technol.*, vol. 228, pp. 141–148, Sep. 2012, doi: 10.1016/J.POWTEC.2012.05.009.

[62] H. P. Kurz and G. Münz, “The influence of particle size distribution on the flow

properties of limestone powders," *Powder Technol.*, vol. 11, no. 1, pp. 37–40, Jan. 1975, doi: 10.1016/0032-5910(75)80020-9.

[63] H. P. Tang *et al.*, "Effect of Powder Reuse Times on Additive Manufacturing of Ti-6Al-4V by Selective Electron Beam Melting," *JOM*, vol. 67, no. 3, pp. 555–563, Mar. 2015, doi: 10.1007/S11837-015-1300-4.

[64] A. B. Spierings and G. Levy, "Comparison of density of stainless steel 316L parts produced with selective laser melting using different powder grades," *Proc. Annu. Int. solid Free. Fabr. Symp. Austin*, pp. 342–353, 2009.

[65] S. Ziegelmeier *et al.*, "An experimental study into the effects of bulk and flow behaviour of laser sintering polymer powders on resulting part properties," *J. Mater. Process. Technol.*, vol. 215, no. 1, pp. 239–250, 2015, doi: 10.1016/J.JMATPROTEC.2014.07.029.

[66] J. Schwedes, "Review on testers for measuring flow properties of bulk solids (based on an IFPRI-Report 1999)," *Granul. Matter*, vol. 5, 2003, doi: 10.1007/s10035-002-0124-4.

[67] "ASTM D7481-09, Standard Test Methods for Determining Loose and Tapped Bulk Densities of Powders using a Graduated Cylinder," *ASTM Int.*, vol. 04.09, p. 4, 2018, doi: 10.1520/D7481-09.

[68] E. C. Abdullah and D. Geldart, "The use of bulk density measurements as flowability indicators," *Powder Technol.*, vol. 102, no. 2, pp. 151–165, Mar. 1999, doi: 10.1016/S0032-5910(98)00208-3.

[69] "ASTM B213-20, Standard Test Methods for Flow Rate of Metal Powders Using the Hall Flowmeter," *ASTM Int.*, vol. 02.05, p. 4, 2020, doi: 10.1520/B0213-20.

[70] D. Geldart, E. C. Abdullah, A. Hassanpour, L. C. Nwoke, and I. Wouters, "Characterization of powder flowability using measurement of angle of repose," *China Particuology*, vol. 4, no. 3–4, pp. 104–107, Jul. 2006, doi: 10.1016/S1672-2515(07)60247-4.

[71] R. Freeman, "Measuring the flow properties of consolidated, conditioned and aerated powders - A comparative study using a powder rheometer and a rotational shear cell," *Powder Technol.*, vol. 174, no. 1–2, pp. 25–33, May 2007, doi: 10.1016/J.POWTEC.2006.10.016.

[72] M. Krantz, H. Zhang, and J. Zhu, "Characterization of powder flow: Static and dynamic testing," *Powder Technol.*, vol. 194, no. 3, pp. 239–245, Sep. 2009, doi: 10.1016/J.POWTEC.2009.05.001.

[73] "ASTM B243-22, Standard terminology of powder metallurgy," *ASTM Int.*, vol. 02.05, p. 10, 2022, doi: 10.1520/B0243-22.

[74] E. O. Olakanmi, "Effect of mixing time on the bed density, and microstructure of

selective laser sintered (sls) aluminium powders," *Mater. Res.*, vol. 15, no. 2, pp. 167–176, 2012.

[75] P. W. Cleary and M. L. Sawley, "DEM modelling of industrial granular flows: 3D case studies and the effect of particle shape on hopper discharge," *Appl. Math. Model.*, vol. 26, no. 2, pp. 89–111, 2002.

[76] N. P. Karapatis, G. Egger, P. E. Gygax, and R. Glardon, "Optimization of powder layer density in selective laser sintering," 1999.

[77] R. M. German , *Powder metallurgy science*. Princeton, N.J.: Metal Powder Industries Federation, 1994.

[78] B. H. Rabin, G. R. Smolik, and G. E. Korth, "Characterization of entrapped gases in rapidly solidified powders," *Mater. Sci. Eng. A*, vol. 124, no. 1, pp. 1–7, Apr. 1990, doi: 10.1016/0921-5093(90)90328-Z.

[79] H. E. Eaton and N. S. Bornstein, "Determination of entrapped argon in powdered metal alloys," *Metall. Trans. A*, vol. 9, no. 9, pp. 1341–1342, 1978, doi: 10.1007/BF02652260.

[80] R. Cunningham *et al.*, "Analyzing the effects of powder and post-processing on porosity and properties of electron beam melted Ti-6Al-4V," vol. 5, no. 7, pp. 516–525, 2017, doi: 10.1080/21663831.2017.1340911.

[81] Y. Cui *et al.*, "Materials Research Express TOPICAL REVIEW • OPEN ACCESS To cite this article: Ahmad Y Al-Maharma et al," *Mater. Res. Express*, vol. 7, p. 122001, 2020, doi: 10.1088/2053-1591/abcc5d.

[82] "Optimizing Metal Powders for Additive Manufacturing | Additive Manufacturing." https://www.additivemanufacturing.media/articles/optimizing-metal-powders-for-additive-manufacturing-exploring-the-impact-of-particle-morphology-and-powder-flowability (accessed May 24, 2022).

[83] I. E. Anderson, E. M. H. White, and R. Dehoff, "Feedstock powder processing research needs for additive manufacturing development," *Curr. Opin. Solid State Mater. Sci.*, vol. 22, no. 1, pp. 8–15, 2018, doi: 10.1016/j.cossms.2018.01.002.

[84] M. Mitterlehner *et al.*, "Comparative Evaluation of Characterization Methods for Powders Used in Additive Manufacturing," *J. Mater. Eng. Perform.*, vol. 30, doi: 10.1007/s11665-021-06113-4.

[85] "TI-6AL-4V material data — Metal powder | Sandvik." https://www.metalpowder.sandvik/en/products/metal-powder-alloys/titanium/ti-6al-4v-material-data/ (accessed May 19, 2022).

[86] "China Spherical Titanium Ti6al4V Alloy Powder for 3D Printing Powder 0-45 Microns - China Ti6al4V Alloy Powder, Powder Injection Molding." https://gzslam.en.made-in-

china.com/product/EFMnlNzKgJcf/China-Spherical-Titanium-Ti6al4V-Alloy-Powder-for-3D-Printing-Powder-0-45-Microns.html (accessed May 19, 2022).

[87] A. B822–17, "Standard test method for particle size distribution of metal powders and related compounds by light scattering," *ASTM Int.*, 2017.

[88] B. Liu, R. Wildman, C. Tuck, I. Ashcroft, and R. Hague, "INVESTIGATION THE EFFECT OF PARTICLE SIZE DISTRIBUTION ON PROCESSING PARAMETERS OPTIMISATION IN SELECTIVE LASER MELTING PROCESS".

[89] M. Badrossamay, E. Yasa, J. Van Vaerenbergh, and J. P. Kruth, "Improving productivity rate in SLM of commercial steel powders," *Tech. Pap. - Soc. Manuf. Eng.*, vol. TP09PUB17, pp. 1–13, 2009.

[90] A. B. Spierings, N. Herres, and G. Levy, "Influence of the particle size distribution on surface quality and mechanical properties in AM steel parts," *Rapid Prototyp. J.*, 2011.

[91] K. Abd-Elghany and D. L. Bourell, "Property evaluation of 304L stainless steel fabricated by selective laser melting," *Rapid Prototyp. J.*, vol. 18, no. 5, pp. 420–428, Jan. 2012, doi: 10.1108/13552541211250418.

[92] A. Simchi, "The role of particle size on the laser sintering of iron powder," *Metall. Mater. Trans. B*, vol. 35, no. 5, pp. 937–948, 2004.

[93] C. T. Schade, T. F. Murphy, and C. Walton, "Development of atomized powders for additive manufacturing," 2014.

[94] M. Miedzinski, "Materials for Additive Manufacturing by Direct Energy Deposition. Thesis, Chalmers University of Technology," 2017.

[95] S. J. Dapkunas and A. Jillavenkatesa, "NIST recommended practice guide :," 2001, doi: 10.6028/NBS.SP.960-1.

[96] "Particle Size & Particle Shape Analyzer: CAMSIZER X2." https://www.microtrac.com/products/particle-size-shape-analysis/dynamic-image-analysis/camsizer-x2/ (accessed May 23, 2022).

[97] R. Li, J. Liu, Y. Shi, L. Wang, and W. Jiang, "Balling behavior of stainless steel and nickel powder during selective laser melting process," *Int. J. Adv. Manuf. Technol.*, vol. 59, no. 9, pp. 1025–1035, 2012.

[98] A. Strondl, O. Lyckfeldt, H. Brodin, and U. Ackelid, "Characterization and control of powder properties for additive manufacturing," *Jom*, vol. 67, no. 3, pp. 549–554, 2015.

[99] J.-M. Oh, B.-G. Lee, S.-W. Cho, S.-W. Lee, G.-S. Choi, and J.-W. Lim, "Oxygen effects on the mechanical properties and lattice strain of Ti and Ti-6Al-4V," *Met. Mater. Int.*, vol. 17, no. 5, pp. 733–736, 2011.

[100] A. Hodgson and S. Haq, “Water adsorption and the wetting of metal surfaces,” *Surf. Sci. Rep.*, vol. 64, no. 9, pp. 381–451, Sep. 2009, doi: 10.1016/J.SURFREP.2009.07.001.

[101] V. Karde and C. Ghoroi, “Fine powder flow under humid environmental conditions from the perspective of surface energy,” *Int. J. Pharm.*, vol. 485, no. 1–2, pp. 192–201, 2015, doi: 10.1016/j.ijpharm.2015.03.021.

[102] R. J. Hebert, “Viewpoint: metallurgical aspects of powder bed metal additive manufacturing,” *J. Mater. Sci.*, vol. 51, doi: 10.1007/s10853-015-9479-x.

[103] R. B. Fricioni and L. Essig, “Inert Gas Fusion,” *Mater. Charact.*, pp. 226–232, Dec. 1986, doi: 10.31399/ASM.HB.V10.A0001747.

[104] B. Thomas Young and M. D. For Sec, “HI, An Essay on the Cohesion of Fluids.” [Online]. Available: https://royalsocietypublishing.org/

[105] V. Bérard, E. Lesniewska, C. Andrès, D. Pertuy, C. Laroche, and Y. Pourcelot, “Affinity scale between a carrier and a drug in DPI studied by atomic force microscopy,” *Int. J. Pharm.*, vol. 247, no. 1–2, pp. 127–137, 2002, doi: 10.1016/s0378-5173(02)00400-3.

Chapter 2

Motivation and Objectives

2 Motivation and Objectives

2.1 Motivation

The motivation behind this challenging research work is three-fold.

i. *Promising structural alloys*: Years of academic research has gone into developing Ti-Fe-based ultrafine eutectic and near-eutectic alloys with remarkable mechanical properties. As discussed in the previous chapter, cast ingots (few mm in dimensions) of such alloys have demonstrated high compressive strengths (> 2 GPa) similar to bulk metallic glasses (BMGs), while retaining more than 15 % plasticity at room temperature [1–3]. This suggests a unique balance of properties, that have been further fine-tuned and enhanced using alloying elements and higher length-scale dendrites in several studies [4–11]. Based on initial trials, we expect additively manufactured Ti-Fe-based ultrafine eutectics, as near-net-shape components, to possess high strength (Compressive strength > 1.8 GPa), enhanced plasticity (elongation > 10 %) at room temperature, excellent crack propagation resistance and resistance to wear. This would mean they can compete actively with several existing Ti-based and other structural alloys. For example, one of our target applications is building compressor wheels of high-pressure turbocharger impellers used in diesel engines. They are used with exhaust gas recirculation where abrasive erosion remains the major issue. Current impellers are being machined from extruded aluminium alloys and applied with coatings to prevent abrasive wear [12]. Cast Ti-6Al-4V costs more, but offers a better structural material in terms of low cycle fatigue life [13]. However, SLM-made Ti-Fe-Nb-Sn ultrafine eutectics can provide an adequate balance of these properties along with much better strength-to-density ratio and building accuracy for their geometrical complexity, while completely eliminating the need for coatings.

Further, LMD-produced Fe-Ti (Fe-rich) ultrafine eutectic is expected to show high strength and wear resistance properties lying between popular tool steels and sub-µm cemented carbides. It is expected to be thermally stable (at least up to 600 °C) and would cost less. In addition, LMD has a much more portable set-up than SLM and can be used to rapidly build hybrid parts where certain features are printed on a cast piece, making it perfect for onsite tools production and repair. This offers a competitive advantage for several tooling applications like rotary die-cutting units for diapers, extrusion dies, injection moulding dies, etc. AM-ultrafine eutectics have the potential to be the ‘novel’ structural materials for the automotive and tools industry.

ii. *Technical reasons*: Rapid solidification studies on Ti-Fe-(Nb, Sn) ultrafine eutectic alloys have shown outstanding mechanical results but have only managed to produce small specimens few mm in thickness. The main reason being the technical limitations posed by the used casting methods in complying with the alloys’ strict solidification criteria. The inter-lamellar spacing ‘λ’ is quite sensitive to solidification conditions and is known to decrease with increasing growth velocity or solidification rate, as described by the Jackson-Hunt relation

[14] for binary eutectic growth. Suction casting or arc-melting can only produce specific shapes and small sizes good enough for experimental purposes. They are incapable of providing uniform and high cooling rates necessary for such ultrafine microstructures over large dimensions in order to produce near-net-shape components without significant heterogeneities. This has largely restricted their industrial use. On the other hand, powder-based AM techniques like SLM having inherently very high cooling rates (ranging 10^6 K/s) or LMD (with cooling rates ranging $10^4 – 10^5$ K/s) are appropriate for such microstructural growth and their track and layer-wise building approach maintains an almost constant cooling rate throughout the component bulk. In addition to other advantages, AM offers the accuracy and designing freedom essential for dealing with geometrical complexities of components. AM seems like the best alternative for industrialising these alloys. This strongly motivates the development of high-quality powders for SLM and LMD trials.

iii. *Limited alloys for AM*: The portfolio of additively manufactured commercial alloys is very limited [15] and this development would be a valuable addition that would further boost the competitiveness of additive manufacturing.

2.2 Objectives

The main objectives of the thesis are as follows:

i. <u>Optimisation of atomisation techniques to produce powders of the chosen compositions</u>

The main aim is to produce the best quality pre-alloyed powders of the chosen compositions: two Ti-rich (Ti-Fe-(Nb, Sn)-based) for SLM and one Fe-rich (Fe-Ti binary) for LMD processes. The sub-goals within this objective are:

- Optimisation of alloy production by experimenting with casting conditions and raw materials. They must adhere to specific geometries and purity standards as required by the gas atomisation techniques for producing powders.
- Atomisation of the alloys using three distinct gas atomisation set-ups whose working principles are explained in section 1.3.1 of chapter 1.
- A detailed characterisation of the obtained powders, especially their physical properties, based on the required standards for SLM and LMD. This information acts as the first feedback for optimising the choice of atomisation technique and parameters for further producing large quantities. The second feedback comes from SLM and LMD trials performed by our partners.

ii. Study of rapid solidification behaviour in powder particles of different sizes in order to create a knowledge dataset

The associated unconventional cooling rates/thermal gradients in AM can often generate residual stresses, non-equilibrium microstructures and defects, especially in transition regions between layers & tracks [16]. Eutectics are sensitive towards compositional/stress heterogeneities and no proper post-processing treatments have been designed for them so far. Therefore, for AM to work, it is extremely important to establish the processing-microstructure-property relationships for these alloys and their powders. This is addressed by the following goals:

- Transfer rapid solidification knowledge for similar alloys from literature into the microstructural analysis of pre-alloyed powders that have been sieved into different particle size ranges, thus experiencing different crystallisation kinetics.
- Study the influence of particle size and/or solidification kinetics on key microstructural features (like inter-lamellar spacing λ, eutectic morphology and phase distribution), chemical composition and ultimately, the nano-hardness behaviour.
- Identify certain phase transformation mechanisms and outline the microstructural evolution followed during gas atomisation, hence bridging an important knowledge gap.

  This is expected to facilitate and fasten decision-making processes regarding useful particle sizes, processing parameters and powder reusability during AM of these alloys. This study aims to improve our overall understanding of eutectic and near-eutectic systems in meta-stable equilibriums.

iii. Development of an advanced image analysis tool for one-step screening of powders using tomography data

Conventional powder characterisation methods can measure limited properties at a time and fail to quantify certain features accurately like sphericity of particles, location and size of pores, satellite density, etc. The main objective is to improve and fasten the process of screening physical properties of powders for initial AM trials by:

- Developing a new methodology in *Fiji (ImageJ)* and *Avizo* softwares for 3D image analysis of X-Ray Computed Tomography (XCT) data with high accuracy.
- Quantifying several features like porosity, size and shape distribution of powder particles using the tool.
- Validating the accuracy of the tool by comparing against conventional characterisation methods.

iv. Mechanical characterisation of AM-built samples

The main aim is to characterise the compressive and tensile strength of the chosen alloys fabricated by SLM and LMD.

- Characterise macro-mechanical behaviour under tension and compression at room and higher temperatures (up to 600 °C) in air.
- Characterise micromechanical behaviour using nanoindentation and micro-pillar compression (for LMD-built alloy).
- Compare micromechanical behaviour of LMD-built alloy to that of samples consolidated by Field Assisted Hot Pressing (FAHP), a rapid solid state sintering technique, of the same pre-alloyed powders.

The following table shows the distribution of the main objectives into specific chapters of this thesis which contain the corresponding results and conclusions.

Objectives	Chapter
i. Optimisation of atomisation techniques to produce powders of the chosen compositions ii. Study of rapid solidification behaviour in powder particles of different sizes in order to create a knowledge database	Chapter 4
iii. Development of an advanced image analysis tool for one-step screening of powders using tomography data	Chapter 5
iv. Mechanical characterisation of AM-built samples	Chapter 6

REFERENCES

[1] J. Das and T. Maity, “A few aspects on the processing and deformation behavior of advanced eutectic alloys,” *Trans. Indian Inst. Met.*, vol. 65, no. 6, pp. 571–576, 2012, doi: 10.1007/s12666-012-0185-y.

[2] D. A. T. A. J. Louzguine-Luzgin, “High-strength ti-based alloys containing fe as one of the main alloying elements,” *Mater. Trans.*, vol. 59, no. 10, pp. 1537–1544, 2018, doi: 10.2320/matertrans.M2018114.

[3] J. Das, K. B. Kim, F. Baier, W. Löser, and J. Eckert, “High-strength Ti-base ultrafine eutectic with enhanced ductility,” *Appl. Phys. Lett.*, vol. 87, no. 16, pp. 1–3, 2005, doi: 10.1063/1.2105998.

[4] D. V. Louzguine, H. Kato, and A. Inoue, “High strength and ductile binary Ti-Fe composite alloy,” *J. Alloys Compd.*, vol. 384, no. 1–2, pp. 10–12, 2004, doi: 10.1016/j.jallcom.2004.03.114.

[5] J. H. Han *et al.*, “Influence of a bimodal eutectic structure on the plasticity of a (Ti 70.5 Fe29.5)91 Sn9 ultrafine composite,” *Appl. Phys. Lett.*, vol. 93, no. 20, pp. 91–94, 2008, doi: 10.1063/1.3029745.

[6] J. H. Han *et al.*, “Effect of microstructure modulation on mechanical properties of Ti-Fe-Sn ultrafine eutectic composites,” *Met. Mater. Int.*, vol. 17, no. 6, pp. 873–877, 2011, doi: 10.1007/s12540-011-6002-z.

[7] G. H. Cao *et al.*, “Sn and Nb modified ultrafine Ti-based bulk alloys with high-strength and enhanced ductility,” *Appl. Phys. Lett.*, vol. 102, no. 6, pp. 1–5, 2013, doi: 10.1063/1.4792592.

[8] G.-H. Zhao, S. V Ketov, H. Mao, A. Borgenstam, and D. V. Louzguine-Luzgin, *Ti-Fe-Sn-Nb hypoeutectic alloys with superb yield strength and significant strain-hardening*, vol. 135. 2017. doi: 10.1016/j.scriptamat.2017.03.033.

[9] G. H. Cao *et al.*, “Formation of a bimodal structure in ultrafine Ti-Fe-Nb alloys with high-strength and enhanced ductility,” *Mater. Sci. Eng. A*, vol. 609, pp. 60–64, 2014, doi: 10.1016/j.msea.2014.04.088.

[10] G. A. Song *et al.*, “Heterogeneous eutectic structure in Ti-Fe-Sn alloys,” *Intermetallics*, vol. 19, no. 4, pp. 536–540, 2011, doi: 10.1016/j.intermet.2010.11.030.

[11] G. A. Song *et al.*, “Optimization of mechanical properties of Ti-Fe-Sn alloys by controlling heterogeneous eutectic structure,” *Intermetallics*, vol. 23, pp. 27–31, 2012, doi: 10.1016/j.intermet.2011.12.005.

[12] M. F. Moreira, “Failure analysis in aluminium turbocharger wheels,” *Eng. Fail. Anal.*, vol. 61, pp. 108–118, Mar. 2016, doi: 10.1016/J.ENGFAILANAL.2015.11.024.

[13] A. Emara, M. Soliman, H. A. Monieb, and S. M. Abdelrazek, “Material Selection for a Turbocharger Centrifugal Compressor Wheel,” *SAE Tech. Pap.*, vol. 2020-January, 2020, doi: 10.4271/2020-01-5066.

[14] K. A. Jackson and J. D. Hunt, “Lamellar and Rod Eutectic Growth,” *Trans. Met. Soc. AIME*, vol. 236, no. 8, pp. 1129–1142, 1966.

[15] T. DebRoy *et al.*, “Scientific, technological and economic issues in metal printing and their solutions,” *Nat. Mater.*, vol. 18, no. 10, pp. 1026–1032, 2019, doi: 10.1038/s41563-019-0408-2.

[16] N. T. Aboulkhair, N. M. Everitt, I. Ashcroft, and C. Tuck, “Reducing porosity in AlSi10Mg parts processed by selective laser melting,” *Addit. Manuf.*, vol. 1–4, pp. 77–86, Oct. 2014, doi: 10.1016/J.ADDMA.2014.08.001.

Chapter 3

Experimental Procedure

3 Experimental procedure

This chapter describes all the experimental work that was performed within this thesis in order to achieve the objectives presented in the previous chapter. It is divided into three main sections: Materials, Processing and Characterisation. The first section presents the studied alloys in terms of composition and raw materials used for trials. It also describes the production of pre-alloyed powders of the studied compositions by three different atomisation methods, their nomenclature, sieving and classification into designated size ranges for charcacterisation. The second section 'Processing' provides details on the processing of selected powder compostions by three different processing techniques, i.e. Selective Laser Melting (SLM), Laser Metal Deposition (LMD) and Field Assisted Hot Pressing (FAHP). The last section 'Characterisation' describes all the characterisation techniques used for analysing the powders as well as the processed or built material.

3.1 Materials

3.1.1 Alloy selection

The three alloy compositions explored in this thesis are: **$Ti_{66}Fe_{27}Nb_3Sn_4$**, **$Ti_{73.5}Fe_{23}Nb_{1.5}Sn_2$** and **$Fe_{82.4}Ti_{17.6}$** (all at %). Table 3.1 further shows them converted into weight-percent.

Table 3.1: Weight-percent composition of the chosen alloys

Composition (wt %)	Ti	Fe	Nb	Sn
$Ti_{66}Fe_{27}Nb_3Sn_4$	58.3	27.8	5.1	8.8
$Ti_{73.5}Fe_{23}Nb_{1.5}Sn_2$	68	25	2.5	4.5
$Fe_{82.4}Ti_{17.6}$	15.5	84.5	-	-

As seen in the Ti-Fe phase diagram (in Figure 1.4 of chapter 1), $Fe_{82.4}Ti_{17.6}$ lies close to eutectic point '**L → α-Fe + Fe_2Ti**' located at 16 at % Ti. $Ti_{66}Fe_{27}Nb_3Sn_4$ is close to the other eutectic '**L → β-Ti + FeTi**' at 29.5 at % Fe, with Nb and Sn as additional alloying elements. However, $Ti_{73.5}Fe_{23}Nb_{1.5}Sn_2$ is a Ti-rich non-eutectic composition. These compositions were carefully designed by our project partners based on thermodynamic calculations (using Thermocalc) and rapid AM trials using in-situ mixing of elementary powders or powder blends. The raw materials mentioned in Table 3.2 were finalised for alloy casting (with minimum heterogeneities and impurities) and for the in-house atomisation trials (explained in the next section).

Table 3.2: Composition and supplier information of the finally selected raw materials for alloy casting and in-house atomisation trials

Material (supplier)	Ti	Fe	Mn	Cr *(all wt %)*	Nb	Al	Sn	Si	O
Fe-Ti (Masteurope)	72.7 ± 0.2	26.5 ± 0.2	0.3	0.4	-	-	-	-	< 1
Fe-Nb (GfE AMG)	-	35.4	-	-	63.7	0.68	0.05	0.05	0.02
Fe (Alfa Aesar)	-	99.98	-	-	-	-	-	-	-
Sn (Clerins)	-	-	-	-	-	-	99.9	-	-
Ti (Alfa Aesar)	99.9	-	-	-	-	-	-	-	0.06

3.1.2 Powder production

Three gas atomisation methods were used for producing pre-alloyed powders of the selected compositions. Table 3.3 classifies and names the powder batches produced by all methods.

Table 3.3: Nomenclature, target compositions and production methods used for studied powders

Powder name	Target alloy composition (at %)	Produced by
CGA	$Ti_{66}Fe_{27}Nb_3Sn_4$	Vacuum induction melting inert gas atomisation (VIGA) at *Nanoval GmbH & Co. KG*
CFA	$Ti_{66}Fe_{27}Nb_3Sn_4$	Electrode induction melting gas atomisation (EIGA) at *Nanoval GmbH & Co. KG*
AMA	$Ti_{66}Fe_{27}Nb_3Sn_4$	Arc-Melting Atomisation (AMA) at *Arcast Inc.*
AMA2	$Ti_{73.5}Fe_{23}Nb_{1.5}Sn_2$	Arc-Melting Atomisation (AMA) at *Arcast Inc*
CFA-FeTi	$Fe_{82.4}Ti_{17.6}$	Electrode induction melting gas atomisation (EIGA) at *Nanoval GmbH & Co. KG*

The atomisation methods VIGA, EIGA and AMA are explained in section 1.3.1 of chapter 1. *Nanoval GmbH & Co. KG* (Berlin, Germany) uses very specific and exclusive set-ups based on principles of VIGA and EIGA, referred to as *Crucible-based Gas Atomisation (CGA)* and *Crucible-Free Atomisation (CFA)* respectively in this thesis. The powder batches are named after the corresponding acronyms of the atomisation set-ups used for producing them.

CGA involved melting the alloy in a graphite crucible before pouring it into a conical funnel-like ceramic nozzle fixed above a high velocity vertical stream of Argon. In CFA method, powders (namely CFA and CFA-FeTi from Table 3.3) were produced by using cast rods of the alloys being passed through induction coils, instead of using a crucible. Ingots of 50 mm in diameters and 400 – 480 mm length were cast by a supplier *Less Common Metals* (UK) using magnesia crucibles. They were then machined into the specific geometry necessary for CFA, as shown in Figure 3.1. The necessary raw materials were sourced by *Nanoval GmbH & Co. KG* and *Less Common Metals* themselves from trusted suppliers.

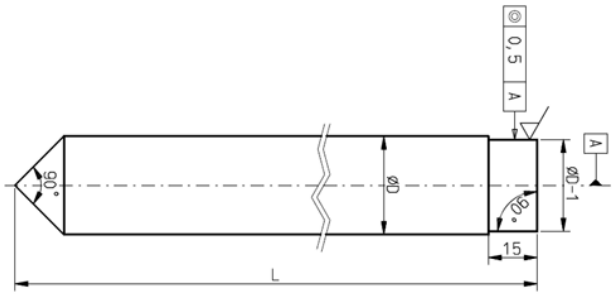

Figure 3.1: Specified geometry for material to be atomised by CFA, L ≥ 400 mm [source: *Nanoval GmbH & Co. KG*]

On the other hand, AMA and AMA2 powders were produced by Arc-Melting Atomisation (AMA) at *Arcast Inc.*(USA) where the raw materials mentioned in Table 3.2 were shipped to them. They were melted on a cold copper crucible before pouring on to a vertical Argon stream. Initial arc-melting atomisation trials were performed at *IMDEA Materials Institute* using a lab-scale *Arcast Arc 200* arc-melting furnace equipped with a horizontal Argon nozzle. The experience and characterisation results were shared with all suppliers in order to optimise their atomisation process for meeting our bulk powder requirements. However, detailed parameters of the atomisation processes used by external suppliers were not shared due to confidentiality issues.

Following atomisation, the powders were sieved into different size ranges which are summarised in Table 3.4. All Ti-rich compositions (CGA, CFA, AMA and AMA2) were developed for Selective Laser Melting (SLM) and consisted of a '*SLM range'* of 20 – 63 µm sizes. The sizes below and above these limits were named as *'fine'* and *'coarse'* respectively. CFA-FeTi powder was developed for Laser Metal Deposition (LMD) purposes and had 45 – 90 µm powders sieved out as the '*LMD range'*. An intermediate size range 20 – 45µm of this powder was left lying between the *'fine'* and '*LMD range'.* The size ranges for processing by SLM and LMD, i.e. 20 – 63 µm and 45 – 90 µm respectively, were so selected because these sizes are considered appropriate for those processing methods (as mentioned in Section 1.3.2.3 of Chapter 1).

Table 3.4: Classification of studied powders into defined size ranges by sieving

Alloy	Fine		SLM/LMD range	Coarse
CGA	< 20 µm		20 – 63µm	> 63 µm
CFA	< 20 µm		20 – 63µm	> 63 µm
AMA	< 20 µm		20 – 63µm	> 63 µm
AMA2	< 20 µm		20 – 63µm	> 63 µm
CFA-FeTi	< 20 µm	20 – 45µm (extra)	45 – 90 µm	> 90 µm

The SLM range of Ti-rich powders was further sieved into two smaller size ranges, 20 – 45 µm and 45 – 63 µm, for some studies and was mentioned clearly while discussing the results in the following chapters. Similarly, the LMD range of CFA-FeTi was sieved into 45 – 71 µm and 71 – 90 µm whenever necessary.

3.2 Processing

The materials in the form of gas-atomised powders were processed by three main techniques: SLM, LMD and FAHP. The following subsections present the processes along with the respective materials and processing parameters used. The choice of powder batches for final processing by SLM and LMD was based on powder characterisation results and initial AM trials, which are explained in details in chapter 4. Further, as mentioned in the objectives in chapter 2, CFA-FeTi ($Fe_{82.4}Ti_{17.6}$) powder was consolidated by FAHP in order to compare the micro-mechanical behaviour of produced samples to that of LMD-built $Fe_{82.4}Ti_{17.6}$.

3.2.1 Selective Laser Melting (SLM)

Selective Laser Melting (SLM) of AMA2 $Ti_{73.5}Fe_{23}Nb_{1.5}Sn_2$ powder (in size range 20 – 63 µm) was carried out by our collaborators at *German Aerospace Center DLR* (Germany). The basic working principle of a SLM system is explained in section 1.2.1 of chapter 1. A SLM solutions 280 HL machine with a 400 W fibre laser was used for this purpose. All builds were performed in a high purity Argon atmosphere using a Ti-6Al-4V baseplate that was pre-heated from the bottom. A temperature of ≈ 600 °C was maintained at the top of the building plate. Two sets of laser power and scanning rates were used, i.e. 120 W power with scan rate 600 mm/s and 100 W power with scan rate 450 mm/s. Layer thickness and hatch distance were fixed at 30 µm and 100 µm respectively for all builds. Samples of dimensions 46 mm × 12 mm × 8 mm were produced from which tensile and compression specimens were extracted later for quasi-static tests (explained in details in sections 3.3.10 and 3.3.11). The choice of laser power and scanning rate did not significantly affect the microstructure or mechanical behaviour of extracted specimens, whose test results were thus compiled together.

3.2.2 Laser Metal Deposition (LMD)

Laser Metal Deposition (LMD) of CFA-FeTi ($Fe_{82.4}Ti_{17.6}$) powder (in size range 45 – 90 µm) was performed by our collaborators at *Fraunhofer Institute for Laser Technology ILT* (Germany). The basic working principle of a LMD system is explained in section 1.2.1 of chapter 1. A Fraunhofer ILT continuous coaxial powder delivery nozzle with a fibre coupled diode laser system was used for the builds. A gas stream of Argon was used for feeding the powder (at a rate of 2.2 g/min) while also shielding the melt pool from the atmosphere. Builds were performed on a S235 steel build plate, pre-heated to 500 °C, using laser power of 1050 W and a beam diameter of 1.5 mm. A bidirectional hatching strategy was used for depositing with a velocity of 1200 mm/min and layer height of 0.5 mm. Samples of dimensions 25 mm × 25 mm × 8 mm, 50 mm × 25 mm × 5 mm and 43 mm × 25 mm × 5 mm were produced from which tensile and compression specimens were extracted for quasi-static tests (explained in details in sections 3.3.10 and 3.3.11). Before extracting specimens, all built samples were stress-relieved by annealing in an Argon atmosphere at 750 °C for 2h.

3.2.3 Field Assissted Hot Pressing (FAHP)

Field Assisted Hot Pressing (FAHP) is a solid state sintering process which produces dense consolidated material from powders by simultaneously applying uniaxial pressure and temperature through an alternating current. The powder is placed inside a graphite die with two conductive punches in a set-up shown schematically in Figure 3.2(a). The punches apply pressure for compaction, while the passing current simultaneously causes Joule heating and local melting at the particle contact points, thus assisting neck formation. The Joule heating also causes high speed difussion, local vapourisation and cleaning of powder surfaces [1–3]. This set up requires lower sintering temperatures and less sintering or holding time than conventional furnace-based sintering methods, thus avoiding grain growth and allowing preservation of material microstructures or phases. This is why FAHP was preferred for processing our pre-alloyed powders ($Fe_{82.4}Ti_{17.6}$) containing ultrafine lamellar microstructures. The microstructure and micromechanical behaviour of samples consolidated by this rapid sintering technique were later compared to those consolidated by LMD using very high cooling and solidification rates of laser melting. Unlike LMD, FAHP does not involve complete melting of the powders.

FAHP of CFA-FeTi ($Fe_{82.4}Ti_{17.6}$) powder (in the size range 45 – 90 µm) was performed in a Gleeble 3800 equipment (*Dynamic System Inc.*, USA) with a horizontal design. As shown in Figure 3.2(a) , the powder is placed inside the graphite die (in a cylindrical cavity of diameter 10 mm) and covered by graphite punches on both sides. The whole process was conducted in a vacuum (≈ 10^{-5} mbar) atmosphere. The applied pressure on powder and the sintering temperature were controlled by controlling the force on the puches and the current that flows through them. A continuous low frequency alternating current was supplied through

the punches which are connected to the water-cooled jaws of Gleeble via Tungsten carbide anvils. The powder temperature was monitored using thremocouples placed in the graphite cylindrical die and one of the punches. The three main processing parameters in FAHP are the applied pressure, sintering temperature and the sintering/holding time, i.e. the time for which sample is held at the maximum temperature and pressure. Figure 3.2(b) shows the temperature and pressure profile for one of the samples. It was heated up to 1230 °C at a rate of 100 °C/min. A pressure of 50 MPa was applied after reaching 400 °C and maintained. After 10 min of holding time at 1230 °C, the current and force were cut off allowing the sample to cool under Argon atmosphere. The sintering temperature and holding/sintering time were varied to produce four samples of $Fe_{82.4}Ti_{17.6}$ processed by FAHP, as shown in Table 3.5.

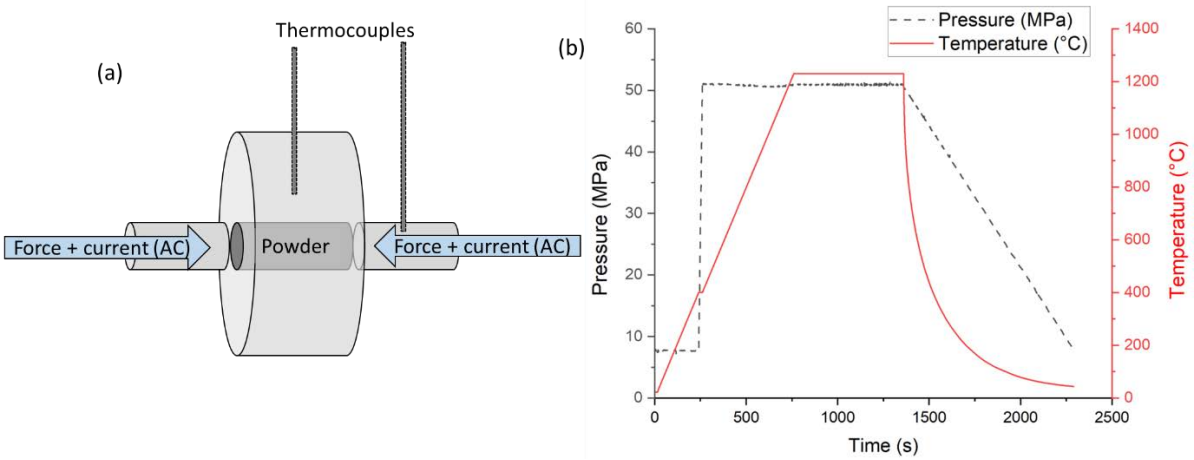

Figure 3.2: (a) Schematic showing the graphite cylindrical die used for FAHP consolidation, (b) Plot showing the thermal and pressure cycle of FAHP process (for sintering temperature 1230 °C, pressure 50 MPa and holding time 10 min)

Table 3.5: Processing parameters of FAHP-processed $Fe_{82.4}Ti_{17.6}$ samples

Sample serial no. ($Fe_{82.4}Ti_{17.6}$)	**Sintering Temperature (°C)**	**Pressure (MPa)**	**Sintering/holding time (min)**
1	1150	50	2
2	1150	50	10
3	1230	50	2
4	1230	50	10

3.3 Characterisation

3.3.1 Powder flowability

The flowability of powders in the AM size range was measured using a Hall flowmeter, as described in ASTM B213-97 standard. It measures the time required for a given mass of powder (50 g) to flow freely through a Hall funnel.

3.3.2 Powder density

Apparent density of powders, which characterises the mass of powder required to fill a volume-calibrated container while flowing freely through a Hall funnel above, was determined as per ASTM B212 standard.

Tap density is the density measured after the powder (of known mass) was placed in a graduated cylinder and tapped at a particlular frequency to settle the particles, under conditions specified by ASTM B527-06 standard.

3.3.3 Particle Size Distribution of powders by laser diffraction

Particle Size Distribution (PSD) of powders was determined by laser diffraction using the equipment *Mastersizer 2000 (Malvern Instruments)* as per ISO 13320-1 standard. It comes with a *Hydro2000* dispersion unit where powder samples (≈ 1 g) were introduced into distilled water that is constantly being swirled or rotated to ensure efficient dispersion of particles. A laser beam was sent through this medium by an optical bench and its scattering behavior was captured by detectors to obtain information on dispersed particles. The analysis is performed by an in-built software using equations from Mie theory which assume the interacting particles are perfect translucent spheres [4]. The light scattering/diffraction angle is inversely proportional to the interacting particle's diameter, while the intensity of the diffracted light is proportional to the particle's volume [5]. Summation of diffraction patterns produced by all particles randomly interacting with the laser beam returns a volume-weighted distribution of intensities across various scattering angles which are a function of particle diameters. A PSD based on volume % or cumulative volume % is plotted by the software which also identifies the important D-values (D_{10}, D_{50} and D_{90}). However, powder particles are not always perfect spheres and the diameters/volumes reported here actually refer to the diameters/volumes of equivalent spheres which produce the same diffraction pattern as the interacting particles. In order to make them more representative of particle dimensions and minimise the error for non-spherical shapes, the technique allows free rotation of interacting particles in the dispersing medium and averaging of calculations over several measurements. This technique can not provide information on particle shapes. Further, the calculations require knowledge of the interacting material´s refractive index and absorption coefficient. For our alloy compositions, this information was substituted by readily available data for their main constituting elements, i.e. Ti or Fe (for $Fe_{82.4}Ti_{17.6}$).

3.3.4 Inert Gas Fusion (for Oxygen content)

The Oxygen content in powders and consolidated alloys was measured destructively by inert gas fusion in a LECO TC-500 analyzer (as per ASTM E1409 standard). Metallic samples were placed in a high purity graphite crucible and fused in a furnace. The Carbon in the crucible reduces Oxygen in the sample to CO or CO_2. A Nickel basket was used as a flux to help release the Oxygen from our reactive alloys containing Ti. All gases produced during fusion were

carried by a inert carrier gas through a series of Infra-Red (IR) and Thermal Conductivity (TC) detectors that quantified the gases.

3.3.5 X-ray Diffraction (XRD)

X-ray Diffraction (XRD) was performed using a *PANalytical Empyrean* X-ray diffractometer for determining phases in powders of all size ranges as well as in consolidated alloys. Cu K_α radiation (voltage 45 kV, current 40 mA) was used for all measurements. Powder samples were spread on a spinning stage while measuring the diffraction angle from $2\theta = 20\,^\circ$ to $120\,^\circ$. In case of consolidated samples, a motorized 5-axis (Chi-Phi-XYZ) cradle was used instead. Metallic samples with flat surfaces were prepared up to the same standards as for microscopy.
The program HIGHSCORE was used for identifying the phases as well as for performing a Rietveld refinement on some basic parameters in order to fit the raw data. This fitting was used to empirically estimate the respective phase fractions from each pattern.

3.3.6 Electron Microscopy

Scanning Electron Microscope (SEM) *Zeiss EVO MA15* was used to characterize powder morphology, as well as the chemical compositions of bulk alloys and powders using a built-in Energy dispersive X-ray (EDX) system from *Inca*. A dual beam microscope *FEI Helios Nanolab 600i*, equipped with an EDX system *(Oxford)*, was used for microstructural characterisation of powders and consolidated alloys at high magnifications. Further, phase maps were acquired using an attached Electron Backscattered Diffraction (EBSD) system by Oxford instruments at acceleration voltage of 20 kV and 1.4 nA current. This helped in phase identification along with XRD analysis, especially for microstructures inside powder particles. All microscopy samples were embedded in a conductive resin (using *Buehler Simplimet2*), prepared metallographically to obtain a mirror polish and finally surface-finished with colloidal silica.

SEM micrographs were also used to determine the inter-lamellar spacing (λ) of the lamellar eutectics observed in our microstructures. A special **image analysis tool**, based on *ImageJ*, was developed to do this efficiently and accurately, which is described in **Appendix A.**

3.3.7 X-ray Computed Tomography

A *General Electric Phoenix Nanotom* system was used for X-ray Computed Tomography (XCT) characterisation. Powder samples in the sieved 'SLM/LMD' size range (see Table 3.4) were introduced in a thin plastic capillary (diameter around 1 mm) tube and sealed. Some powders were also embedded in a bakelite resin via cold mounting (60% of resin powder mixed with 40 % of metallic powder sample by mass), followed by cutting out of a thin cuboidal specimen (6 mm x 1.5 mm x 1 mm) for XCT measurements. In a resin, individual powder particles tend to be more separated in space, thus potentially assissting the segmentation and data analysis later. The tomograph was set to 120 kV and 80 µA using a W target with 0.1 mm Cu filter. The

flat panel detector of 2304 × 2304 pixels was placed at 326 mm from the X-ray tube (source) and the samples were placed at 5 mm from the source leading to 65.2X magnification and a pixel size of 0.77 µm. For each measurement, 1600 radiographs (computed as the average of 8 consecutive radiographs) were acquired with an exposure time of 1 s for 360 ° sample rotation, leading to a total measurement time of 4 h 10 min.

XCT scans were also performed on bulk specimens of LMD-built $Fe_{82.4}Ti_{17.6}$. Compression specimens (cylindrical 6 mm long, 4 mm diameter) and tensile specimens (maximum dimensions 23 mm × 12 mm × 2.5 mm) were characterized for investigating internal cracks and porosity distributions. The tomograph was set to 130 kV and 40 µA using a W target with 0.2 mm Cu filter. The flat panel detector of 2304 × 2304 pixels was placed at 200 mm from the X-ray tube (source) and the samples were placed at 12.3 mm from the source leading to 16.3X magnification and a pixel size of 3 µm. For each measurement, 1600 radiographs (computed as the average of 9 consecutive radiographs) were acquired with an exposure time of 0.5 s for 360 ° sample rotation, leading to a total measurement time of 2 h 15 min.

Additionally, a synchrotron X-ray tomography (S-XCT) was used at ID19 beamline of the *European Synchroton Research Facility (ESRF)* for some powders to compare the resolution with lab-based XCT. A pink beam of 80 keV energy was used and the samples were placed at 145 m from the X-ray source. A detector of 2560 × 1980 pixels was placed at 110 mm from the sample. Since a parallel beam is used for S-XCT, the magnification is obtained with optics (after using a scintillator) leading to a magnification of 10X and a pixel size of 0.72 µm. 5300 projections were acquired with an exposure time of 100 ms for 360 ° sample rotation, leading to a total measurement time of 10 min.

XCT data were reconstructed using *Phoenix datos |X 2.0 reconstruction v2.2.1* software. In case of S-XCT data, an in-house software developed by ESRF was used for reconstruction. *ImageJ* and *VGStudio Max 2.2* were used for additional treatments and visualisation of volumes. Further, an advanced image analysis tool was developed using *Fiji (ImageJ)* and *Avizo* softwares for one-step screening of powders using XCT data. It was used to characterise multiple important features like internal porosity, powder morphology and particle size distribution (PSD) based on a single XCT measurement. The tool methodology and results are presented in chapter 5 in details. Also, the volume-based PSDs determined by this methodology were validated against the PSDs determined by conventional laser diffraction technique explained in section 3.3.3. Both methods were evaluated for their pros and cons.

3.3.8 Nanoindentation

All nano-hardness tests were performed using the *Hysitron Triboindenter TI 950* system. For powders (embedded in a resin), single indents were performed by a Berkovich type diamond indenter on at least 20 random powder particles in all size ranges. The load increased gradually for 5 s until a maximum of 150 mN was reached, which was maintained for 10 s before slowly unloading over the next 5 s.

Nanoindentation was also performed on LMD-built $Fe_{82.4}Ti_{17.6}$ and FAHP-built $Fe_{82.4}Ti_{17.6}$. Two types of tests were performed using a Berkovich type diamond indenter:

i. Load-based: A 25 x 25 grid of indents (separated by 2.5 µm horizontally and vertically) was made until a fixed maximum load of 400 mN was reached.
ii. Strain-based: A 25 x 25 grid of indents (separated by 2.5 µm horizontally and vertically) was made at a constant strain rate of 0.1/s until a fixed maximum depth (h_{max}) of 200 nm was reached.

All samples were prepared by the same standards as for microscopy.

3.3.9 Micro-pillar Compression

Focussed ion (Ga+) beam of the dual beam microscope *FEI Helios Nanolab 600i* was used for carving out micro-pillars by milling the surfaces of LMD-built $Fe_{82.4}Ti_{17.6}$ and FAHP-built $Fe_{82.4}Ti_{17.6}$ samples. Micro-pillars of square cross-sections (big: 5 µm × 5 µm and small: 2 µm × 2 µm) were chosen as they offer better visibility of shear bands or disclocation slip on the sides and their mechanical properties remain identical to cylindrical pillars [6]. Pillars were carved to have an aspect ratio (height to edge) between 2 and 3, in order to avoid buckling under compression.

The samples, prepared to surface standards for electron microscopy, were mounted on the stage and tilted by 52 ° to make the sample surface perpendicular to the ion beam. A region of interest (ROI) of area 5 µm × 5 µm (2 µm × 2 µm for small pillars) was identified on the surface. Three steps of milling were performed for carving a micro-pillar at the ROI: (i) *rough milling using 9.3 nA ion current* was done to remove material from a large surrounding area of 25 µm × 25 µm (18 µm × 18 µm for small pillars) while masking an area of 8.5 µm × 8.5 µm (4.5 µm × 4.5 µm for small pillars) defined around the ROI, (ii) *finer milling using 2.5 nA current* was performed to further remove surrounding material in a smaller area of 18 µm × 18 µm (13 µm × 13 µm for small pillars) falling within the previously milled region, while masking an area of 6 µm × 6 µm (2.75 µm × 2.75 µm for small pillars) defined around the ROI and finally, (iii) *tapering removal and polishing using small current of 80 pA* was performed on side surfaces of the pillar formed out of the masked regions in previous steps, until desired edge dimensions of ≈ 5 µm (≈ 2 µm for small pillars) were obtained at the ROI. The samples were tilted to 53.5 ° and 50.5 ° for the ion beam to access pillar side surfaces. The milling depth or time in the first two steps were controlled such that the desired aspect ratio (height to edge) between 2 and 3 is achieved. The edges and heights of the carved micro-pillars were measured while imaging under SEM. SEM micrographs of carved pillars before and after compression are shown in Figure 6.9 of chapter 6.

Pillars were compressed using the *Hysitron Triboindenter TI 950* system equipped with a diamond flat punch of diameter 10 µm (5 µm for small pillars). Pillars were deformed by 10 % of their initial height under a constant strain rate of 10^{-3}/s. Sneddon's correction [7] was applied to the obtained load-displacement curves to account for elastic deformation of the

surrounding material. Then, engineering stress vs. engineering strain curves were determined based on the measured cross-sectional areas and heights of pillars.

At least 5 micro-pillars of cross-section 5 µm × 5 µm were carved and compressed on the surface of each sample for determining the average compressive yield strength. Smaller pillars of cross-section 2 µm × 2 µm were carved only on the LMD-built $Fe_{82.4}Ti_{17.6}$ sample at specific sites in the microstructure showing particular eutectic morphologies (explained in details in section 6.1.2 of chapter 6). All micro-pillars for LMD-built $Fe_{82.4}Ti_{17.6}$ were carved and loaded along an axis perpendicular to the build direction.

3.3.10 Compression tests

Quasi-static compression tests were performed under uniaxial loading on specimens of LMD-built $Fe_{82.4}Ti_{17.6}$ and SLM-built $Ti_{73.5}Fe_{23}Nb_{1.5}Sn_2$. A *Universal Electromechanical Machine INSTRON 3384* was used for this purpose. As shown in Figure 3.3, it was attached to a furnace *IBERTEST IB-TR3-3-1100* which can heat in air up to 1100 °C. It is capable of enclosing the specimen and locally maintaining a defined temperature around it throughout testing. Installed thermocouples inside the furnace can be positioned very close to the test specimen.

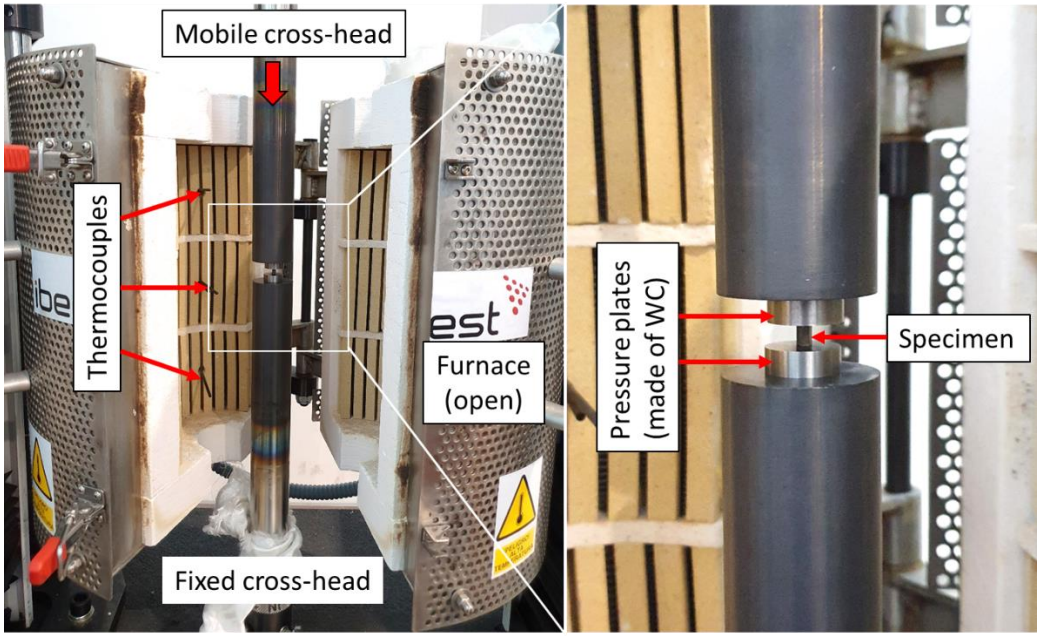

Figure 3.3: Experimental set-up used for conducting quasi-static compression tests on the *Universal Electromechanical Machine INSTRON 3384* at temperatures up to 600 °C in air

Cylindrical specimens of height 6 mm and diameter 4 mm, as shown in Figure 3.4(a), were used for all quasi-static compression tests conducted at a constant strain rate of 0.67/min (cross-head displacement rate 1 mm/min).

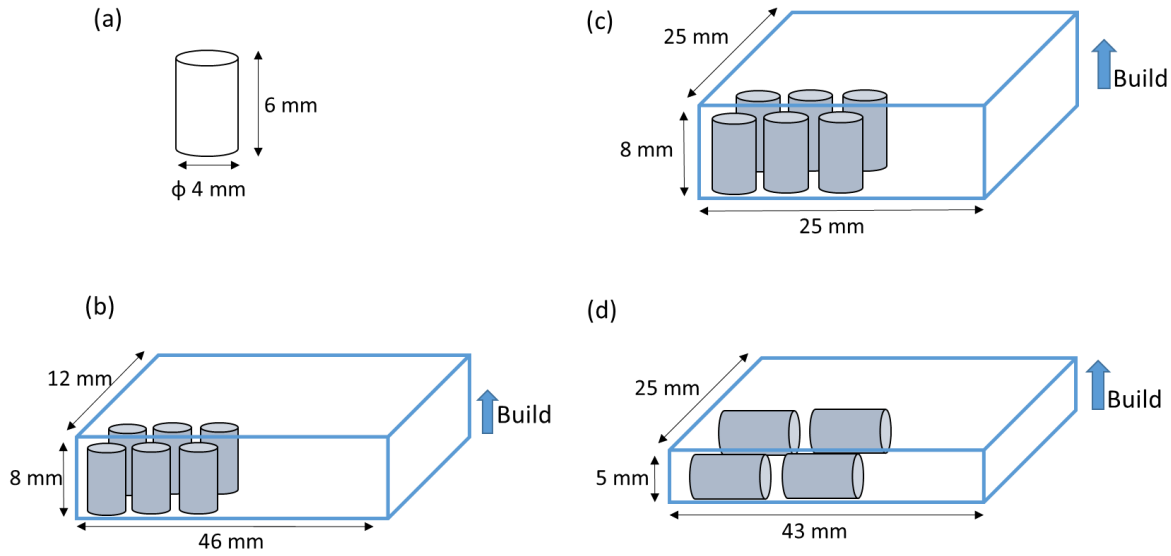

Figure 3.4: (a) Geometry of compression specimens used for all quasi-static tests. Schematics showing orientation of the extracted compression specimens from blocks of (b) SLM-built-$Ti_{73.5}Fe_{23}Nb_{1.5}Sn_2$ and (c, d) LMD-built $Fe_{82.4}Ti_{17.6}$

For SLM-built $Ti_{73.5}Fe_{23}Nb_{1.5}Sn_2$, tests were performed on specimens (whose building direction lied parallel to the uniaxial loading axis) at room temperature, 450 °C and 600 °C. In case of LMD-built $Fe_{82.4}Ti_{17.6}$, specimens built along directions both parallel and perpendicular to the loading axis were tested at room temperature, 500 °C, 550 °C and 600 °C. Figure 3.4 (b-d) schematically show the block dimensions built by SLM/LMD processing and the relative orientation of cylindrical specimens extracted from them using Electrical Discharge Machining (EDM). At least 5 specimens were tested for each measurement condition. For all tests conducted at high temperatures (above room temperature), a 10 min of holding time was allowed after attaining the defined temperature in order to ensure thermal homogeneity in and around the specimen before starting the test. The temperature was maintained constant during the test and until the specimens fractured or cross-head movement stopped, following which the heating was turned off and the furnace was left open to allow a natural cooling in air.

3.3.11 Tensile tests

Quasi-static tensile tests were performed under uniaxial loading on specimens of LMD-built $Fe_{82.4}Ti_{17.6}$ and SLM-built $Ti_{73.5}Fe_{23}Nb_{1.5}Sn_2$. The same equipment *Universal Electromechanical Machine INSTRON 3384* with an attached furnace *IBERTEST IB-TR3-3-1100*, as introduced in the previous section, was used for this purpose. As shown in Figure 3.5, the tensile sample holders were installed on it which were specifically designed for the tensile sample geometry shown in Figure 3.6(a).

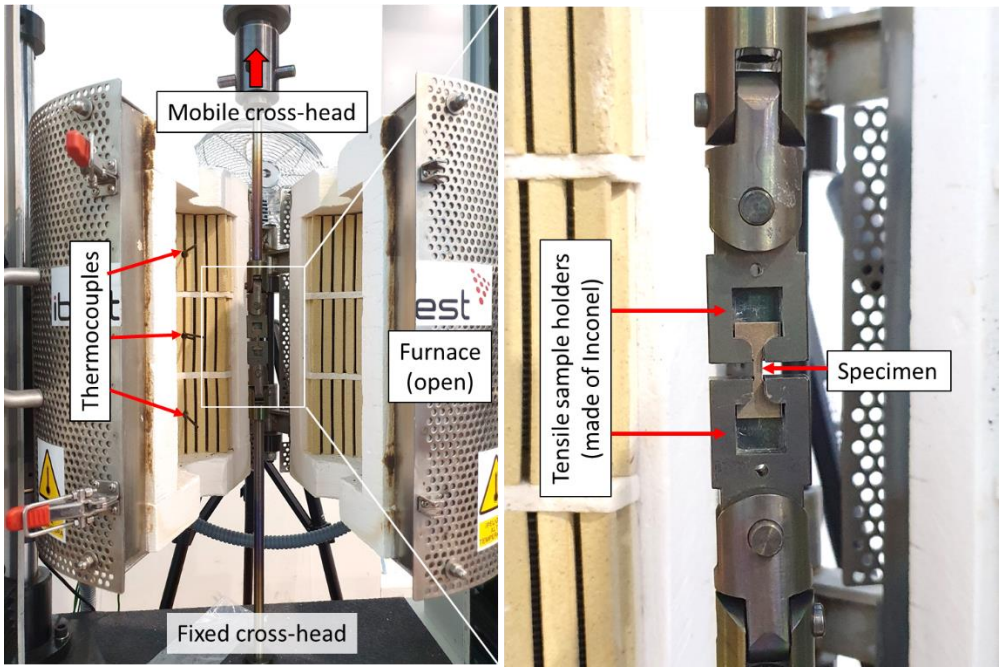

Figure 3.5: Experimental set-up used for conducting quasi-static tensile tests on the *Universal Electromechanical Machine INSTRON 3384* at temperatures up to 600 °C in air

Flat tensile specimens of geometry shown in Figure 3.6(a), were used for all quasi-static tensile tests conducted at a constant strain rate of 0.09/min (cross-head displacement rate 0.3 mm/min). Figure 3.6(b, c) schematically show the block dimensions built by SLM/LMD processing and the relative orientation of flat tensile specimens extracted from them using Electrical Discharge Machining (EDM). In both cases, heights of the crack-free built material produced by LMD/SLM only allowed extraction of the 23 mm long specimens in a plane such that the building direction is always perpendicular to the loading axis of the tensile tests.

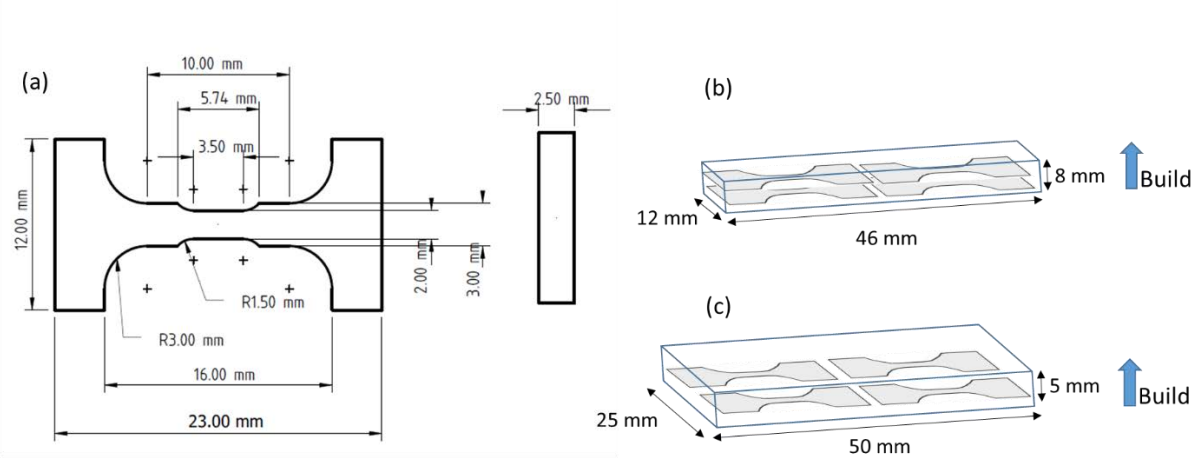

Figure 3.6: (a) Geometry of tensile specimens used for all quasi-static tensile tests. Schematics showing orientation of the extracted specimens from blocks of (b) SLM-built-$Ti_{73.5}Fe_{23}Nb_{1.5}Sn_2$ and (c) LMD-built $Fe_{82.4}Ti_{17.6}$

For SLM-built $Ti_{73.5}Fe_{23}Nb_{1.5}Sn_2$, tests were performed on specimens at room temperature, 450 °C, 500 °C, 550 °C and 600 °C. In case of LMD-built $Fe_{82.4}Ti_{17.6}$, specimens were tested at

room temperature, 550 °C and 600 °C. At least 3 specimens were tested for each measurement condition. For all tests conducted at high temperatures (above room temperature), a 10 min of holding time was allowed after attaining the defined temperature in order to ensure thermal homogeneity in and around the specimen before starting the test. The temperature was maintained constant during the test and until the specimens fractured or cross-head movement stopped, following which the heating was turned off and the furnace was left open to allow a natural cooling in air.

This ends the chapter on experimental procedure. The next chapters present the main results of the reported experiments. They are discussed along the lines of established objectives with individual chapters focussing on: characterisation and solidification behaviour of the studied powders, new methodology for advanced image analysis of powder tomography data and characterisation of the AM-built alloys.

REFERENCES

[1] C. S. Bonifacio, T. B. Holland, and K. Van Benthem, “Evidence of surface cleaning during electric field assisted sintering,” *Scr. Mater.*, vol. 69, no. 11–12, pp. 769–772, Dec. 2013, doi: 10.1016/J.SCRIPTAMAT.2013.08.018.

[2] Z. A. Munir, U. Anselmi-Tamburini, and M. Ohyanagi, “The effect of electric field and pressure on the synthesis and consolidation of materials: A review of the spark plasma sintering method,” *J. Mater. Sci.*, vol. 41, no. 3, pp. 763–777, Feb. 2006, doi: 10.1007/S10853-006-6555-2.

[3] N. Chawake, L. D. Pinto, A. K. Srivastav, K. Akkiraju, B. S. Murty, and R. S. Kottada, “On Joule heating during spark plasma sintering of metal powders,” *Scr. Mater.*, vol. 93, pp. 52–55, Dec. 2014, doi: 10.1016/j.scriptamat.2014.09.003.

[4] M. Instruments, “Mastersizer 2000 User Manual,” 2007.

[5] H. Li, J. Li, J. Bodycomb, and G. S. Patience, “Experimental Methods in Chemical Engineering: Particle Size Distribution by Laser Diffraction—PSD,” *Can. J. Chem. Eng.*, vol. 97, no. 7, pp. 1974–1981, Jul. 2019, doi: 10.1002/CJCE.23480.

[6] D. Kiener, C. Motz, and G. Dehm, “Micro-Compression Testing: A Critical Discussion of Experimental Constraints,” *Mater. Sci. Eng. A*, vol. 505, pp. 79–87, Apr. 2009, doi: 10.1016/j.msea.2009.01.005.

[7] I. N. Sneddon, “The relation between load and penetration in the axisymmetric boussinesq problem for a punch of arbitrary profile,” *Int. J. Eng. Sci.*, vol. 3, no. 1, pp. 47–57, May 1965, doi: 10.1016/0020-7225(65)90019-4.

Chapter 4

Powder Characterisation and Solidification studies

4 Powder characterisation and solidification studies

This chapter presents results and discussions concerning characterisations of all powders listed in Table 3.3 of chapter 3. Based on these results, powder batches and the respective atomisation methods were selected for bulk production of pre-alloyed powders for AM trials. In additon, this chapter also presents studies on rapid solidification behaviour of powder particles in different size ranges (and thus, experiencing different solidification kinetics). It is divided into two main sections: 'Ti rich powders' covering results of powders with Ti-rich target compostions, i.e. near-eutectic $Ti_{66}Fe_{27}Nb_3Sn_4$ (CGA, CFA, AMA powders) and non-eutectic $Ti_{73.5}Fe_{23}Nb_{1.5}Sn_2$ (AMA2 powder); and 'Fe-rich powder' covering results of CFA-FeTi powder with target composition $Fe_{82.4}Ti_{17.6}$. Each section starts with a subsection discussing characterisation of important physical properties and chemical compositions of powders. It is followed by subsections discussing solidification behaviour of each powder based on microstructural characterisations (like phase composition and distribution, eutectic morphology, etc.) across all size ranges. Solidification models are proposed for each studied powder. Finally, an additional subsection is dedicated to discussing the infuence of particle size (or solidification kinetics) on inter-lamellar spacing λ of the eutectic matrix and nano-hardness behaviour of powder particles.

4.1 Ti-rich powders

4.1.1 Physical and chemical characterisation

Figure 4.1 shows representative SEM micrographs of CGA, CFA, AMA and AMA2 powders in three size ranges (as defined in Table 3.4 of chapter 3). All particles showed a spherical morphology as expected in a gas atomised powder. Few satellites were visible, yet their density remained low.

Among the CGA, CFA and AMA powders which have the same target composition $Ti_{66}Fe_{27}Nb_3Sn_4$, AMA showed the best flowability with a Hall flow time of 17.6 s/50g as compared to 33 s/50g for CGA powder in the SLM size range (20 – 63 µm). As shown in Table 4.1, it showed the highest densities (apparent and tap) among the three and the lowest Hausner ratio (HR) of 1.17. Powder AMA2 of target composition $Ti_{73.5}Fe_{23}Nb_{1.5}Sn_2$ showed a low flow time and HR similar to AMA. Overall, the four powders show a HR < 1.28 and Hall flowtime between 17.6 to 33 s/50g. Commercial Ti-6Al-4V powders used for LPBF usually have a Hall flowtime of around 27 s/50g and can vary between 26.2 to 35.3 s/50g depending on the gas atomisation technique used [1], [2]. In this regard, these Ti-rich pre-alloyed powders can be considered to possess fairly good flowability with Arc-Melting Atomisation (AMA) method producing the best results.

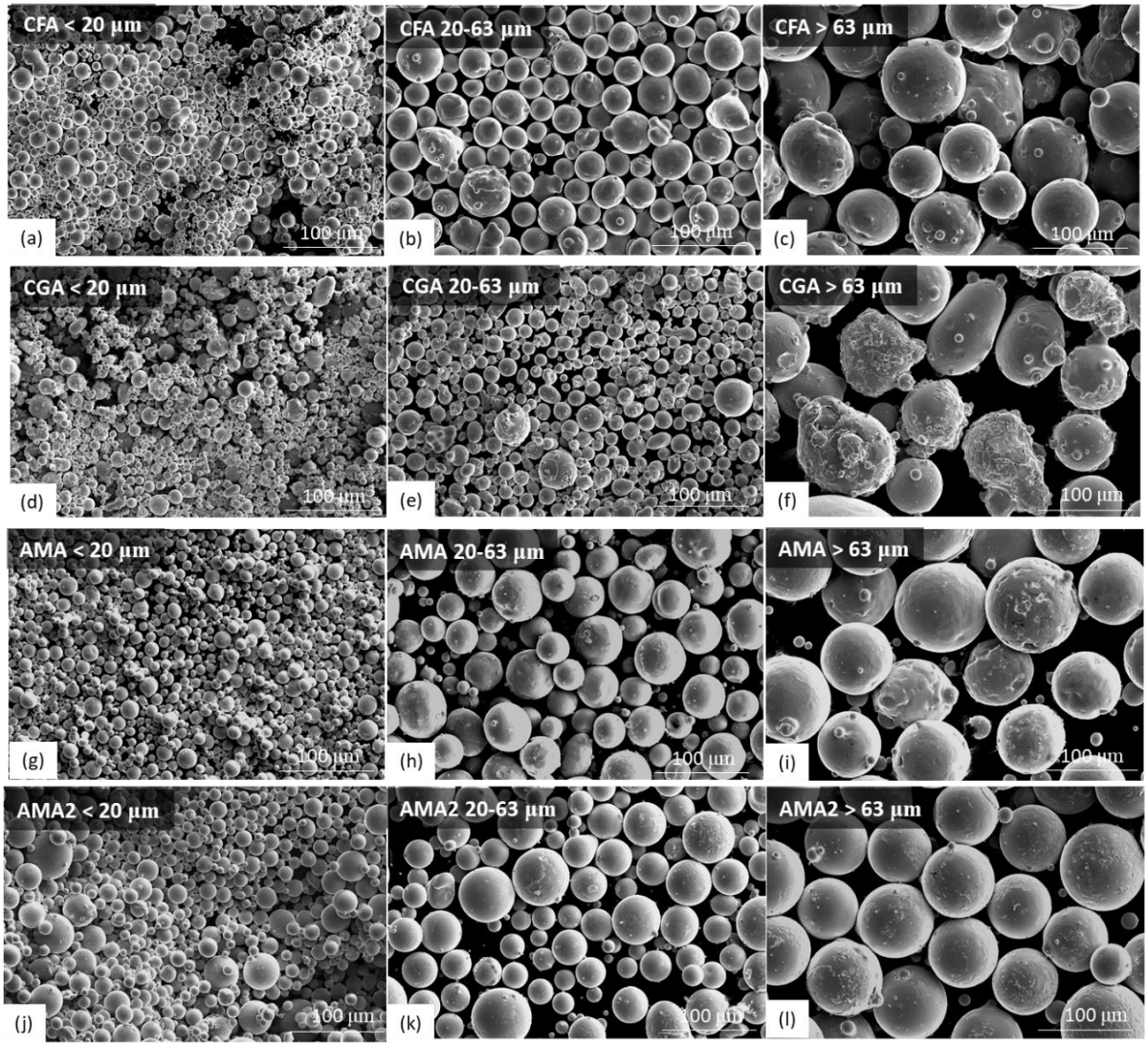

Figure 4.1: SEM micrographs showing the morphologies of produced Ti-rich pre-alloyed powders in three size ranges: (a to c) CFA $Ti_{66}Fe_{27}Nb_3Sn_4$,(d to f) CGA $Ti_{66}Fe_{27}Nb_3Sn_4$, (g to i) AMA $Ti_{66}Fe_{27}Nb_3Sn_4$ and (j to l) AMA2 $Ti_{73.5}Fe_{23}Nb_{1.5}Sn_2$

Table 4.1: Density and flowability measurements for all Ti-rich powders

Powder (20 – 63 µm)	**ρ apparent (g/cm^3)**	**ρ tap (g/cm^3)**	***Flowability (s/50g)***	***Hausner Ratio (HR)***
CFA	3.02	3.79	24.5	1.25
CGA	2.89	3.69	33.0	1.28
AMA	3.38	4.00	17.6	1.18
AMA2	3.16	3.70	18.4	1.17

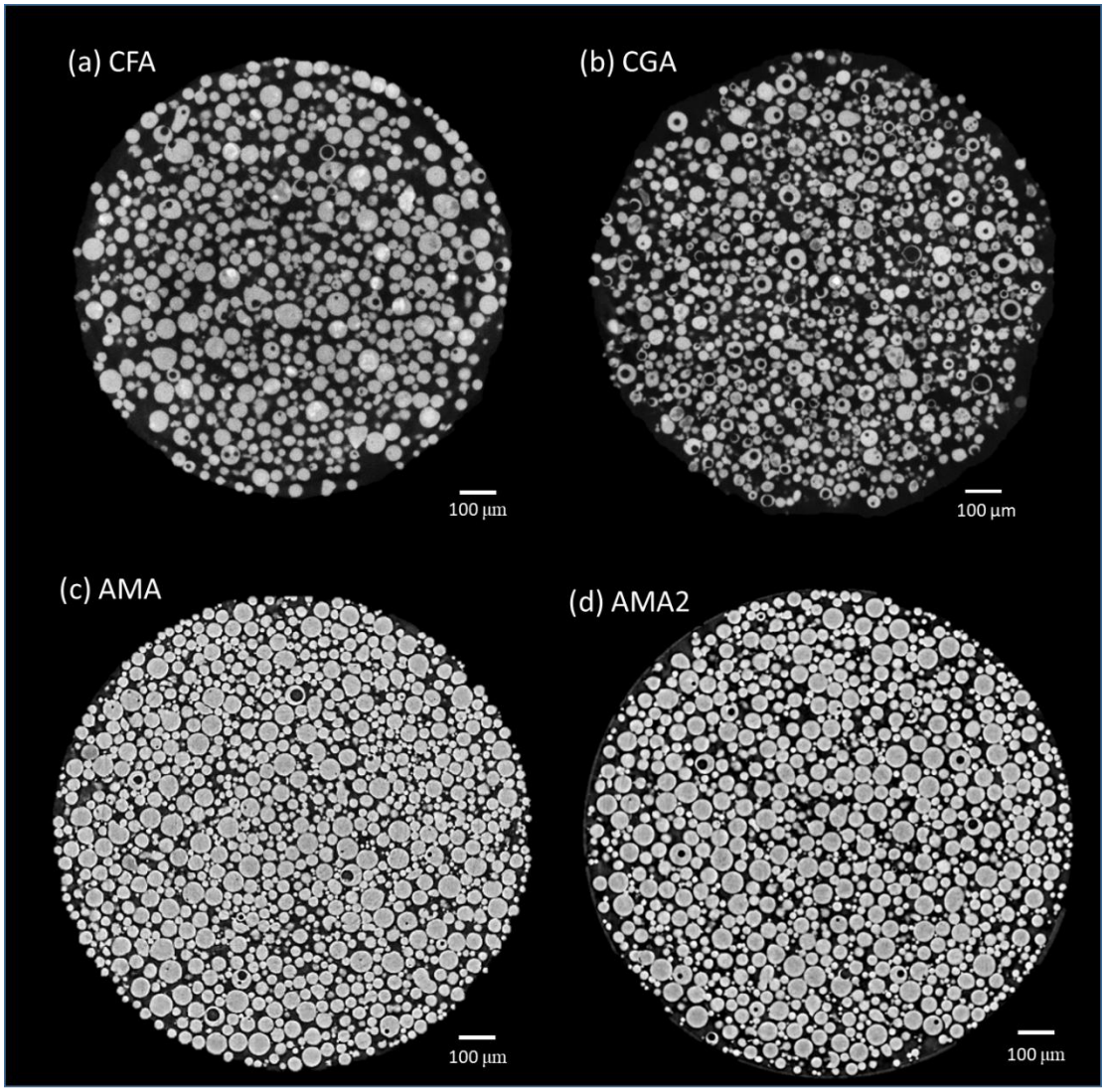

Figure 4.2: Representative XCT slices of a volume measured for a) CFA, (b) CGA, (c) AMA and (d) AMA2 powder in the SLM size range (20 – 63 µm). Slices show transverse cross-sections of a plastic capillary tube containing the powders

Figure 4.2 shows typical tomography slices observed in the XCT of all powders in the SLM size range where macropores can be observed in the cross-sections. A careful obervation of these tomography slices and the SEM micrographs in Figure 4.1 suggests the presence of relatively larger particles on average in AMA and AMA2 powders. These powders also seem to have relatively low concentration of internal pores in the SLM size range. On the other hand, CGA powder appears to consist of relatively smaller particles on average that feature high internal porosity. These observations were later confirmed by advanced analysis of XCT data and Particle Size Distribution (PSD) characterisation of powders.

The XCT data was treated in multiple steps using *Fiji (ImageJ)* and *Avizo* following a newly developed methodology which is described in Chapter 5 in details. The methodology was able to accurately estimate the closed or internal porosity of powders.

Table 4.2 summarises the porosity results for all Ti-rich powders in the SLM size range. Porosity volume % was quite low in these powders, with AMA showing the lowest (0.2 vol %) value. CGA showed the highest volume % of internal pores (1.9 %) which is more than 9 times that of AMA. Further, the number % of particles with internal pores was calculated using Equation 4.1 and assuming that one particle features a maximum of one internal pore. CGA also showed the largest number % of particles with internal pores, while it was the lowest for AMA2 powder.

$$Number\ \%\ of\ particles\ with\ closed\ pores = \frac{Number\ of\ closed\ pores\ in\ XCT\ volume}{Number\ of\ powder\ particles\ in\ XCT\ volume} \times 100$$

Equation 4.1

Table 4.2: Internal porosity of Ti-rich powders as determined my XCT data analysis (described in chapter 5)

Powder (20 – 63 µm)	**Closed porosity Vol %**	**Particles with pores Number %**
CFA	0.4	18.0
CGA	1.9	36.1
AMA	0.2	18.5
AMA2	0.4	9.5

The Particle Size Distributions (PSDs) of all powders based on volume %, as determined by laser diffraction are shown in Figure 4.3. AMA and AMA2 powders contained relatively larger particles as compared to their CGA and CFA counterparts. The measured D_{10}, D_{50} and D_{90} values mentioned in the figure indicate the same. This explains their relatively lower Hall flow times and higher densities (lower HR) as compared to CGA and CFA powders, since smaller particles tend to have the opposite effect on these properties (see section 1.3.2.3 of chapter 1). Larger concentration of voids, lower density and high fraction of small particles in the PSD seem to contribute towards the relatively highest Hall flow time of CGA powder in the SLM range. The process parameters for CGA need to be further optimised in order to obtain better physical properties.

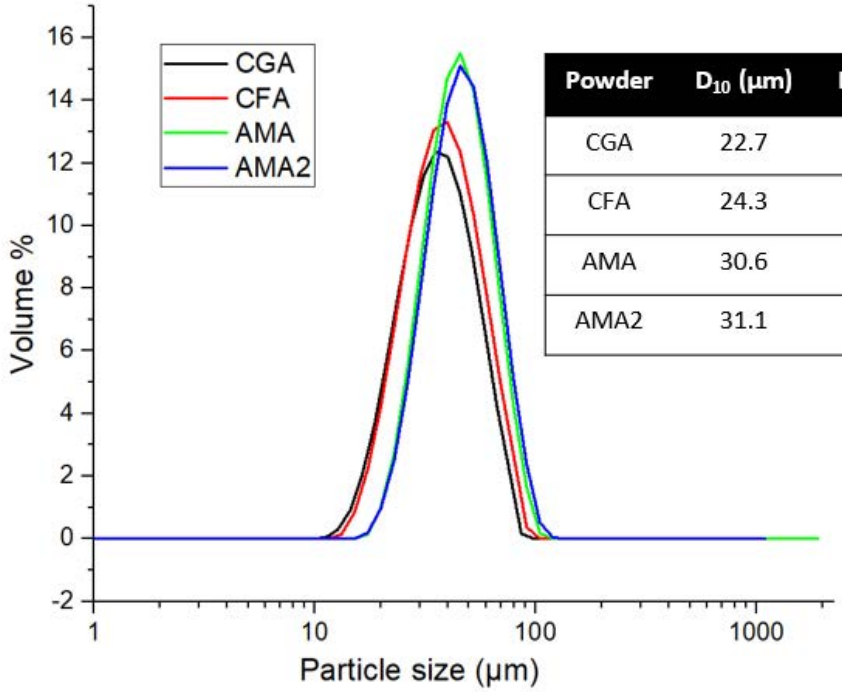

Powder	D_{10} (µm)	D_{50} (µm)	D_{90} (µm)
CGA	22.7	38.3	62.7
CFA	24.3	40.6	66.5
AMA	30.6	47.8	73.5
AMA2	31.1	49.3	76.6

Figure 4.3: Particle size distribution by volume percent for CFA and CGA powders in the SLM size range (20 – 63 µm)

The average chemical compositions of all powders measured in the three size ranges are summarised in Table 4.3 to Table 4.6. They also include the O_2 content (in ppm) measured by inert gas fusion (explained in section 3.3.4 of chapter 3). All four cases produced average compositions close to the target values, with relatively largest dispersion in the CGA powder particles as evident from the standard deviations. Among the powders with $Ti_{66}Fe_{27}Nb_3Sn_4$ target composition, CGA and AMA powders showed a slightly higher Fe content on average as compared to CFA powders. As seen in Table 4.4, coarse CGA particles contained 2.7 wt % more Fe on average than those produced by CFA. Consequently, the average Ti content was lower in CGA powders (2.9 wt % in coarse particles as compared to CFA), while showing no significant differences for Nb and Sn content. On the other hand, AMA powders maintained a Ti content close to the target but showed the lowest Nb content of ≈ 3.3 wt % among the three. Further, they had a highest Sn content of ≈ 9.6 wt %.

Looking at the O_2 content, it is concluded that arc-melting atomisation produced the cleanest powders. As seen in Table 4.5 and Table 4.6, AMA and AMA2 powders showed the lowest contamination by O_2, with 663 and 910 ppm of O_2 in the SLM range respectively. These are low and acceptable levels considering that a commercial Ti-6Al-4V powder produced for AM showed 1400 ppm of O_2 when measured by the same technique (inert gas fusion). Further, the contamination increased with decreasing particle size for AMA technique with fine powders showing the highest O_2 content. CFA powders showed the highest O_2 content of all powders with over 10000 ppm in the SLM range (see Table 4.3) which is far beyond acceptable levels. Unlike AMA technique, CFA showed an opposite trend of O_2 contamination with respect to size with coarse (> 63 µm) particles having almost double amount of O_2 than the

fine (< 20 µm) ones. The high O_2 content probably arises from the induction casting process of rods. The rods used as feedstock for CFA were cast from magnesia crucibles and showed ≈ 6640 ppm of average O_2 content when analyzed by inert gas fusion. Thus, although CFA, as a crucible-less technique, minimizes the powder contamination from crucible, it does not eliminate Oxygen-pick up during the overall process. Al also appeared as a contaminant in the CFA powders which is present as a common impurity in the raw materials used for alloying. The CGA powder had relatively lower O_2 content, 2400 ppm in the SLM range (see Table 4.4). Nevertheless, it is still high by the commercial powder standards. The CGA powder also showed some contamination by C, most likely from the graphite crucible used during atomisation.

Table 4.3: Chemical composition of $Ti_{66}Fe_{27}Nb_3Sn_4$ (at %) CFA powder measured for all size ranges

CFA powder	wt % Ti	wt % Fe	wt % Nb	wt % Sn	wt % Al	ppm of O_2
Target	58.3	27.8	5.1	8.8	0	0
Coarse	59.0 ± 0.8	27.2 ± 2.5	4.9 ± 0.5	8.2 ± 2.1	0.7 ± 0.1	18300
SLM	58.6 ± 1.3	26.5 ± 1.5	5.3 ± 0.3	8.8 ± 0.7	0.8 ± 0.1	10300
Fine	58.1 ± 0.2	27.4 ± 0.1	5.4 ± 0.2	8.3 ± 0.2	0.7 ± 0.1	9700

Table 4.4: Chemical composition of $Ti_{66}Fe_{27}Nb_3Sn_4$ (at %) CGA powder measured for all size ranges

CGA powder	wt % Ti	wt % Fe	wt % Nb	wt % Sn	wt % C	ppm of O_2
Target	58.3	27.8	5.1	8.8	0	0
Coarse	56.1 ± 5.2	29.9 ± 4.6	4.7 ± 0.5	8.9 ± 0.9	≈ 0.3	2700
SLM	56.8 ± 6.7	29.2 ± 6.1	4.9 ± 0.7	8.6 ± 0.9	≈ 0.3	2400
Fine	57.1 ± 5.1	29.1 ± 5	5.2 ± 1	8.6 ± 0.6	0	2600

Table 4.5: Chemical composition of $Ti_{66}Fe_{27}Nb_3Sn_4$ (at %) AMA powder measured for all size ranges

AMA powder	wt % Ti	wt % Fe	wt % Nb	wt % Sn	ppm of O_2
Target	58.3	27.8	5.1	8.8	0
Coarse	58.2 ± 1.2	28.9 ± 1.2	3.3 ± 0.3	9.6 ± 0.5	608
SLM	58.4 ± 1.1	28.7 ± 0.8	3.2 ± 0.4	9.7 ± 0.3	663
Fine	58.5 ± 0.9	28.7± 0.6	3.2 ± 0.4	9.6 ± 0.6	1150

Table 4.6: Chemical composition of $Ti_{73.5}Fe_{23}Nb_{1.5}Sn_2$ (at %) AMA2 powder measured for all size ranges

AMA2 powder	wt % Ti	wt % Fe	wt % Nb	wt % Sn	ppm of O_2
Target	68	25	2.5	4.5	0
Coarse	69.0 ± 0.9	23.9 ± 1.3	2.8 ± 0.2	4.4 ± 0.3	829
SLM	69.0 ± 0.6	23.9 ± 0.7	2.7 ± 0.2	4.4 ± 0.2	910
Fine	69.1 ± 0.9	23.9 ± 0.8	2.6 ± 0.3	4.3 ± 0.3	1085

4.1.2 Solidification in CFA $Ti_{66}Fe_{27}Nb_3Sn_4$ powder

XRD patterns for CFA powder in three size ranges, with peaks identified, are shown in Figure 4.4. They clearly indicate differences in the constituting phases formed during cooling of the atomised particles. The phase fractions for all size ranges calculated by a preliminary Rietveld refinement are mapped in Figure 4.5. Up to six phases were identified in the CFA powders, including an oxide Fe_2Ti_4O. Apart from commonly occurring β-Ti and FeTi phases, $FeTi_2$ was a significant phase in fine particles. $FeTi_2$ is a meta-stable phase, which does not exist in the equilibrium Ti-Fe phase diagram. Nb always stayed in the solid solution and none of the powders showed presence of a Nb-containing phase. Besides, α-Ti was observed exclusively in CFA powders.

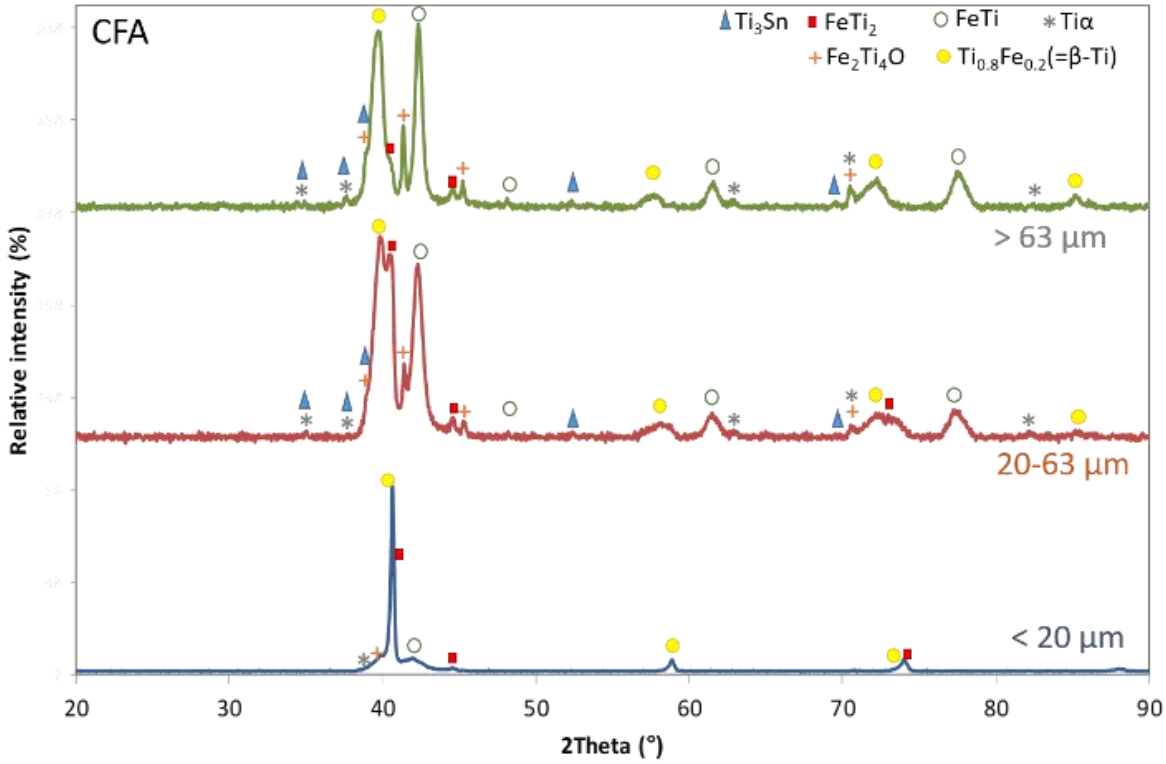

Figure 4.4: XRD patterns with identified peaks for all size ranges of CFA $Ti_{66}Fe_{27}Nb_3Sn_4$ powders

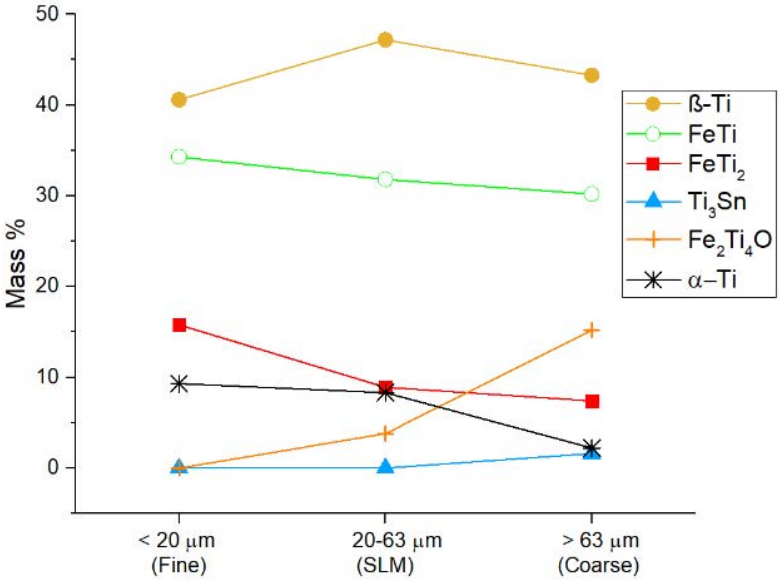

Figure 4.5: Phase fraction by mass percent in three size ranges of CFA powders, as estimated by Rietveld refinement of XRD patterns

The fine (< 20 µm) powder particles contained the largest fraction of metastable $FeTi_2$ indicating very high solidification rates. The XRD analysis further revealed that this phase started disappearing as particle size increases and crystallisation kinetics become slower. Meanwhile, the FCC oxide Fe_2Ti_4O, also known as Oxygen-stabilised $FeTi_2$, increased with particle size. This coincides with the observed trend of higher O_2 content in larger particles (see Table 4.3).

Microscopic analysis of powder cross-sections, coupled with insights from XRD, helped explain the solidification behaviour of the alloy under different kinetics operating in differently sized particles. Figure 4.6 shows the representative microstructures in different size ranges. The schematic in Figure 4.7 summarises the important microstructural features and the apparent reactions occurring during solidification of particles in different size ranges.

The fine particles mostly consisted of primary β-Ti and some eutectic phase (β-Ti + FeTi). A few dendrites of Fe_2Ti_4O, 1 – 2 µm in length, were also observed, as seen in Figure 4.6(a) and schematically represented in Figure 4.6(a). They were surrounded by relatively brighter $FeTi_2$. No peaks corresponding to Ti_3Sn were detected by XRD and no Sn-containing independent phase was observed in most particles. However, EDS had revealed a fair amount of Sn in their chemical composition (see Table 4.3) suggesting that it mostly remained in solid solution. Although Rietveld refinement data suggests a quite significant amount of FeTi and α-Ti in fine particles, they were not so prominent in the microscopic analysis. It should be noted that this is a very preliminary refinement only meant to be suggestive.

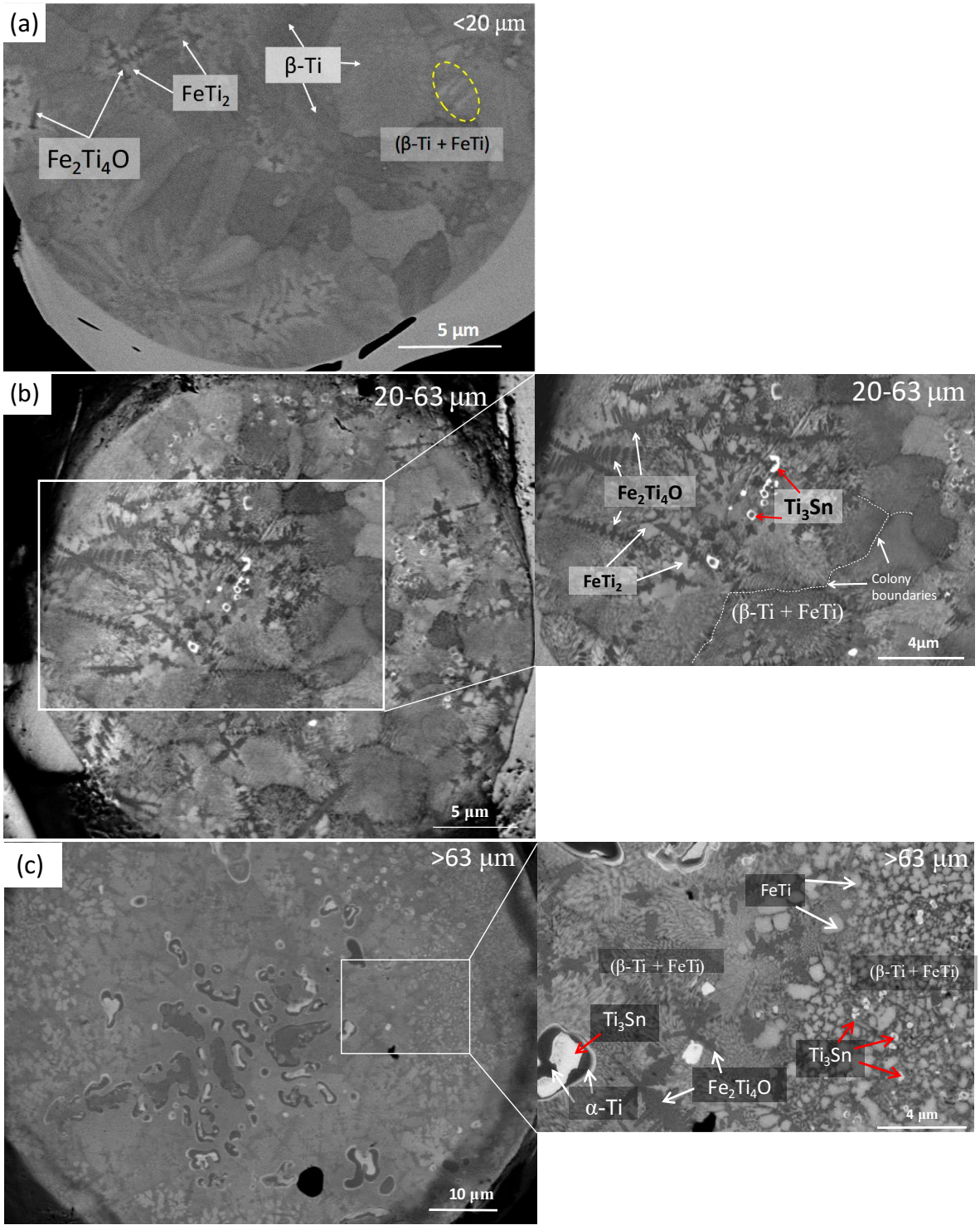

Figure 4.6: SEM micrographs (BSE mode) showing typical microstructures (with phases marked) observed in $Ti_{66}Fe_{27}Nb_3Sn$ powders produced by CFA across (a) fine (< 20 µm), (b) SLM (20 – 63 µm) and (c) coarse (> 63 µm) size ranges

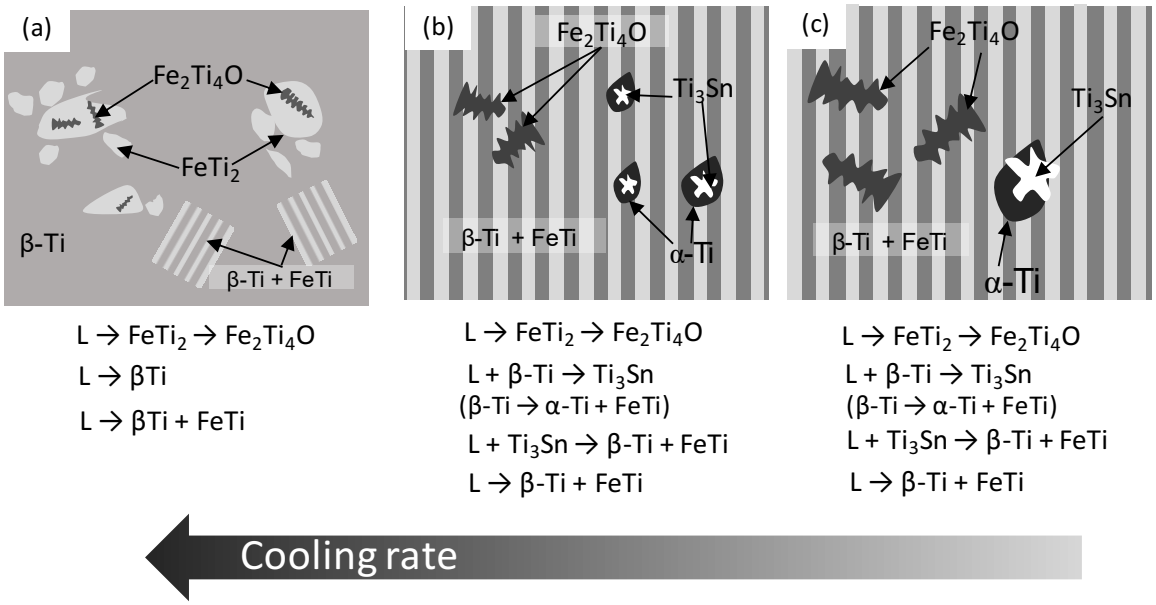

Figure 4.7: Schematic showing the most relevant microstructural features, along with reactions involved, for CFA powders of (a) fine (< 20 µm), (b) SLM (20 – 63 µm) and (c) coarse (> 63 µm) size ranges

Particles in the SLM (20 – 63 µm) and coarse (> 63 µm) size ranges showed primary µm-scale dendrites of Fe_2Ti_4O, as shown in Figure 4.6 (b, c). The FCC oxide phase Fe_2Ti_4O, remained little in fine particles and reached its highest proportion in coarse powders. Much like fine powders, some meta-stable $FeTi_2$ was always observed around them suggesting that they formed upon oxidation of the metastable phase. Surprisingly, none of them featured primary β-Ti as dendrites. Wang et al. [3] had previously observed the formation of Fe_2Ti_4O as an O_2 stabilising phase between eutectic (β-Ti + FeTi) cells produced by laser synthesis of elemental powders (see Figure 1.15 in section 1.2.6 of chapter 1). It was attributed to the high cooling rates and O_2 content. As also mentioned in section 1.2.6, Gussone et al. [4] encountered η-$Fe_2Ti_4O_x$ dendrites during SLM of Fe-32.5Ti (wt %) alloy involving elemental powders. The reported microstructures in Figure 1.17 are quite similar to microstructures of SLM and coarse CFA powders, except for the existence Sn-related phase. They further concluded that Fe_2Ti_4O is a hard and brittle phase whose distribution influences the mechanical behaviour of the fabricated sample. This reflects the importance of controlling O_2 content during atomisation or casting of feedstock rods for this alloy.

Ti_3Sn was observed in both size (SLM and coarse) ranges growing as irregularly shaped dendrites that were always accompanied by some α-Ti, as shown in Figure 4.6(c) and Figure 4.7(b, c). Samal et al. [5] had reported similar findings in suction cast $Ti_{71}Fe_{29-x}Sn_x$ (x = 0, 2, 2.5, 3, 4.5) alloys, as mentioned in section 1.2.5 of Chapter 1. This means Ti_3Sn in SLM and coarse powders formed via the peritectic reaction: **L + β-Ti → Ti_3Sn** followed by the eutectoid transformation of β-Ti: **β-Ti → α-Ti + FeTi**. Further, it was heterogeneously distributed around the microstructure and appeared to grow coarser with increasing particle size. Coarse irregular Ti_3Sn dendrites, always coexisting with the lower contrast α-Ti, can be observed

inside coarse (> 63 µm) powder particles (Figure 4.6c). However, the micrograph also shows more homogeneously distributed and finer Ti_3Sn phase near the surface of the particle as compared to its interior. This represents a competition between the phase´s nucleation and growth kinetics. Similar to the thermal heterogeneity observed in freely-cooled cast metallic samples, the powder particle surfaces experienced higher undercooling and initial cooling rate during atomisation, thus favouring nucleation but leaving no time for growth. The slower crystallization kinetics of the bulk allowed Ti_3Sn to coarsen leading to Sn segregation in coarse (> 63 µm) powder particles.

As mentioned in section 1.2.5 of chapter 1, formation of Ti_3Sn by the peritectic reaction (**L + β-Ti → Ti_3Sn**) further moves the remaining liquid composition to the invariant point P (Figure 1.12) with a liquid richer in Fe. This leads to the ternary quasi-peritectic reaction: **L + Ti_3Sn → β-Ti + FeTi**. This is followed by the eutectic reaction: **L → β-Ti + FeTi** forming the eutectic matrix from the residual melt. Figure 4.7(b and c) schematically show the generated microstructure and summarise the proposed reactions.

A non-lamellar cellular morphology was observed near the particle surface in the coarse powders suggesting high nucleation rates in this region. The micrograph in Figure 4.6(c) clearly shows a transition towards lamellar eutectic in the powder particle interior. This again emerges from the heterogenous cooling experienced between the particle surface and its interior.

$Ti_{66}Fe_{27}Nb_3Sn_4$ powders produced by CFA mostly followed the same solidification pathway as that of suction-cast $Ti_{71}Fe_{29-x}Sn_x$ (x = 0, 2, 2.5, 3, 4.5) alloys studied by Samal et al. [5], despite some compositional differences. However, the formation of non-equilibrium phase $FeTi_2$ and of µm-scale Fe_2Ti_4O oxides are new phenomena that need further investigation.

4.1.3 Solidification in CGA $Ti_{66}Fe_{27}Nb_3Sn_4$ powder

Figure 4.8 shows the XRD patterns with phase identification and Figure 4.9 the resulting phase fractions obtained from Rietveld refinement of the raw data for CGA powders in three different size ranges. The microstructures represented by the SEM micrographs in Figure 4.10, appeared quite different from their CFA counterparts, despite both powders having very similar chemical compositions (see Table 4.3 and Table 4.4). Unlike CFA powders, up to 5 phases were identified in this case. No oxide or α-Ti were detected, however, the observed Carbon contamination led to the occurrence of TiC in these powders. Much like CFA powders, Nb was only present in solid solution.

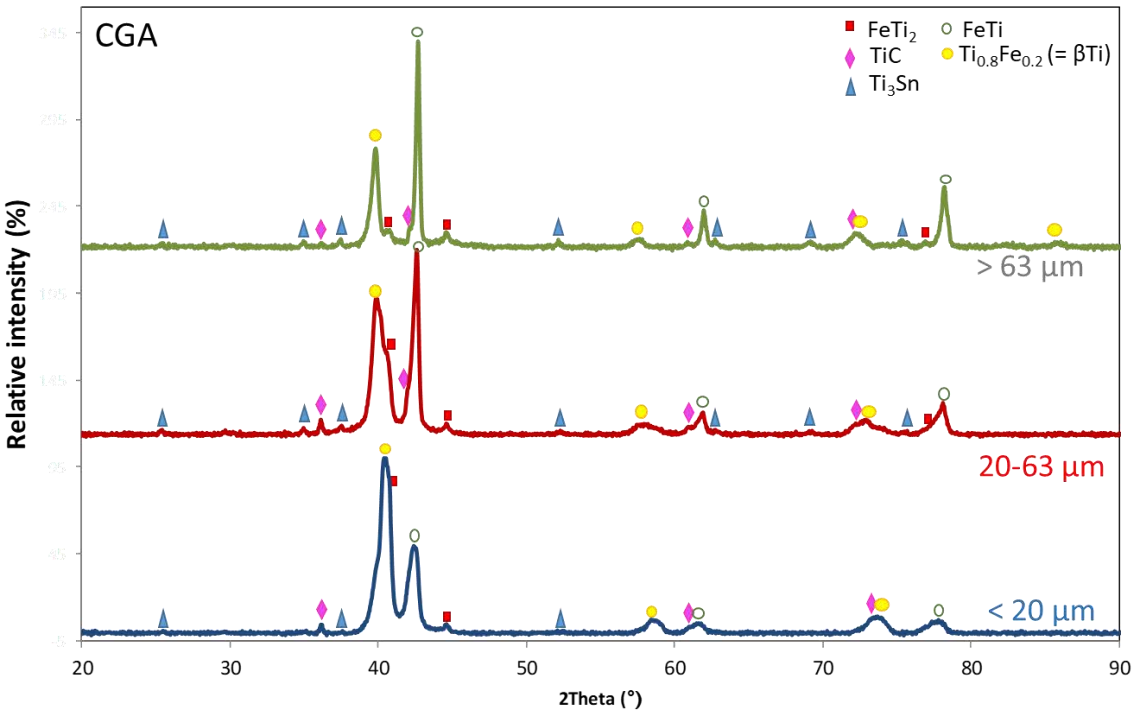

Figure 4.8: XRD patterns with identified peaks for all size ranges of CGA $Ti_{66}Fe_{27}Nb_3Sn_4$ powders

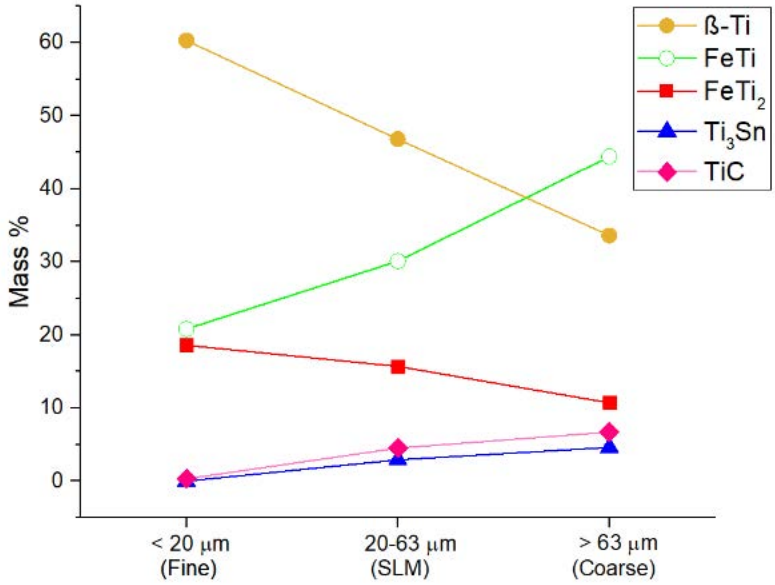

Figure 4.9: Phase fraction by mass percent in three size ranges of CGA powders, as estimated by Reitveld refinement of XRD patterns.

According to XRD data and the Rietveld refinement shown in Figure 4.9, the β-Ti decreases from fine to coarse particles and it is compensated by the amount of FeTi in the same size range, remaining close to 80 % of mass. The meta-stable $FeTi_2$ content was the highest in fine

(< 20 µm) powders produced by CGA as well and decrease slightly as the particle size increases. The large difference in crystallisation kinetics between the different particle size ranges is evidenced by the different microstructures observed in Figure 4.10 and the schematic in Figure 4.11 indicating the apparent reactions and solidification behaviours.

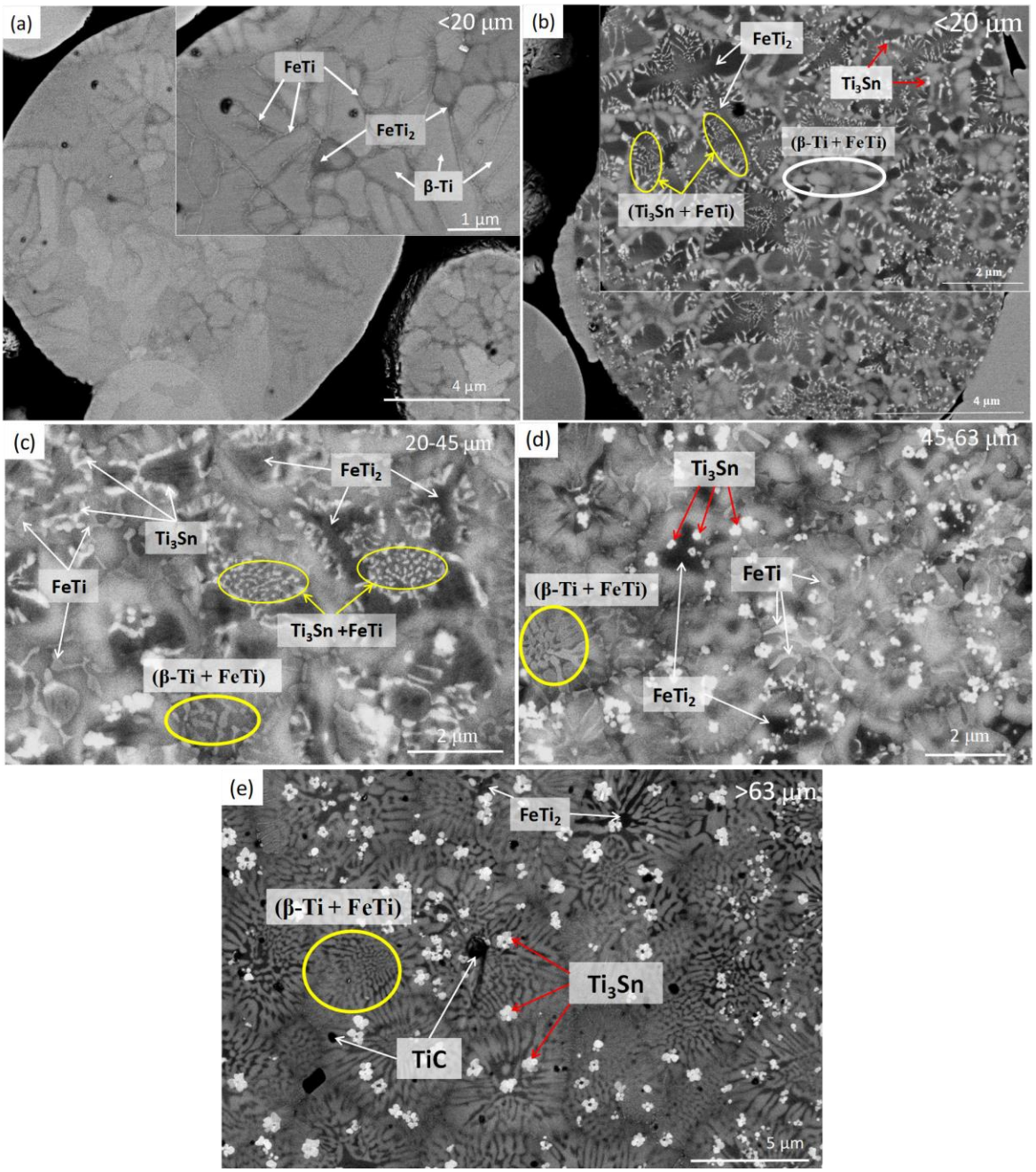

Figure 4.10: SEM micrographs (BSE mode) showing typical microstructures (with phases marked) observed in $Ti_{66}Fe_{27}Nb_3Sn$ powders produced by CGA across (a, b) fine (< 20 µm), (c) 20 – 45 µm, (d) 45 – 63 µm and (e) coarse (> 63 µm) size ranges.

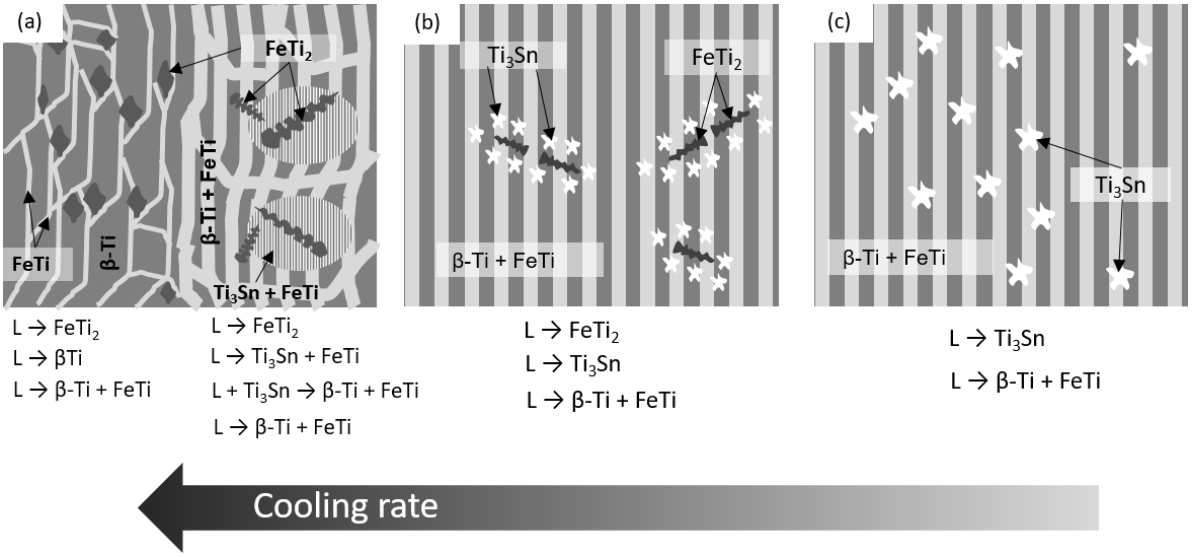

Figure 4.11: Schematic showing the most relevant microstructural features, along with reactions involved, for CGA powders of (a) fine (< 20 µm), (b) SLM (20 – 63 µm) and (c) coarse (> 63 µm) size ranges

Two types of microstructures were observed in many fine CGA powders. The ones that didn´t feature any Ti_3Sn phase, shown in Figure 4.10(a), consisted mostly of primary β-Ti. Lamellas of FeTi were seen spreading across β-Ti and low-contrast meta-stable $FeTi_2$ was observed along the boundaries. Some other fine powders produced by CGA featured Ti_3Sn that appeared to grow as a fine lamellar eutectic along with FeTi, as shown in Figure 4.10(b). Bright Ti_3Sn along with fine lamellas of gray FeTi, were located around the dark dendrites of meta-stable $FeTi_2$. A second much coarser and irregular eutectic (β-Ti + FeTi) was observed surrounding them. Such 'bimodal nanoeutectic' composites containing eutectics of different length scales have been observed and studied in suction-cast hypereutectic alloys of Song et al. [6], [7], as described in section 1.2.5 of chapter 1. The presence of a bimodal nanoeutectic indicates that Ti_3Sn formed from the liquid by a univariant reaction: **L → FeTi + Ti_3Sn** creating the ultrafine (FeTi + Ti_3Sn) binary eutectic observed in Figure 4.10(b) and Figure 4.11(a-right half). The average Fe content in CGA powders is ≈ 29 – 30 wt % (≈ 28 – 29 at %), as indicated in Table 4.4, which would place this initial melt composition on the Fe-rich side of the invariant quasi-peritectic point P in the ternery Ti-Fe-Sn phase diagram (see Figure 1.12 in chapter 1). The finer eutectic (FeTi + Ti_3Sn) formed via univariant reation when the melt composition was moving along univariant line A-P towards P. Then, the growth of light-gray contrast FeTi dendrites occurred via the quasi-peritectic reaction: **L + Ti_3Sn → β-Ti + FeTi** at the invariant point P. Finally, the remaining melt underwent the eutectic reaction: **L → β-Ti + FeTi** forming the coarser secondary eutectic observed. High fraction of meta-stable $FeTi_2$ in fine powders suggests non-equilibrium solidification due to rapid cooling.

The intermediate size range SLM (20 – 63 µm) was further split into two narrower size ranges for better microscopic analysis. A careful look at the microstructures in Figure 4.10(c and d) reveals a smooth transition from one solidification pathway to the other. For particles of sizes 20 – 45 µm, we observed the metastable $FeTi_2$ dendrites breaking up. Meanwhile, ultrafine

(FeTi + Ti_3Sn) eutectic appeared to lose its lamellar morphology. In fact, Ti_3Sn appeared to coalesce together near the diminishing $FeTi_2$ dendrites, as indicated in Figure 4.10(c). In the 45 – 63 µm sized particles represented by Figure 4.10(d), we noticed that most of the Ti_3Sn has grown independently (suggesting formation by **L → Ti_3Sn**). They have nucleated as fine particles in and around the remaining $FeTi_2$ dendrites which had shrunk even further. The eutectic (FeTi + Ti_3Sn) had almost disappeared. At the same time, the lamellar eutectic (β-Ti + FeTi) became more apparent as it grew further. This indicates that a transition had occurred and it is schematically shown in Figure 4.11(b). FeTi emerged as the largest phase in coarse particles, with 10.8 % more mass % than β-Ti. On the other hand, β-Ti remained the largest phase in powders produced by CFA across all size ranges, as reported in Figure 4.5 of section 4.1.2. This is attributed to the fact that CGA powders contained slightly higher Fe content than the CFA powders (see Table 4.3 and Table 4.4 in section 4.1.1), making their final average Fe content to be 29 – 30 wt %. The invariant quasi-peritectic point P in the Ti-Fe-Sn Gibbs plot (see Figure 1.12) lies at 27.4 ± 0.7 at % or 29.2 ± 0.8 wt % Fe. The difference between average Fe content of CGA and CFA powders, combined with higher standard deviations observed in CGA powder compositions, might be significant enough to place their initial melt compositions on opposite sides of Point P.

The coarse (> 63 µm) particles had a microstructure completely different from the fine ones discussed earlier, Figure 4.10(d). They featured a single lamellar eutectic (β-Ti + FeTi) and fine Ti_3Sn dendrites. The Ti_3Sn dendrites were quite homogeneously distributed (no signs of Sn segregation, unlike CFA powders) and displayed a free dendritic growth morphology with several arms, and barely remaining $FeTi_2$. This indicates that they formed directly from the liquid by the reaction: **L → Ti_3Sn**. This was followed by the eutectic reaction: **L → β-Ti + FeTi** forming the lamellar eutectic matrix. These reactions, as reported by Samal et el. [5] and schematically depicted in Figure 4.11(c), were also observed in 1 mm thin suction-cast specimens of $Ti_{71}Fe_{25.15}Sn_{3.85}$ alloy, even though it lies on the Ti-rich side of invariant point P.

Furthermore, meta-stable $FeTi_2$, its apparent role in Ti_3Sn formation, and the relevant reactions, if any, still need to be understood properly.

4.1.4 Solidification in AMA $Ti_{66}Fe_{27}Nb_3Sn_4$ powder

XRD patterns with peaks identified are presented in Figure 4.12 for AMA powders of all size ranges. Figure 4.13 shows the phase fractions obtained by a preliminary Rietveld refinement.

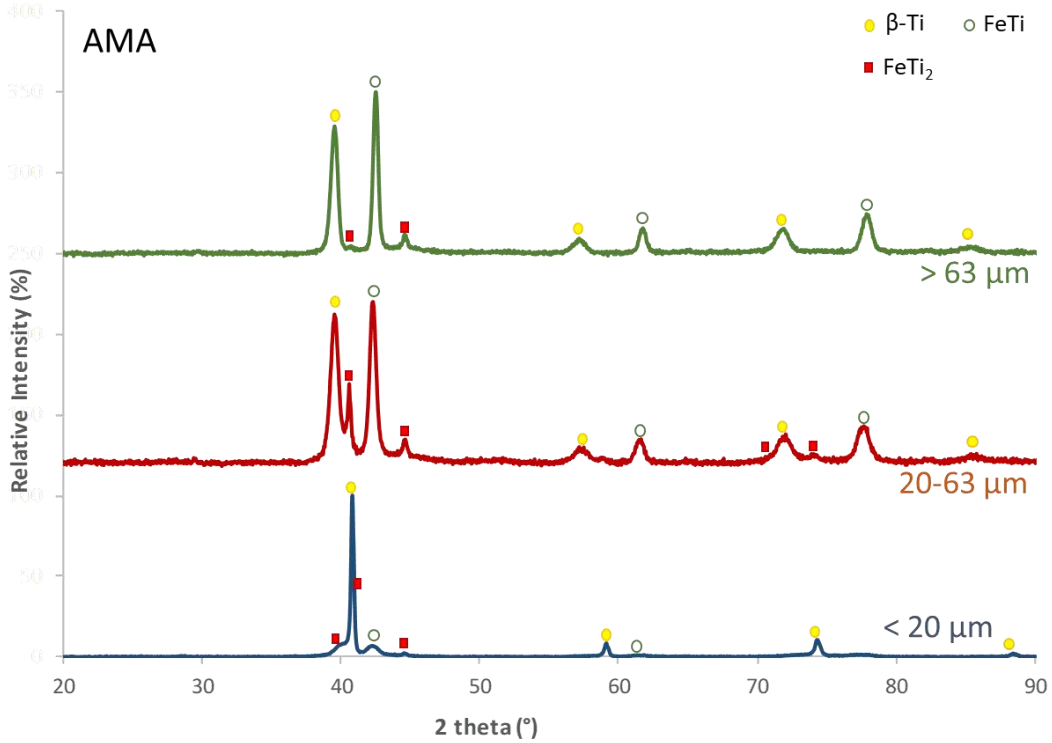

Figure 4.12: XRD patterns with identified peaks for all size ranges of AMA $Ti_{66}Fe_{27}Nb_3Sn_4$ powders

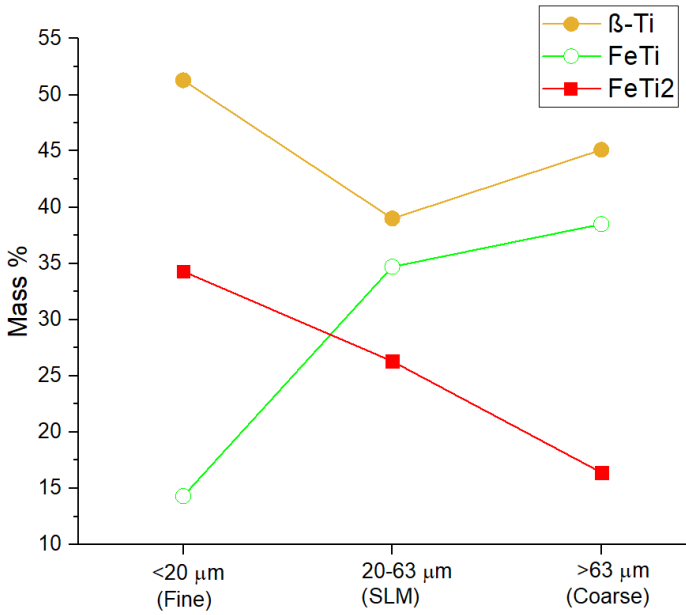

Figure 4.13: Phase fraction by mass percent in three size ranges of AMA powders, as estimated by Reitveld refinement of XRD patterns

Unlike the CGA and CFA powders of similar compositions where up to six phases were identified, AMA powders consisted of only three phases: β-Ti, FeTi and meta-stable $FeTi_2$. No oxides or other undesirable phases resulting from contamination were observed. Sn did not form any phase in particles across any size range, despite the AMA powders containing the highest average Sn content among all powders (see Table 4.5 in section 4.1.1). Thus, Sn as well as Nb always stayed in solid solution in AMA-produced powder.

As in case of other powders, $FeTi_2$ showed the highest proportion in fine (< 20 µm) powders and decreased with increasing particle size. Figure 4.13 also reveals that β-Ti remained the dominating phase with the highest mass % across all sizes ranges. The typical microsctructures of the powders in three different size ranges are presented in Figure 4.14 which help understand the distribution of these phases at different crystallisation kinetics. The schematics in Figure 4.15 further summarise the solidification behaviour while also mentioning the proposed reactions leading to the observed microstructures.

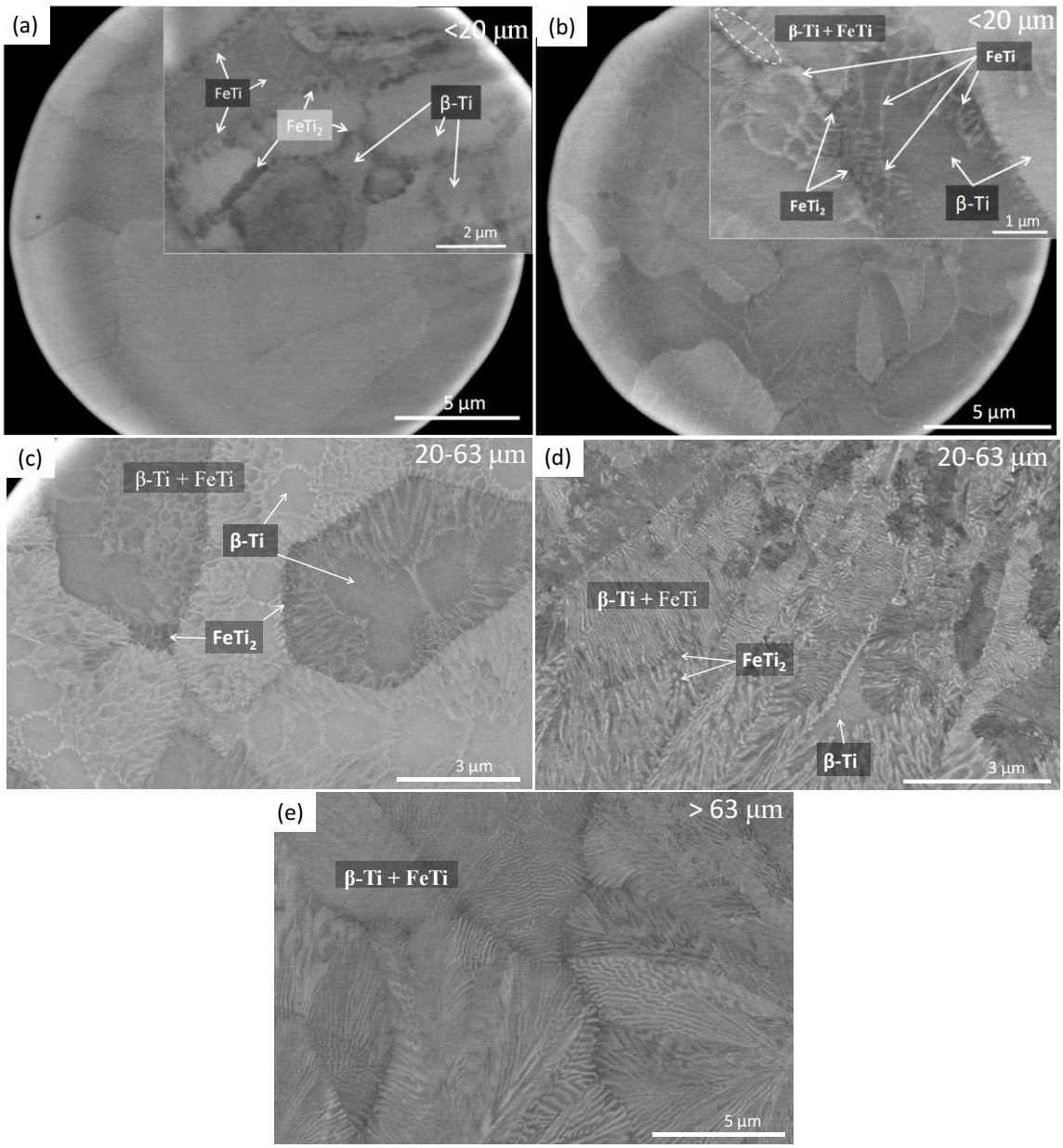

Figure 4.14: SEM micrographs (BSE mode) showing typical microstructures (with phases marked) observed in $Ti_{66}Fe_{27}Nb_3Sn$ powders produced by AMA across (a, b) fine (< 20 µm), (c, d) SLM (20 – 63 µm) and (e) coarse (> 63 µm) size ranges

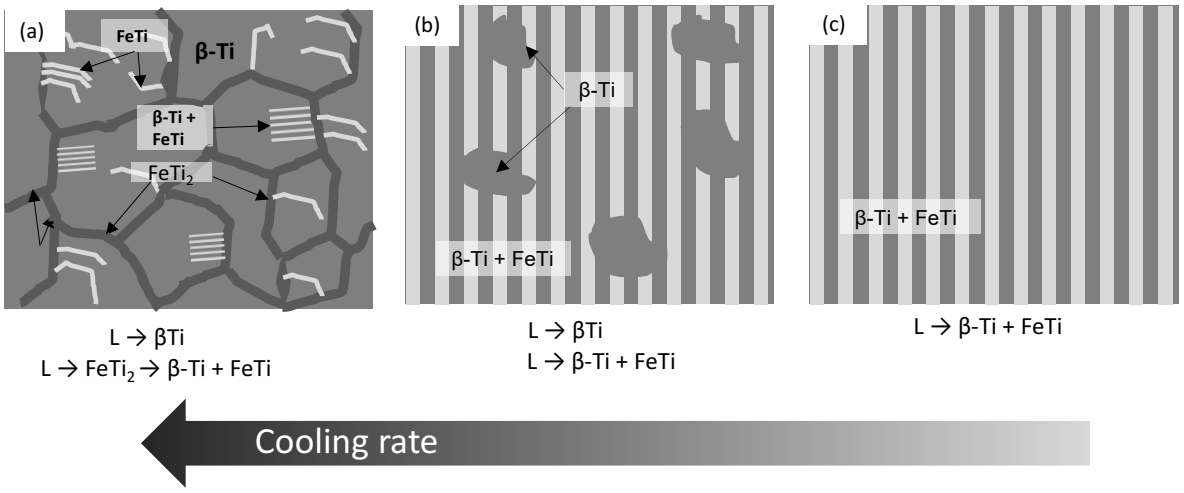

Figure 4.15: Schematic showing the most relevant microstructural features, along with reactions involved, for AMA powders of (a) fine (< 20 µm), (b) SLM (20 – 63 µm) and (c) coarse (> 63 µm) size ranges

As shown in figure Figure 4.14(a, b), the fine powders consisted of grains of primary β-Ti with relatively dark meta-stable $FeTi_2$ existing along the boundaries. Bright FeTi was observed nucleating around $FeTi_2$ and growing into β-Ti grains irregularly as lamellas. They were also observed to grow as regular lamellar eutectic (β-Ti + FeTi) at certain locations near the boundaries, as shown in Figure 4.14(b) and in Figure 4.15(a) of the schematic. Their close proximity to $FeTi_2$ hints that the meta-stable phase might be formed as an inter-mediate step during the eutectic rection, suggesting **L → $FeTi_2$ → β-Ti + FeTi**. The fast crystallisation kinetics did not allow the reaction to complete and very little eutectic was formed in the final microstructure.

As the kinetics slow down in the SLM size range (20 – 63 µm), we see a greater degree of completion of this reaction with more eutectic matrix growing and diminishing of β-Ti phase, as shown in Figure 4.14(c, d). Small amount of meta-stable $FeTi_2$ were observed near the eutectic colony boundaries. Based on the solidification behavior observed in fine particles earlier, it might be assumed that these boundaries started off as grain boundries of primary β-Ti and and were converted to eutectic colony boundaries as the eutectics grew inwards reducing the β-Ti into embedded dendrites. This explains the drop in total β-Ti content that was observed in XRD as reported in Figure 4.13, while FeTi content increased significantly. This hierarchically structured euctectic microstructure is simplistically represented in the schematic in Figure 4.15(b).

A similar solidification behaviour was observed in powder particles of eutectic compostion Ti-Fe32.5 (wt %). Particles in the SLM size range (20 – 63 µm) of this composition produced by the same method of Arc-melting Atomisation (AMA) were characterised under SEM for comparison. As shown in Figure 4.16, FeTi was observed nucleating near boundaries of β-Ti grains and growing as the lamellar eutectic (β-Ti + FeTi) towards the grain interiors. EBSD also revealed the presence of meta-stable $FeTi_2$ along the β-Ti boundaries similar to AMA-produced $Ti_{66}Fe_{27}Nb_3Sn_4$. This, as well as the presence of primary β-Ti suggest that the cooling

rates of gas atomisation were too high for obtaining equilibrium products in this eutectic composition.

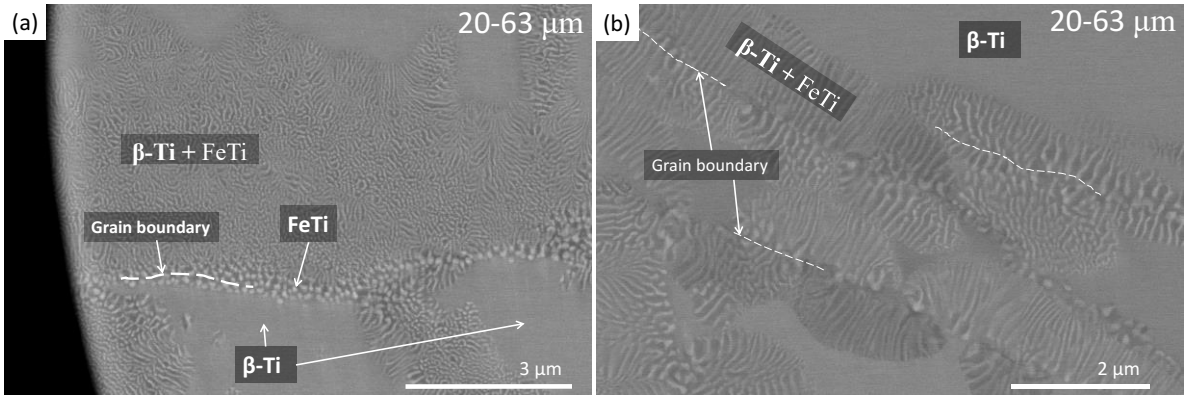

Figure 4.16: SEM micrographs (BSE mode) showing typical microstructures (with phases marked) observed in Ti-Fe32.5 (wt %) powders produced by AMA in (a, b) SLM (20 – 63 µm) size range

On the other hand, coarse (> 63 µm) particles of AMA-produced $Ti_{66}Fe_{27}Nb_3Sn_4$ consisted almost entirely of the lamellar eutectic matrix, as shown in Figure 4.14(e) and schematically represented in Figure 4.15(c). This shows the highest degree of completion of the eutectic reaction occurred at this crystallisation kinetics. XRD revealed an increase in β-Ti and FeTi contents compared to SLM particles, as reported in Figure 4.13, while meta-stable $FeTi_2$ was reduced to its lowest proportion.

AMA powders remained free from any contamination related undesirable phases and presented a simple solidification behaviour similar to pure eutectic powders produced by the same atomisation method. However, the absence of any Sn-containing phase, unlike powders produced by other atomisation methods, and the role of meta-stable $FeTi_2$ in the eutectic formation further need to be investigated.

Based on the differences in solidification behaviour observed between CFA, CGA and AMA powders of $Ti_{66}Fe_{27}Nb_3Sn_4$, we can say that this alloy is quite sensitive to small constitutional variations as well as the atomisation method used and their process parameters, which in turn define the solidification rates. Unfortunately, it is not possible at this stage to properly relate the process parameters (melt temperature, Argon pressure, etc.) with the cooling rates.

4.1.5 Solidification in AMA2 $Ti_{73.5}Fe_{23}Nb_{1.5}Sn_2$ powders

AMA2 powder batch was produced by the same method Arc-Melting Atomisation (AMA) as the AMA powder of composition $Ti_{66}Fe_{27}Nb_3Sn$, discussed in the previous section. However, the composition of AMA2 $Ti_{73.5}Fe_{23}Nb_{1.5}Sn_2$ was designed to be more off-eutectic and Ti-rich. Figure 4.17 shows the XRD data for different size ranges of AMA2 powders. Figure 4.18 shows the mass fraction distribution of the four identified phases obtained by Rietveld refinement

of the corresponding patterns. Interestingly, two overlapping peaks, with less than 0.5° of difference in their 2θ positions were detected for BCC Ti which remained the largest phase in all powders. This suggests the occurrence of two solid solutions of β-Ti with slightly different solute contents. The peaks with the higher 2θ positions are marked as β-Ti' and match with the peak positions of $Ti_{0.75}$ $Fe_{0.25}$ (β-Ti with Fe content of 25 at %) phase available in the database. The other set of peaks with lower 2θ lie between the peak positions for $Ti_{0.75}$ $Fe_{0.25}$ and $Ti_{0.8}$ $Fe_{0.2}$ reported in the database. On this basis, the BCC Ti phase (marked as β-Ti) can be speculated to have an iron content of 22 – 23 at % Fe. This is quite similar to the overall Fe content in the alloy. Additionally, intermetallic FeTi and an α-Fe phase, $Fe_{0.975}Ti_{0.025}$ containing 2.5 at % Ti in the solid solution, were also detected in powders of all size ranges. Powders of the more near-eutectic composition $Ti_{66}Fe_{27}Nb_3Sn_4$ produced by CGA, CFA and AMA did not feature any α-Fe phase or two sets of peaks for β-Ti. The equilibrium Ti-Fe or Ti-Fe-Sn phase diagrams (see Figure 1.4 and Figure 1.12 in chapter 1) do not predict an iron-rich phase for this Ti-rich composition. However, Sn and Nb, whose contents were the lowest in the AMA2 composition $Ti_{73.5}Fe_{23}Nb_{1.5}Sn_2$, stayed in the solid solution similar to AMA-produced $Ti_{66}Fe_{27}Nb_3Sn_4$ powders.

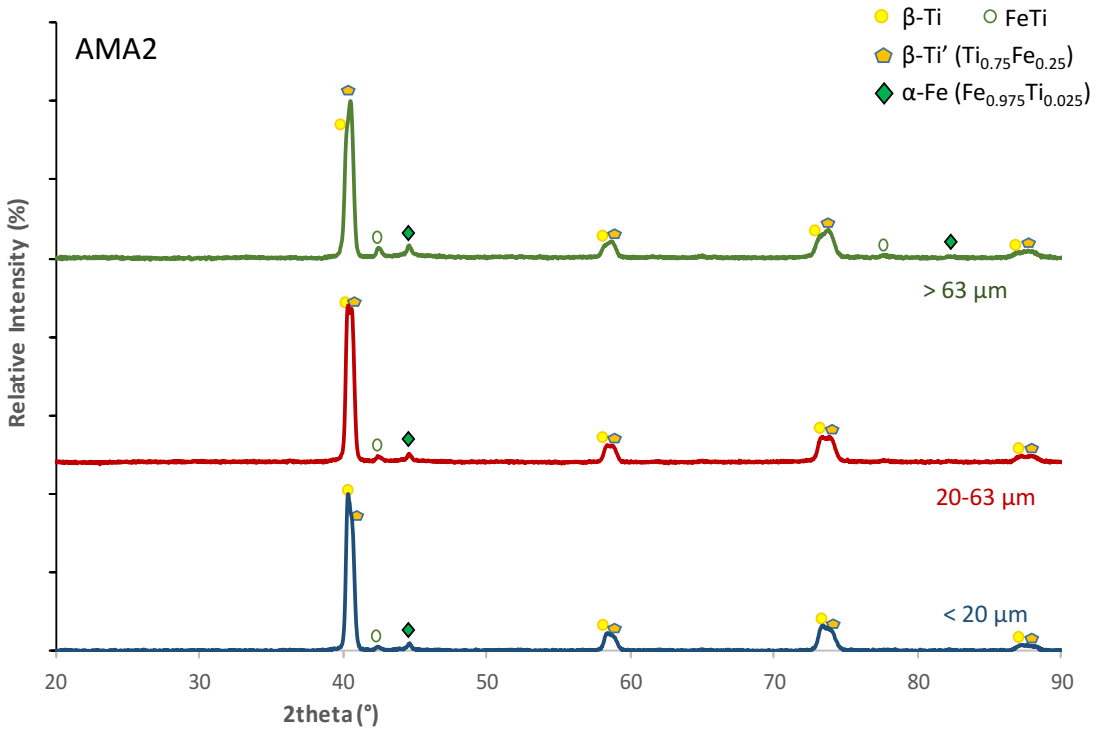

Figure 4.17: XRD patterns with identified peaks for all size ranges of AMA2 $Ti_{73.5}Fe_{23}Nb_{1.5}Sn_2$ powders

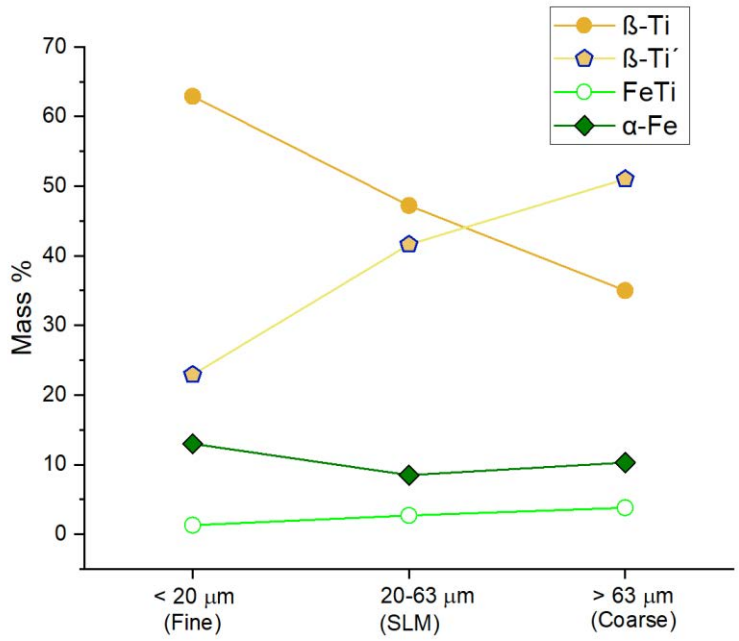

Figure 4.18: Phase fraction by mass percent in three size ranges of AMA2 $Ti_{73.5}Fe_{23}Nb_{1.5}Sn_2$ powders, as estimated by Reitveld refinement of XRD patterns

Based on the refinement resuts in Figure 4.18, β-Ti was the dominant phase in fine particles, while β-Ti' evolved as the largest phase in the coarse particles. Their contents were comparable in the SLM range. Meanwhile, α-Fe content decreased very slightly with size and the opposite happened for FeTi. Figure 4.19 show the occurence of these phases in microstructures of different powder size ranges undergoing different crystallisation kinetics. The schematics in Figure 4.20 further simplify the solidification behaviour across these sizes and mention the proposed reactions.

The fine particles show a microstructure with large grains of primary β-Ti featuring relatively high-contrast wave-like zones, as marked by dotted lines in Figure 4.19(a). They appear to be rich in β-Ti' phase and feature small bright precipitates of intermetallic FeTi. This is simplistically represented by the schematic in Figure 4.20(a). The two BCC Ti phases are completely coherent and crystallographically the same, but the slight differences in solute concentrations can create different contrasts under SEM-BSE mode. This effect was further enhanced with the proper image acquisition settings in order to highlight the contrast. A fine bright-and-dark banded structure was observed in some β-Ti grains, as indicated by loops in Figure 4.19(a). This structure is more clearly visible in the SLM and coarse size range particles in Figure 4.19(b-e). This structure is too fine to be characterised accurately by SEM-based techniques and would require more advanced techniques like TEM. However, we can speculate based on availabe information that it consists of α-Fe ($Fe_{0.975}Ti_{0.025}$) and β-Ti. Also, in the SLM and coarse range, the grains appear more homogenous and do not feature waves of irregular contrasts. In these particles (shown in Figure 4.19(b-e) and schematic of Figure 4.20(b, c)), some grains feature the bands, i.e., they are (β-Ti + α-Fe), while some other grains

(β-Ti') do not. Further, the intermetallic FeTi has grown larger with powder particle size and is mainly localised along the boundaries of the Ti grains.

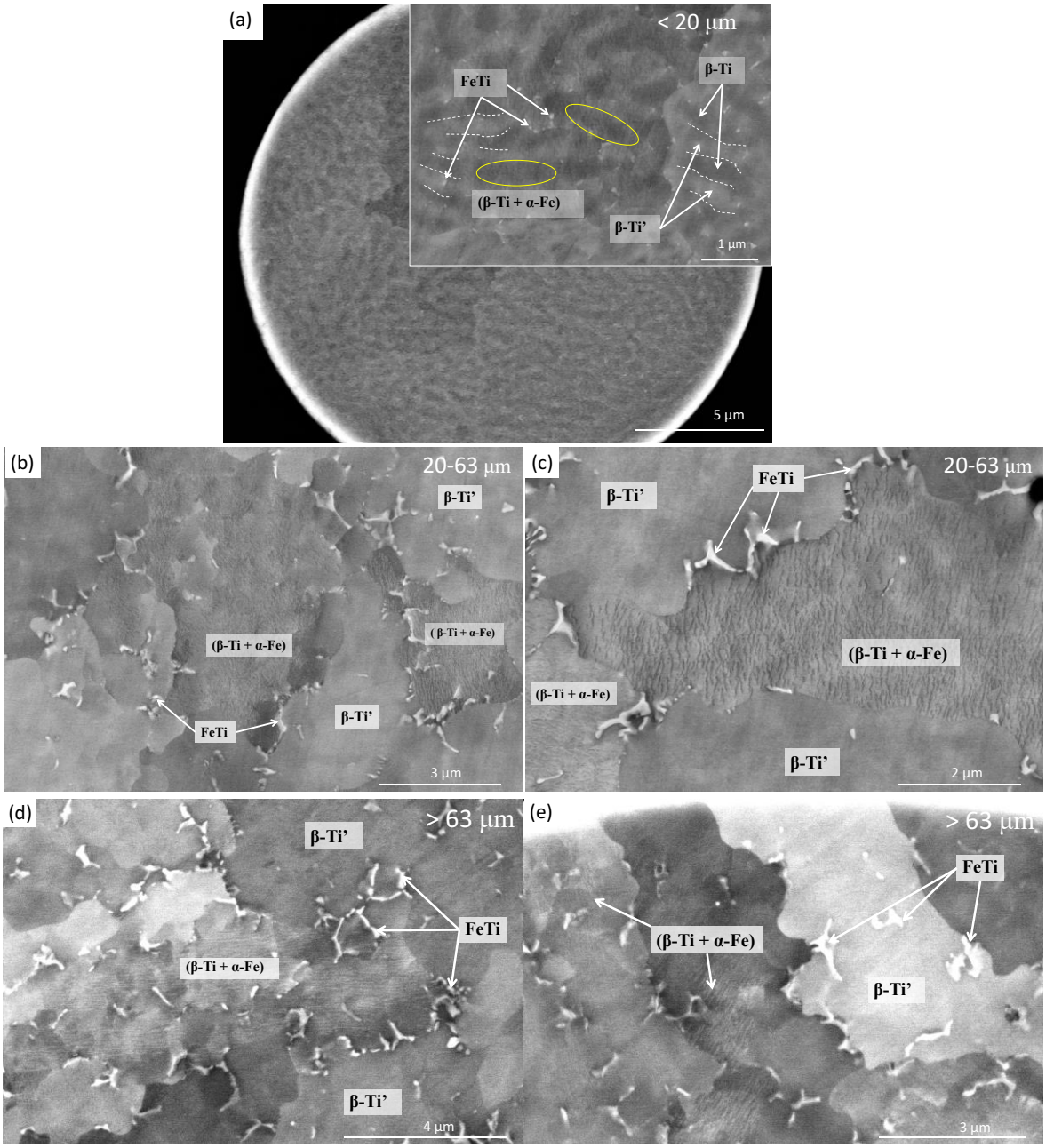

Figure 4.19: SEM micrographs (BSE mode) showing typical microstructures (with phases marked) observed in AMA2 $Ti_{73.5}Fe_{23}Nb_{1.5}Sn_2$ powders across (a) fine (< 20 µm), (b, c) SLM (20 – 63 µm) and (d, e) coarse (> 63 µm) size ranges

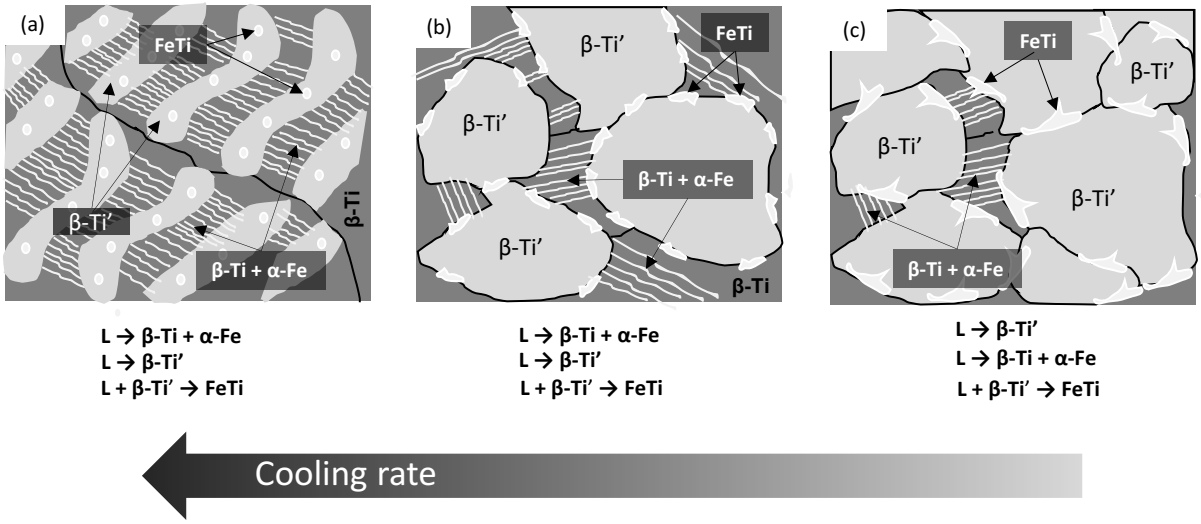

Figure 4.20: Schematic showing the most relevant microstructural features, along with reactions involved, for AMA2 $Ti_{73.5}Fe_{23}Nb_{1.5}Sn_2$ powders of (a) fine (< 20 µm), (b) SLM (20 – 63 µm) and (c) coarse (> 63 µm) size ranges

Based on these observations, we can say that BCC Ti is the first phase to form in particles of all size ranges and it forms via two pathways. One is the formation of supersaturated β-Ti' by **L → β-Ti'**. The second is the formation of β-Ti with slightly less solute content and the same overall Fe content as the liquid. This could happen when solute atoms do not have enough time to diffuse into a phase up to its solubility limit. They could also cluster together during this process to form a solute-rich phase, like $Fe_{0.975}Ti_{0.025}$ (α-Fe) in this case. The fine particles experience the fastest crystallisation kinetics and this would explain why they contain more β-Ti than β-Ti'. The second solidification pathway **L → β-Ti + α-Fe** seems to be dominating at these kinetics. However, waves or bands of β-Ti' are formed as the solutes reach their local diffusion length limits at these fast kinetics. At relatively slower kinetics in SLM (20 – 63 µm) and coarse particles(> 63 µm), we see these waves have almost disappeared. β-Ti' and β-Ti (+ fine bands of α-Fe) co-exist as separate and more homogenous grains. Eventually, the pathway **L → β-Ti'** dominates as particles get larger and kinetics get slower, with β-Ti' emerging as the biggest phase in coarse particles (see XRD refinement results in Figure 4.18). For all particles, the next step is the formation of FeTi via **L + β-Ti' → FeTi**. Intermetallic FeTi was seen nucleating as small precipitates near β-Ti' waves in the Ti grains of the fine particles. As the kinetics slow down in larger particles, it grows and surrounds the more homogenous Ti grains, as represented in the schematic in Figure 4.20(b, c).

A further in-depth study of this powder is being planned using more advanced characterisation techniques (like TEM) in order to explain the unique microstructure. In addition, suction casting experiments and thermodynamics calculations performed by our collaborators revealed that the morphology and phase fraction of intermetallic FeTi in $Ti_{73.5}Fe_{23}Nb_{1.5}Sn_2$ can be tailored easily by controlling heat treatments and SLM processing conditions (unpublished work from our collaborator *DLR*, Germany). They found that FeTi can precipitate as dispersoids in β-Ti with nearly the same fraction as in the eutectic and it would

possible to achieve a "composite" alloy composed of β-Ti and FeTi, with part of the intermetallic FeTi as lamellas and the other as dispersoids. Thus, this alloy provides a unique design opportunity.

4.1.6 Variation of inter-lamellar spacing λ and nano-hardness behaviour

Besides phases and their distribution, the length-scale is an important microstructural feature that was investigated in these powders. Inter-lamellar spacing λ of binary eutectic (β-Ti + FeTi) was measured and plotted for the near-eutectic $Ti_{66}Fe_{27}Nb_3Sn_4$ powders, i.e., CFA, CGA and AMA, which were segregated into narrow size ranges. The methodology developed for the determination of λ is described in **Appendix A** with some examples. Since fine (< 20 µm) particles lacked any significant lamellar eutectic phase (discussed in sections 4.1.2, 4.1.3 and 4.1.4), they were excluded from these measurements. Figure 4.21 shows the average λ, with error bars representing the standard deviation, for powders produced by all three methods. All λ values lie in the ultrafine range (miniumum and maximum λ detected are 27.6 nm and 187.7 nm, respectively). Average λ values increase almost linearly with size. This means that smaller particles contained finer eutectics, with CFA producing finer eutectic microstructures as compared to CGA and AMA. Since smaller particles experience higher cooling/solidification rates, the observed trend in Figure 4.21 also reflects an inverse relationship between λ and solidification rate. The Jackson-Hunt relation for binary eutectic growth defines it as $\lambda^2 v = K$, where 'v' is the solidification front velocity and 'K' is a Jackson-Hunt constant [8]. Contieri et al. [9] conducted arc-melting directional solidification of Ti-32.5 Fe (wt %) alloy and had further determined 'K' for (β-Ti + FeTi) eutectic growth to be 22.27 x 10^{-15} m^3/h. Substituting our measured minimum and maximum λ values into this relation yields very high solidification rates of 0.176 × 10^{-3} m/s to 8.1 × 10^{-3} m/s. In the paper of Gussone et al. [4], they reported the microstructure of SLM manufactured Ti-32.5Fe (wt %) alloy (see Figure 1.17 in section 1.2.6 of chapter 1). The mean λ values of the (β-Ti + FeTi) eutectic colonies varied from ≈ 160 nm to ≈ 50 nm. They overlap well with the λ range detected in our powders indicating that the solidification rates of SLM Ti-rich eutectics are quite similar to that of gas atomisation. Thus, the microstructural study of gas atomised powders could provide insights into the microstructure formation during laser additive manufacturing of similar alloys.

Further, very similar mean λ values in case of CGA and AMA powders across all size ranges suggest that both atomisation techniques led to approximately the same solidification rates in $Ti_{66}Fe_{27}Nb_3Sn_4$ powders. CFA offered the highest solidification rates among all techniques leading to lower average λ. In addition to featuring coarser eutectics, CGA and AMA powders also showed a slightly higher dispersion of λ values across particles as compared to CFA, as is evident from the error bars. These results reveal some of the inherent differences in powder solidification behaviour arising from the atomisation method used.

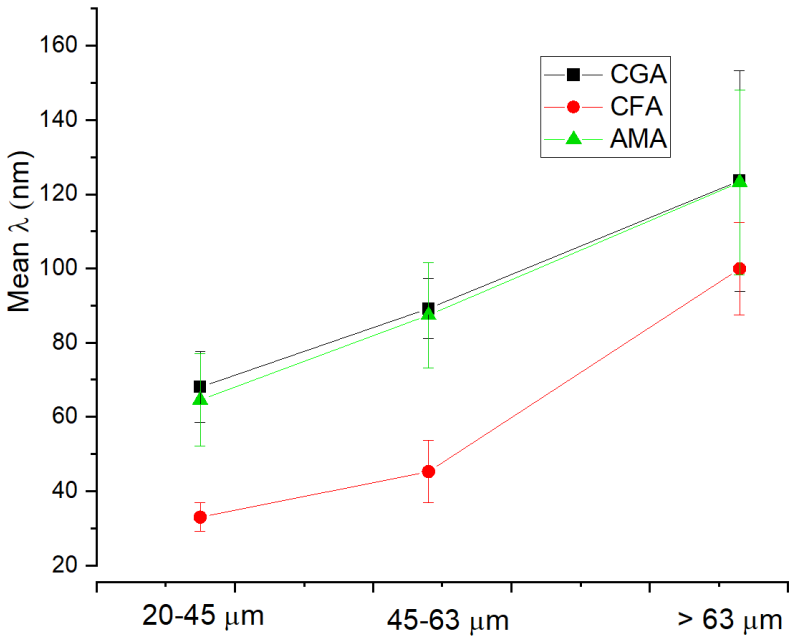

Figure 4.21: Mean λ along with stand deviations as error bars for three size ranges of CFA, CGA and AMA $Ti_{66}Fe_{27}Nb_3Sn_4$ powders

Figure 4.22 shows nano-hardness results for CFA, CGA and AMA powders which have been grouped into narrow size ranges, same as for λ analysis (be aware that fine particle range (< 20 μm) is exluded because nanoindentation is not reliable). Much like their inter-lamellar spacing λ, CGA and AMA powders showed very similar average nano-hardness. The values did not show any significant variation with particle size and lied between 8 and 9 GPa. The CFA powders featuring relatively finer eutectic showed an average hardnesses of around 10 GPa for all sizes > 45 μm. However, there was a significant drop in their hardness to 6.4 GPa in the smallest particle range (20 – 45 μm). CGA and AMA were relatively harder (CGA showing mean of 9.5 GPa) in this range. This might be attributed to the fact that CFA powders have exclusive phases like α-Ti and Fe_2Ti_4O in the microstructure which might have an adverse effect on hardness in this size range.

As we saw, λ of eutectic (β-Ti + FeTi) clearly increased with size across the concerned particle size ranges. Although lower λ is associated with better mechanical properties, particle size did not seem to influence the powder hardness behaviour significantly. Only a slight softening was observed for smaller particles in the SLM (20 – 63 μm) range, i.e., particles < 45 μm produced by CFA. Further, similar hardness values for CGA and AMA powders also means that the presence of intermetallic Ti_3Sn dendrites in CGA powders, which were absent in AMA powders (see sections 4.1.3 and 4.1.4), did not have any significant effect on hardness behaviour.

In addition, AMA2 powder of the more Ti-rich composition $Ti_{73.5}Fe_{23}Nb_{1.5}Sn_2$ was not compared in Figure 4.22 and showed average nano-hardness of 7.7 ± 0.8 GPa in the SLM (20 – 63 μm) range. As mentioned in section 4.1.5, it did not contain any lamellar (β-Ti + FeTi),

but featured desperdoids of intermetallic FeTi. It can be considered comparable but slightly softer than the $Ti_{66}Fe_{27}Nb_3Sn_4$ powders shown in Figure 4.22.

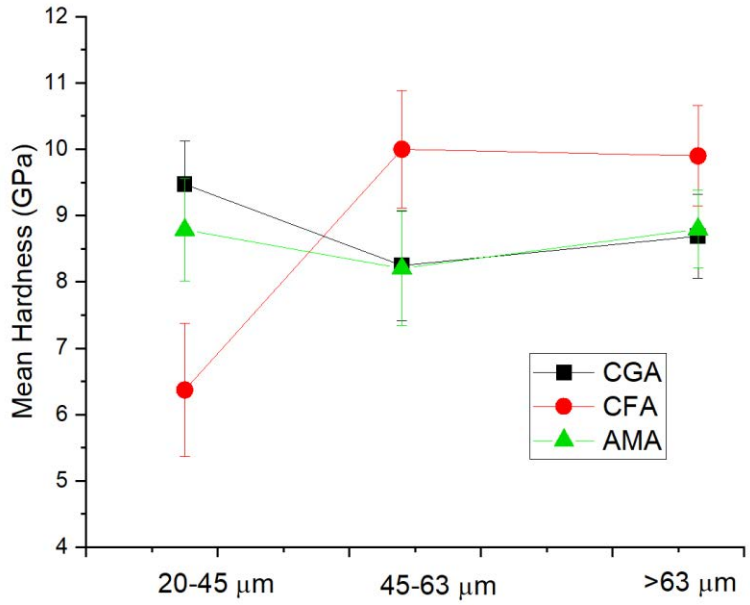

Figure 4.22: Average nano-hardness values with standard deviations as error bars measured for CFA, CGA and AMA $Ti_{66}Fe_{27}Nb_3Sn_4$ powders in three size ranges

4.2 Fe-rich powder

4.2.1 Physical and chemical characterisation

A binary composition $Fe_{82.4}Ti_{17.6}$ (at %) lying very close to the Fe-rich eutectic on Ti-Fe phase diagram (84 at % Fe and 16 at % Ti, see Figure 1.4 in chapter 1) was gas atomised by CFA method. This powder batch produced for the purpose of LMD processing was named CFA-FeTi.

Figure 4.23 shows SEM micrographs of CFA-FeTi powders with a spherical morphology. Similar to the Ti-rich powders, they featured a few satellites whose overall density was quite low.

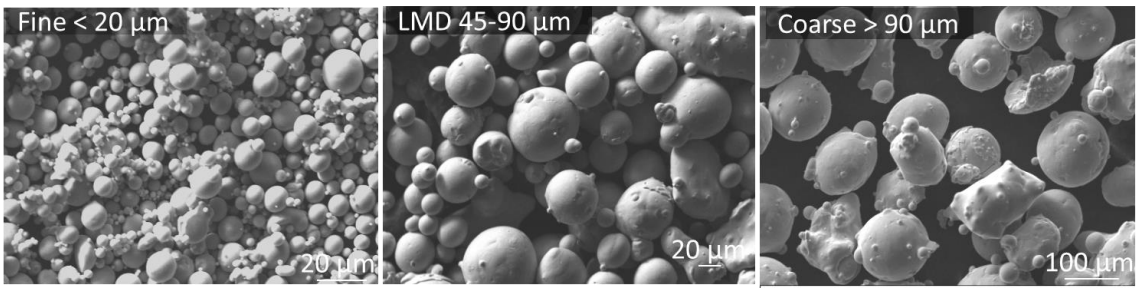

Figure 4.23: SEM micrographs showing morphology of particles in various size ranges for the CFA-FeTi ($Fe_{82.4}Ti_{17.6}$) powder

Figure 4.24 shows a typical tomography slice of the CFA-FeTi powder in the LMD range as characterised by XCT. The porosity quantifications are summarised in Table 4.7 which were obtained after extensive treatment of the tomography data as per the new methodology described in chapter 5. Internal porosity remained very low (0.6 %) and 21.2 % of particles featured internal pores, assuming one pore is present per particle (calculated using Equation 4.1).

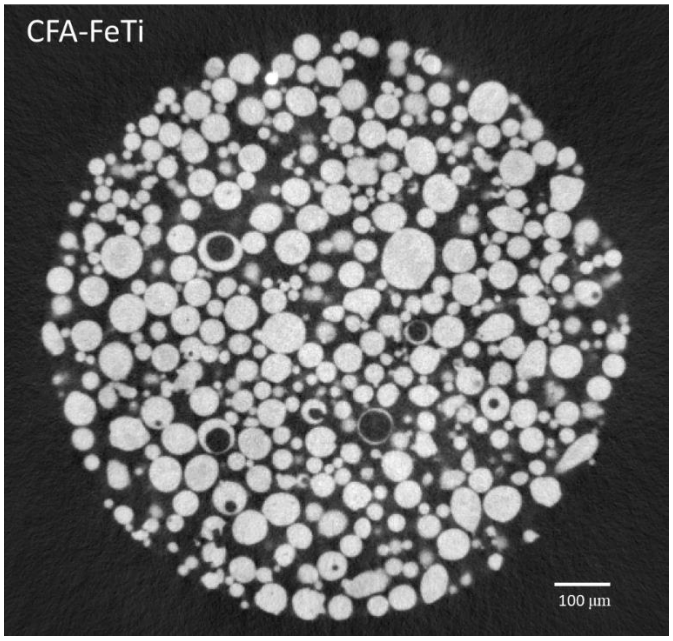

Figure 4.24: Representative XCT slice of a volume measured for CFA-FeTi powder in the LMD size range (45 – 90 µm). Slice shows transverse cross-section of a plastic capillary tube containing the powder

Table 4.7: Internal porosity of Fe-rich powder CFA-FeTi as determined my XCT data analysis (described in chapter 5)

Powder (20 – 63 µm)	**Closed porosity Vol %**	**Particles with pores Number %**
CFA-FeTi	0.6	21.2

The particle size distribution measured in the LMD (45 – 90 µm) size range, as shown in Figure 4.25, revealed a d_{50} of 67.4 µm. Further, for this sieved out range of 45 – 90 µm particles, a d_{10} of 42.8 µm and a d_{90} of 106.8 µm was observed. This indicates a wide PSD with several particles (more than 10 vol %) being smaller than 45 µm and a significant fraction being larger than 90 µm.

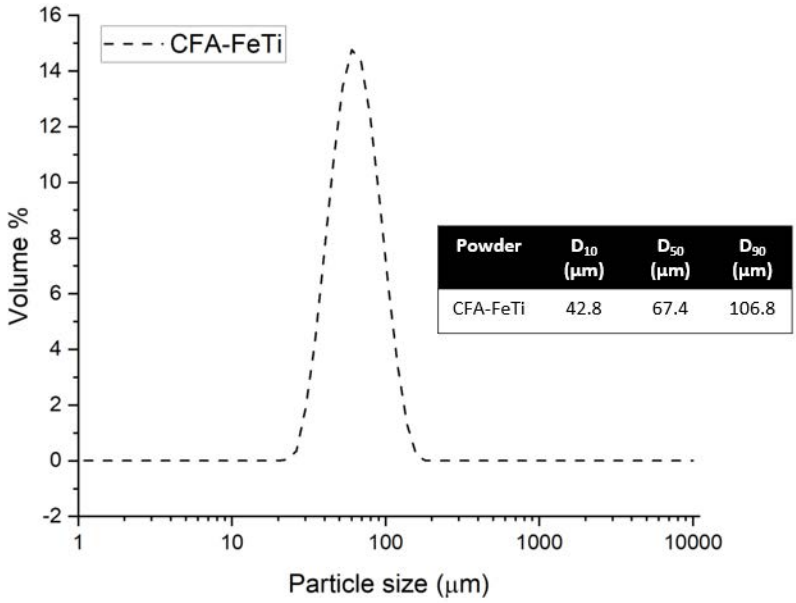

Figure 4.25: Particle size distribution represented as Cumulative frequency (wt %) and frequency (wt %) distribution for the $Fe_{82.4}Ti_{17.6}$ powder (45 – 90 µm) produced by CFA

The powder size range (45 – 90 µm) selected for LMD is relatively larger than those selected for SLM and in this case, appeared to flow freely. Flowability and density measurements were not deemed necessary by our partners responsible for fabrication, who directly proceeded to LMD trials after morphological and chemical characterisation. Also, the powder quantity available to us was insufficient for those standardised tests.

Table 4.8 presents the average chemical compositions of the powder in all size ranges. They seemed to be contamination-free, but had a slightly higher than target Ti content, with the LMD (45 – 90 µm) size range showing the highest average (17.3 wt %) and standard deviation. However, only 600 ppm of O_2 content was detected in the LMD size range. This is much cleaner as compared to the $Ti_{66}Fe_{27}Nb_3Sn_4$ powders produced by the same method CFA (see Table 4.3 in section 4.1.1). Also, it lies well below the O_2 content measured in commercial Ti-6Al-4V powders (≈ 1400 ppm) by the same method (inert gas fusion). Similar to the Ti-rich CFA powders, larger particles contained more O_2.

Table 4.8: Chemical composition of CFA-FeTi powder measured for all size ranges

(wt %)	Fe	Ti	ppm of O_2
Target	84.5	15.5	0
Coarse	83.7 ± 0.6	16.3 ± 0.6	782
LMD	82.7 ± 2.6	17.3 ± 2.6	600
Fine	84.0 ± 0.3	16.0 ± 0.3	401

4.2.2 Solidification in CFA-FeTi powder

The XRD patterns of CFA-FeTi powders in three size ranges, as shown in Figure 4.26, revealed the presence of mainly two equilibrium phases: α-Fe (BCC) and Fe_2Ti (HCP). γ-Fe (FCC) was an additional phase detected only in the fine (< 20 µm) powder, which hints towards the role of high cooling rates as this form of iron is not thermodynamically stable below 912 °C (see Ti-Fe phase diagram in Figure 1.4 of chapter 1). Figure 4.27 shows the phase fractions obtained by Rietveld refinement of the corresponding XRD patterns. α-Fe was the dominant phase in fine and LMD range powders. γ-Fe disappears with increase in particle size, while intermetallic Fe_2Ti grows larger to surpass α-Fe in the coarse (> 90 µm) particles. The difference between mass % of α-Fe and Fe_2Ti changes from 11 % in fine particles to only 3.6 % in coarse particles. Keeping in mind the accuracy of this preliminary refinement, we can say that they become comparable with similar phase fractions in the coarse (> 90 µm) size range.

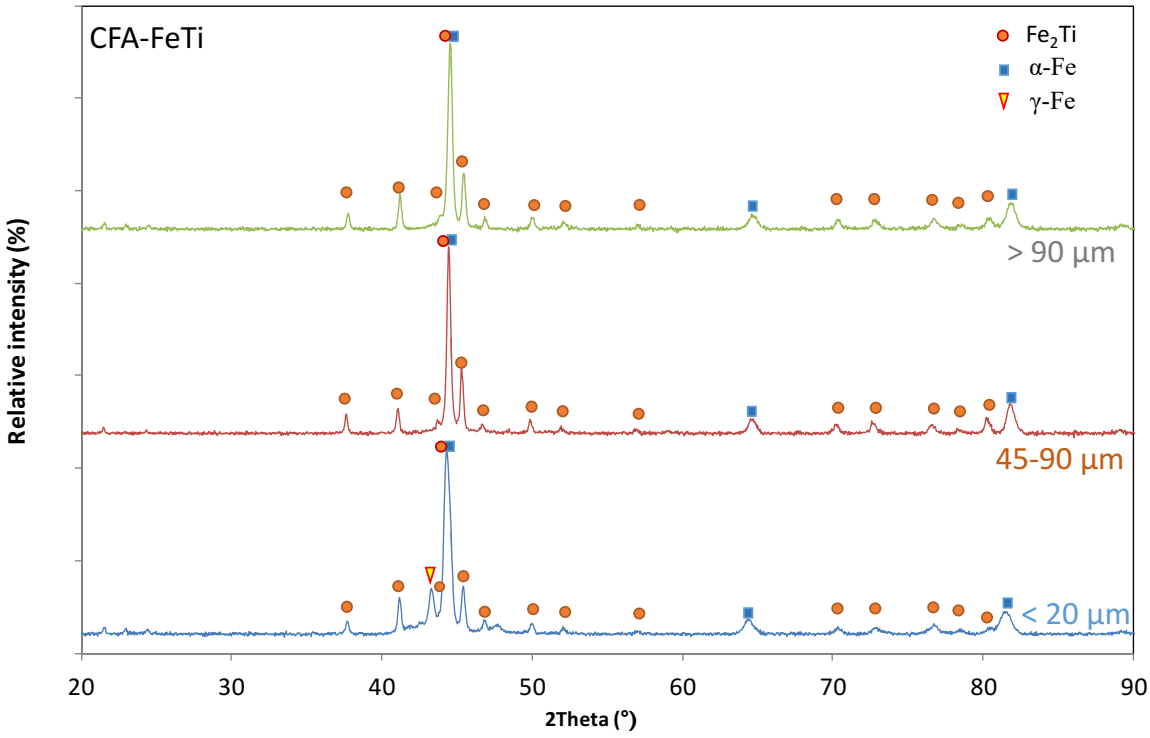

Figure 4.26: XRD patterns with identified peaks for three size ranges of CFA-FeTi powder ($Fe_{82.4}Ti_{17.6}$)

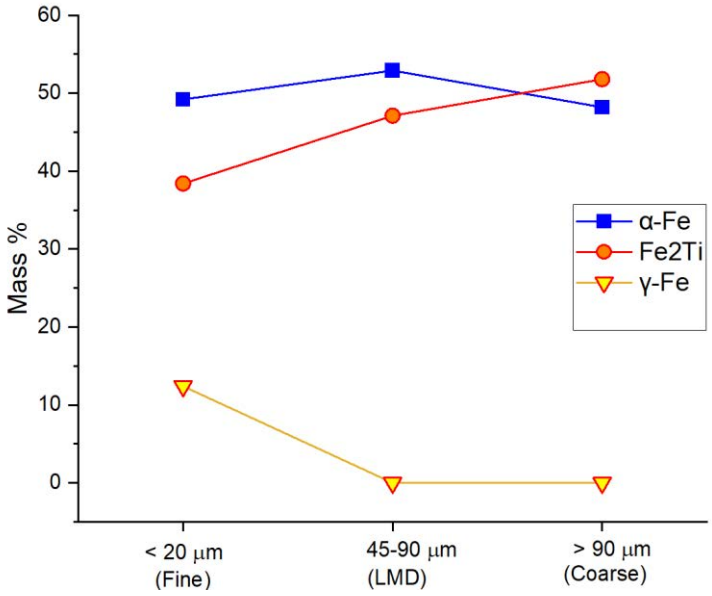

Figure 4.27: Phase fraction by mass percent in three size ranges of CFA-FeTi powders, as estimated by Reitveld refinement of XRD patterns

Phase map created by EBSD analysis of the LMD size range powder, shown in Figure 4.28, revealed the presence of primary Fe_2Ti dendrites. This is in line with our expectations, since our alloy is hypereutectic considering the Ti content. They were embedded in a lamellar and irregular lamellar eutectic matrix of (α-Fe + Fe_2Ti).

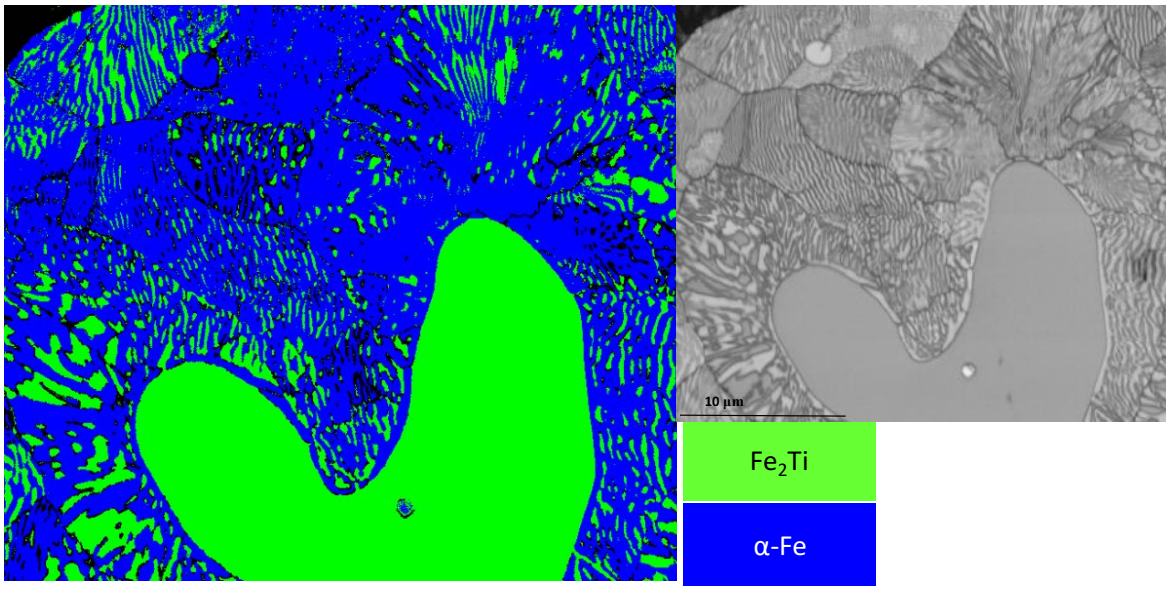

Figure 4.28: EBSD Phase colour map, accompanied by the corresponding band contrast image to the right, for CFA-FeTi ($Fe_{82.4}Ti_{17.6}$) powder (45 – 90 μm)

Figure 4.29 shows the typical microstructures observed in powders of different size ranges. Phases are marked based on information from EBSD, EDX and XRD. The schematic in Figure

4.30 simplifies the solidification behaviour while mentioning the proposed reactions leading to the microstructures observed.

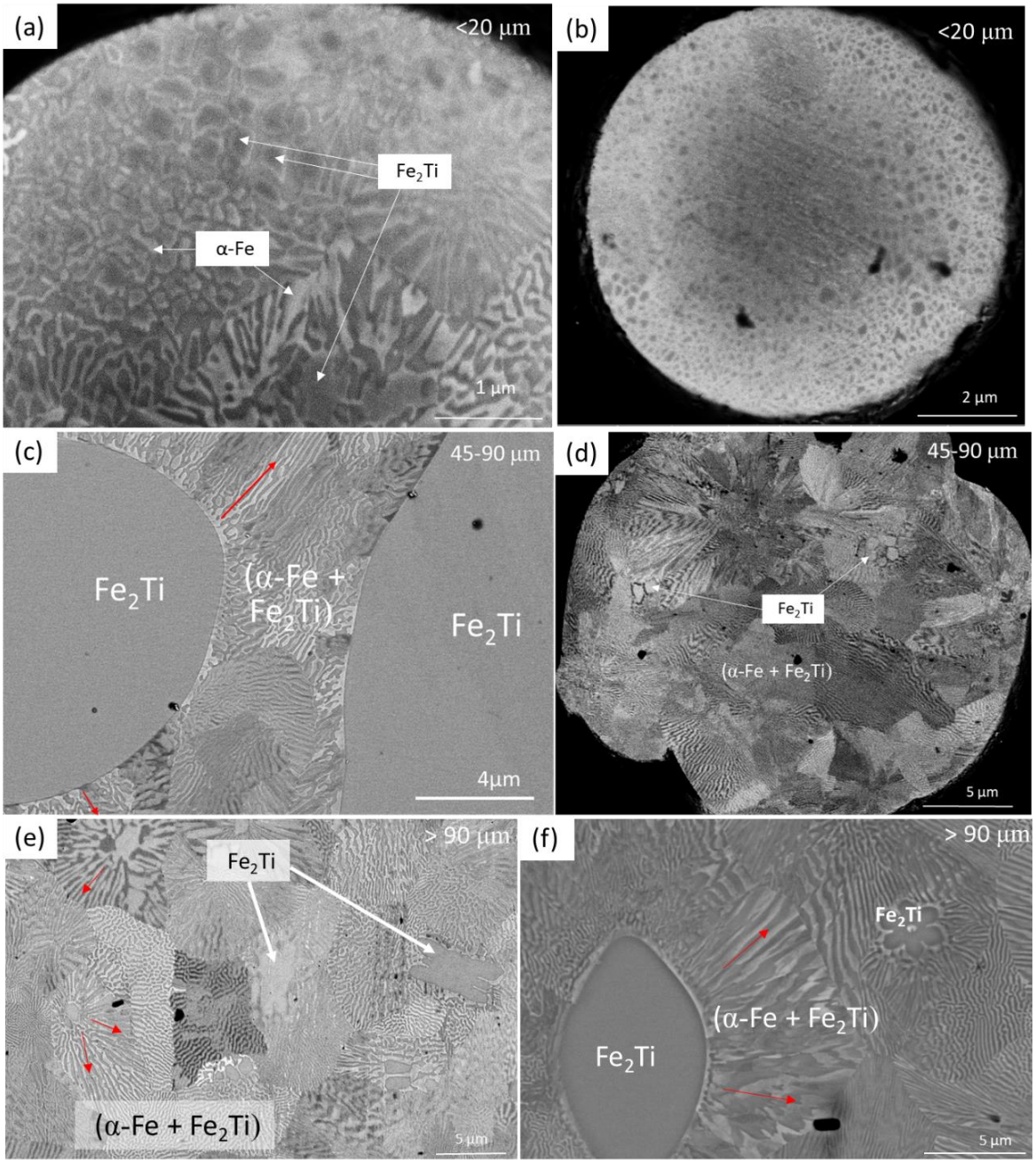

Figure 4.29: SEM micrographs showing typical microsctructures (with phases marked) observed in CFA-FeTi ($Fe_{82.4}Ti_{17.6}$) powders across (a,b) fine (< 20 µm), (c,d) LMD (45 – 90 µm) and (e,f) coarse (> 90 µm) size ranges

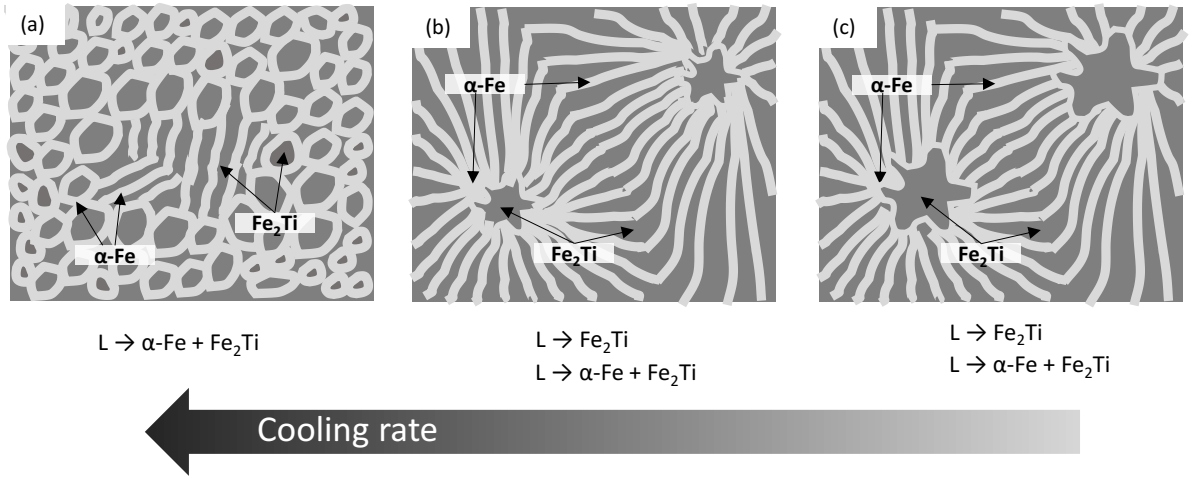

Figure 4.30: Schematic showing the most relevant microstructural features, along with reactions involved, for CFA-FeTi powders of (a) fine (< 20 µm), (b) LMD (45 – 90 µm) and (c) coarse (> 90 µm) size ranges

SEM micrographs of the fine powder, as shown in Figure 4.29(a,b), revealed a cellular or globular morphology near the powder surface. It transitioned into lamellar and irregular lamellar morphologies towards the interior, as depicted schematically in Figure 4.30(a). This has been observed in CFA-$Ti_{66}Fe_{27}Nb_3Sn_4$ powders as well for (β-Ti + FeTi) eutectic, as mentioned in section 4.1.2. High thermal gradients and undercooling on the surface favours nucleation over growth, thus forming several cells or globules of phases. In this case, cells of intermetallic Fe_2Ti (grey contrast) were always surrounded by layers of brighter α-Fe. They form as result of the eutectic reaction **L → α-Fe + Fe_2Ti**. This kind of morphology as a result of nucleation of Fe_2Ti was observed in the inter-layer boundaries (ILBs) of DED-built Fe-17.6 at % Ti by Requena et al. [10], reported in Figure 1.18 of chapter 1. They also reported a phase-field model that simulated the formation of a globular inter-layers by heterogenous nucleation on the remelted particles of the previous layer. Although nucleation of Fe_2Ti in discrete powder particles solidifying during gas atomisation is expected to be homogenous, the resulting globular microstructures look quite similar. Also, Fe_2Ti phase was rarely observed to exist as large-scale primary dendrites in the fine powders investigated. As per EDX and XRD, the fine powders seemed to have the lowest average Ti and Fe_2Ti content among the three size ranges (see Table 4.8 and Figure 4.27). Although a small quantity of γ-Fe was detected in fine powders during XRD, this phase was not clearly visible under SEM.

The powders in the LMD and coarse size ranges clearly showed primary Fe_2Ti phases embedded in the eutectic matrix, as in Figure 4.28 and Figure 4.29(c-f). In coarse particles, Fe_2Ti often showed a flower-like shape with six arms suggesting free dendritic growth directly from the liquid during solidification (**L → Fe_2Ti)**. Further, the lamellar/irregular lamellar eutectics appeared to grow away from several Fe_2Ti phases (marked by red arrows) in LMD and coarse particles. These observations suggest that primary Fe_2Ti is the first phase to be formed in these size ranges via **L → Fe_2Ti** and is followed by the eutectic reaction **L → α-Fe + Fe_2Ti**.

4.2.3 Variation of inter-lamellar spacing λ and nano-hardness behaviour

The λ for (α-Fe + Fe_2Ti) eutectic, measured from SEM images using the methodology described in **Appendix A**, is plotted for particles of different size ranges in Figure 4.31. Fine particles (< 20 µm) are excluded as they showed very little lamellar eutectic content under SEM. The 20 – 45 µm range is considered and the LMD range (45 – 90 µm) is further split into 45 – 71 µm and 71 – 90 µm for better accuracy.

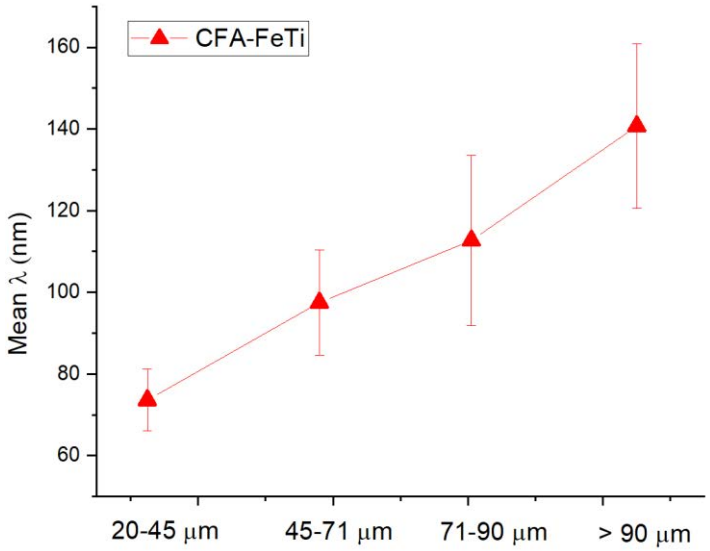

Figure 4.31: Mean λ along with stand deviations as error bars for four size ranges of CFA-FeTi ($Fe_{82.4}Ti_{17.6}$) powders

Mean λ values increase almost linearly with particle size very much like in $Ti_{66}Fe_{27}Nb_3Sn_4$ powders. The minimum λ detected in 20 – 45 µm range was 60.7 nm, while the maximum as detected in the coarse (> 90 µm) range was 172.5 nm. This indicates that under the high cooling rates of gas atomisation, both (α-Fe + Fe_2Ti) and (β-Ti +FeTi) eutectics grow in some agreement with the Jackson-Hunt binary eutectic growth law $\lambda^2 v = K$, where 'v' is the solidification front velocity and 'K' is a Jackson-Hunt constant [8]. Tokoro et al. [11] determined $K = 271 \times 10^{-18}$ m^3/s for (α-Fe + Fe_2Ti) eutectic using unidirectional solidification experiments. Using this value along with maximum and minimum λ measured, we can say that the solidiifcation rates in these powders varied from 9.12×10^{-3} m/s to 73.55×10^{-3} m/s. Requena et al. [10] had reported average λ ranging 190 ± 25 nm in the DED-built $Fe_{82.4}Ti_{17.6}$ alloy involving elemental powders. Using the Jackson-hunt relation, they detemined the solidification rate to be around 7.5×10^{-3} m/s. As discussed in chapter 6 of this thesis, LMD processing of the studied CFA-FeTi powders resulted in a lamellar eutectic microstructure with average λ of 206 ± 51 nm which corresponds to an average solidification rate of 6.4×10^{-3} m/s. Thus, pre-alloyed $Fe_{82.4}Ti_{17.6}$ powders experienced higher (within the same order of magnitude) solidification rates during gas atomisation (CFA technique), as compared to laser-melting by DED or LMD.

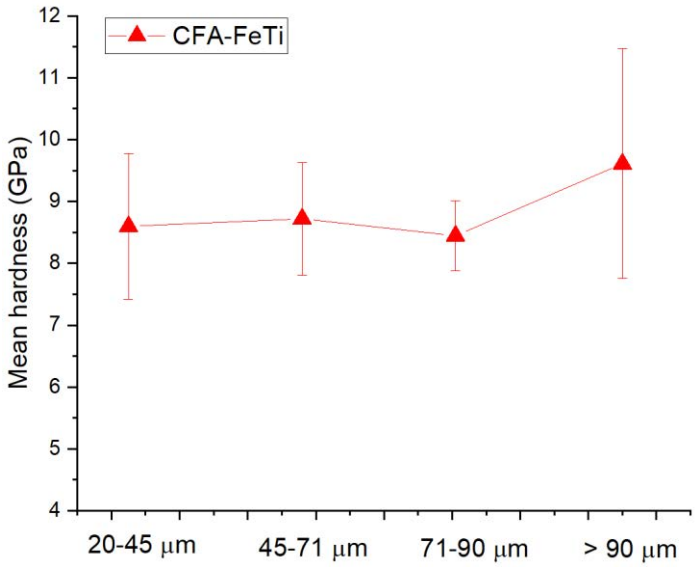

Figure 4.32: Average nano-hardness values with standard deviations as error bars measured for of CFA-FeTi ($Fe_{82.4}Ti_{17.6}$) powders in four size ranges

Figure 4.32 shows the nano-hardness results for CFA-FeTi powder measured in the same particle size ranges, as those used for studying variation of λ. Nanoindentation results were not reliable for fine particles (< 20 µm) embedded in resin, thus, were excluded. Average nano-hardness remained fairly constant and did not vary significantly with particle size. It always lied between 8 and 9 GPa. This result is similar to that of $Ti_{66}Fe_{27}Nb_3Sn_4$ powders. Coarse (> 90 um) particles showed a slightly higher mean hardness of 9.5 GPa, but they also showed the highest dispersion in values as evident from the error bars. Although λ clearly decreases with particle size and lower λ usually means better mechanical properies, we do not see any significant effect of λ on nano-hardness of powders.

This ends the discussion on characterisation and solidification studies conducted on various powders within this thesis. Important conclusions and comments on developing these new pre-alloyed powders for laser-AM have been listed in the next section.

4.3 Partial Conclusions

Atomisation trials discussed in this study have, first of all, exposed the main drawbacks and advantages of standardised CGA, CFA and AMA processes for producing pre-alloyed powders of $Ti_{66}Fe_{27}Nb_3Sn_4$, $Ti_{73.5}Fe_{23}Nb_{1.5}Sn_2$ and $Fe_{82.4}Ti_{17.6}$

i. For the Ti-rich compositions, AMA produced powders with the highest purity (≤ 910 pmm of O_2 in the SLM size range) and the best physical properties, although they featured PSDs with a greater fraction of large particle sizes as compared to CFA and CGA. CGA process parameters should be further optimised for improving powder physical properties.

ii. Further, Ti-rich powders remained sensitive to Carbon and Oxygen contamination from crucibles used in the overall powder production process. Melting in a graphite crucible led to undesirable carbide phases in CGA $Ti_{66}Fe_{27}Nb_3Sn_4$ powder. The high Oxygen content in cast (using ceramic crucibles) feedstock rods for CFA led to unwanted oxide phase in $Ti_{66}Fe_{27}Nb_3Sn_4$ powder. Fe-rich near-eutectic composition $Fe_{82.4}Ti_{17.6}$ produced by CFA did not face this issue.

iii. Besides the issue of contamination in $Ti_{66}Fe_{27}Nb_3Sn_4$ powders, all four Ti-rich powders retained compositions very close to the target. CGA and AMA powders showed slightly high Fe content, with CGA showing relatively high variation among powder particles. A fine tunning of the composition is process dependent and it should be adjusted upon several iterations.

iv. CFA produced $Fe_{82.4}Ti_{17.6}$ powders with good physical properties and low contamination (≤ 600 ppm of O_2 in the LMD size range). They contained slightly more than intended Fe content (≈ 17.3 wt % instead of target 15.5 wt %). **They qualified to go forward with LMD processing.**

v. Microstructural studies revealed relationships between particle size range, their observed microstructures and underlying solidification pathways leading to them. Powder particle size is clearly related to, and can possibly predict, the solidification pathway selected as well as its degree of completion or microstructural growth achieved. However, the differences in microstructures observed between CFA, CGA and AMA-produced powders were also influenced by small constitutional variations as well as the atomisation method used and their process parameters, which in turn define the solidification rates.

vi. The binary lamellar eutectics (β-Ti + FeTi) and (α-Fe + Fe_2Ti) observed in powder microstructures were ultrafine featuring inter-lamellar spacing 'λ' between 27.6 –

187.7 nm for $Ti_{66}Fe_{27}Nb_3Sn_4$ and between 60.7 – 172.5 nm for $Fe_{82.4}Ti_{17.6}$ powders. Calculations based on the Jackson-Hunt relation for binary eutectic growth revealed that solidification rates experienced by these powders were similar to those encountered during SLM/LMD processing of the same or similar compositions. This suggests that gas atomisation can be potentially used to study rapid solidification and Laser-AM processing.

vii. The average λ of observed binary lamellar eutectics in powders increased almost linearly with increasing powder particle size. Going by the Jackson-Hunt relation for binary eutectic growth, this reaffirms the fact that smaller particles solidify faster during atomisation. However, particle size and λ do not strongly affect powder nano-hardness, which lies between 8 to 10 GPa for most powders.

viii. Finally, **the AMA2 powder of target composition $Ti_{73.5}Fe_{23}Nb_{1.5}Sn_2$ was selected for SLM processing.** Trials involving CFA and AMA powders of near-eutectic composition $Ti_{66}Fe_{27}Nb_3Sn_4$ witnessed cracking and demanded serious processing optimisation which did not fit the project's timeline and go beyond the scope of this thesis. Although AMA2 does not feature a lamellar eutectic phase, it was chosen because the powder showed promising results in physical and chemical assessments (especially with respect to O_2 contamination), while providing a unique design opportunity. Our collaborators predicted, based on suction casting experiments and thermodynamics calculations, that the distribution of intermetallic FeTi in $Ti_{73.5}Fe_{23}Nb_{1.5}Sn_2$ alloy microstructure can be tailored easily to achieve a "composite" alloy composed of β-Ti and FeTi, with part of the intermetallic FeTi being lamellar and the other as dispersoids.

REFERENCES

[1] N. Nkhasi, W. du Preez, and H. Bissett, “Plasma spheroidisation of irregular Ti6Al4V powder for powder bed fusion,” *Metals (Basel).*, vol. 11, no. 11, pp. 1–13, 2021, doi: 10.3390/met11111763.

[2] B. Xie, Y. Fan, and S. Zhao, “Characterization of Ti6Al4V powders produced by different methods for selective laser melting,” *Mater. Res. Express*, vol. 8, no. 7, p. 076510, Jul. 2021, doi: 10.1088/2053-1591/AC10D1.

[3] C. S. Wang, K. S. Zhang, H. J. Pang, Y. Z. Chen, and C. Dong, “Laser-induced self-propagating reaction synthesis of Ti-Fe alloys,” *J. Mater. Sci.*, vol. 43, no. 1, pp. 218–221, 2008, doi: 10.1007/s10853-007-2146-0.

[4] J. Gussone *et al.*, “Ultrafine eutectic Ti-Fe-based alloys processed by additive manufacturing – A new candidate for high temperature applications,” *Appl. Mater. Today*, vol. 20, pp. 1–11, 2020, doi: 10.1016/j.apmt.2020.100767.

[5] S. Samal, B. Mondal, K. Biswas, and Govind, “Electron microscopic study on the suction cast in situ Ti-Fe-Sn ultrafine composites,” *Metall. Mater. Trans. A Phys. Metall. Mater. Sci.*, vol. 44, no. 1, pp. 427–439, 2013, doi: 10.1007/s11661-012-1404-1.

[6] G. Song *et al.*, *Heterogeneous eutectic structure in Ti–Fe–Sn alloys*, vol. 19. 2011. doi: 10.1016/j.intermet.2010.11.030.

[7] G. A. Song *et al.*, “Optimization of mechanical properties of Ti-Fe-Sn alloys by controlling heterogeneous eutectic structure,” *Intermetallics*, vol. 23, pp. 27–31, 2012, doi: 10.1016/j.intermet.2011.12.005.

[8] K. A. Jackson and J. D. Hunt, “Lamellar and Rod Eutectic Growth,” *Trans. Met. Soc. AIME*, vol. 236, no. 8, pp. 1129–1142, 1966.

[9] R. J. Contieri, E. S. N. Lopes, M. Taquire De La Cruz, A. M. Costa, C. R. M. Afonso, and R. Caram, “Microstructure of directionally solidified TiFe eutectic alloy with low interstitial and high mechanical strength,” *J. Cryst. Growth*, vol. 333, no. 1, pp. 40–47, 2011, doi: 10.1016/j.jcrysgro.2011.07.007.

[10] G. Requena *et al.*, “Ultrafine Fe-Fe2Ti eutectics by directed energy deposition: Insights into microstructure formation based on experimental techniques and phase field modelling,” *Addit. Manuf.*, vol. 33, no. August 2019, p. 101133, 2020, doi: 10.1016/j.addma.2020.101133.

[11] K. Tokoro and Y. Kimura, “Structural and Magnetic Properties of Unidirectionally Solidified Fe-Fe2Ti Eutectic Alloys,” *Tetsu-to-Hagane*, vol. 60, no. 3, pp. 386–396, Mar. 1974, doi: 10.2355/TETSUTOHAGANE1955.60.3_386.

Chapter 5

Advanced image analysis of Powder Tomography data

5 Advanced image analysis of powder tomography data

This chapter focuses on the development of X-ray Computed Tomography (XCT) as a one-step screening technique for powders. It presents a methodology for performing advanced image analysis of powder XCT data in order to accurately quantify key physical features (like porosity, size distribution, morphology, etc.), thus eliminating the need for separate characterisation techniques used conventionally in powder metallurgy. The chapter consists of four sections, first one being a detailed description of the image analysis methodology. All the main steps and the final workflow for treating powder XCT volumes are explained as separate sub-sections. The rest of the three sections are dedicated to the results obtained by applying this methodology to the studied powders, specifically concerning the internal porosity, particle size distribution and 3D morphology of powders. Further, volume-based Particle Size Distributions (PSDs) determined by this methodology are validated against those obtained by conventional laser diffraction technique. The last section on 3D morphology describes a simplistic model to quantify and assess morphological quality of powders based on three parameters (Sphericity, Aspect Ratio and Volume) determined by this methodology. The sub-sections describe step-by-step creation of a visual database of morphologies using a reference powder (AMA2) developed for SLM. The database is used to classify particles of 'ideal' 3D morphologies in a volume and estimate the qualification ratio (number % of 'ideal' particles) of powders produced by different atomisation methods.

5.1 The methodology

The methodology followed for treating the XCT data of powders can be grouped into three main steps: Image Filter, Segmentation and Separation, as shown in the schematic in Figure 5.1. The first two steps were carried out in *Fiji (ImageJ)*, while the third step was performed in *Avizo*. The first step is intended to largely reduce noise from the images without losing quality. The second step aims to accurately identify and classify pixels belonging to particles and background in the grayscale images, eventually converting them to binary 'black and white'. The third step aims to separate any particles that are touching each other in the volume via a watershed algorithm executed in 3D. Each of these steps are explained in details in the following sections.

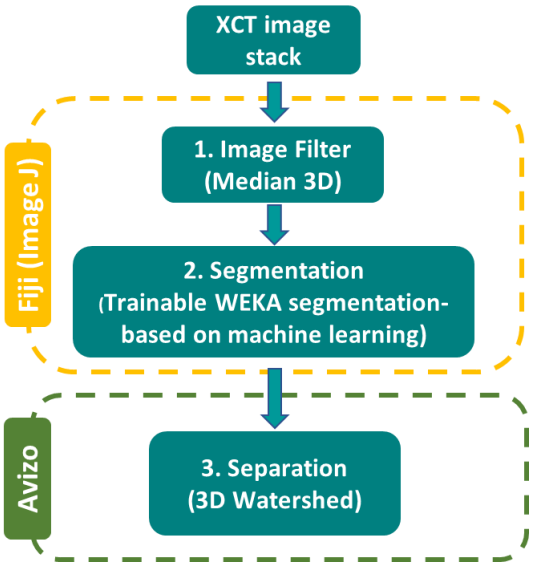

Figure 5.1: Flowchart showing three main steps of the developed image analysis methodology for powder XCT data

A volume of size 1800 × 1800 × 1800 voxels (resolution 1 voxel = 0.77^3 µm^3, 1 voxel is defined as a cube of side 1 pixel) is used as an example for explaining the methodology. A slice of this image stack, representing the transverse cross-section of a plastic capillary tube containing powder particles, is shown in Figure 5.2. The cropped and magnified image of 600 × 600 pixels represents a slice of the volume of interest (VOI) (of size 600 x 600 x 600 voxels) that was cropped out. In order to save computer processing time, initially this VOI with a relevant number of particles (approximately 2000) was used for testing and optimising the three steps, as is described in the following sections. Once results were found satisfactory, the steps and parameters were implemented over the complete volume of 1800 × 1800 × 1800 voxels.

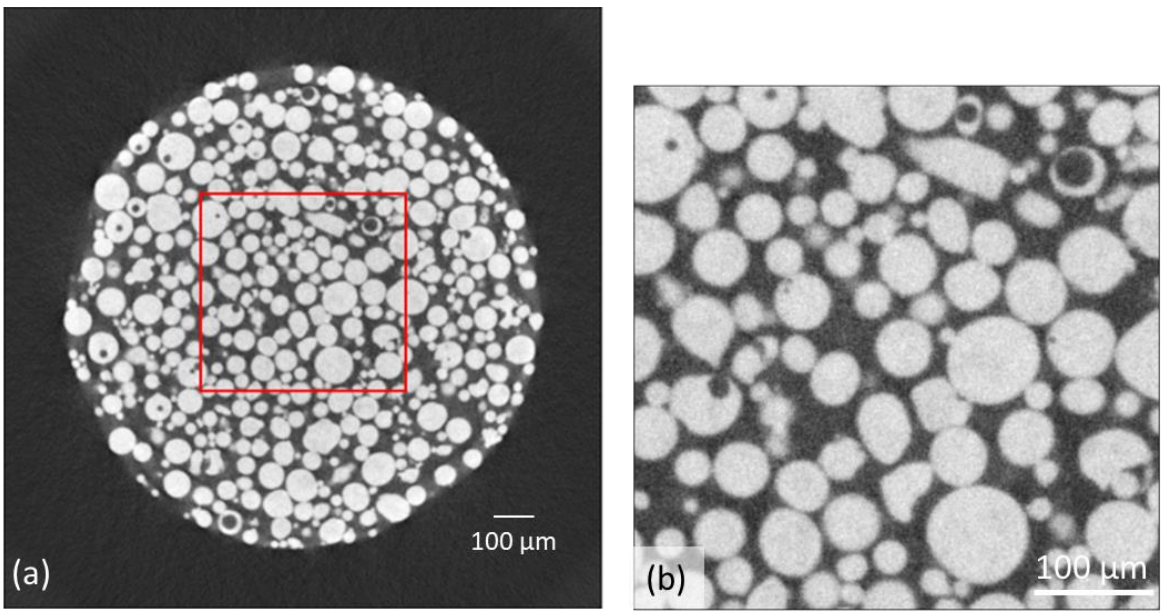

Figure 5.2: (a) A slice from the example grayscale volume of 1800 × 1800 × 1800 voxels (resolution 1 voxel = 0.77^3 µm^3) with a red square marking the cropped volume of interest (VOI), (b) magnified slice from the VOI of 600 × 600 × 600 voxels

5.1.1 Image Filter

The Median 3D filter available in *Fiji* is used for this step. To do so, the *Process* dropdown menu was selected in the main menu, followed by choosing the *Filters* option and then finally *Median 3D*. This filter was used to reduce image noise while preserving particle edges, to a certain extent.

The Median 3D filter works by replacing each pixel in the image with the median value of neighbouring pixels [1]. To define the closest pixels, the filter uses three parameters as input that will determine the radius on the X, Y, and Z axis of the neighbourhood where the median is calculated. In this case, after various trials, the three parameters were chosen to have a value of 2. Figure 5.3 shows the same slice (from the cropped VOI of 600 x 600 x 600 voxels) before and after applying the filter.

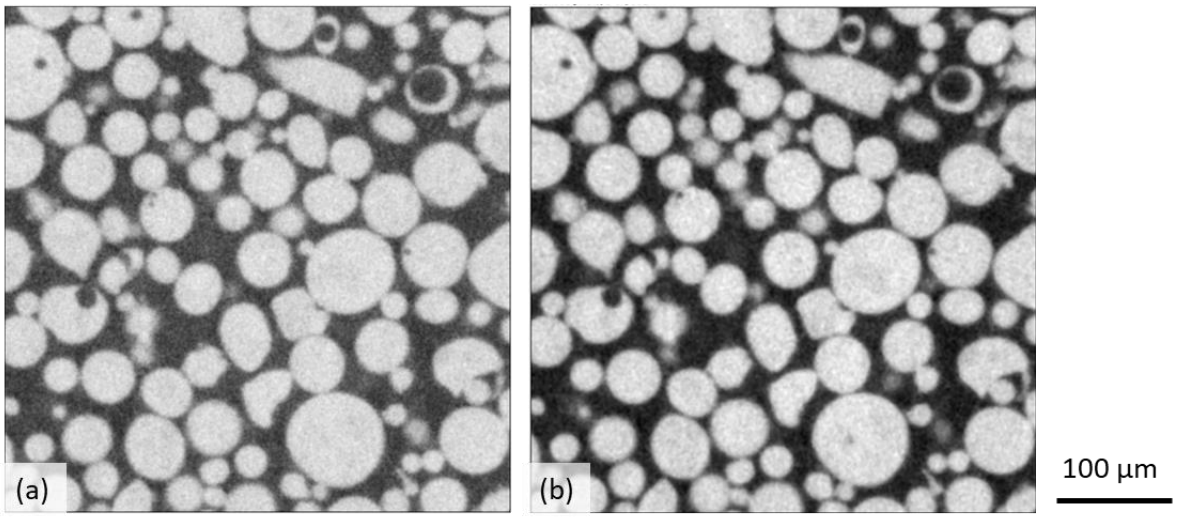

Figure 5.3: Grayscale slice from VOI of 600 × 600 × 600 voxels (resolution 1 voxel = 0.77^3 µm^3) (a) before and (b) after applying the Median 3D filter

5.1.2 Segmentation

Initially, classical segmentation methods using global and local thresholding were tried with multiple approaches and post processing operators (involving smoothening and morphological operators to increase detectability of particle details). Since the results were not fully convincing (compared to visual or manual segmentation), it was decided to test other segmentation options, such as those based on machine learning.

A plugin available in *Fiji* called 'Trainable Weka Segmentation' was chosen for segmenting the filtered grayscale images. It can be accessed by the *Plugins* dropdown menu, followed by the *Segmentation* sub-menu. This plugin offers machine learning algorithms that can be used with image features to achieve very accurate pixel-by-pixel classification. For training the software, a stack of several grayscale images is fed into the classifier where some of the pixels are classified manually into two classes, namely, particle and background.

The machine learning based classifier in this plugin uses an optimized Random Forest algorithm [2]. It connects the data of user-defined or classified pixels to various decision trees and then, makes a classification based on a weighted vote between them. The plugin offers several complementary image features to be considered, as shown in Figure 5.4, which presents the settings window of the plugin. Five pre-defined features were used for our samples, namely Gaussian blur, Hessian, Sobel filter, Membrane projections and difference of Gaussians. The window also shows the respective parameters used along with these features.

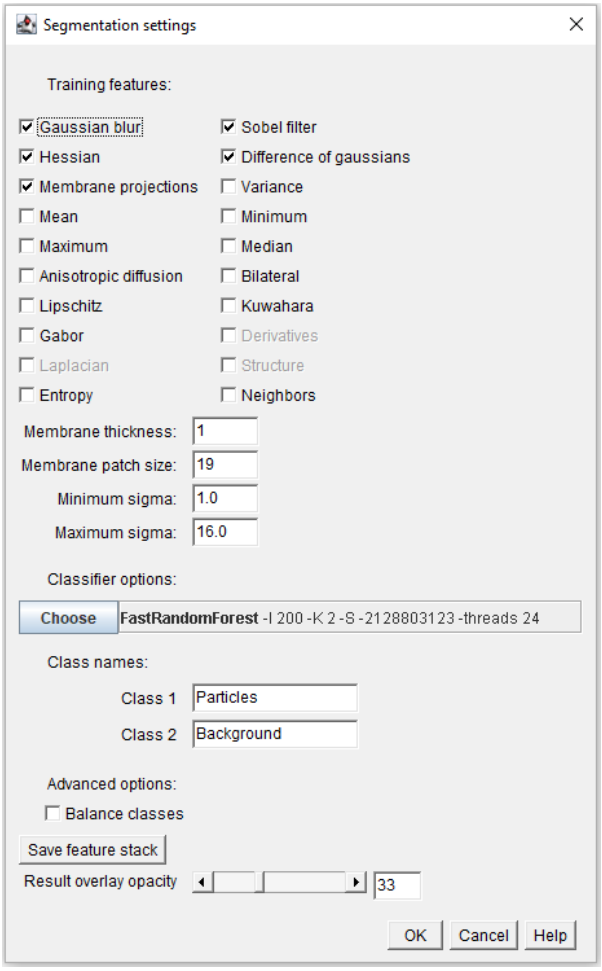

Figure 5.4: Segmentation settings with all relevant parameters used for the plugin Trainable WEKA segmentation (based on machine learning) in *Fiji*

From the complete example volume of 1800 slices, 10 equally spaced slices (i.e. 1 for each 180 slices) were selected for training in order to have sufficient input of grayscale values sampled evenly across the volume. Further, all images were converted to 8-bit and their contrast and brightness were homogenised through histogram adjustment (the grey level of the background air was corrected so the mean of all 'background' pixels was 50, while a mean 'particle' grey level of 200 was chosen) before using the plugin. Additionally, a macro in *Fiji* was developed to speed up the classification of manually selected pixels or Regions of Interests (ROIs) into the two classes during training. It also allowed us to easily save and load

ROIs into the software in order to keep improving the classifier models with more input data until satisfactory results were obtained. This macro can be found in **Appendix B** of the thesis.

After training, the classifier with segmentation settings shown in Figure 5.4 provided accurate results within a reasonable computational time. It was saved as a model and then applied over the volume of 600 × 600 × 600 voxels. The result was a binary stack with background as black pixels (value 0) and particles as white pixels (value 255). The saved classifier model can be used later to segment other data including the whole example volume of 1800 × 1800 × 1800 voxels. Figure 5.5 shows the filtered 600 × 600 image (from the previous step, shown in Figure 5.3(b)) and the corresponding binary segmented image obtained after segmentation by WEKA.

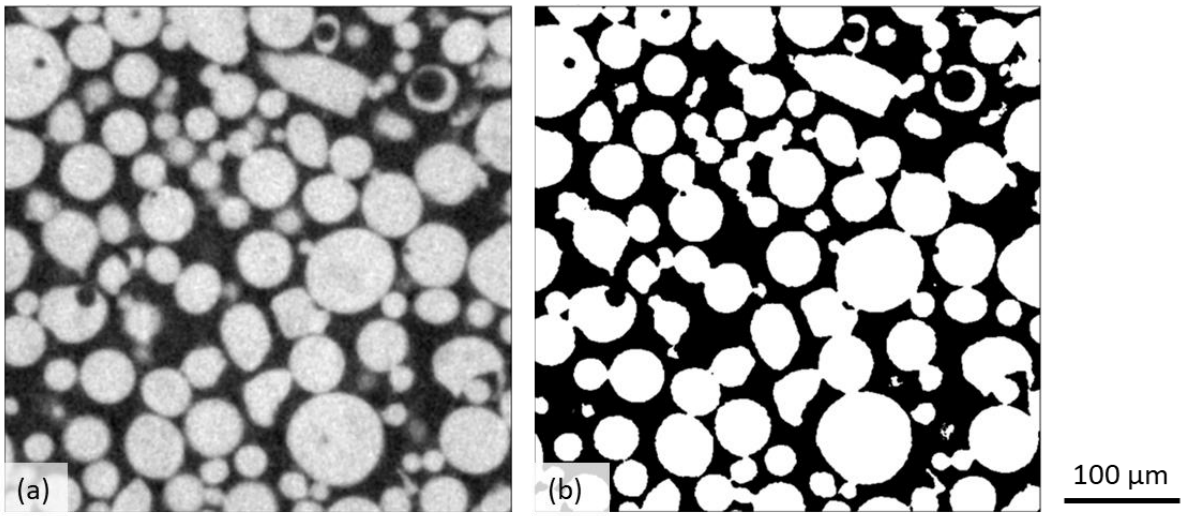

Figure 5.5: (a) Grayscale slice from VOI of 600 × 600 × 600 voxels (resolution 1 voxel = 0.77^3 μm^3) after Median 3D filter (also shown in figure Figure 5.3(b)), and (b) the corresponding binary slice after WEKA machine learning segmentation in *Fiji*

Computationally speaking, this plugin takes ≈ 5 min to train with 10 slices of 1800 x 1800 pixels while using a 2 x Intel XEON E5-2690 V3 - 2.6 GHz/30 Mb 12 Core – 256 GB RAM system. Further, it takes ≈ 30 h to segment the whole volume of 1800 × 1800 × 1800 voxels (resolution 1 voxel = 0.77^3 μm^3) while running as a mono-core process. On the other hand, it took ≈ 14 s to segment the same volume by global thresholding and ≈ 33 min if local thresholding is used. These classical methods run on multiple cores, but fail to produce satisfactory results. Thus, by using WEKA, we traded off computation time for accuracy. It is a reasonable trade off considering the fact that computational time for segmentation can be reduced significantly by using simple processing tools to distribute work among multiple cores and an attached NVIDIA Quadro M6000 24 GB GPU system. It is a work in progress (beyond scope of the thesis). Further, the training process is largely automated and does not need to be repeated for treating similar powder XCT volumes.

5.1.3 Separation

As seen in binary segmented image in Figure 5.5(b), several particles are attached to others around them. In order to accurately characterise them as individual powder particles, it is essential to separate them in 3D.

The most widely used algorithm for fragmenting connected objects in 3D based on a binary mask (such as the binary volume returned by WEKA in the previous section) is Watershed segmentation [3–5]. *Avizo*, a commercial software for scientific/industrial data visualisation and analysis, licensed to our research facility by *Thermo Fischer Scientific*, is capable of executing this algorithm in 3D. Although the concept behind watershed was originally devised in 1978 by Digabel and Lantuejoul, it was developed into an object segmentation algorithm in 1991 by Vincent and Soille [6]. Since then, it has been used for separating connected objects in images across various fields like medicine, cartography, biology, videography and materials science and engineering [7].

Watershed segmentation treats a grayscale image as a topographical relief where the height of each pixel is proportional to its intensity [6, 8]. In other words, bright pixels would represent ridges and dark pixels would be classified as valleys. Watershed segmentation aims to join these ridges or the local maxima points across this relief, thus forming the so-called 'watersheds'. In a simulated flood across this relief, these lines would separate the waters collected in different valleys or basins. The schematic in Figure 5.6(a) shows such a topographic relief with catchment basins in valleys around the local minima and the watersheds separating them. In order to determine watersheds precisely and efficiently, *Avizo* uses marker-based watershed approach. This approach selects one marker or 'seed' inside each object, as well as in the background regions in the image. The markers are selected points of local minima in the topographical relief and can be visualised as punctured holes at the bottom of the valleys. Then, this uneven surface is theoretically submerged into a water bath or flooded slowly from below. Consequently, water pours in through the holes or markers into the respective valleys. This is also referred to as the growing or expansion of seeds. For this approach to work, the water entering from different holes cannot be allowed to mix. Thus, dams are built at the points of first contact which become the identified boundaries or 'watersheds' of the basins and eventually, that of the objects being separated in the image. The marker-based approach allows the user to select the markers or seeds directly or indirectly. This is a very critical step since the position and number of chosen seeds (or local minima) decide the lines of watersheds and eventually, the final number of separate objects. A schematic is presented in Figure 5.6(b) which explains this in a simplified way for two dimensions. Ignoring a local minimum as seed would mean no local separation, while over-seeding would result in local break-ups of objects. Thus, the use of seeds gives the user additional control over the accuracy and computational cost while using this algorithm.

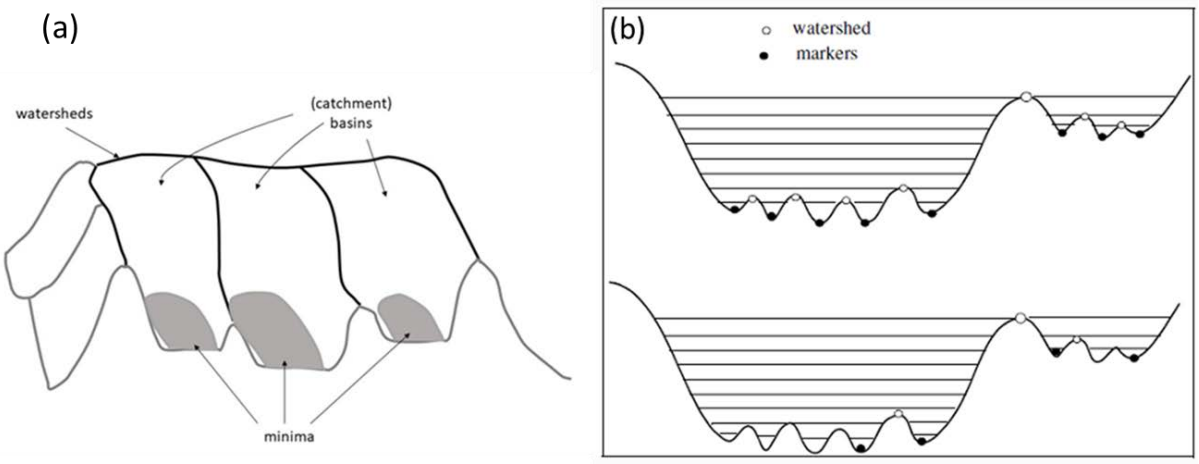

Figure 5.6: Schematics showing (a) a topographic relief with defined basins and watersheds, (b) role of markers/seeds in deciding watershed lines during flooding [9, 10]

The marker-based watershed approach in *Avizo* requires serial implementation of several steps or operations, which are mentioned in Figure 5.7. However, as the figure indicates, *Avizo* offers a second option to automatically implement them using a single function called '*Separate objects*' (with simplified selection of parameters), making the overall process quicker and user-friendly [10]. But, in order to properly demonstrate the marker-based watershed approach, operations were performed step-by-step while explaining the respective results, as part of this methodology section. Following this, the implementation of *'Separate Objects'* function has also been explained.

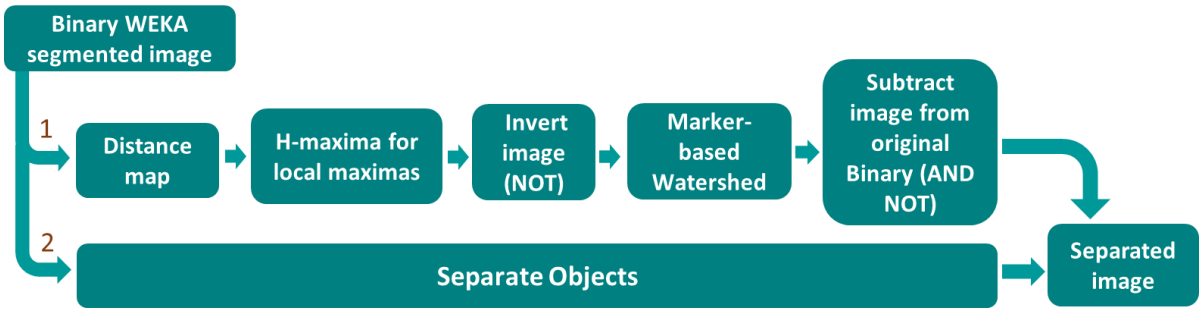

Figure 5.7: Schematic representation of the steps required to perform marker-based watershed in *Avizo*

As a first step, a 3D distance map operation was performed on the binary segmented volume of 600 × 600 × 600 voxels obtained in section 5.1.2. This creates a grayscale volume where voxel intensity represents the minimum distance from each non-zero voxel (in the input binary segmented volume) to the nearest zero-value voxel. *Avizo* offers several types of 3D distance maps and the most suitable one for this case was Chamfer Distance Map.

The most common distance map is the so-called Euclidean distance map. It is characterized by the fact that it performs the distance transforms without considering the orientation of the objects in the image. It calculates distance between pixels by simply using the Pythagoras theorem to compute linear distance between any two points in a cartesian system. However,

the main drawbacks of this algorithm are the long processing times and that it does not work correctly for images with complex objects [11].

Other algorithms, based on the Chamfer metrics, have been developed to address these issues. The most well-known ones among them include chessboard, city block and Chamfer distance maps. In Chamfer metrics, the distance transform is performed using a rectangular coordinate system. It is a discrete algorithm and takes less computational time to run. To create the distance map, it first obtains the distances in a region of interest and then keeps extending it until distances for the entire image are obtained [12]. If two points x and y are defined in a 3 × 3-pixel region of interest, the distance between them is governed by the following equation:

$$\|(x,y)\|_{(a,b)} \equiv max(|x|,|y|) \cdot a + min(|x|,|y|) \cdot (b-a)$$

Equation 5.1

where the parameter *a* represents the axial distance and *b* represents the diagonal distance.

After applying the Chamfer distance map to the binary segmented volume of 600 × 600 × 600 voxels, the slice shown in Figure 5.5(b) looks like the grayscale slice in Figure 5.8(b). The particle interiors looked very well-differentiated in the distance map with the innermost pixels appearing the brightest. This grayscale volume of 3D distance maps was used as input for generating the topographic relief for watershed algorithm.

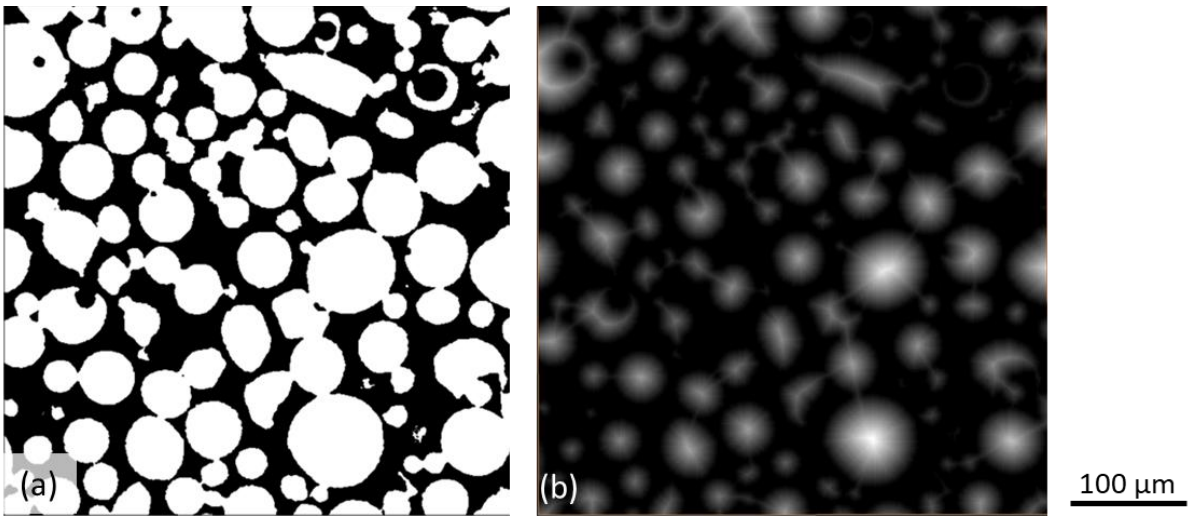

Figure 5.8: (a) Slice from binary segmented volume of 600 × 600 × 600 voxels (resolution 1 voxel = 0.77^3 µm^3), also shown in Figure 5.5(b), and (b) the corresponding slice from the Chamfer 3D distance map volume generated by *Avizo*

As indicated in the flowchart shown in Figure 5.7, the next step is to use the H-Maxima command for precisely identifying maxima points of the grayscale distance map. The algorithm behind this is based on a transform that bears the same name. The local maxima points in the grayscale image are identified and reduced by a factor (decided by a contrast coefficient), which is followed by a grayscale reconstruction by dilation. This results in

flattening and merging of local maxima peaks in the reconstructed image. The new regional maxima thus formed are called H-maxima. The contrast coefficient is specified by the user by inputting a value (usually between 1 and 5) in the contrast window of the command parameters. H-maxima command is applied on the distance map volume. Thus, the created H-maxima volume will be defined as the innermost voxels of the particles (as they would locally appear the brightest on a distance map). Figure 5.9 presents the same slice, which was shown in Figure 5.8(b), after applying the H-maxima command with a contrast value of 2. H-maxima were marked as coloured pixels. As the contrast value is increased, more and more local maxima that are closely located are merged into a single H-maxima, thus, reducing the number of final isolated maxima. The opposite happens as the value is decreased, with the minimum possible value being 1.

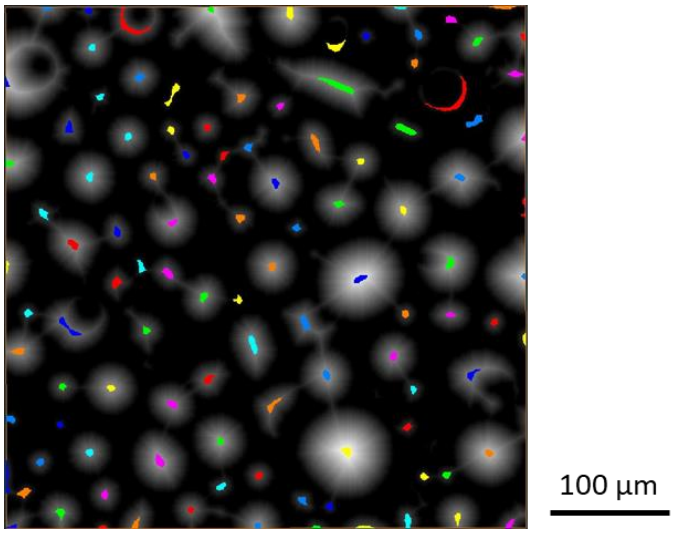

Figure 5.9: H-maxima regions (also called markers/seeds) labelled as coloured pixels on the slice shown in Figure 5.8(b), after applying the H-maxima command (contrast value 2) in *Avizo*

These H-maxima regions are the seeds for the marker-based watershed algorithm executed later. Therefore, it is crucial to choose an appropriate contrast value that places one seed inside each individual particle to be isolated. High contrast value or less total seeds will lead to insufficient separation and merger of closely located particles. A low contrast value might lead to excess of seeds that undesirably break up individual powder particles, especially if the data features some noisy local maxima. The following section 5.1.4 is dedicated to this issue. It explains, analytically and visually, the important role of contrast value on object separation by marker-based watershed. It also explains why the value 2 was selected for this particular volume.

Once the markers were obtained by H-maxima command, the 3D distance map volume had to be inverted. To do this, the NOT command was used. The markers will remain in the same position as before, only now they will be minima instead of maxima. This step is necessary because watershed algorithm acts on the local minima and expands them towards higher intensity values (via a simulated flood in the relief) to determine the lines of watershed. Therefore, the markers had to be minimal rather than maximal as defined in H-Maxima.

After obtaining the inverse of the 3D distance map, the marker-based watershed algorithm was applied on it to create a volume with the watershed lines. It is a binary volume with only these lines as non-zero pixels. This volume was further subtracted from the original binary segmented volume (obtained in section 5.1.2) using the AND NOT command. This removes or inverts the common non-zero pixels, i.e. the lines of watersheds running through some particles where they touch each other, from the original binary volume. A slice from the resulting volume is shown in Figure 5.10(b) with all the individual powder particles well-separated. The lines of watershed around each particle, which were determined by marker-based watershed and then subtracted later, are shown in Figure 5.10(a).

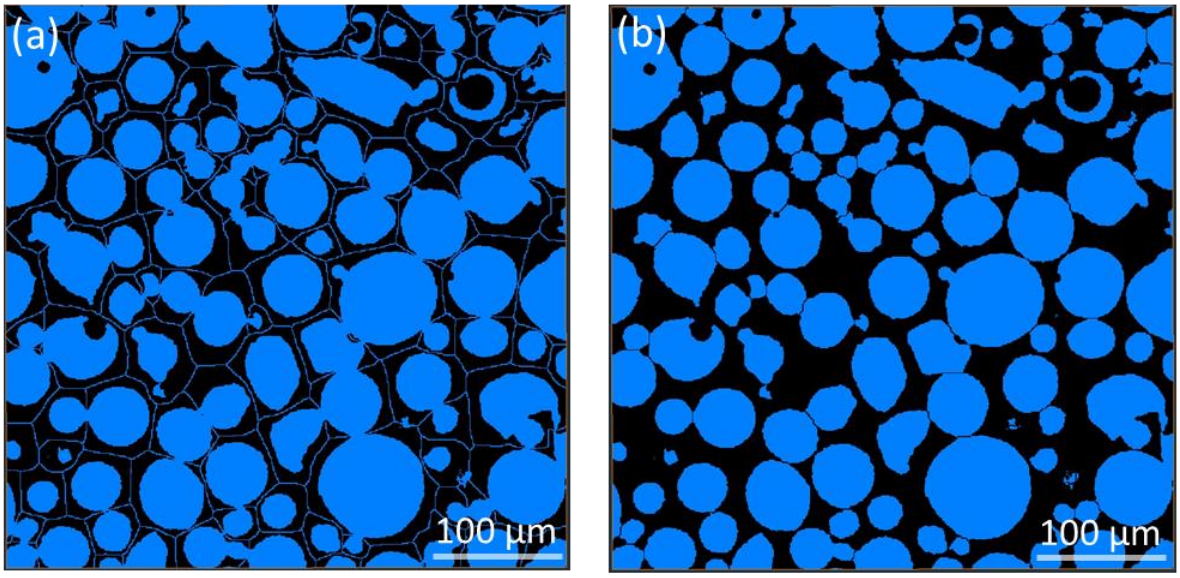

Figure 5.10: Slices from the volume of 600 × 600 × 600 voxels (resolution 1 voxel = 0.77^3 µm^3) after the 'separation' step showing (a) watershed lines around objects as determined by marker-based watershed in *Avizo*, (b) Separated objects without watershed lines

The second option for separating connected objects via marker-based watershed in *Avizo* is the function '*Separate Objects'*. It executes all the operations explained until now as a single step and returns the final volume represented by the slice in Figure 5.10(b). All the necessary input parameters for executing this function are shown in Figure 5.11.

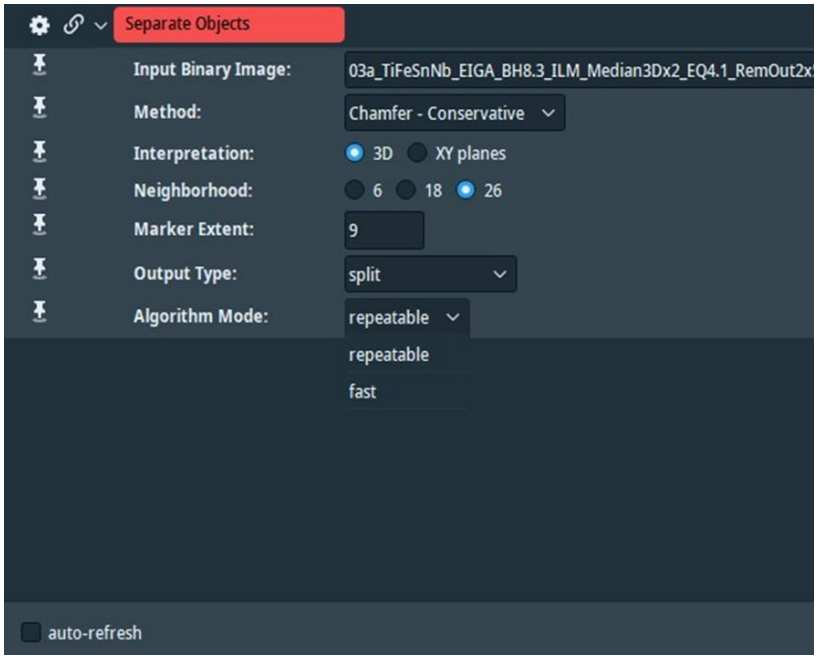

Figure 5.11: Command window of the function 'Separate Objects' in *Avizo*

The first parameter is called *Method* and is related to the type of distance map used. As explained earlier, the Chamfer distance map (option called 'Chamfer - conservative') should be selected here. The second is called the *Marker Extent* and it decides the placement of markers in the volume. This parameter is the same as 'Contrast' value in the H-Maxima command. Thirdly, there are *Interpretation* and *Neighbourhood* parameters. In the *Interpretation* parameter, it is necessary to specify whether it is based on a 2D or 3D input. When 3D is selected, the *Neighbourhood* parameter had to be specified which had options of considering 6, 18, or 26 neighbouring particles. For our case, 3D interpretation with 26 neighbours should be selected, as recommended by the *Avizo* user guide [10]. Further, the *Output type* parameter determines how the result is shown. The *split* option could be selected to obtain a volume with only the separated particles, the *line* option to obtain only the watershed lines of the volume, the *basins* or *basins2* options in which the valleys created by the watershed are obtained with or without the watershed lines respectively and finally, the *connected object* option that shows the volume as a single connected object, with the individual particles differentiated by colours. In this case, the *split* option should be selected in order to obtain the same type of final volume as represented by the slice in Figure 5.10(b). Finally, the last parameter that has to be specified is how the algorithm should be executed, i.e., in *repeatable* or *fast* manner. The repeatable option should be selected because it is more accurate, although it demands relatively more computational time.

This ends the explanation of the three main steps performed within this methodology. The operations described for the cropped volume of 600 × 600 × 600 voxels can be applied with the same parameters to the whole example volume of 1800 × 1800 × 1800 voxels. However, this is not the complete methodology and the final workflow that was followed for treating XCT volumes is presented in section 5.1.5 (see Figure 5.15). It also explains an additional step

(*Fill Holes 3D* command) that was added after segmentation (second step) in order to calculate internal porosity of powders and perform object separation more accurately by watershed.

The following section 5.1.4 describes how to optimise contrast factor/marker extent during marker-based watershed to get the best possible results. It studies the evolution of relevant 3D characteristics in a particular volume of powder particles as marker-based watershed is implemented (in 3D) for varying contrast values. It also describes the limitations of the process.

5.1.4 Watershed in 3D: effect of contrast/marker extent value

As explained in the previous section, the contrast value or marker extent parameter are very critical to the marker-based watershed algorithm. They decide the number and size of seeds used for determining the lines of watershed ("flooded" region around the seeds). In order to determine the most appropriate value, while saving computational time, a representative sub-volume is cropped and initially separated via watershed using many possible contrast values. For our example volume of 1800 × 1800 × 1800 voxels, the sub-volume used was of size 400 × 400 × 400 voxels containing approximately 600 particles. It was separated via watershed using contrast values ranging from 1 to 11. After separation, the *Label analysis* command of *Avizo* was used to extract numerical and statistical information of the separated particles in the sub-volume. This includes very relevant characteristics like Volumes, Sphericity and total number of powder particles. *Avizo* calculates the 3D volume of particles based on the following equation [10].

$$Volume3d = Voxelcount \times cx \times cy \times cz$$

Equation 5.2

where cx, cy and cz are the dimensions of a voxel across x, y and z axes. It multiplies the volume of each voxel with the total number of voxels in an object. In the considered volume, *cx = cy = cz =* 0.718 µm.

The sphericity of a particle is defined as the ratio between the surface area of a sphere with the same volume as the particle and the actual surface area measured for the particle. It is equal to 1 for a perfect sphere. Sphericity is not an in-built measure in *Avizo* and was created as a custom measure using the following equation.

$$Sphericity = \frac{\pi^{1/3}(6Volume3d)^{2/3}}{Area3d}$$

Equation 5.3

where Volume3d and Area3d are the measured volume and surface area of the 3D object respectively.

Area3d is the total area of the object boundary which is calculated by *Avizo* using certain intercepts to estimate the exposed surface of the outer voxels [10]. Since the considered objects are discretely made up of voxels, this estimate becomes less accurate for very small objects and can result in unreasonable values of Area3d and sphericity for particles consisting of few voxels. In order to avoid such particles from the analysis, only particles larger than 1000 voxels (equivalent diameter 9.6 µm) with sphericity values less than or equal to 1 were considered. It further gets rid of any residual voxels in the volume originating from experimental noise or artefacts.

Figure 5.12 shows the variation of several features calculated for the studied sub-volume of 400 × 400 × 400 voxels with respect to the contrast value or marker extent used for watershed separation. In Figure 5.12(a), MeanVol is the average volume3d of all the particles obtained. Meanvol14 is the average of the largest fourteen volumes measured. The third parameter is the total number of individual particles.

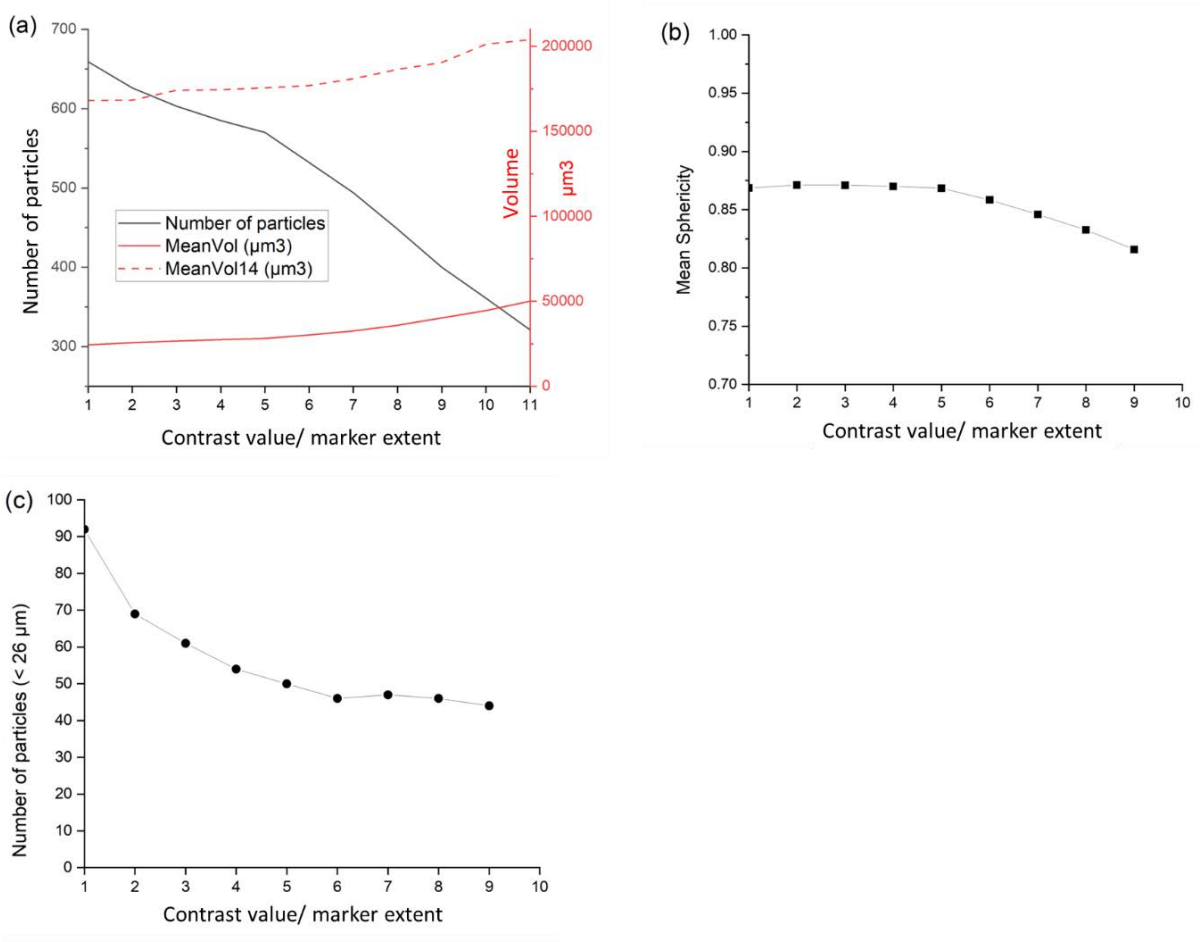

Figure 5.12: Variation of determined (a) volume parameters and total number of powder particles, (b) mean sphericity of particles and (c) number of particles below 26 µm of equivalent sphere diameter (9202.8 µm^3 volume) with respect to used contrast values/marker extents for watershed separation of a volume of 400 × 400 × 400 voxels (resolution 1 voxel = 0.77^3 µm^3) in *Avizo*

Both volume parameters (MeanVol and MeanVol14) keep increasing slightly as the contrast value is increased. Meanwhile, the number of particles keeps falling. This effect is so significant that the number of individual particles at the highest contrast value is about half of what was obtained at the lowest. These trends indicate the merging of particles happening with increase in contrast value, including for very big particles with the largest volumes. It originates from the fact that high contrast value in the watershed algorithm means fewer total seeds or markers and thus, not mapping seeds inside each potential particle. Further, it was noticed that the rate of decrease in the number of particles was slightly higher beyond contrast value 5, evident from a slightly steeper slope. Also, the average sphericity of particles, shown in Figure 5.12(b), starts declining sharply beyond this value. It is almost constant until contrast value of 5. This suggests that a significant number of largely spherical powder particles started merging to produce objects with undesirable shapes beyond this point. Thus, 5 can be considered as an upper limit for the contrast values until where particle shapes mostly remain reasonable. In principle, a lower threshold or limit of contrast value should also exist below which watershed leads to over-estimation of particle numbers and under-estimation of volume as a result of unnecessary breaking-ups of particles. However, we do not observe a clear change in trend towards the lower contrast values for the parameters plotted in Figure 5.12(a, b). Therefore, in order to identify a lower limit, we looked specifically at the number of small particles. The powder particles in the discussed XCT volume lied in the sieved size range of 20 – 63 µm. Assuming that break-ups or over-segmentation of particles would result in formation of new smaller particles, we looked at the number of particles below an equivalent sphere diameter of 26 µm (Volume of 9202.8 μm^3 or ≈ 20160 voxels) for contrast values of 1 to 5 (see Figure 5.12(c)). Although lower contrast value meant more particles in general, a significant increase in the particle numbers was recorded while moving from contrast value 2 to 1. This hints at 2 being the lower limit, thus finalizing our range of interest for identifying the optimum contrast value to be from 2 to 5.

The optimum value does not cause excessive breaking-up of particles nor causes frequent merging of separate particles into bigger ones. Further, more than one contrast values might produce optimum results for a given volume and there might not be significant differences between values that are close to each other. At this stage, visual clues provided by some of the challenging slices in the sub-volume were put to use. Slices with several connected particles, preferably of diverse shapes and sizes, were selected and inspected for differences after applying marker-based watershed with contrast values from 2 to 5. Figure 5.13 shows two such slices with particles separated using contrast values 2, 3 and 4. Individual particles are assigned random solid colours for better visualisation. There were very few differences among results of the three contrast values, except some connected particles (marked by white circles) can be seen better separated for contrast of 2. They are merged into bigger objects when contrast of 3 or 4 was used. This trend increases further for contrast value of 5.

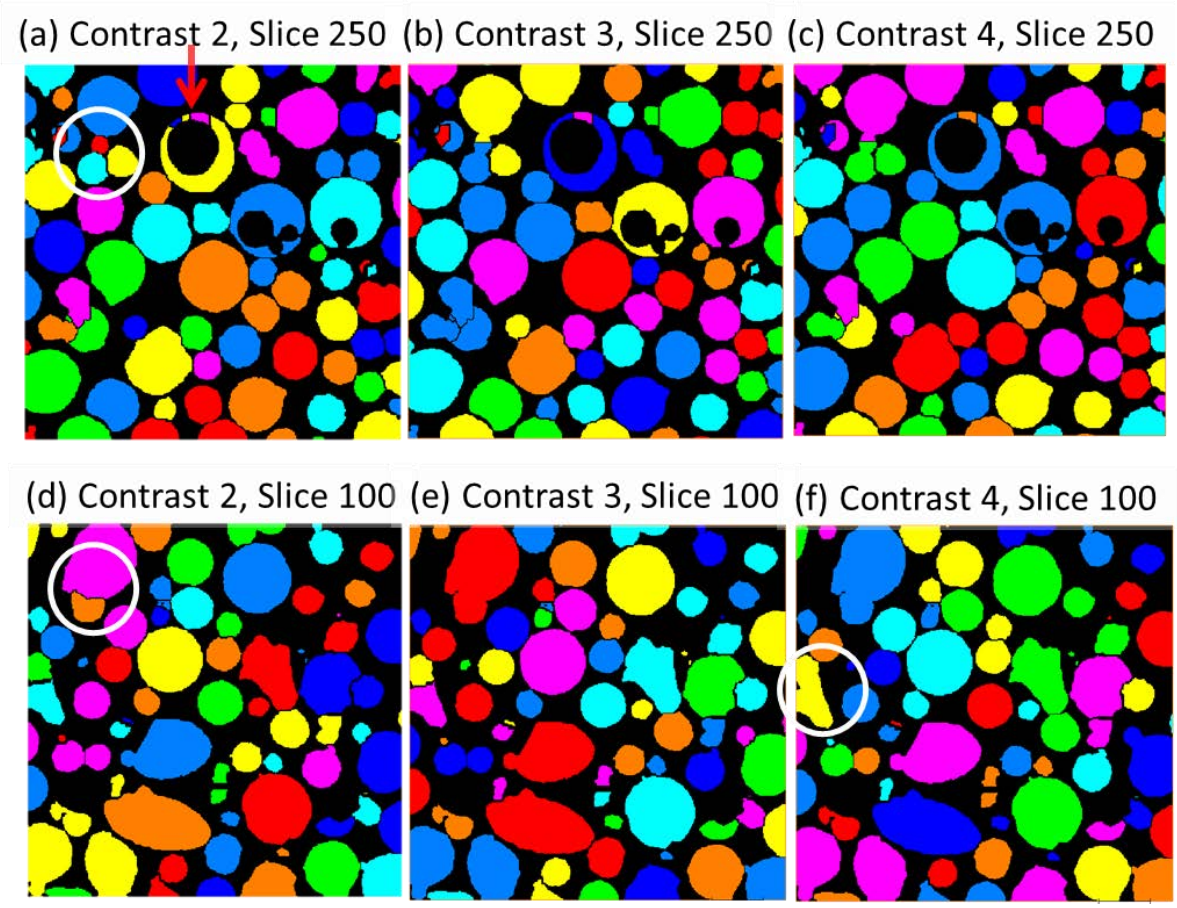

Figure 5.13: Slice number 250 (a-c) and number 100 (d-f) of the watershed separated volume of 400 × 400 × 400 voxels (resolution 1 voxel = 0.77^3 µm^3). Left to right, three contrast values 2, 3 and 4 are used and separated particles are coloured randomly. Observed differences are marked by white circles and unresolved errors are indicated by red arrows.

It is a fact that some particles are genuinely fused together as result of collisions during atomisation to form elongated particles or particles with satellites (see section 1.3.2.2 in chapter 1). Errors might be introduced into this methodology at the binary segmentation step or at the watershed separation step if they are separated as two or more particles in the final volume. This is mainly the result of the resolution and measured grayscale distribution not being good enough to differentiate between fused and touching particles. This error is reduced significantly when samples of powder dispersed and embedded in resin are used for measurement, unlike the volume discussed here which was measured by filling a plastic capillary with powder. Particles are more dispersed in a resin, thus strongly reducing the probability of touching each other. On the other hand, it also means fewer particles in a measured volume size and the necessity to work with very large volumes to have the same statistics. Another issue faced by this methodology is the breaking up of some particles with large internal or external pores during separation. The cross-sections of such particles appear as “ring” or “moon-shaped” in the 2D slices. One particle facing this problem is marked by a red arrow in Figure 5.13(a) and as shown, the issue persisted for all contrast values. In order

to reduce such errors and to further analyse the closed porosity in the measured powder samples, additional steps were added to the routine which are discussed in the next section.

Keeping these issues in mind, it was concluded that **contrast value 2 is optimum** for implementing watershed in 3D on this volume. It would be later used to extrapolate the procedure to the full volume of 1800 × 1800 × 1800 voxels. This is also why contrast value 2 was used while explaining the separation step by marker-based watershed in section 5.1.3. In order to further highlight the strong effect of contrast value on the watershed algorithm for separation, Figure 5.14 shows the same two slices, as used in Figure 5.13, for the extreme cases of contrast values 1 and 9 compared against the chosen optimum value of 2.

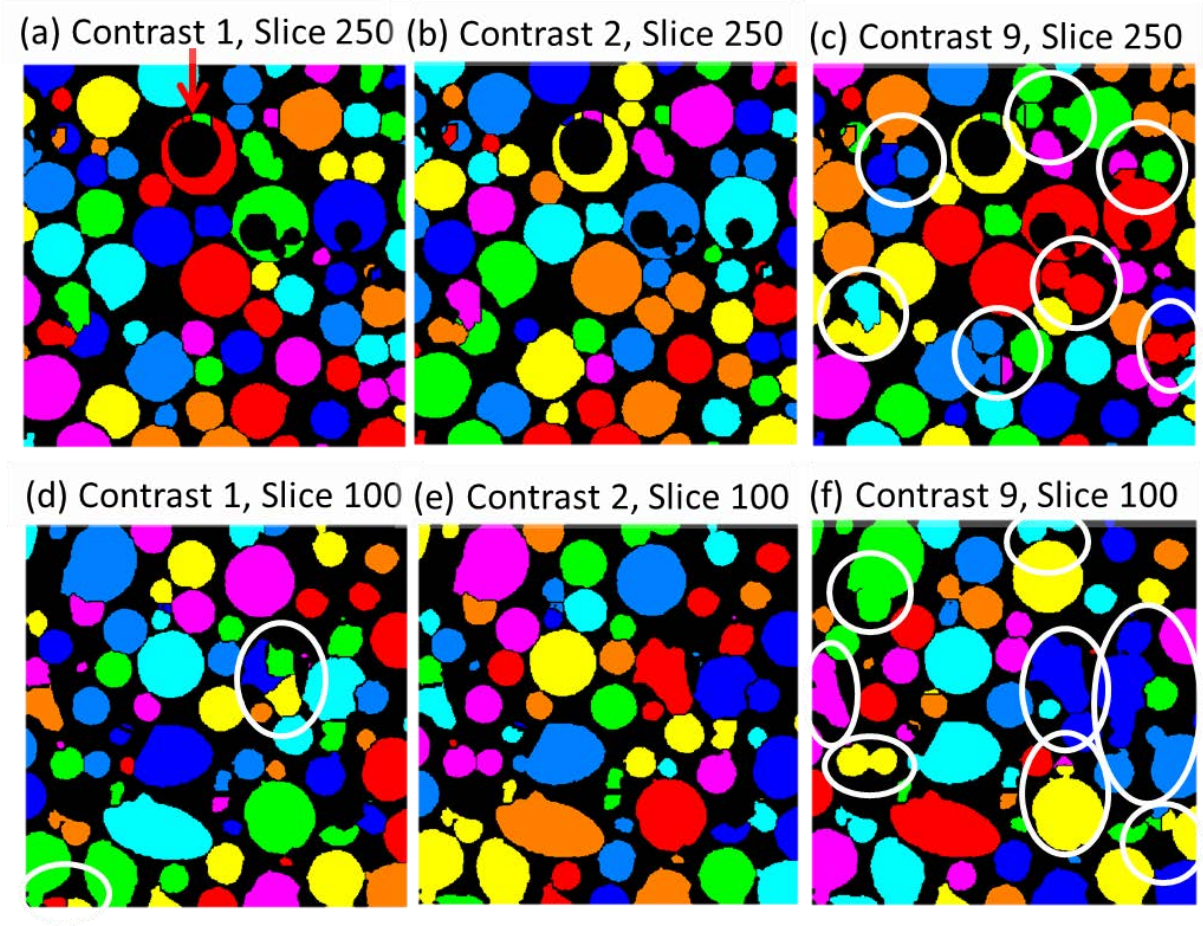

Figure 5.14: Slice number 250 (a-c) and number 100 (d-f) of the watershed separated volume of 400 × 400 × 400 voxels (resolution 1 voxel = 0.77^3 µm^3). Left to right, three contrast values 1, 2 and 9 are used and separated particles are coloured randomly. Observed differences are marked by white circles and unresolved errors are indicated by red arrows.

It should be noted that 1 and 9 were rejected early based on the numerical information presented in Figure 5.12, which is the more definitive and reliable method while making decisions for a 3D operation. However, this 2D representation in just two slices manages to clearly highlight some differences, especially between the results for contrast value 2 and 9. Merging of particles, both small and big are seen happening for the higher contrast value. There is some breaking-up and over-segmentation of particles occurring for the lower value

of 1. These undesirable phenomena are avoided in the slices while using contrast value of 2. But, much like Figure 5.13, the incorrect separation of the porous particle marked by the red arrow persisted for all contrast values.

It is not necessary to perform this exercise for every XCT volume being treated by marker-based watershed (3D). The same contrast value/marker extent should work for volumes measured with similar resolution that feature particles of similar 3D geometry. In our case, contrast value 2 was used for all analysed volumes.

5.1.5 Final Workflow for powder analysis

The final workflow for treating an XCT volume of powder particles is shown in Figure 5.15. For better understanding, picture of a sub-volume is placed below the steps that schematically shows the resulting volumes.

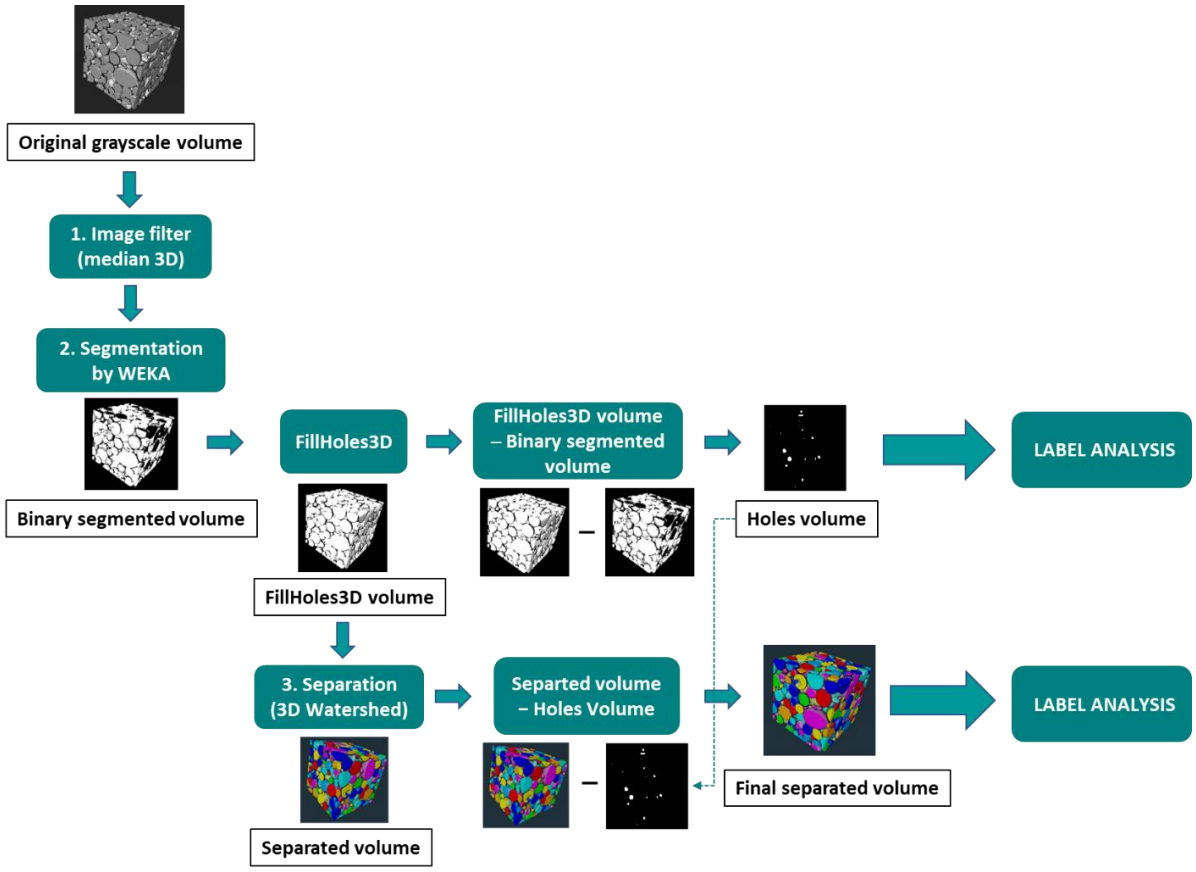

Figure 5.15: Final workflow for treating powder XCT volumes in the developed methodology (shown with schematic sub-volumes for better understanding)

This workflow was implemented on the example volume of 1800 × 1800 × 1800 voxels, using parameter values tested on its sub-volumes (described in the previous sections). The volume was opened in *Fiji* and a Median 3D filter was applied with input radius (along X, Y and Z axis of the neighbourhood) as 2. Segmentation was performed in *Fiji* by applying the same classifier model of WEKA that was saved after training with 10 slices and successfully

segmenting the sub-volume of 600 × 600 × 600 voxels in section 5.1.2. The resulting 'Binary segmented volume' of 1800 × 1800 × 1800 voxels was opened in *Avizo* and a *Fill Holes 3D* command was applied to it. As the name suggests, this command fills in the gaps in the volume by turning particles with internal pores into full particles. The resulting volume is referred to as 'FillHoles3D volume' in the workflow. Then, the 'Binary segmented volume' was subtracted from the 'FillHoles3D volume', thus creating a new volume that only consisted of the internal pores of powder particles, referred to as the 'Holes volume'. This volume was later used for analysing the internal porosity in powder samples which is an essential part of their overall assessment. Further, the 'FillHoles3D volume' was used for the separation step in *Avizo*. Marker-based watershed (3D) with a contrast value/marker extent of 2 was performed on it to create the resulting 'Separated volume'. Next, the volume containing only internal porosity, i.e. the 'Holes volume' was subtracted from this 'Separated volume' to get a volume with separated and original powder particles (with their internal pores) as measured. This result is the 'Final separated volume' that was used for obtaining all the necessary size and shape related characteristics of the powder. The *Label analysis* command in *Avizo* was used for labelling all individual objects in a volume and extracting their relevant geometrical properties. It was applied to the 'Final separated volume' and the 'Holes volume' (for extracting porosity related data).

It is very important that the watershed separation is performed on the 'FillHoles3D volume' and the internal porosity is introduced later into the resulting volume after separation. It avoids the errors in separation faced by particles with large internal pores, which was mentioned in the previous section 5.1.4 and marked in the slices shown in Figure 5.13 and Figure 5.14. However, we are only filling the internal or closed pores in the original volume before separation and some particles with large open porosities might continue to face this issue. But their numbers would be very insignificant as compared to the overall statistics of the particles in the volume and those errors can be ignored.

Figure 5.16(a) shows the 'Final separated volume' of size 1800 × 1800 × 1800 voxels obtained at the end of this workflow, while Figure 5.16(b) shows the 'Holes volume' consisting of all the closed pores present in the final volume. Each individual powder particle/pore has been labelled and coloured randomly by *Label Analysis* command.

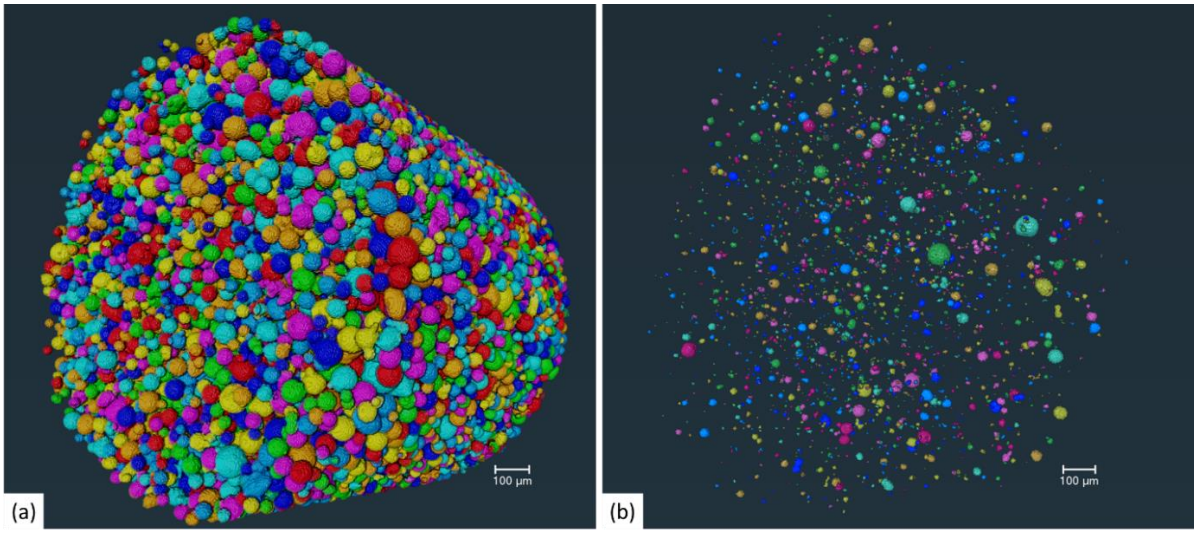

Figure 5.16: Volume rendering in Avizo showing (a) the 'Final separated volume' and (b) the 'Holes volume' volume of sizes 1800 × 1800 × 1800 voxels (resolution 1 voxel = 0.77^3 µm^3), as obtained at the end of the Final workflow shown in Figure 5.15

This ends the section describing the methodology of powder XCT data analysis. The following sections discuss and evaluate the results obtained in terms of internal porosity, size and shape distribution of the studied powders.

5.2 Results: Internal porosity analysis

Results concerning internal/closed porosity of measured powders, as determined by this methodology, have already been presented in Table 4.2 (section 4.1.1) and Table 4.7 (section 4.2.1) of chapter 4. These results were important part of the powder characterisation and screening process. Porosity volume % was quite low in the studied powders, with AMA showing the lowest (0.2 vol %) value. CGA showed the highest volume % of internal pores (1.9 %) which is more than 9 times that of AMA. Rest of the studied powders (CFA, AMA2 and CFA-FeTi) showed porosity ≤ 0.6 vol %. Further, the number % of particles with internal pores was calculated (using Equation 4.1, section 4.1.1 of chapter 4) assuming that one particle features a maximum of one internal pore. CGA also showed the largest number % of particles with internal pores (36.1 %), while it was the lowest for AMA2 powder (9.5 %). Thus, in terms of internal porosity, CGA produced powders performed relatively worse than the powders produced by other atomisation methods.

5.3 Results: Particle size analysis

As previously mentioned in section 5.1.4, *Avizo* returns the volume of each powder particle as the measure Volume3d based on Equation 5.2. It further calculates the equivalent diameter, i.e. the diameter of a sphere with a volume equal to that of the particle, based on the following equation.

$$Equivalent\ diameter = \sqrt[3]{\frac{6 \times Volume3d}{\pi}}$$

Equation 5.4

These measures allow us to plot the cumulative volume % of particles for every equivalent diameter in a powder sample, thus obtaining a particle size distribution. Particle size distributions or PSDs (in terms of volume %) were also obtained conventionally by laser diffraction method (described in section 3.3.3 of chapter 3). The results were presented in Figure 4.3 and Figure 4.25 of chapter 4. Figure 5.17 below compares the distribution of cumulative volume % calculated for each equivalent diameter, and as determined by the two methods, i.e. particle analysis by XCT and laser diffraction. It was done for four powder samples, namely CGA, CFA, CFA-FeTi and AMA2 which were produced by three atomisation methods in total, indicated by their respective names. Before measuring, the powders were sieved to obtain a size range of 20 – 63 µm, except for CFA-FeTi which was sieved for size range of 45 – 90 µm.

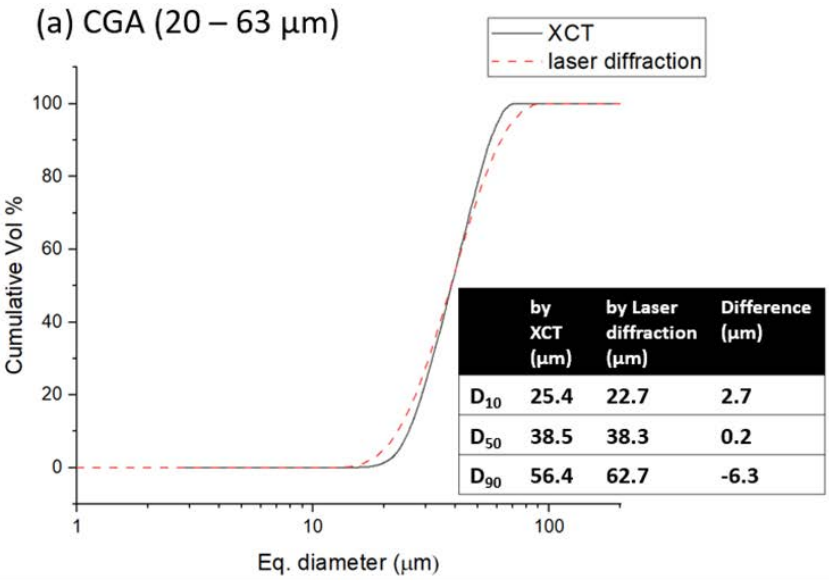

	by XCT (µm)	by Laser diffraction (µm)	Difference (µm)
D_{10}	25.4	22.7	2.7
D_{50}	38.5	38.3	0.2
D_{90}	56.4	62.7	-6.3

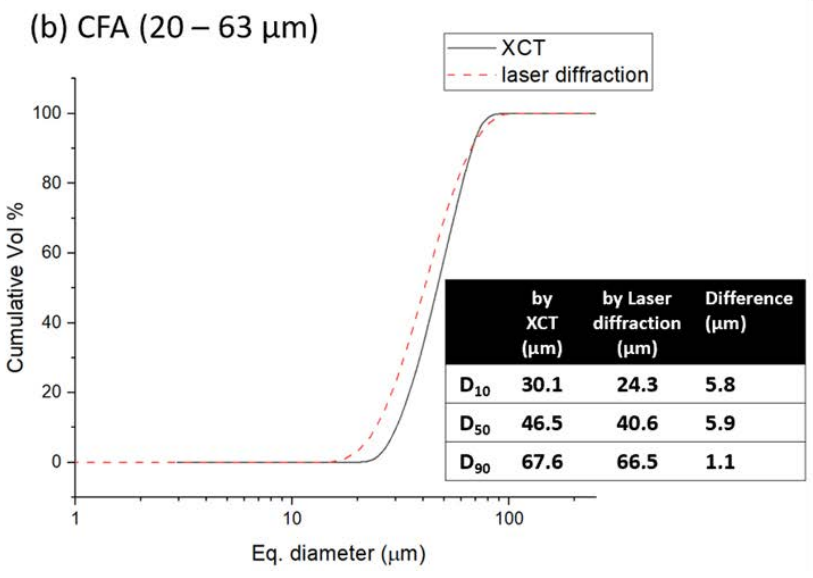

	by XCT (µm)	by Laser diffraction (µm)	Difference (µm)
D_{10}	30.1	24.3	5.8
D_{50}	46.5	40.6	5.9
D_{90}	67.6	66.5	1.1

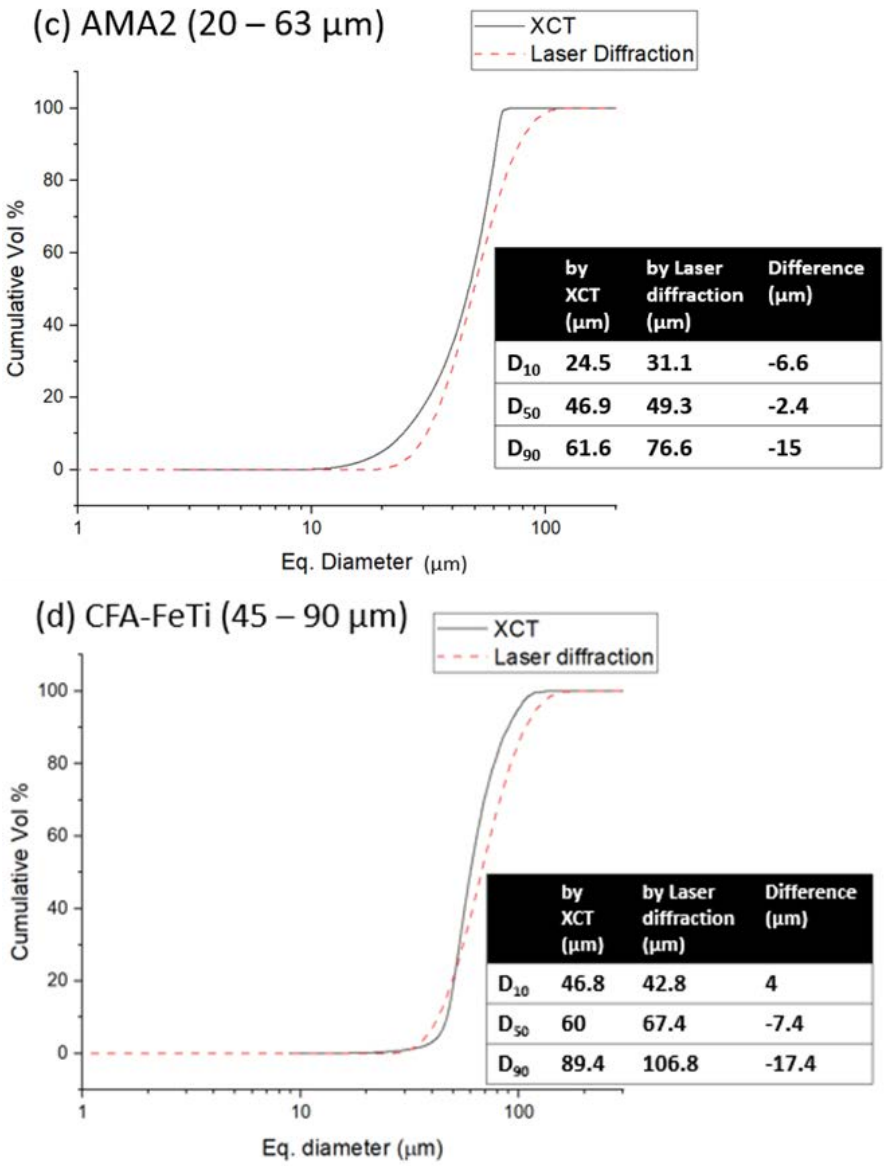

	by XCT (µm)	by Laser diffraction (µm)	Difference (µm)
D_{10}	24.5	31.1	-6.6
D_{50}	46.9	49.3	-2.4
D_{90}	61.6	76.6	-15

	by XCT (µm)	by Laser diffraction (µm)	Difference (µm)
D_{10}	46.8	42.8	4
D_{50}	60	67.4	-7.4
D_{90}	89.4	106.8	-17.4

Figure 5.17: Cumulative volume % vs. equivalent diameter, as determined by the two methods: particle analysis by XCT and laser diffraction, for powders (a) CGA (sieved 20 – 63 µm), (b) CFA (sieved 20 – 63 µm), (c) AMA2 (sieved 20 – 63 µm) and (d) CFA-FeTi (sieved 45 – 90 µm). Inset tables show and compare the respective D_{10}, D_{50} and D_{90} values determined.

For all cases, some differences were observed in the PSDs obtained by the two techniques, as evident from the cumulative curves and the differences between their respective D_{10}, D_{50} and D_{90} values. Mismatches or deviations between the two curves (representing XCT and laser diffraction) can be observed happening for particles of lower volumes or equivalent diameters, for the larger ones as well as for the median diameters represented by D_{50}.

Above 90% cumulative volume, XCT clearly reported more cumulative volume % for the same equivalent diameters as compared to laser diffraction in all cases, except for CFA (Figure 5.17(b)) where they were very similar. This resulted in lower D_{90} values for XCT data in the three cases and almost the same D_{90} for both techniques in CFA powder. In case of AMA2 (Figure 5.17(c)) and CFA-FeTi (Figure 5.17(d)), the D_{90} values determined by laser diffraction

fell quite beyond the upper limit of the size range set by sieving (i.e. 63 µm for AMA2 and 90 µm for CFA-FeTi). Therefore, values determined by XCT can be considered more reasonable for these powders. XCT determined the D_{90} values to be within the range, while also showing the largest deviation (up to 17.4 µm in CFA-FeTi) from laser diffraction data among all reported parameters for all powders. In case of CFA, both techniques determined D_{90} to be slightly higher (by up to 4.6 µm) than the upper limit of 63 µm.

Below 20% cumulative volume, laser diffraction reported more cumulative vol % for the same equivalent diameters in all powders, except for AMA2 where it was the opposite. Consequently, the D_{10} values were lower according to laser diffraction data except for AMA2.

In the medium range of 40 to 60 % cumulative volume, XCT data measured higher cumulative volume % for the same particle sizes in case of CFA-FeTi and AMA2 powders, while it remained lower than laser diffraction data for CFA powder. In case of CGA, both curves representing the two techniques overlapped in this range. CGA showed the least average deviation between the two curves, also evident from the differences between the extracted D_{10}, D_{50} and D_{90} parameters. Based on these results, it can be safely said that particle size or volume was not correlated to the sensitivity of the two measuring or analysing techniques and the deviations arising between them.

Among the Ti-rich powders (i.e. CGA, CFA and AMA2), XCT data analysis showed AMA2 to have the volume distribution skewed towards larger particles, as shown in Figure 5.18(b). On the other hand, CGA was more biased towards smaller particles, although some overlap was seen between the two for fine particles up to 20 µm (reflected in similar D_{10} values determined by XCT, as reported in Figure 5.17). CFA showed a relatively normal distribution without skew. It lied more towards the right (i.e. bigger sizes) as compared to other two powders. It recorded the highest D_{10} and D_{90} among all three and a D_{50} similar to AMA2, as per XCT data analysis (see Figure 5.17). According to laser diffraction data shown in Figure 5.18(a), all curves were relatively smoother normal distributions. However, unlike XCT data, the distribution of AMA2 was observed to be clearly shifted towards larger particle sizes as compared to other powders. The calculated D_{10}, D_{50} and D_{90} of AMA2 were also the highest (see Figure 5.17). It meant AMA2 clearly consisted of the largest particles on average. CGA lied slightly more to the left as compared to CFA and also showed the lowest D_{50} and D_{90} values among all three. Thus, both methods indicated CGA to have relatively the smallest particles on average. Such a PSD could mean lower powder flowability for CGA because smaller particles tend to agglomerate. As discussed already in section 4.1.1 of chapter 4, it was one of the factors contributing towards the highest Hall flowtime reported for CGA among all powders.

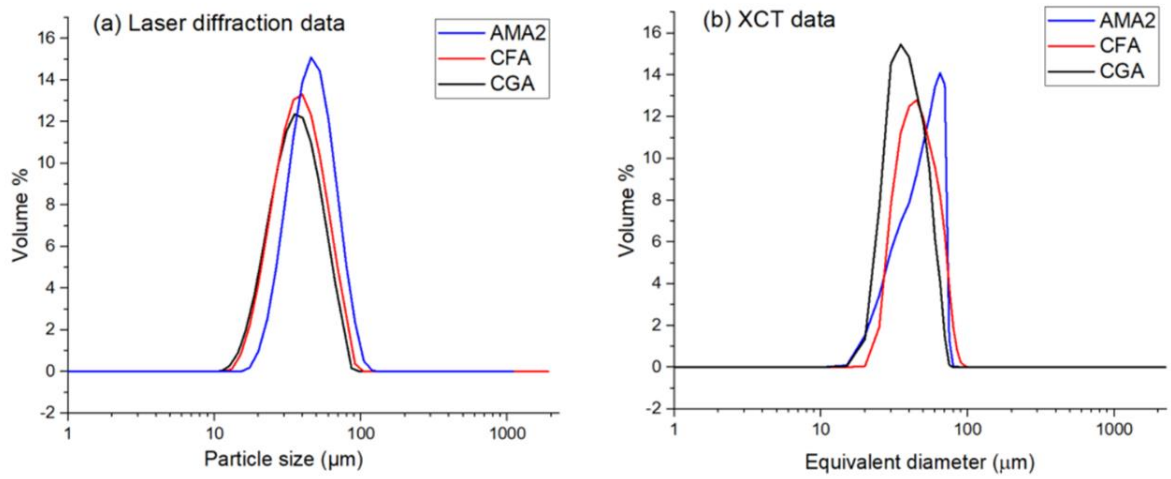

Figure 5.18: Particle Size Distributions (Volume % vs. particle size or equivalent diameter) of AMA2, CFA and CGA powders (sieved to size range 20 – 63 µm) as determined by (a) laser diffraction and (b) particle analysis by XCT

For obtaining a particle size distribution, laser diffraction performed in *Mastersizer 2000*, has statistical advantage over the XCT image analysis methodology. Each powder sample analysed by XCT was a volume containing between 27000 and 47000 particles. On the other hand, the wet test performed using the *Mastersizer 2000* required around 1 g of powder suspended in a liquid medium (see section 3.3.3 of chapter 3). For this weight range of powder, a calculation can be made to estimate the approximate number of analysed powder particles based on some simple assumptions. If all particles are assumed to have the same diameter as the median particle size (or D_{50}) and a density ρ, the number of particles n in a given weight W of powder is given by $n = \frac{6W}{\rho \times \pi \times D_{50}^3}$. For CFA powder, substituting D_{50} as 40.6 µm (as measured by laser diffraction) and ρ as 5.48 g/cm^3 (theoretical density), the calculations reveal ≈ 5 × 10^6 particles in 1 g of powder. The projected particle numbers were in the order of millions for all the powder samples measured by laser diffraction. This is two orders of magnitude more than the particle numbers in analysed XCT volumes. Nevertheless, the XCT volumes represent powder samples that are statistically large enough and are analysed using a methodology that provides much more accurate estimates of each individual particle´s volume.

For a high-resolution measurement with voxel sizes much smaller than the dimensions of the measured 3D object, the XCT image analysis methodology provides a volume measurement very close to reality. It considers all internal/open porosity and is unaffected by the object shape. On the other hand, laser diffraction technique assumes particles to be perfect translucent spheres and uses equations of Mie theory to estimate their diffraction equivalent diameters (diameter of sphere producing the same diffraction pattern as the interacting particle) and volume distributions across those diameters (see section 3.3.3 of chapter 3 for more details). This means non-spherical and porous powder particles are not well-represented by this method. Although it averages out multiple measurements of particles that are freely rotating in a dispersing medium, there is no complimentary information on

shape or geometry of interacting particles to estimate this error. Further, the calculations involved in laser diffraction technique require accurate knowledge of the interacting material´s refractive index and absorption coefficient. For our alloys, these properties were unknown and were assumed to be equal to that of the major constituting element. Unlike laser diffraction, the XCT based particle analysis method is not limited to particle size/volume data and returns a lot of other useful data (such as shape parameters, density and porosity) that can be used to accurately estimate errors/deviations in volume and size-based calculations, if necessary. As shown in the following section, this method also allows classification of various powder particles in a volume on the basis of morphological features and accurately measured 3D shape parameters.

5.4 Results: 3D Morphology analysis

As mentioned in section 1.3.2.2 of chapter 1, powder shape is correlated to important properties like flow, powder-packing ability, apparent density and density of final AM parts. Powder particles used as AM feedstock should have high sphericity, high aspect ratio and low internal porosity to obtain the best results. XCT-based image analysis can provide very reliable assessments of these parameters for a studied powder based on a single measurement. Evaluation of internal porosity has already been discussed in section 5.2. In this section, we assessed and quantified the shape distribution of powder particles using sphericity (S), aspect ratio (AR) and Volume3d parameters returned by *Avizo* for an analysed XCT volume. Zhou et al. [5] used these parameters to differentiate the ideal (almost spherical shape and smooth surface) powder particles from irregular ones using k-means clustering of XCT data. They further calculated the 'qualification ratio' for different powder samples, which was defined as the number percent of ideal particles among all the analysed particles in a particular volume. We successfully mapped the three parameters to distinctly observed morphological features in powder particles of a representative XCT volume and created a visual database. This allows us to choose the desirable particle morphologies and identify the range of the shape parameters associated with them. This information can then be used to calculate the qualification ratio for a powder sample.

Sphericity (S) of each particle is calculated by *Avizo* using Equation 5.3. It considers the volume and surface area of a particle. A shape that maximizes the volume and minimizes its surface area will have high sphericity. Ideally, this shape is a perfect sphere with sphericity equal to 1. A decrease in volume due to open/closed porosity in powder particles reduces sphericity. Further, an increase in surface area due to surface roughness or superficial features like satellites can also reduce sphericity.

Aspect ratio is a parameter that is extracted from the covariance matrix M computed by *Avizo* for every particle:

$$M = \begin{bmatrix} M_{2x} & M_{2xy} & M_{2xz} \\ M_{2xy} & M_{2y} & M_{2yz} \\ M_{2xz} & M_{2yz} & M_{2z} \end{bmatrix}$$

Where matrix elements are the second order moments for inertia of the particle.

The first order moments define an object´s centre of mass, while the second order moments contain information related to the object shape and orientation. Three eigenvalues of the covariance matrix in increasing order of their magnitudes are represented by λ_{small}, λ_{medium} and λ_{large}. Eigenvector given by λ_{large} represents the direction of the object´s major inertia axis which defines its Orientation. The eigenvalues are used to define shape parameters using the following equations.

$$Elongation = \frac{\lambda_{medium}}{\lambda_{large}} \quad \text{Equation 5.5}$$

$$Flatness = \frac{\lambda_{small}}{\lambda_{medium}} \quad \text{Equation 5.6}$$

$$Aspect\ ratio\ (AR) = \frac{\lambda_{small}}{\lambda_{large}} = Elongation\ \times Flatness \quad \text{Equation 5.7}$$

Aspect ratio (AR), lying between 0 and 1, is the ratio of the smallest to the largest eigenvalue of the covariance matrix. It reflects the overall ellipsoidal nature of an object shape and is equal to 1 for a perfect sphere. AR was created as a custom measure in *Avizo* and is mathematically equal to the product of the in-built parameters Elongation and Flatness of the object.

These 3D estimates of powder Sphericity (S) and Aspect ratio (AR) performed using XCT-based image analysis in *Avizo* are far more accurate and realistic as compared to measures provided by traditional morphology assessment techniques for powders. As explained in section 1.3.2.2 of chapter 1, microscopy and high-resolution static imaging tools (like Morphologi G3, Camsizer M1) only provide quantified shape-related information based on 2D images or projections of powder particles, which can be misleading.

For creating the visual database of particle morphologies, a volume of 2020 × 1960 × 990 voxels (resolution 1 voxel = 0.72^3 µm^3) belonging to AMA2 powder was chosen. It consisted of 22941 particles that were sieved into a size range of 20 – 63 µm. It was cropped (to save computational time while rendering and to avoid crowding while taking pictures of particles for the visual database) from a larger volume of 2760 × 2760 × 1980 voxels which was analysed using this methodology to reveal a D_{50} of 46.9 µm (reported in section 5.3). Figure 5.19 shows a 3D plot between Sphericity (S), Aspect Ratio (AR) and Volume3d parameters returned by *Avizo* for all particles (represented by red spheres) in the considered volume. In order to avoid unreasonable estimates of parameters that could occur in objects consisting of only few voxels and to further avoid voxels originating from any residual noise, only

particles consisting of more than 1000 voxels (equivalent diameter 8.9 µm) with sphericity/AR values less than or equal to 1 were considered for the analysis.

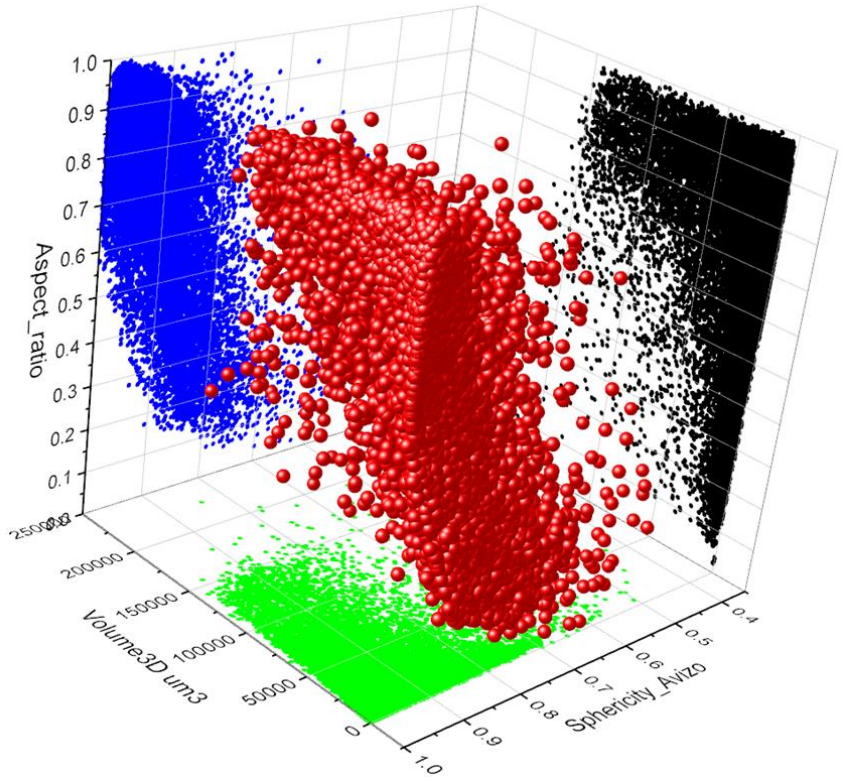

Figure 5.19: 3D scatter plot between Sphericity (S), Aspect Ratio (AR) and Volume3d parameters returned by Avizo for a volume of 2020 × 1960 × 990 voxels (resolution 1 voxel = 0.72^3 µm^3) belonging to AMA2 powder (sieved 20 – 63 µm). 2D projections are also shown on the respective planes.

The plot also shows 2D projections of the data revealing some relationships among the parameters. The Volume3d vs. AR scatter plot, shown as black points, indicated a high spread of AR values for particles with lower volumes. As the volumes increase, particles tend to be concentrated more towards the high end of AR values. The Volume3d vs. Sphericity (S) scatter plot, represented by green points, showed the same trend. Further, all particles appeared to have S > 0.35 and the maximum S can be observed to decline slightly with increasing volume. Aspect Ratio (AR) vs. Sphericity (S) scatter plot, represented by blue points, showed a concentration of points in the high AR-high S corner which suggests a good overall powder morphology. Also judging by the concentration of points, a small decrease in S is related to a relatively larger decrease and dispersion in AR of particles. Close to S = 1, most particles showed AR > 0.55. Only a 10% decrease in S (S = 0.9) results in AR of several particles falling below 0.3.

The approach for creating the visual database involved dividing the considered volume into 27 smaller groups of particles or minor volumes by defining three ranges (representing low, medium and high) of values for each shape parameter. In other words, the 3D plot shown in Figure 5.19 was discretized into 27 cuboids that represent all possible cases as the three

parameters vary across the defined low, medium and high range of values. High resolution picture (s) of representative particles in 3D, as rendered by *Avizo*, were captured for each of these cuboids. Once the desirable cuboids were selected (based on the representative pictures), the limits set by the walls of the cuboids, i.e. the corresponding shape parameter values, were used to filter the ideal particles. The number, position and size of the cuboids depend on the assigned ranges of values for each parameter, which were done manually based on the observed distribution of particles and key morphological differences between them. The cuboids had enough particles to be representative and were placed far enough from each other to show significant differences. The use of more than three ranges of values for each parameter will increase the number of cuboids, thus creating a larger and more accurate database. But, it will also increase the computational cost and time. For quantifying the morphological differences observed in our gas atomised powders which are largely spherical and smooth, dividing each parameter into three ranges of values was sufficient.

To begin the discretization (of 3D plot in Figure 5.19), the considered XCT volume was divided into three sub-volumes based on three ranges of values for Volume3d: *Low-volume particles* with Volume3d ≤ 25000 μm^3 (Eq. diameter ≤ 36.3 µm), *Medium-volume particles* with 50000 μm^3 ≤ Volume3d ≤ 100000 μm^3 (45.7 µm ≤ Eq. diameter ≤ 57.6 µm) and *High-volume particles* with Volume3d ≥ 125000 μm^3 (Eq. diameter ≥ 62 µm). Each sub-volume or group of particles was again divided into three sub-groups based on three ranges of values observed for the second parameter, Sphericity (S). Finally, for particles falling in each range of S, three ranges of AR values are identified using the AR vs. S scatter plot creating three further divisions. Therefore, all 9 possible combinations are considered as the two parameters S and AR vary through low, medium and high range of values in a particular sub-volume. We get 27 combinations in total for all three sub-volumes and each combination represents a cuboid in the 3D plot.

Table 5.1 shows important quantitative information regarding each of these sub-volumes created on the basis of parameter Volume3d.

Table 5.1: Important characteristics of three sub-volumes defined on the basis of Volume3d

Sub-volume	**Number % of particles (volume %)**	**Mean Eq. diameter (µm) (min, max)**	**Mean Sphericity (min, max)**	**Mean Aspect Ratio (min, max)**
Low volume particles (Volume3d ≤ 25000 μm^3)	72.1 (25.2)	23.8 ± 5.9 (9.0, 36.3)	0.93 ± 0.06 (0.48, 0.99)	0.72 ± 0.22 (0.02, 0.99)
Medium volume particles (50000 μm^3 ≤ Volume3d ≤ 100000 μm^3)	10.4 (31.0)	51.2 ± 3.4 (45.7, 57.6)	0.90 ± 0.07 (0.44,0.99)	0.79 ± 0.16 (0.07, 0.99)
High volume particles (Volume3d ≥ 125000 μm^3)	2.0 (11.5)	64.2 ± 1.8 (62.0, 75.5)	0.88 ± 0.07 (0.56, 0.98)	0.76 ± 0.19 (0.11,0.98)

The low volume category contained the largest number of particles, while the medium volume particles represented the maximum volume %. In ascending order, the mean equivalent diameters for the three volume-based categories lied roughly around the D_{10}, D_{50} and D_{90} values of the powder sample (AMA2), as presented in section 5.3. As per the standard deviation values, the low volume particles showed the highest dispersion in size. The mean sphericities lied around 0.9 for all categories with low deviations. Comparatively, the mean aspect ratios showed more deviations and lied between 0.7 to 0.8. The volume limits were chosen such that they are round figures and the medium volume category covers most of particles of sizes around the D_{50} value. The other two categories were simply placed at the lower/higher ends of the scale and equally far from this category with respect to volume. In the following sections, particle morphologies observed in each of three categories or sub-volumes are evaluated.

5.4.1 3D morphology analysis: Low volume particles

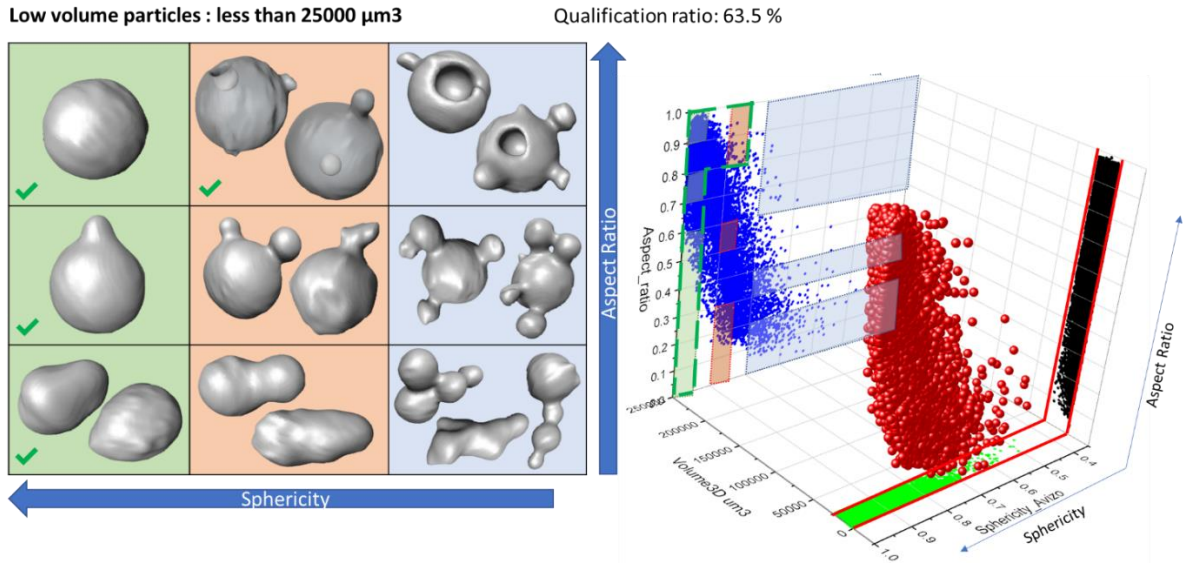

Figure 5.20: Visual database of particle morphologies as a 3 × 3 matrix representing high, low and medium ranges of Sphericity (S)(along columns) and Aspect Ratio (AR)(along rows) for the sub-volume 'Low volume particles (Volume3d ≤ 25000 µm^3)'. Matrix elements are colour-coded with respect to marked rectangles on the AR vs. S projection (with blue points) of the respective 3D scatter plot shown on the right. Selected 'ideal' morphologies are marked by green ticks on the image matrix. Identified limits of AR-S parameters for 'ideal' morphology are marked by a polygon of dashed thick green lines on the AR vs. S projection.

Figure 5.20 shows the visual database of particle morphologies along with a 3D plot for the `low volume particles´. As mentioned earlier, each of three sub-volumes was discretized into 9 cuboids based on ranges of Sphericity (S) and Aspect Ratio (AR). For the sake of simplicity, the figure only shows the 2D projections of these cuboids as rectangles on the AR vs. S projection plane of the 3D plot. All particles falling within the limits set for the Volume3d parameter are shown as red spheres. The volume limits are marked by thick red lines on the

other 2D projection planes of the plot and actually represent the thickness for our cuboids (i.e. the third dimension for the marked rectangles). The visual database is presented as a 3 × 3 matrix representing 3D morphologies of particles falling inside each of the 9 cuboids. The matrix columns are colour coded with respect to rectangles on the AR vs. S scatter plot marking ranges of low to high S from the right (blue) to the left (green) column respectively. Meanwhile, the AR values increase along the matrix rows from bottom to top.

As mentioned previously, Sphericity (S) is related to porosity and superficial features, while Aspect ratio (AR) quantifies the overall shape of a particle. The top left corner of the visual database corresponding to (high S ≥ 0.95, high AR ≥ 0.9) combination presented the almost perfect sphere shape with a very smooth surface. In the same column, a medium AR (0.7 – 0.8) was associated with one small protrusion or elongation on the smooth surface of this almost spherical shape. For low AR (≤ 0.6), these elongations became more profound resulting in teardrop shaped particles with smooth surfaces. As we move to the second column representing medium S (0.85 – 0.9), we observed up to two satellites and small open/closed porosities in the high AR (≥ 0.8) particles. Their shapes are still quite spherical. As we approach medium AR (0.5 – 0.6) values, satellites or superficial protrusions became larger. At low AR (≤ 0.3), elongated ellipsoids and fusion between two particles of comparable sizes are observed. In the last column with low S (≤ 0.8), we observed a worse version of the middle column. Bigger porosities and up to three satellites in the top row (high AR ≥ 0.6). The middle row or medium AR (0.3 – 0.4) particles show more prominent and up to 4 satellites. In the last row with low AR (≤ 0.2) and low S (≤ 0.8), we observed very elongated particles indicating fusion of more than 3 particles of comparable sizes. At low volumes, errors in watershed separation are more likely to occur due to insufficient grayscale resolution, which was mentioned earlier in section 5.1.4. This means some separate particles might get classified as one fused particle. Therefore, only particles larger than 1000 voxels (equivalent diameter 8.9 µm) were considered for all analysis and the pictures shown are reliable representation of the sufficiently large number of particles lying within this cuboid that were checked for morphology.

Looking at this visual database for low volume particles, it can be said that particles represented in the first green column (high S, all AR) and first row of the second red column (i.e. medium S, high AR) would be desirable morphologies for us. They are quite spherical with smooth surfaces and contain minimum surface protrusions and porosities. A small green tick is placed in the bottom left corner of each accepted morphology in the matrix. However, the user of the database can choose to be stricter and select fewer morphologies from the matrix depending on the required powder specifications.

The next step is to identify the limiting shape parameters using accepted morphologies from the database. In this case, the limits are (S ≥ 0.95, AR ≤ 1) and (0.85 ≤ S ≤ 0.95, AR ≥ 0.8). All particles falling within the limits of these shape parameters were classified as ‘ideal’ particles. These values were derived directly by merging together rectangles marked on the AR vs. S projection plane in Figure 5.20, that correspond to the accepted morphologies. The limits

represent boundaries of the polygon thus created which is shown by dashed thick green lines on the projection plane. It also covers the particles lying in the gaps between the accepted rectangles (that were manually assigned for the purpose of discretization of the data as explained earlier). The qualification ratio, i.e. the number percent of ideal particles among all analysed particles in this volume range was 63.5 %. This is fairly good number and means majority of particles qualified based on morphology. They showed an average Sphericity of 0.97 ± 0.01 and Aspect Ratio of 0.85 ± 0.07.

5.4.2 3D morphology analysis: Medium volume particles

Figure 5.21 shows the visual database of particle morphologies along with a 3D plot for the medium volume particles in the same format as low volume particles in the previous section. All particles falling within the Volume3d parameter limits are shown as red spheres. The 2D projections of the 9 discretized cuboids are shown as rectangles on the AR vs. S projection plane of the 3D plot. They are colour-coded with respect to the 3 × 3 matrix, as in the previous section, that forms the visual database of representative morphologies.

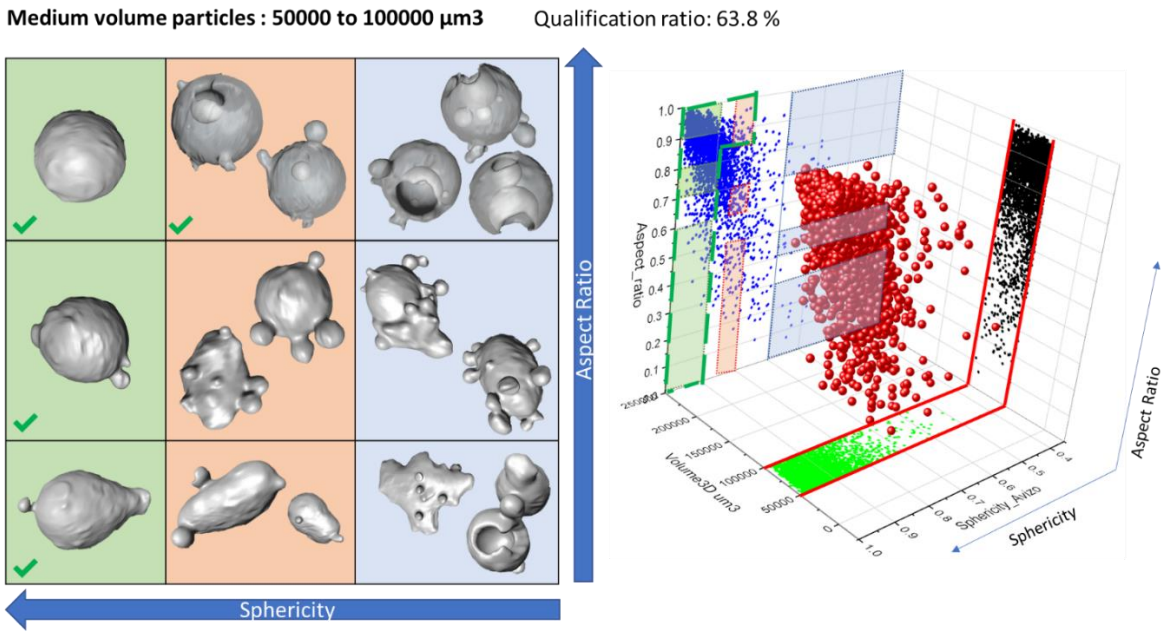

Figure 5.21: Visual database of particle morphologies as a 3 × 3 matrix representing high, low and medium ranges of Sphericity (S)(along columns) and Aspect Ratio (AR)(along rows) for the sub-volume 'Medium volume particles (50000 µm^3 ≤ Volume3d ≤ 100000 µm^3)'. Matrix elements are colour-coded with respect to marked rectangles on the AR vs. S projection (with blue points) of the respective 3D scatter plot shown on the right. Selected 'ideal' morphologies are marked by green ticks on the image matrix. Identified limits of AR-S

parameters for ‘ideal’ morphology are marked by a polygon of dashed thick green lines on the AR vs. S projection.

The top left corner of the visual matrix representing high S (≥ 0.9) and high AR (≥ 0.9) consists of spherical particles with no satellites. The particle surfaces for all morphologies, in general, seem rougher than the low volume particles discussed in previous section. This was also reflected in Table 5.1 as slightly lower average Sphericity (0.9 ± 0.07) for this volume range as compared to low-volume (0.93 ± 0.06) powders.

In the high Sphericity range, medium AR (0.7 – 0.8) leads to quite spherical particles with a prominent satellite and up to 3 satellites in total. Low AR (≤ 0.6) shows more elongated tear-drop shaped particles and prominent satellite as well. As we move to the red column representing medium Sphericity (0.8 – 0.85), high AR (≥ 0.85) particles show spherical morphology with open/closed porosity and up to 3 satellites. Particles start getting elongated and satellites become more prominent in the medium AR range. Several satellites (around 5) on rough particle surfaces were observed. For low AR (≤ 0.5) values in the medium S range, ellipsoidal elongated particles and fusion between particles of comparable sizes were seen, very much like in low volume particles. Additionally, these medium volume particles also featured up to 3 satellites on their relatively rougher surface. In the next blue column featuring low Sphericity (≤ 0.7), the high AR (≥ 0.7) particles show much larger and multiple open/closed pores as compared to their medium sphericity counterparts on the left while still showing an overall spherical shape. The drop in sphericity is mainly caused by porosity for high AR particles. As we move towards medium AR (0.4 – 0.5) and low S particles, unique ‘splat cap’ and elongated morphologies with several satellites on rough surfaces are observed. Particles with low AR (≤ 0.3) exhibited irregular shapes, as well as fused particles which were broken and/or with large porosities. The morphologies for medium and low AR particles listed in the blue ‘low S’ column were not observed in case of low volume particles, thus indicating an effect of particle volume on morphology.

Based on the discussed characteristics, all high sphericity particles and medium sphericity particles with high AR were classified as ‘ideal’. These are represented in the green column and first row of the red column in the visual database along with small green ticks next to the pictures. The limiting shape parameters identified using these morphologies are (S ≥ 0.9, AR ≤ 1) and (0.8 ≤ S ≤ 0.9, AR ≥ 0.85). The polygon demarcating these limits is shown in Figure 5.21 by dashed thick green lines on the AR vs. S projection plane. The clustering of blue points in this region suggests a majority of powder particles being desirable. The qualification ratio was 63.8 % for this volume range of particles. The qualified ‘ideal’ particles showed average Sphericity of 0.94 ± 0.03 and average AR of 0.86 ± 0.09.

5.4.3 3D morphology analysis: High volume particles

Figure 5.22 shows the visual database of particle morphologies along with a 3D plot for the high volume particles in the same format as low and medium volume particles in previous sections. All particles falling within the Volume3d parameter limits are shown as red spheres. Since only 2 % of the particles in the analysed volume fall in this volume range (see Table 5.1), it can be noticed that this 3D plot features the least number of points out of all three. The 2D projections of the 9 discretized cuboids are shown as rectangles on the AR vs. S projection plane of the 3D plot. They are colour-coded with respect to the 3 × 3 matrix, as in the previous sections, that forms the visual database of representative morphologies.

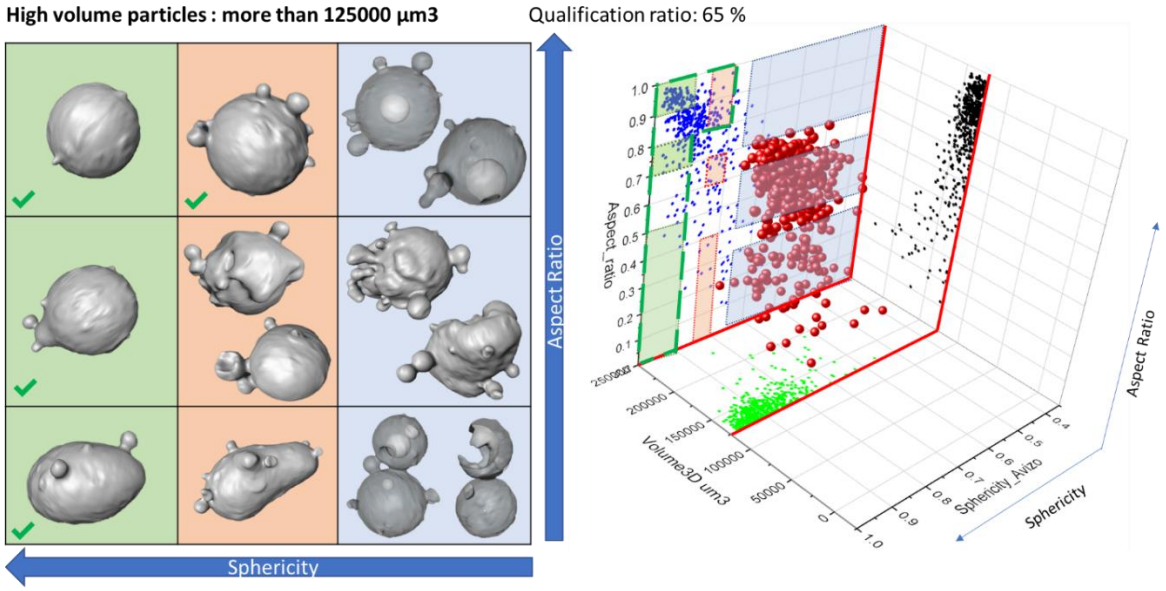

Figure 5.22: Visual database of particle morphologies as a 3 × 3 matrix representing high, low and medium ranges of Sphericity (S)(along columns) and Aspect Ratio (AR)(along rows) for the sub-volume 'High volume particles (Volume3d ≥ 125000 µm^3)'. Matrix elements are colour-coded with respect to marked rectangles on the AR vs. S projection (with blue points) of the respective 3D scatter plot shown on the right. Selected 'ideal' morphologies are marked by green ticks on the image matrix. Identified limits of AR-S parameters for 'ideal' morphology are marked by a polygon of dashed thick green lines on the AR vs. S projection.

High volume particles of all morphologies featured rough surfaces, similar to that of medium volume particles. As per Table 5.1, they showed lower average sphericity (0.88 ± 0.07) than medium (0.9 ± 0.07) and low (0.93 ± 0.06) volume particles. Even the most spherical particles lying in the top left corner of the matrix, representing high Sphericity (≥ 0.9) and high AR (≥ 0.9) values, featured two to three small satellites on their rough surfaces. As we move down to medium AR (0.7 – 0.8) values in the same column, we observed the same surface roughness on a largely spherical shape that also showed one significant protrusion and up to two prominent/major satellites. Further moving down to low AR (≤ 0.5) values, the protrusion became more profound resulting in oblong particles with up to two prominent satellites and a rough surface. In the red column of morphologies with medium S (0.8 – 0.85), the high AR

particles possessed quite a spherical shape and rough surfaces with up to 5 satellites. For medium AR (0.8 – 0.85), the visual matrix shows particles with splat caps and multiple satellites. It also shows quite spherical particles, with satellites, that were fused with other broken smaller particles. At low AR (≤ 0.4), the morphology became very elongated with multiple satellites. As the sphericity decreases to low (≤ 0.75) range values, represented in the rightmost blue column of the visual database, we observed open/closed pores in the high volume particles when they exhibited high AR (≥ 0.7). Their shapes were quite spherical with up to 5 satellites on rough surfaces, similar to morphology of medium S and high AR particles (same row, previous column). In the medium AR (0.4 – 0.6) category, we see splat caps (similar to the previous column again, but with more satellites) and agglomerated particle morphology. They exhibited multiple satellites and fused smaller particles resembling agglomeration. Further, low AR (≤ 0.3) was characterised by two fused spherical particles of similar sizes exhibiting large open/closed porosities and up to 4 satellites.

Based on the discussed characteristics, all high sphericity particles and medium sphericity particles with high AR were classified as 'ideal'. These are represented in the green column and first row of the red column in the visual database along with small green ticks next to the pictures. It should be noted that there was no porosity at all in the qualified high volume particles, unlike the low and medium volume cases (see Figure 5.20 and Figure 5.21) where medium sphericity range particles exhibited some pores.

The limiting shape parameters identified using these morphologies are (S ≥ 0.9, AR ≤ 1) and (0.8 ≤ S ≤ 0.9, AR ≥ 0.8). The polygon demarcating these limits is shown in Figure 5.22 by dashed thick green lines on the AR vs. S projection plane. It is noticeable from the clustering of blue points that majority of particles fall within these limits. The qualification ratio was 65 % for this volume range of powder. The qualified 'ideal' particles showed average Sphericity of 0.91 ± 0.04 and average AR of 0.86 ± 0.09. Section 5.4.4 summarises and compares the characteristics of qualified powder particles across all three sub-volumes.

5.4.4 3D morphology analysis: summary

Comparing the morphology in all three volume ranges (as reported in Figure 5.20, Figure 5.21 and Figure 5.22), it can be said that particle surfaces were the smoothest for low volumes or sizes. This is also reflected as highest average sphericity in Table 5.1 among all sub-volumes. Particle morphology in the green high sphericity column was not very different for the three cases, except that particle surfaces became rough at medium/high volumes and exhibited more satellites. In low and medium volume powders, porosity showed more variation in size and was present in particles featuring a wider range of S and AR values. Some 'medium S - high AR' category particles containing small open/closed pores in these volumes were qualified as 'ideal' particles. But, porosity was not observed at all in 'ideal' high volume particles and showed up only in particles of 'low sphericity' (S ≤ 0.75) category. Also, the pores observed were quite significant in size relative to the particles, thus contributing to the overall

low sphericity value. This means that the porosity observed at higher volumes is usually larger and found in fewer particles as compared to medium or low volume powders.

Table 5.2 summarises the characteristics of all particles classified as 'ideal' for the three sub-volumes.

Table 5.2: Important morphological characteristics of classified 'ideal' powder particles in the three sub-volumes

For 'ideal' morphologies	Qualification Ratio (%) (volume %)	Mean Eq. diameter (µm) (min, max)	Mean Sphericity (min, max)	Mean Aspect Ratio (min, max)
Low volume particles (Volume3d $\leq$ 25000 µm^3)	63.5 (58.6)	23.1 ± 5.9 (9.0, 36.3)	0.97 ± 0.01 (0.85,1)	0.85 ± 0.07 (0.38, 0.99)
Medium volume particles (50000 µm^3 $\leq$ Volume3d $\leq$ 100000 µm^3)	63.8 (63.5)	51.1 ± 3.4 (45.7, 57.6)	0.94 ± 0.03 (0.8, 0.99)	0.86 ± 0.09 (0.3, 0.99)
High volume particles (Volume3d $\geq$ 125000 µm^3)	65.0 (63.8)	63.7 ± 1.2 (62.0, 69.9)	0.91 ± 0.04 (0.8, 0.98)	0.86 ± 0.09 (0.4, 0.98)

The qualification ratios (number %) were very similar and fairly high across all volumes, i.e. 63.5 to 65 %. Thus, there was no significant effect of volume on qualification ratio. The mean sizes or equivalent diameters of the 'ideal' particles were very similar to the mean sizes of all particles in the respective sub-volumes (shown in Table 5.1). This indicates a very uniform distribution of 'ideal' or desirable morphologies across all sizes in the sub-volumes.

In all volume ranges, the desirable particle morphologies represent high mean Sphericities ($\geq$ 0.91) and AR ($\approx$ 0.85) with very low standard deviations. The mean sphericity decreased very slightly with increasing volume, which was visible as increased surface roughness and satellites. The mean AR of 'ideal' particles remained relatively constant across the volumes. The minimum and maximum recorded values indicate that AR of selected particles varied between 0.3 and 0.99, while their sphericity values lied between 0.8 and 1.

Further, there is also a noticeable effect of volume on morphology of the disqualified particles, i.e. those that were deemed undesirable. Irregularly shaped particles were observed exclusively in the medium volume range. Splat caps were observed only in medium and high volume powders. They also featured a relatively wider range of S and AR values at high volume. Low volume powders did not show any splat caps, but featured very elongated particles as a result of fusion between similar sized particles.

5.4.5 3D morphology analysis: atomisation methods

The 3D morphology analysis methodology described for AMA2 powder in the previous sections successfully identified the 'ideal' or desirable shape parameter values that can used to assess morphology of any powder in principle. The volume parameter limits that control the size and position of the analysed sub-volumes may have to be modified to properly represent the powder's size distribution. However, this should not have a significant effect on the measured qualification ratio, if the powder has a majority of 'ideal' particles and they are distributed uniformly across all sizes. This was the case for the analysed AMA2 powder and is an indicator of good powder quality. Evaluations of two other powder samples, namely CFA and CGA, were made by using the same limiting shape parameters that were determined for AMA2 in the discussed methodology. These are Ti-rich compositions that were produced by two different methods, i.e., Crucible-Free Atomisation (CFA) and Crucible-based Gas Atomisation (CGA). Table 5.3 summarises and compares the important morphological results determined by this methodology for all three powders that were produced by three different atomisation methods.

Table 5.3: Important morphological characteristics of classified 'ideal' particles in three powders (sieved 20 – 63 µm) produced by different atomisation methods (shown across three volume ranges defined by Volume3d parameter)

Powder	**AMA2 (Arc-Melting Atomisation)**			**CFA (Crucible-Free Atomisation)**			**CGA (Crucible-based Gas Atomisation)**		
Volume range	*Qualification ratio (%)*	*Mean S of ideal particles (min, max)*	*Mean AR of ideal particles (min, max)*	*Qualification ratio (%)*	*Mean S of ideal particles (min, max)*	*Mean AR of ideal particles (min, max)*	*Qualification ratio (%)*	*Mean S of ideal particles (min, max)*	*Mean AR of ideal particles (min, max)*
Low volume Volume3d ≤ 25000 µm³	63.5	0.97 ± 0.01 (0.85, 1.00)	0.85 ± 0.07 (0.38, 0.99)	64.6	0.96 ± 0.01 (0.86, 0.99)	0.85 ± 0.07 (0.44, 0.98)	16.4	0.94 ± 0.02 (0.85, 0.98)	0.85 ± 0.05 (0.57, 0.98)
Medium volume 50000 µm³ ≤ Volume3d ≤ 100000 µm³	63.8	0.94 ± 0.03 (0.80, 0.99)	0.86 ± 0.09 (0.30, 0.99)	63.1	0.95 ± 0.02 (0.83, 0.98)	0.80 ± 0.13 (0.24, 0.98)	10.0	0.92 ± 0.02 (0.83, 0.97)	0.79 ± 0.11 (0.41, 0.97)
High volume Volume3d ≥ 125000 µm³	65.0	0.91 ± 0.04 (0.80, 0.98)	0.86 ± 0.09 (0.40, 0.98)	52.5	0.93 ± 0.03 (0.82, 0.97)	0.79 ± 0.13 (0.35, 0.97)	5.4	0.90 ± 0.03 (0.86, 0.93)	0.81 ± 0.15 (0.54, 0.92)

CFA powder showed very similar qualification ratios to the reference powder AMA2 in the low and medium volume range. It was ≈ 10 % lower in the high volume range. The D_{90} value of CFA powder volume as determined by XCT was higher than that of AMA2, as discussed in section 5.3. This means it had a relatively larger fraction of particles falling in the high volume range, but only 52.5 % of them qualified as 'ideal' particles. The mean AR of qualified particles can be seen to have dropped slightly in the medium and high volume range of CFA powder. However, the mean sphericities were at par with AMA2 powder particles in all volume ranges. Overall, CFA produced a good quality powder morphology, that slightly deteriorated at high volumes.

On the other hand, CGA powder performed quite poorly showing the lowest qualification ratios of all powders in every volume range. Further, there was significant effect of volume and qualification ratios halved while moving to the next higher volume range. Only 16.4 % of particles showed 'ideal' morphology in the low volume range, which reduced to just 5.4 % at high volumes. Clearly, CGA produced better powder morphology at smaller powder volumes or sizes and morphologies deteriorated significantly as powder size increases. The qualified particles showed mean Sphericities and AR similar to that of CFA powder. However, the extremely low qualification ratios in all volume ranges meant overall very poor morphological quality. This was observed qualitatively in the 3D scatter plot (between Sphericity (S), Aspect Ratio (AR) and Volume3d parameters determined by *Avizo*) of the CGA powder sample. Figure 5.23 shows the 3D scatter plot for an analysed volume of 962 × 781 × 1919 voxels (resolution 1 voxel = 0.77^3 µm^3) belonging to CGA powder (sieved 20 – 63 µm). It shows the data for 18,352 particles represented by the red spheres.

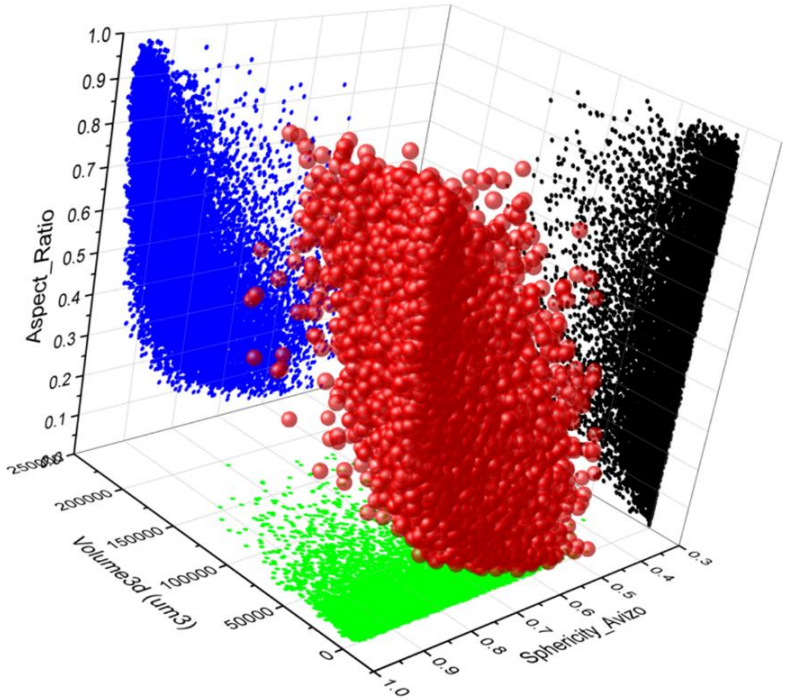

Figure 5.23: 3D scatter plot between Sphericity (S), Aspect Ratio (AR) and Volume3d parameters returned by Avizo for a volume of 962 × 781 × 1919 voxels (resolution 1 voxel =

0.77^3 µm^3) belonging to CGA powder (sieved 20 – 63 µm). 2D projections are also shown on the respective planes.

A comparison with the respective plot of the reference powder AMA2 in Figure 5.19 reveals significant differences in the distribution of chosen 3D shape parameters. As seen in the AR vs. S projection plane, only a small percentage of particles (represented by blue points) appeared to lie in the typical 'high S' or 'medium S-high AR' regions which are associated with 'ideal' morphologies. Unlike AMA2, the blue points were not clustered around the top left corner of 'high AR-high S' values. Instead, points were mostly distributed across the so called medium and low ranges of AR and S values. Further, both laser diffraction and XCT analysis concluded in section 5.3 that CGA powder has a PSD different from AMA2 and consists of smaller particles on average. A redefining of our Volume3d-based sub-volumes (to better represent the PSD) might show some improvement in the quantified results. However, the AR vs. S scatter plot clearly points towards qualification ratios much lower than the reference powder AMA2 and an overall poor morphology.

This factor further contributed to the inferior physical properties of CGA powder. As discussed in section 4.1.1 of chapter 4, CGA showed the highest Hall flowtimes and internal porosity among all powders. It also showed the lowest densities among all $Ti_{66}Fe_{27}Nb_3Sn_4$ powders. High fraction of small particles, bad morphology and high porosity explain the low densities and high flowtimes of this powder.

AMA2 powder, whose morphology was overall good and uniform across all volume ranges, was successfully used for SLM of $Ti_{73.5}Fe_{23}Nb_{1.5}Sn_2$ alloy. The characterisation results of this SLM-built material are discussed in the next chapter.

Hence, this simplistic 3D morphology model based on three parameters (S, AR and Volume3d) could successfully characterise shapes of AMA2 powder and evaluate morphological quality of powders produced by other atomisation methods. Since the limits for desirable or 'ideal' morphology were set by the user, creating an independent visual database for each powder sample would provide more freedom of choice on limiting parameters and classification. This would demand more time and effort, but can be automated via computational tools/algorithms and in turn, would provide more realistic qualification ratios for powder samples depending on their applications.

This ends the chapter on the current status of the developed image analysis methodology intended for advanced characterisation of powders using XCT data. The next section summarises the important conclusions and comments.

5.5 Partial conclusions

i. A methodology was successfully developed for advanced image analysis of powder XCT data. In a novel approach, trainable machine learning-based tool WEKA of *Fiji* was used in combination with 3D watershed separation tools of *Avizo* for accurate segmentation and separation of powder particles measured by XCT. The end results provided reliable and comprehensive set of information for characterisation of powder volumes, shapes and their respective internal pores.

ii. The role of the important watershed parameter 'contrast value or marker extent' in employing the methodology was determined. An analytical approach was provided followed by visual cues for choosing the right parameter value for treating a given volume.

iii. The voxel-based volume measurements obtained for individual particles as a result of this methodology were used to plot volume-based size distributions of several powder samples. Although conventional laser diffraction has a statistical advantage over XCT analysis, the latter provides reliable results while addressing the assumptions and shortcomings of Mie theory. It makes more accurate estimates considering shapes/porosities of individual particles, without requiring optical information. Further, the methodology is not limited to measuring volume/size.

iv. Among studied Ti-rich powders (CFA, CGA and AMA2), conventional laser diffraction revealed normal gaussian distributions of volume-based particle sizes, while XCT analysis methodology showed skewed gaussian distributions for two powders. However, both methods revealed CGA to have the smallest particle sizes on average. Laser diffraction data also indicated AMA2 to have the largest particles on average.

v. A simplistic model was introduced that quantified the shape distribution of particles based on three parameters: Sphericity (S), Aspect ratio (AR) and Volume3d determined by the proposed XCT image analysis methodology. Three ranges (namely high, medium and low) of each parameter were defined in a reference powder volume of AMA2 and representative morphologies were mapped to all 27 combinations to create a visual database. The user was allowed to choose 'ideal' morphologies among them and thus calculate the powder's qualification ratio, i.e., the number percent of 'ideal' particles.

vi. High Sphericity is linked to low surface roughness, low satellite density and low porosity of powders, whereas high AR is linked to an overall spherical shape. Further,

volume also has effects on overall surface roughness, porosity and shape distributions (especially how particles fuse or break to form morphologies that were considered undesirable) that were discussed. The morphologies classified as 'ideal' in all volume ranges belonged to 'High Sphericity-all AR' and 'Medium Sphericity-High AR' category.

vii. AMA2 powder showed high qualification ratios of 63.5 to 65 % with 'ideal' particles distributed uniformly across all volumes/sizes. Evaluation of similar powder compositions produced by CFA and CGA was performed using the limiting 'ideal' shape parameters defined by this reference powder. CGA showed extremely low qualification ratios (5.4 to 16.4 %) that decreased with increasing particle size/volume. CFA showed high qualification ratios similar to that of AMA2 across most sizes, but with a decline of ≈ 10 % for high volume particles (Volume3d ≥ 125000 μm^3 or Equivalent diameter ≥ 62 µm).

REFERENCES

[1] T. Ferreira and W. Rasband, “ImageJ User Guide ImageJ User Guide IJ 1.46r,” 2012, Accessed: May 29, 2023. [Online]. Available: http://fiji.sc/guide.git.

[2] M. Hall, E. Frank, G. Holmes, B. Pfahringer, P. Reutemann, and I. H. Witten, “The WEKA data mining software,” *ACM SIGKDD Explor. Newsl.*, vol. 11, no. 1, pp. 10–18, Nov. 2009, doi: 10.1145/1656274.1656278.

[3] B. Münch, P. Gasser, L. Holzer, and R. Flatt, “FIB-nanotomography of particulate systems - Part II: Particle recognition and effect of boundary truncation,” *J. Am. Ceram. Soc.*, vol. 89, no. 8, pp. 2586–2595, 2006, doi: 10.1111/j.1551-2916.2006.01121.x.

[4] T. Thiede, T. Mishurova, S. Evsevleev, I. Serrano-Munoz, C. Gollwitzer, and G. Bruno, “3D Shape Analysis of Powder for Laser Beam Melting By Synchrotron X-Ray Ct,” *Quantum Beam Sci.*, vol. 3, no. 1, 2019, doi: 10.3390/qubs3010003.

[5] X. Zhou, N. Dai, X. Cheng, A. Thompson, and R. Leach, “Three-dimensional characterization of powder particles using X-ray computed tomography,” *Addit. Manuf.*, vol. 40, Apr. 2021, doi: 10.1016/J.ADDMA.2021.101913.

[6] B. Preim and C. Botha, “Image Analysis for Medical Visualization,” *Vis. Comput. Med.*, pp. 111–175, 2014, doi: 10.1016/B978-0-12-415873-3.00004-3.

[7] R. Romero-Zaliz and J. F. Reinoso-Gordo, “An Updated Review on Watershed Algorithms,” 2018, doi: 10.1007/978-3-319-62359-7_12.

[8] J. Rogowska, “Overview and Fundamentals of Medical Image Segmentation,” *Handb. Med. Imaging*, pp. 69–85, Jan. 2000, doi: 10.1016/B978-012077790-7/50009-6.

[9] B. Preim and C. Botha, “Visual computing for medicine : theory, algorithms, and applications”, Accessed: Mar. 27, 2023. [Online]. Available: https://www.oreilly.com/library/view/visual-computing-for/9780124158733/

[10] “Thermo Scientific TM Avizo TM Software 9 User’s Guide,” 1995.

[11] R. C. Gonzalez, R. E. Woods, and B. R. Masters, “Digital Image Processing, Third Edition,” *J. Biomed. Opt.*, vol. 14, no. 2, p. 029901, 2009, Accessed: Mar. 27, 2023. [Online]. Available: https://www.academia.edu/67778643/Digital_Image_Processing_Third_Edition

[12] M. A. Butt and P. Maragos, “Optimum design of chamfer distance transforms,” *IEEE Trans. Image Process.*, vol. 7, no. 10, pp. 1477–1484, 1998.

Chapter 6

Characterisation of AM-built alloys

6 Characterisation of AM-built alloys

This chapter presents the results and discussions concerning characterisation of alloys built by laser-based AM of pre-alloyed powders. As concluded in chapter 4, CFA-FeTi (target composition $Fe_{82.4}Ti_{17.6}$) and AMA2 (target composition $Ti_{73.5}Fe_{23}Nb_{1.5}Sn_2$) powders were selected for LMD and SLM processing respectively. The chapter is divided into two main sections, one for each alloy produced: LMD-built $Fe_{82.4}Ti_{17.6}$ and SLM-built $Ti_{73.5}Fe_{23}Nb_{1.5}Sn_{2.}$ Each section starts with microstructural characterisation results of the produced alloy followed by mechanical characterisation results of extracted specimens. Mechanical characterisation covers quasi-static compression and tension tests conducted at various temperatures (up to 600 °C) in air. In case of LMD-built $Fe_{82.4}Ti_{17.6}$, an additional subsection is presented discussing the micro-mechanical characterisation of alloy microstructure (using nanoindentation and micro-pillar compression), while further comparing the results to the microstructures produced by Field Assisted Hot Pressing (FAHP) of the same CFA-FeTi powder.

6.1 LMD-built $Fe_{82.4}Ti_{17.6}$

Figure 6.1 shows the typical microstructure observed in the cross-section (build direction is vertical in plane of figure) of as-built $Fe_{82.4}Ti_{17.6}$ alloy using LMD of pre-alloyed CFA-FeTi powders.

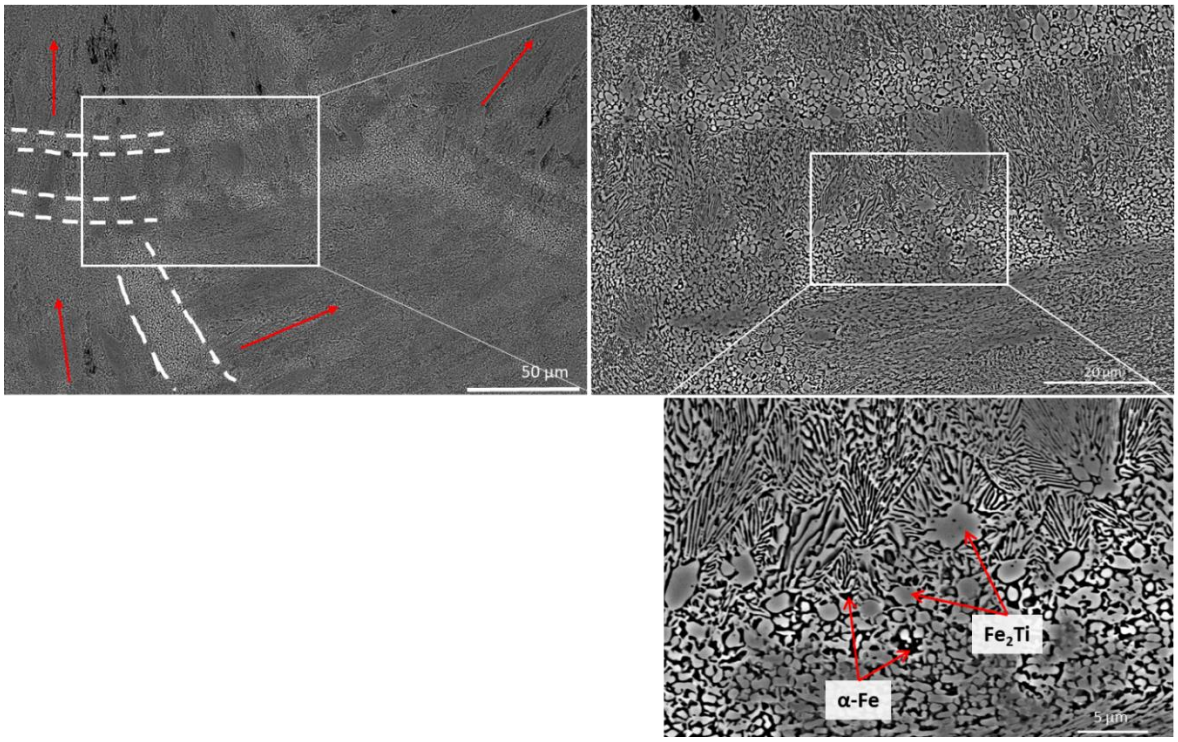

Figure 6.1: SEM micrographs showing typical microstructure observed in LMD-fabricated $Fe_{82.4}Ti_{17.6}$ sample which was polished and etched (build direction is vertical in plane of figure)

Different layers can be identified consisting of ultrafine lamellar or irregular lamellar eutectic (α-Fe + Fe_2Ti), with a globular morphology at the inter-layers (marked by dashed white lines). An average inter-lamellar spacing λ of 206 ± 51 nm and inter-layer thickness of 12.2 ± 0.8 µm were obtained. It is similar to the microstructures observed in DED-fabricated $Fe_{82.4}Ti_{17.6}$ alloy using elemental powders, as reported by our collaborators Requena et al. [1] (see Figure 1.18 in section 1.2.6 of chapter 1). They had obtained similar results for λ and inter-layer boundary thickness, ranging 190 ± 25 nm and 12 ± 5 µm respectively.

The inter-layer region solidifies from the bottom layer of the melt pool during melting and experiences the highest undercooling and nucleation rates. This results in a globular morphology with primary Fe_2Ti phase surrounded by α-Fe layers, as shown in the simulation outcomes reported by Requena et al. [1] (see Figure 1.19 in section 1.2.6 of chapter 1), as well as the microstructures observed in fine powders of $Fe_{82.4}Ti_{17.6}$ (Figure 4.29 of section 4.2.2 in chapter 4). The inter-layers are shaped like arcs originating from the melt pool shape and the lamellar eutectics grow radially from the inter-layers in a preferred direction (marked by red arrows). This solidification pattern can be explained by the thermal gradients existing around a melt pool and preferential growth happening across the maximum thermal gradient [2].

Also, as shown in the Figure 6.1, often more than one inter-layer existed close to each other surrounded by a thin lamellar eutectic layer. This might be the result of re-melting and recrystallisation occurring during fabrication of successive layers.

The following sections present macro- and micro-mechanical characterisation results of LMD-built $Fe_{82.4}Ti_{17.6}$.

6.1.1 Macro-mechanical characterisation

Figure 6.2 summarises the quasi-static compression behaviour observed for LMD-built $Fe_{82.4}Ti_{17.6}$ when load is applied uniaxially parallel to the build direction on a cylindrical specimen. Figure 6.2(a) shows the representative stress-strain curves obtained at various temperatures (up to 600 °C), while Figure 6.2(b) represents the pre-test specimen and loading conditions (details described in section 3.3.10 of chapter 3) The specimen conditions after testing are shown in Figure 6.2(c-f) for their respective test temperatures.

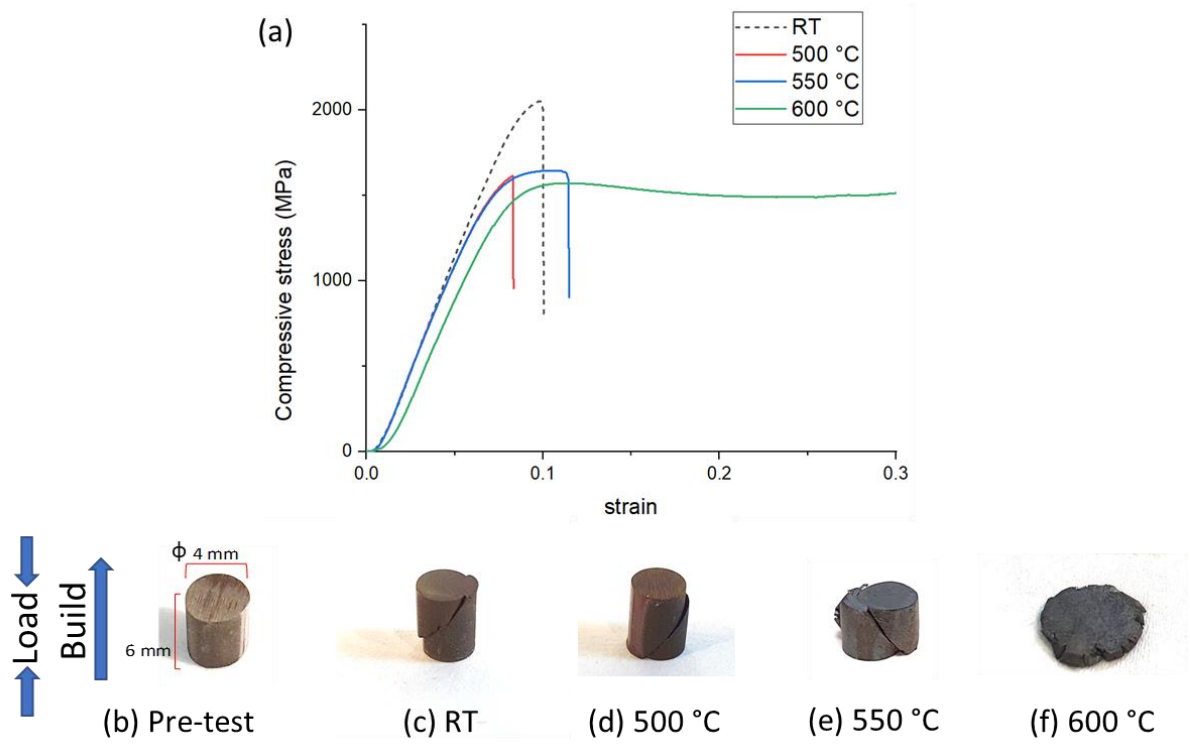

Figure 6.2: (a) Engineering stress vs. engineering strain curves for quasi-static compression tests of LMD-built $Fe_{82.4}Ti_{17.6}$ performed at various temperatures under uniaxial load applied parallel to the build direction, (b) a pre-test specimen showing dimensions and loading direction, (c) specimen conditions after testing at room temperature, (d) 500 °C, (e) 550 °C and (d) 600 °C

The material showed a very high compressive yield strength of ≈ 1800 MPa at room temperature and almost zero plasticity before failing. This kind of brittle behaviour continued until 500 °C with an observed decrease in yield strength with temperature. However, there was an onset of plasticity at 550 °C as deformation up to 15 % was observed in the specimens while demonstrating an average yield strength of 1440 MPa. At 600 °C, the material could be compressed up to 90 % without failure, as shown in Figure 6.2(f). The average yield strength was 1330 MPa at this temperature. All failures until 550 °C occurred as sharp fractures at 45° angle to the loading axis resulting in two pieces, as shown in Figure 6.2(c-e). This indicates brittle fracture caused by dislocation slip under shear. At 600 °C, the specimens underwent quite homogenous bulging, as shown in Figure 6.2(f), with some vertical cracks forming along the cylinder´s curved surface as it was flattened to only 10 % of its height. However, it did not fail or fracture.

Figure 6.3 summarises the alloy´s quasi-static compression behaviour when uniaxial load is applied perpendicular to the build direction. Figure 6.3(a) shows the typical stress-strain curves obtained at various temperatures (up to 600 °C), while Figure 6.3(b) represents the pre-test specimen and loading conditions. The specimen conditions after testing are shown in Figure 6.3(c-e) for their respective test temperatures.

Figure 6.4 shows the evolution of average compressive yield strength with testing temperature for the two uniaxial loading conditions.

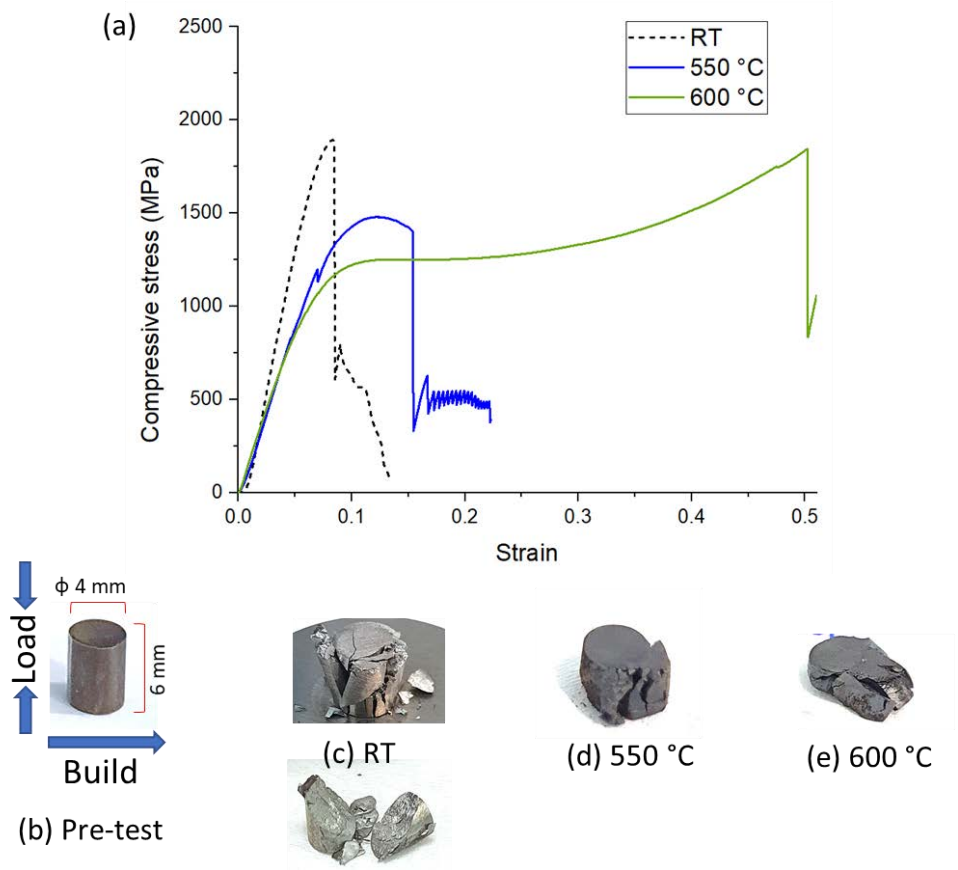

Figure 6.3: (a) Engineering stress vs. engineering strain curves for quasi-static compression tests of LMD-built $Fe_{82.4}Ti_{17.6}$ performed at various temperatures under uniaxial load applied perpendicular to the build direction, (b) a pre-test specimen showing dimensions and loading direction, (c) specimen conditions after testing at room temperature, (d) 550 °C and (e) 600 °C

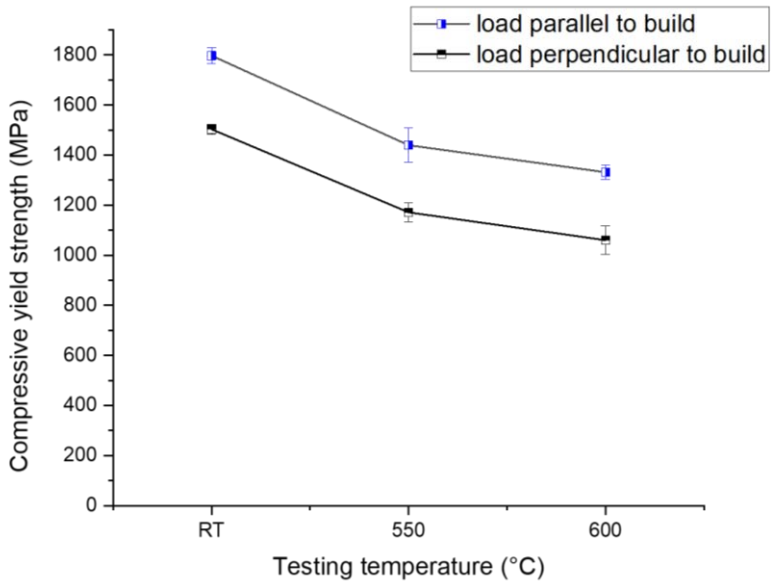

Figure 6.4: Average compressive yield strengths of LMD-built $Fe_{82.4}Ti_{17.6}$ measured at three testing temperatures for loading directions parallel and perpendicular to the build direction

Similar to the case of loading parallel to build direction, the material remained brittle at room temperature until an onset of plasticity was observed at about 550 °C with up to 15 % deformation. However, at 600 °C, the specimens were observed to fail after a deformation of 35 – 50 %. The observed yield strengths were ≈ 20 % lower than the previous loading direction, as represented in Figure 6.4. They remained ≈ 1500 MPa at room temperature and decreased to ≈ 1060 MPa at 600 °C.

Further, the failing of specimens did not occur by a single 45° shearing fracture, but involved breaking of the specimens into more than two pieces via multiple fractures, as shown in Figure 6.3(c-e). This led to relatively rougher stress-strain curves as compared to the previous loading case with more prominent kinks during yielding and fluctuations even after failure as seen in Figure 6.3(a). Figure 6.5 compares the volume rendering of the tomography volumes obtained for fractured specimens tested at room temperature under the two loading directions. When uniaxial loading is perpendicular to the build direction (Figure 6.5(b)), the principal crack (marked by white arrow) can be seen propagating more irregularly across the volume along with several secondary cracks (marked by red arrows) spreading out in multiple directions, thus creating several residual pieces after fracture. In the other case shown in Figure 6.5(a), the crack is sharper and creates quite flat surfaces with few secondary cracks appearing. The observed differences in fracture as the loading direction is changed could be due to the directionality and hardness differences observed in the alloy microstructure concerning the eutectic lamellas and the inter-layers. As reported in the following section 6.1.2, the arc-shaped inter-layers in LMD-built $Fe_{82.4}Ti_{17.6}$ are relatively softer than the lamellar layers. The lamellas forming layers are oriented radially perpendicular to the inter-layers or largely parallel to the build direction. Thus, the path for crack propagation might be influenced by the overall distribution of layers and inter-layers in the sample volume with respect to the loading axis. On the other hand, the distributed porosity inside the material

has no effect on the crack direction or propagation as observed in the 3D rendered volumes from XCT. However, further investigation is required to properly understand the difference in fracture behaviour.

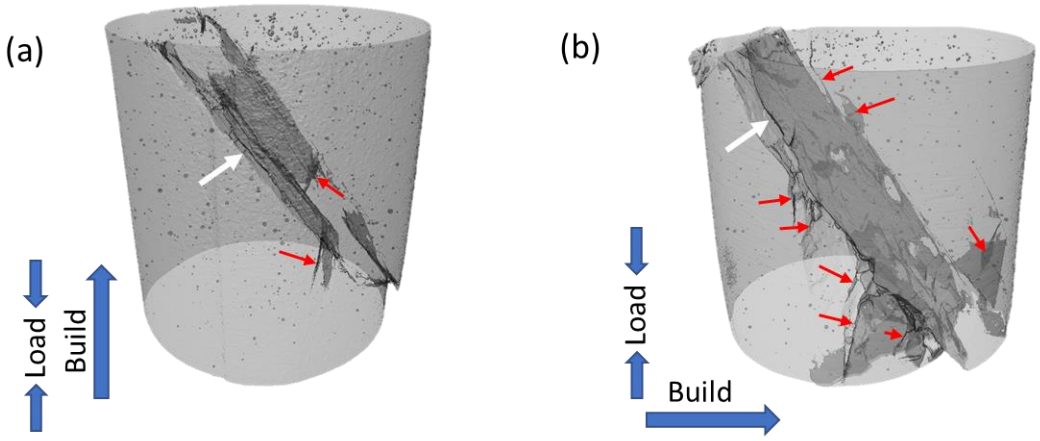

Figure 6.5: Volume rendering of the tomography data for fractured compression samples of LMD-built $Fe_{82.4}Ti_{17.6}$ tested at room temperature under uniaxial loading applied (a) parallel and (b) perpendicular to the build direction

Figure 6.6 summarises the results of quasi-static tensile tests for the LMD-built alloy. Due to dimensional constraints, tensile samples could only be machined such that the uniaxial loading direction always remained perpendicular to the build direction, as represented by the pre-test specimen in Figure 6.6(b). At all testing temperatures, the material failed at very low loads by brittle fracture. A maximum tensile stress of only 200 MPa was reached at 600 °C. Further, fractures were observed to occur at the reduced sections near the grips of the tensile specimens and not just in the 2 mm wide gauge length, as shown in Figure 6.6(d). This behaviour was independent of the test temperature. This poor tensile behaviour can be attributed to the observed thin cracks in the specimen. Figure 6.7(a) shows an X-ray computed tomography slice just below the surface of a tensile specimen in a 3 mm wide (and 10 mm long) reduced section. It was measured before machining the second reduced section (which is 2 mm wide and 3.5 mm long) in the centre, marked approximately by the white dashed lines, to produce the final test specimens seen in Figure 6.6(b). Several fine cracks, marked by red boxes, were visible throughout the reduced section and in the curvature near the grips. The samples were machined using Electrical Discharge Machining (EDM) and therefore no stress is introduced from this process. The observed cracks are probably a consequence of internal stresses built up during LMD. Several micro-pores were visible as dark spots and were distributed quite uniformly throughout the volume, as shown in the volume rendering of the tomography data measured for the entire reduced section in Figure 6.7(b). The pores are coloured in blue to visualise them better in 3D. A basic segmentation of the pores revealed a total porosity of 0.18 % by volume. This is fairly low and suggests a high-density build obtained by LMD. The thin cracks most likely formed as consequence of internal stresses and were

guided by pre-existing defects (micro-porosity) that act as stress concentrators near the sample edge (see Figure 6.7(a)).

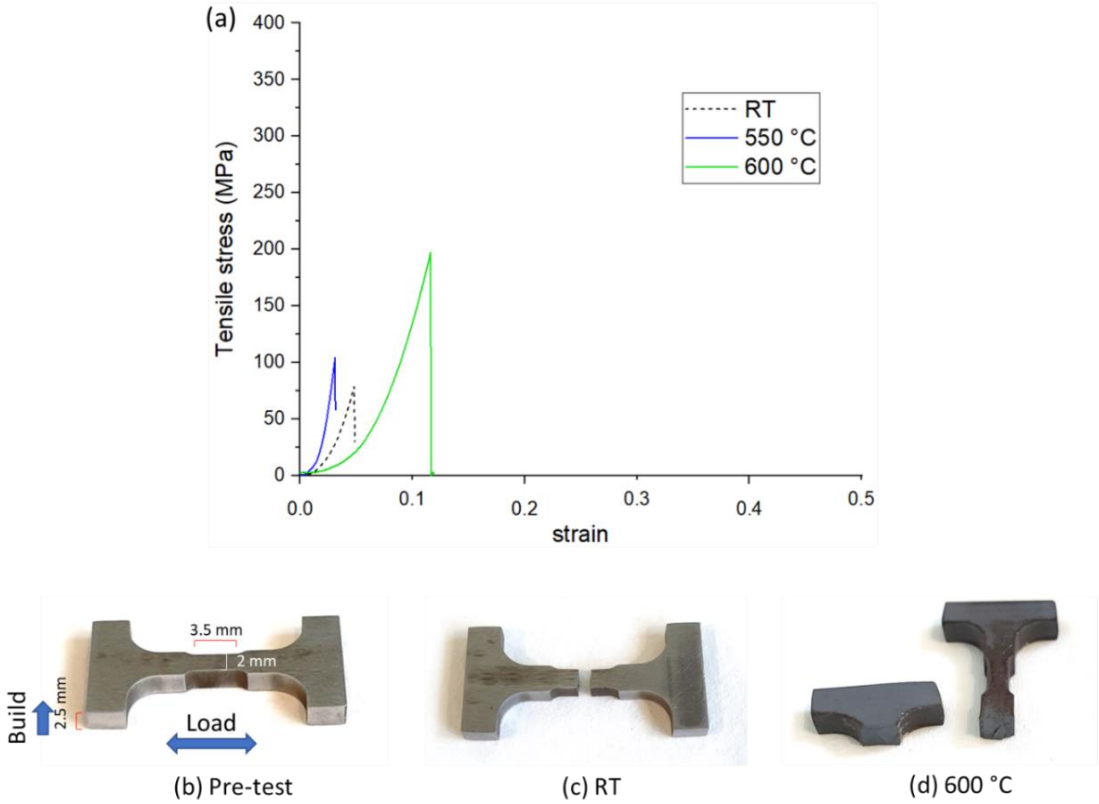

Figure 6.6: (a) Engineering stress vs. engineering strain curves for quasi-static tension tests of LMD-built $Fe_{82.4}Ti_{17.6}$ performed at different temperatures under uniaxial load applied perpendicular to the build direction, (b) a pre-test specimen showing dimensions and loading direction, (c) specimen conditions after testing at room temperature and (d) 600 °C

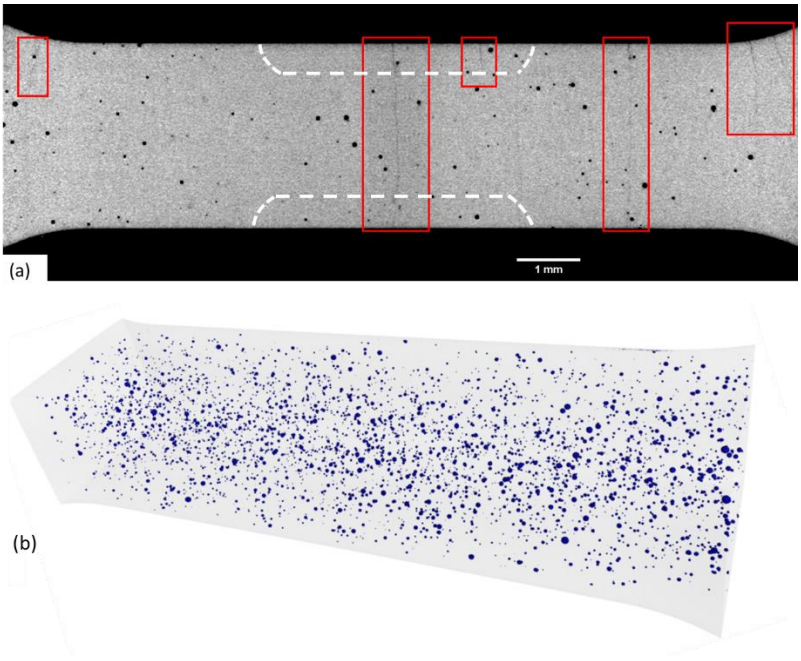

Figure 6.7: (a) X-ray computed tomography slice measured just below the surface of a tensile specimen in the reduced section (10 mm × 3 mm × 2.5 mm) showing macro-pores and thin cracks marked by red boxes. White dashed lines show approximate geometry of the second reduced section (3.5 mm × 2 mm × 2.5 mm) to be machined. (b) Volume rendering of the tomography data showing the spatial distribution of all porosity (coloured in blue) in the reduced section

The macro-mechanical behaviour of the LMD-built $Fe_{82.4}Ti_{17.6}$ alloy using pre-alloyed powders can be said to be brittle at room temperature. Pre-existing manufacturing defects (such as pores and cracks), and probably internal stresses, led to very poor tensile behaviour. Further, some anisotropy was observed in the compression behaviour with respect to the loading direction. Under compression, it acts quite well above 500 °C. It showed high plasticity, especially at 600 °C, while always maintaining a yield strength above 1000 MPa. It needs further efforts to improve the brittle and tensile behaviour, starting with optimization of powder bed pre-heating temperatures and printing conditions, post-processing heat-treatments and surface treatments. However, it could be still considered an impressive candidate for compression-based applications in the intermediate temperature range.

6.1.2 Micro-mechanical characterisation

Figure 6.8 and Figure 6.9 summarise the micro-pillar compression behaviour of the LMD-built alloy. The stress-strain curves obtained as micro-pillars (of cross sections 5 µm × 5 µm and 2 µm × 2 µm) were compressed up to 10 % of their heights while loading uniaxially perpendicular to build direction, are shown in Figure 6.8. SEM micrographs of micro-pillars before and after compression are shown in Figure 6.9. Stress-strain curves for micro-pillars with 5 µm × 5 µm square cross-section, carved at random locations across the alloy microstructure, revealed a high average compressive yield strength of 2254.3 ± 109.9 MPa.

Considering the curves for micro-pillars with 2 µm × 2 µm cross-sections, the `inter-layer´ region featuring globular microstructure appeared to be softer with compressive yield strength of 1560 MPa, while the micro-pillar in the lamellar eutectic region showed a larger yield strength of 2400 MPa. Further, an inflection or a slight change in slope was observed in case of the 5 µm × 5 µm micro-pillars at the start (around 1 % strain). This is due to adjustment of alignment between the flat punch used for compression and large cross-section of these micro-pillars. The SEM micrographs in Figure 6.9 further reveal shear bands appearing along the sides of all micro-pillars after compression, with very prominent bands in the softer globular region. However, more tests need to be performed to have accurate statistics about the difference in micro-pillar yield strength of the two regions. Based on the present results, we can also say that the micro-pillar in the lamellar eutectic region showed a compressive yield strength closer to that of the randomly carved 5 µm × 5 µm micro-pillars. This makes sense since most of the sample consists of lamellar layers, whereas the narrow `inter-layers´ would constitute a much smaller volume fraction.

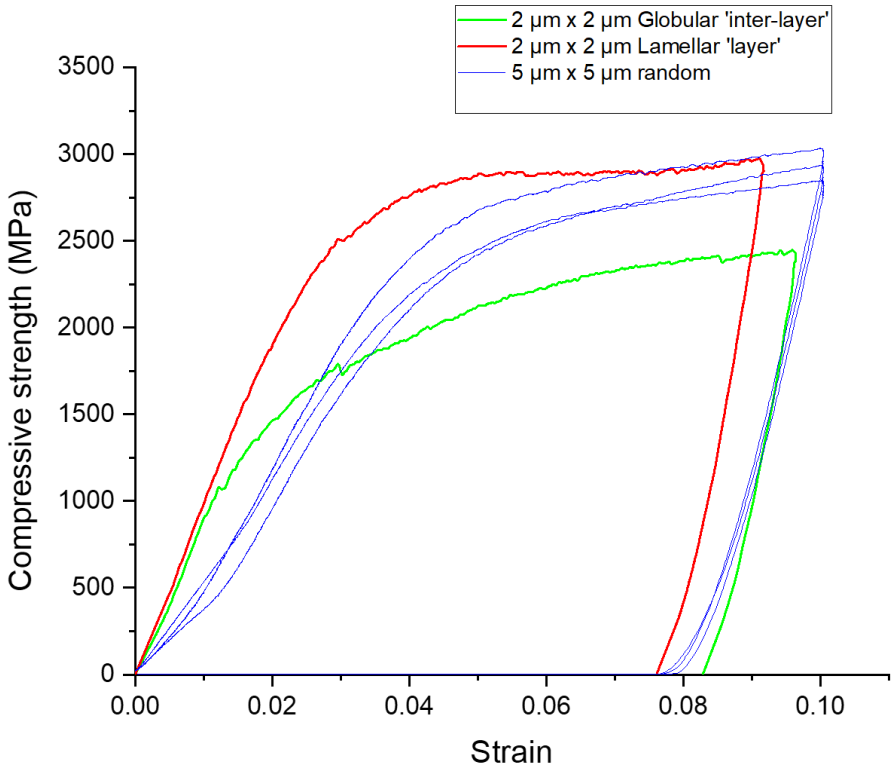

Figure 6.8: Engineering stress vs. engineering strain curves for compression of micro-pillars carved on LMD-built $Fe_{82.4}Ti_{17.6}$ at globular `inter-layer´, lamellar `layer´ and random locations in the microstructure

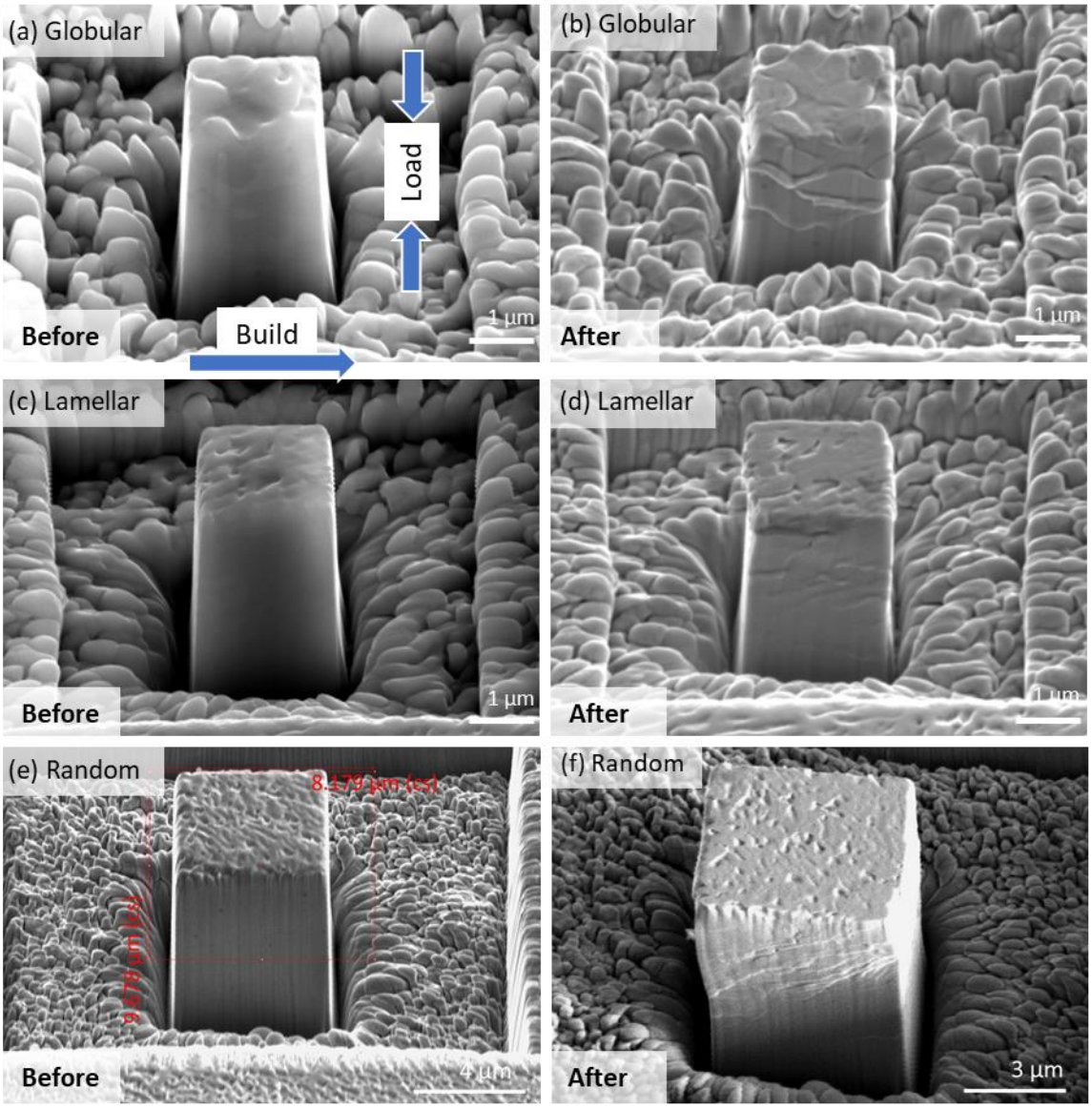

Figure 6.9: SEM micrographs taken before and after compression test (uniaxial load perpendicular to build) of micro-pillars carved on LMD-built $Fe_{82.4}Ti_{17.6}$ across (a, b) globular and (c, d) lamellar eutectic regions with 2 µm × 2 µm cross-sections; (e, f) across random location in the microstructure with 5 µm × 5 µm cross-section

Nanoindentation tests (strain-based) were performed as a grid across two globular inter-layer regions lying close to each other with a thin layer of lamellar eutectic between them, as shown in Figure 6.10(a). The indented alloy cross-section had a building direction perpendicular to the loading direction. Colour-coded hardness maps revealed relatively lower hardness in the globular eutectic regions as shown Figure 6.10(b). In the globular eutectic region, hardness values lied between 3 and 6 GPa, while lamellar regions showed hardnesses between 6.4 and 9.8 GPa with few very hard regions going up to 11 GPa.

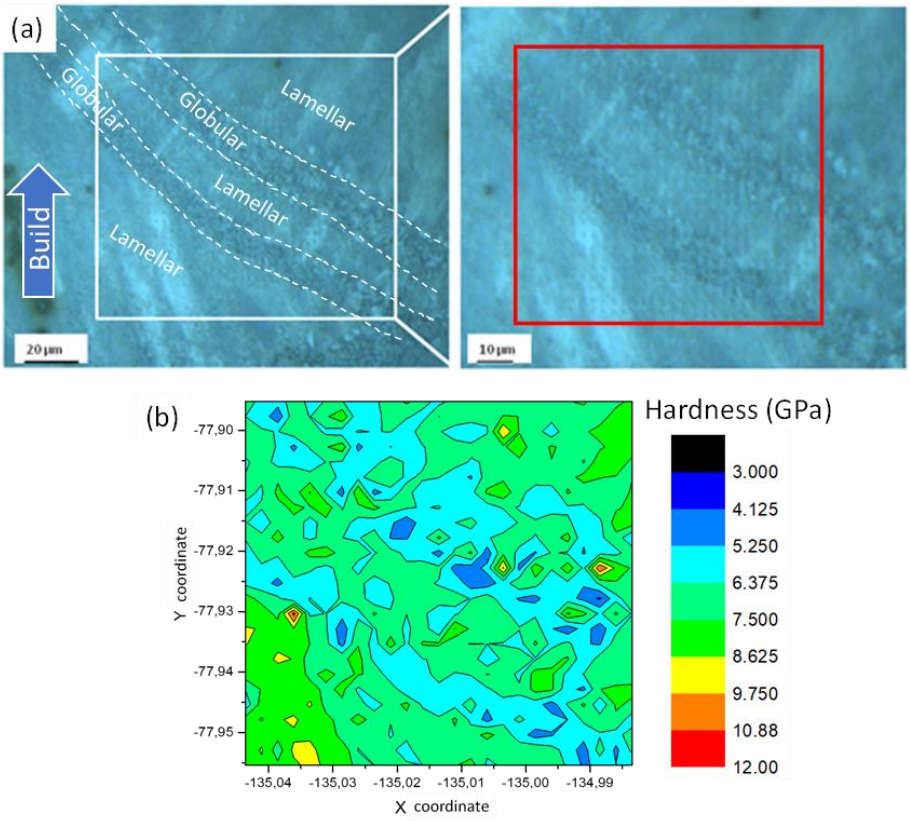

Figure 6.10: (a) Optical images showing visible indents in the nanoindentation grid, marked by red square, performed (perpendicular to build direction) on LMD-built $Fe_{82.4}Ti_{17.6}$ across lamellar and globular eutectic regions, (b) Colour-coded hardness map with its legend obtained for the nanoindentation grid marked by the red square in figure (a)

The micro-mechanical performance of LMD-built $Fe_{82.4}Ti_{17.6}$ was further compared to that of sintered samples prepared by Field Assisted Hot Pressing (FAHP) of the same pre-alloyed powders (45 – 90 µm). As explained in section 3.2.3 of chapter 3, FAHP is a fast solid state sintering technique that simultaneously uses Joule heating and uniaxial pressure to achieve lower sintering temperatures and shorter sintering times, thus largely preserving powder microstructures. Unlike LMD, FAHP does not involve complete melting of the pre-alloyed powder. Figure 6.11 shows the microstructures of four sintered samples processed with four different sets of parameters (maximum temperature achieved, holding time and pressure applied during holding): 1150 °C-2 min-50 MPa, 1150 °C-10 min-50 MPa, 1230 °C-2 min-50 MPa and 1230 °C-10 min-50 MPa.

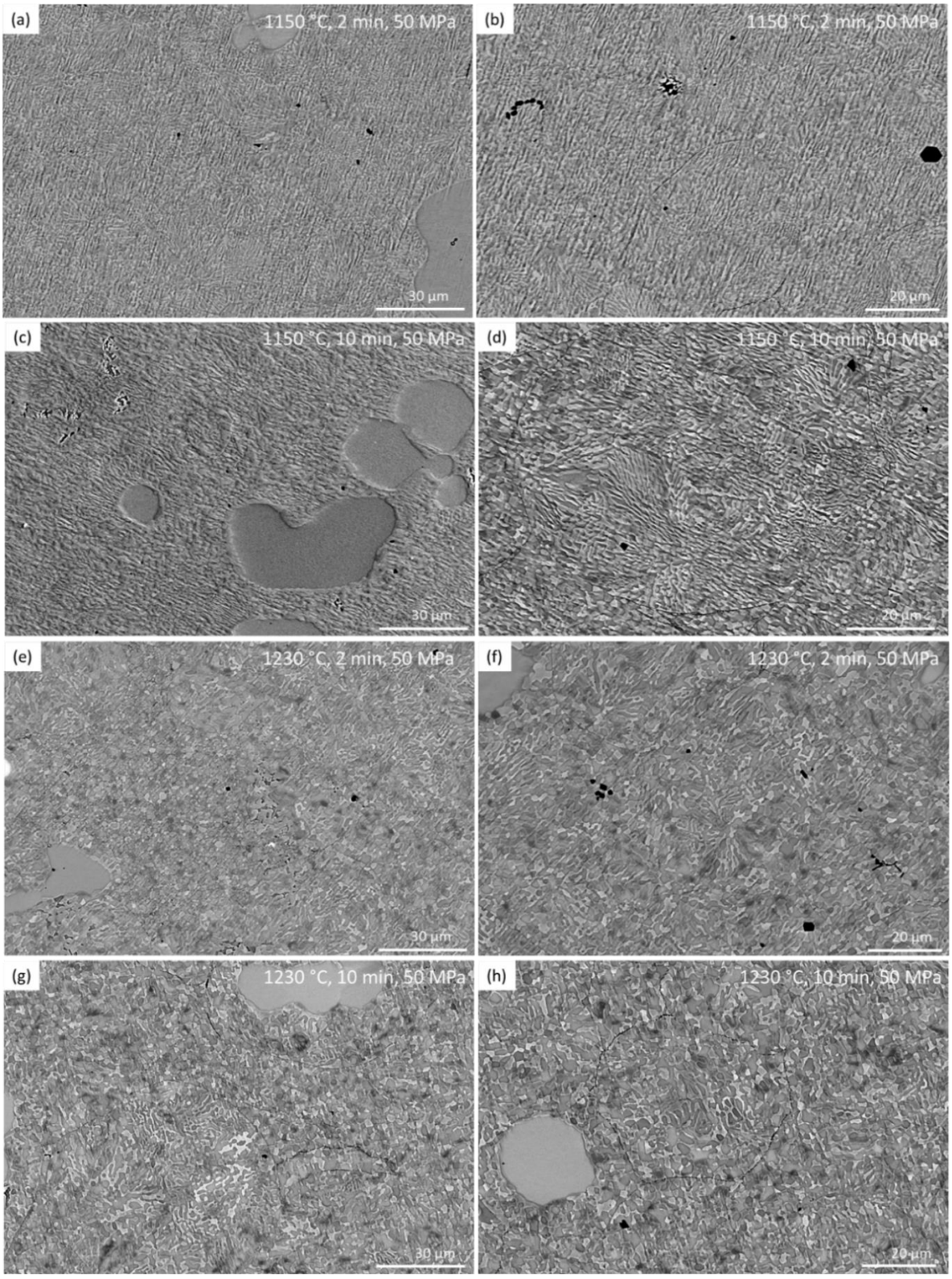

Figure 6.11: SEM micrographs showing microstructures of $Fe_{82.4}Ti_{17.6}$ samples prepared by Field Assisted Hot Pressing (FAHP) for process parameters (a, b) 1150 °C-2 min-50 MPa, (c, d) 1150 °C-10 min-50 MPa, (e, f) 1230 °C-2 min-50 MPa and (g, h) 1230 °C-10 min-50 MPa

The microstructures suggested that all sintered samples had progressed to the final stage of sintering. In all cases, very limited porosity was observed and well-fused grain boundaries

existed without any large inter-particle gaps. Similar to the pre-alloyed $Fe_{82.4}Ti_{17.6}$ powders in the LMD size range (see Figure 4.29 in section 4.2.2 of chapter 4), Fe_2Ti existed as primary dendrites (visible as large grey phases in SEM micrographs) in a eutectic matrix of (α-Fe + Fe_2Ti). However, solid state sintering resulted in a more irregular morphology of the eutectic lamellas as compared to the powders, especially at the higher sintering temperature of 1230 °C. X-ray diffraction followed by a preliminary Rietveld analysis revealed very similar phase fractions in all four sintered samples, i.e., around 40 % α-Fe and around 60 % Fe_2Ti by mass, as shown in Figure 6.12.

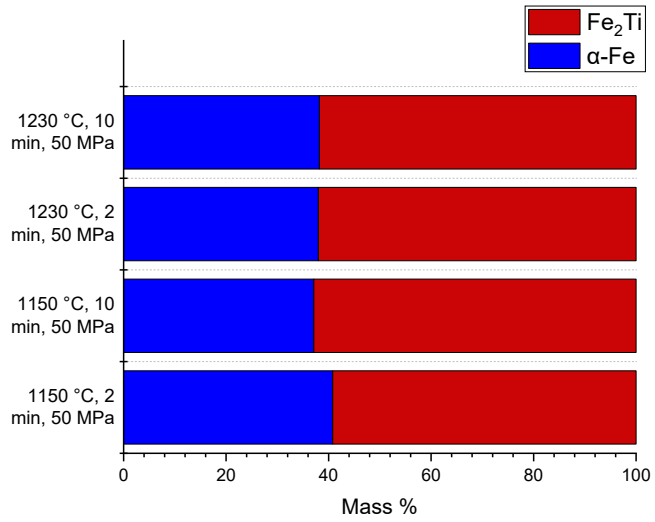

Figure 6.12: Phase fractions (in mass %) of FAHP-processed $Fe_{82.4}Ti_{17.6}$ samples as determined by XRD and a preliminary Rietveld refinement

Figure 6.13(a, b) show the variation of mean inter-lamellar spacing (λ) and compressive yield strength, as determined by micro-pillar (5 µm × 5 µm cross-section) compression, with respect to sintering time for the four samples. Figure 6.13(c) summarises the average compressive yield strengths and mean λ measured for all four sintered samples as well as the LMD-built alloy for comparison.

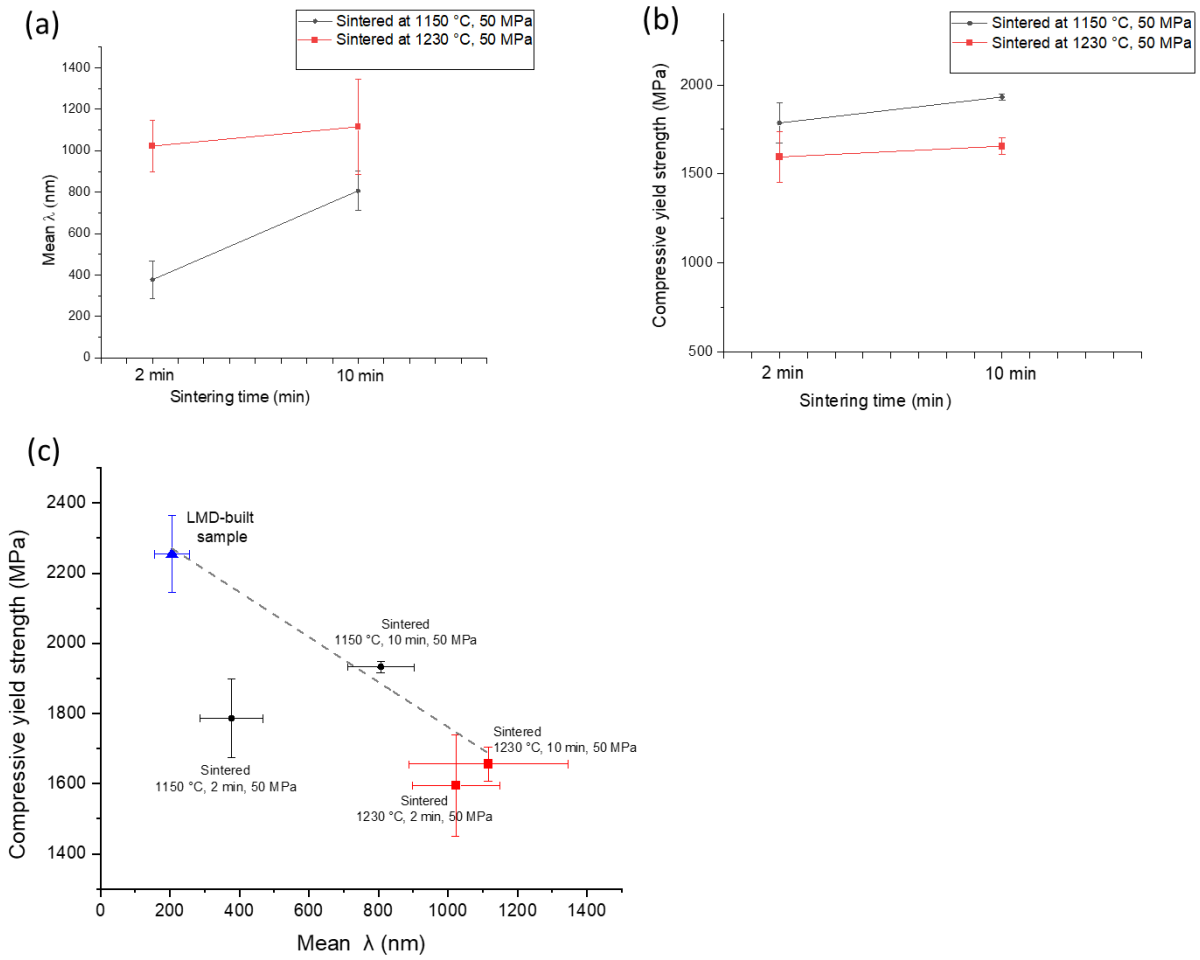

Figure 6.13: (a) Variation of mean λ with sintering time of FAHP-processed $Fe_{82.4}Ti_{17.6}$ samples, (b) Variation of average micro-pillar (5 µm × 5 µm cross-section) compressive yield strength with sintering time of FAHP-processed $Fe_{82.4}Ti_{17.6}$ samples, (c) Variation of average micro-pillar (5 µm × 5 µm cross-section) compressive yield strength with mean λ of four FAHP-processed samples (with their respective parameters) and LMD-built $Fe_{82.4}Ti_{17.6}$

The mean λ increased with sintering time and more steeply in case of the samples sintered at 1150 °C where it became double, as shown in Figure 6.13(a). Further, λ values remained relatively smaller for the lower sintering temperature of 1150 °C and always lied in the ultrafine range. At 1230 °C, they were often larger than 1 µm, with the mean λ being 1022.7 nm after 2 min and 1115.8 nm after 10 min of sintering time. Thus, it can be concluded that higher sintering temperature resulted in a coarser eutectic microstructure. This was also reflected in their compressive yield strength, since lower λ is usually associated with better mechanical properties. The samples sintered at 1150 °C showed more average strength than those at 1230 °C (see Figure 6.13(b)). However, in both cases, there was a slight increase in the average strength with respect to sintering time. It increased by 146.6 MPa in case of samples processed at 1150 °C and by 61 MPa for those at 1230 °C. There was no significant change in the phase fractions of the samples with sintering time (see Figure 6.12), and further, there was an increase in mean λ which would suggest a decrease in strength. Therefore, the

observed slight increase in yield strength can be entirely attributed to the densification process happening during the longer holding time. Densification usually continues during the last stage of sintering where porosity is reduced further and the trapped gases escape the sample. Although the densities should saturate after a certain sintering time, in this case, the process seems to be continuing until 10 min.

As shown in Figure 6.13(c), lower mean λ in the LMD-built sample lead to a higher compressive yield strength as compared to all FAHP-processed samples. The lowest mean λ observed among the sintered samples was 377.5 ± 90.1 nm for the parameter set (1150 °C, 2 min, 50 MPa) and was almost double of what was observed for the LMD-built sample (206 ± 51 nm). The average compressive yield strength as measured by micro-pillar compression was 2254.3 ± 110 MPa for the LMD-built alloy, while the highest one among the sintered samples was 1933 ± 16.5 MPa for the parameter set (1150 °C, 10 min, 50 MPa). Further, the points corresponding to the LMD-built sample and the two densified samples processed by FAHP, i.e. the ones with holding time of 10 min, appear to fall in a straight line (as indicated by the fitted dashed line). This suggests a linear increase in compressive yield strength of micro-pillars as the mean λ decreases. This effect was quite significant, since the average yield strength of the LMD-built sample was ≈ 600 MPa more than that of the sample sintered at (1230 °C, 10 min, 50 MPa) whose mean λ was larger by ≈ 900 nm and lied outside the ultrafine range. Thus, it could be said that lower λ is associated with better micro-mechanical strength.

However, no such correlation was observed between the average nano-hardness and mean λ of these samples. Figure 6.14 plots the average nano-hardness of the LMD-built and the four FAHP-processed samples against their observed mean λ.

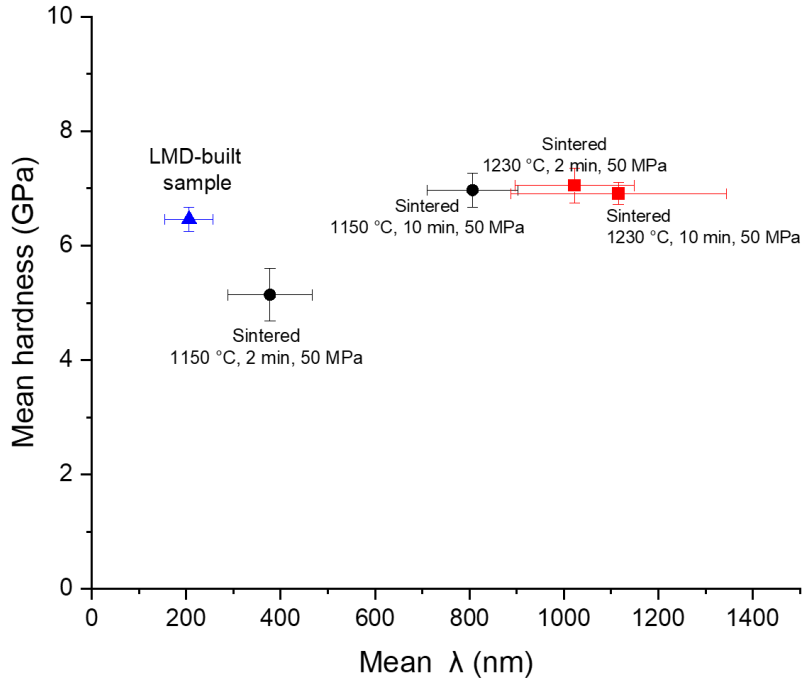

Figure 6.14: Variation of average nano-hardness with mean λ of four FAHP-processed samples (with their respective parameters) and LMD-built $Fe_{82.4}Ti_{17.6}$

Nano-hardness here was determined by a load-based nanoindentation performed on random locations across the sample microstructures. Almost all the samples showed average nano-hardness between 6 and 7 GPa despite having differences in mean λ. A small drop in case of the sample sintered at (1150 °C, 2 min, 50 MPa) was observed which showed average nano-hardness of 5.1 ± 0.5 GPa. However, no clear trend was observed with respect to λ. Thus, it can be inferred that λ does not have a significant effect on the nano-hardness behaviour of samples processed by LMD and FAHP.

6.2 SLM-built $Ti_{73.5}Fe_{23}Nb_{1.5}Sn_2$

This section focuses on the characterisation of SLM-built $Ti_{73.5}Fe_{23}Nb_{1.5}Sn_2$ using pre-alloyed AMA2 powder.

Figure 6.15 shows the typical microstructure observed in the cross-section (build direction is vertical in plane of figure) of as-built alloy $Ti_{73.5}Fe_{23}Nb_{1.5}Sn_2$ using SLM of AMA2 powders.

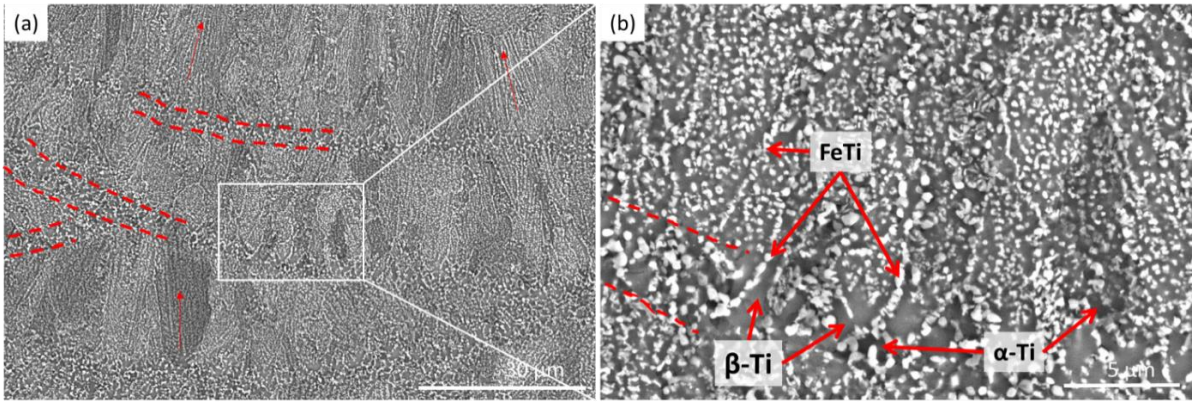

Figure 6.15: SEM micrographs showing typical microstructure observed in SLM-built $Ti_{73.5}Fe_{23}Nb_{1.5}Sn_2$ alloy (build direction is vertical in plane of figure)

Layers and inter-layers (marked by the dashed red lines) can be identified in the microstructure. The inter-metallic FeTi existed as dispersoids in a matrix of β-Ti and relatively low-contrast α-Ti, as shown in Figure 6.15(b). The inter-layers contained relatively less concentration of FeTi dispersoids and were shaped like arcs originating from the melt pool shape. Based on SEM images, the average inter-layer thickness was determined to be 3.5 ± 0.6 µm. FeTi dispersoids were observed to often form linear arrangements that seem to grow radially from the inter-layers in a preferred direction (marked by red arrows in Figure 6.15(a)). Such a pattern was also observed for the lamellar growth of eutectic (α-Fe + Fe_2Ti) in the LMD-built alloy discussed in Figure 6.1 of section 6.1. This is because the preferential growth of lamellas and dispersoids happens along the maximum thermal gradients existing around the melt pool during SLM or LMD process [2]. These linear arrangements of FeTi particles resemble fine lamellas and they exist in a matrix which is also strengthened by a high concentration of dispersoids. The potential for such a unique microstructural design was one of the main reasons behind choosing this non-eutectic composition for SLM.

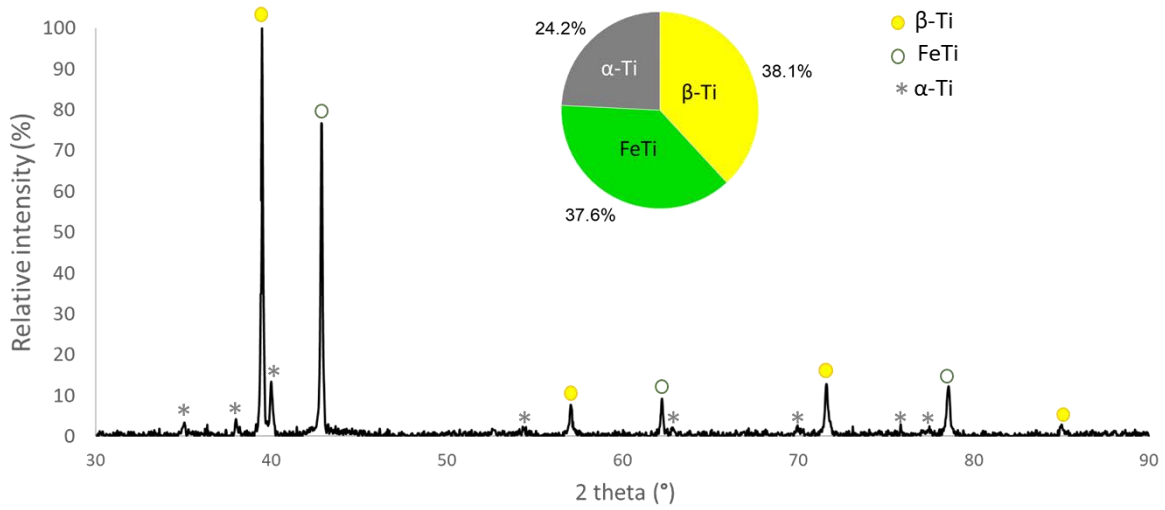

Figure 6.16: XRD pattern of SLM-built $Ti_{73.5}Fe_{23}Nb_{1.5}Sn_2$ with identified peaks and a pie chart showing mass percent composition of phases based on a preliminary Rietveld refinement

Figure 6.16 shows the alloy´s XRD pattern with identified phases and their corresponding mass fractions as determined by a preliminary Rietveld refinement. All three identified phases were present in significant quantities in the alloy with almost equal proportions of β-Ti and FeTi. The microstructure observed here is quite different from what was observed in gas atomised powders of $Ti_{73.5}Fe_{23}Nb_{1.5}Sn_2$ that were used as raw material for the build (see Figure 4.19 in section 4.1.5 of chapter 4). As discussed in section 4.1.5 of chapter 4, the pre-alloyed powders featured two β-Ti solid solutions, very little FeTi and a pure α-Fe phase. No α-Ti was observed in the powders. The differences arise due to the differences in processing conditions, i.e., between gas atomisation and SLM (with a substrate pre-heated to ≈ 600 °C). Crystallisation kinetics of gas atomisation are very fast and resulted in limited nucleation of inter-metallic FeTi which was the last phase to form. Besides, all nucleation was essentially homogeneous and non-directional in powders. As also reported in section, the FeTi dispersoids showed more growth in coarser powder particles which experienced relatively slower crystallisation. By optimising the SLM processing parameters and using a pre-heated substrate, it was possible to reduce the thermal gradient and thus, the cooling rates during solidification after laser melting. This is favourable for FeTi nucleation and growth. It also allowed complete solute diffusion to form a single saturated β-Ti phase. Further, the substrate and pre-existing layers provided sites for heterogenous nucleation of FeTi dispersoids, while the thermal gradients around the melt pool provided a directionality for their growth. The inter-layers, solidifying from the bottom layer of the melt pool, experienced the highest undercooling and initial cooling rates. They showed more resemblance to the gas-atomised powder microstructures due to larger Ti matrix and fewer FeTi dispersoids, as shown in Figure 6.16(b). However, the different kinetics of SLM on a substrate preheated to ≈ 600 °C also favoured the solid state eutectoid reaction β-Ti → α-Ti + FeTi, leading to a significant phase

fraction of α-Ti (HCP) in the alloy microstructure. This is critical in determining the mechanical properties of the alloy and needs to be optimised by proper post-processing heat treatments [3]–[5].

The mechanical characterisation results of this SLM-built alloy are discussed in the following section.

6.2.1 Macro-mechanical characterisation

The macro-mechanical behaviour of the as-built alloy was characterised by quasi-static compression and tension tests. Figure 6.17 summarises the alloy´s compression behaviour when uniaxial load is applied parallel to the build direction. Figure 6.17(a) shows the typical stress-strain curves obtained at various temperatures (up to 600 °C), while Figure 6.17(b) represents the pre-test specimen and loading conditions. The specimen conditions after testing are shown in Figure 6.17(c-e) for their respective test temperatures.

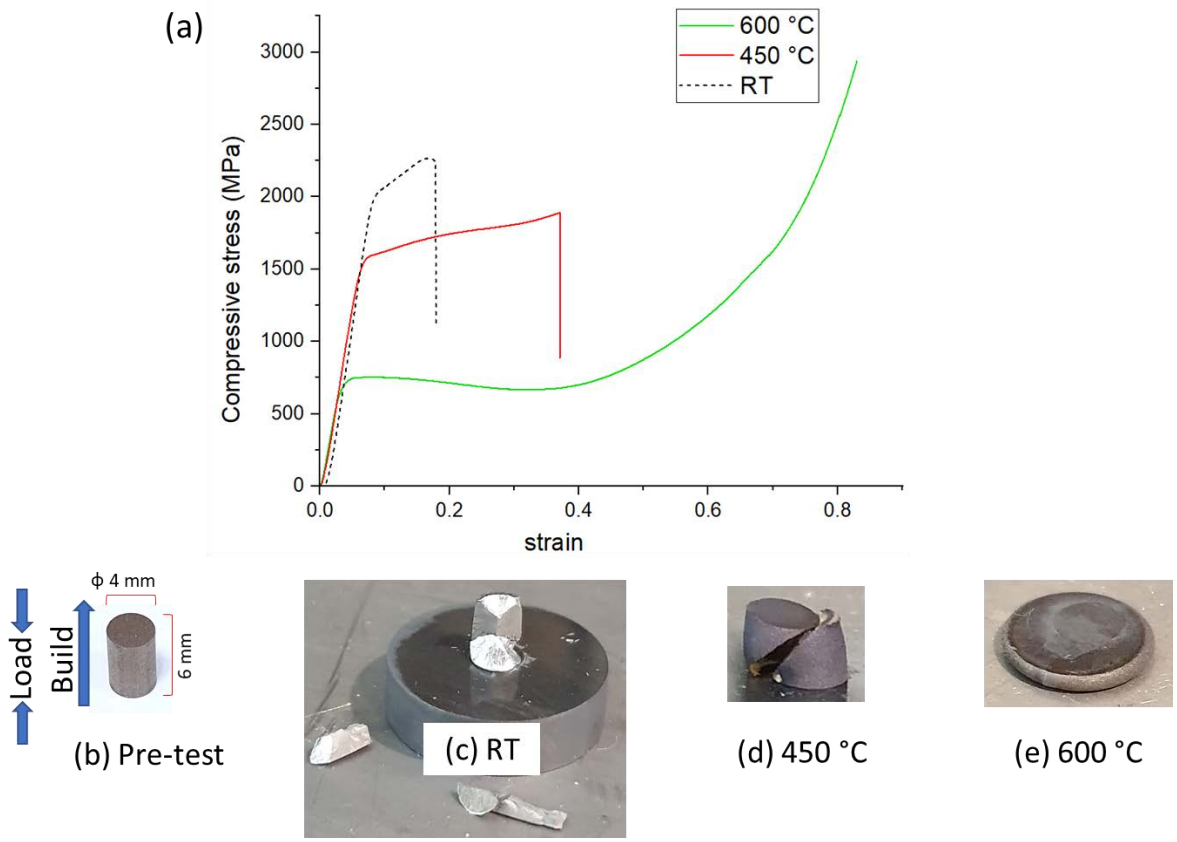

Figure 6.17: (a) Engineering stress vs. engineering strain curves for quasi-static compression tests of SLM-built $Ti_{73.5}Fe_{23}Nb_{1.5}Sn_2$ performed at various temperatures under uniaxial load applied parallel to the build direction, (b) a pre-test specimen showing dimensions and loading direction, (c) specimen conditions after testing at room temperature, (d) 450 °C, (e) 600 °C

The alloy showed a very high compressive yield strength of 1925 MPa at room temperature, while deforming up to 20 % before failure. The fracture at room temperature appeared to be

by brittle shear originating at 45° angle to the loading axis. However, the crack propagated to more planes as it spread across the sample finally breaking it into three or four pieces, as shown in Figure 6.17(c). At 450 °C, the average yield strength was 1445 MPa and samples failed after ≈ 38 % deformation. The specimens underwent some barrelling before failing by a 45° shearing fracture, as shown in Figure 6.17(d). The average yield strength reduced to 660 MPa at 600 °C and samples became completely plastic deforming homogeneously up to 85 % without failure. The samples looked like flattened discs after test without any visible cracks, as shown in Figure 6.17(e).

Figure 6.18 summarises the results of quasi-static tensile tests for the SLM-built alloy.

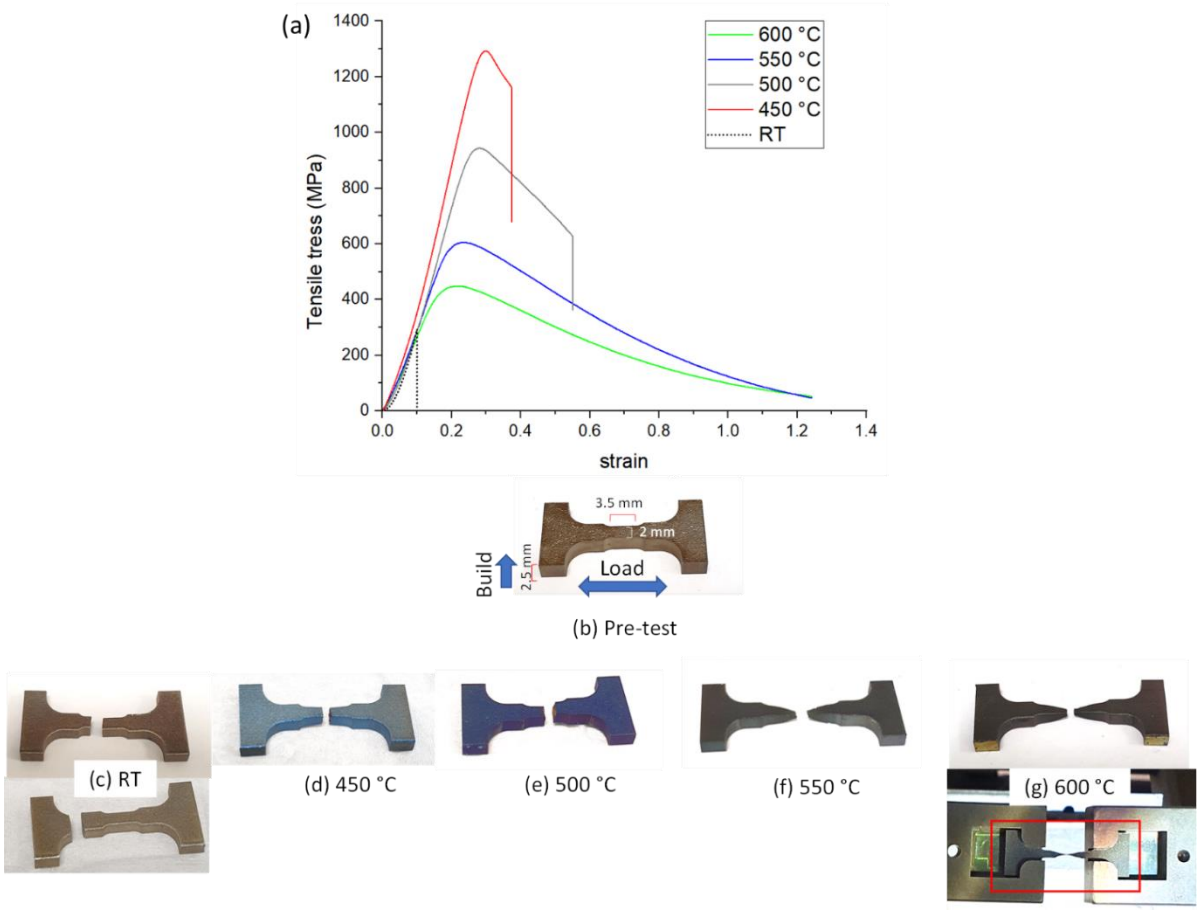

Figure 6.18: (a) Engineering stress vs. engineering strain curves for quasi-static tension tests of SLM-built $Ti_{73.5}Fe_{23}Nb_{1.5}Sn_2$ performed at different temperatures under uniaxial load applied perpendicular to the build direction, (b) a pre-test specimen showing dimensions and loading direction, (c) specimen conditions after testing at room temperature, (d) 450 °C, (e) 500 °C, (f) 550 °C and (g) 600 °C

The uniaxial loading direction always remained perpendicular to the build direction, as represented by the pre-test specimen in Figure 6.18(b). Figure 6.18(c-g) show the specimen conditions after testing at their respective test temperatures (up to 600 °C).

At room temperature, the material showed poor tensile behaviour and the samples failed by brittle fracture at stresses ≤ 300 MPa. Further, fractures were observed to often occur at the reduced sections near the grips of the tensile specimens and not just in the 2 mm wide gauge, as shown in Figure 6.18(c). However, this behaviour improved significantly at higher temperatures, as is evident from the curves in Figure 6.18(a). A tensile yield strength of ≈ 1200 MPa was observed at 450 °C and the samples fractured at the 2 mm wide gauge in the centre (see Figure 6.18(d)) after showing an elongation up to 40 %. This suggests the presence of some defects that act as crack nucleation sites at room temperature and disappear or homogenise at higher temperatures. As the testing temperature is increased further, the yield strength began to drop while the ductility increased, as it happens in case of most metallic materials. At 500 °C, the observed yield strength was ≈ 875 MPa while elongation went up to 57 %. For testing temperatures of 550 °C and 600 °C, the respective average yield strengths were 575 MPa and 393 MPa while the samples became completely ductile, as shown in Figure 6.18(f,g). They underwent a continuous plastic flow without failure, as the stress-strain curves suggest, and their cross-section was reduced to a narrow thread due to necking. They later split into two pieces as a result of non-uniform thermal contraction during cooling, only after the tests had been paused.

This ends the discussion of characterisations performed on the two AM-built alloys. Important conclusions and comments on the overall performance of these new materials are listed in the next section.

6.3 Partial Conclusions

i. Pre-alloyed powders of $Fe_{82.4}Ti_{17.6}$ were successfully processed by LMD to build an alloy with ultrafine lamellar microstructure (λ = 206 ± 51 nm). The arc-shaped `inter-layers´, lying between the lamellar eutectic layers, were 12.2 ± 0.8 µm thick and consisted of a globular eutectic morphology.

ii. Pre-alloyed powders of $Ti_{73.5}Fe_{23}Nb_{1.5}Sn_2$ were successfully processed by SLM to build an alloy with a unique microstructure very different from that of the powders. The alloy featured significant phase fractions of both β-Ti and α-Ti, accompanied by a large fraction of inter-metallic FeTi as dispersoids. In a matrix strengthened by dispersoids, a portion of FeTi further arranged themselves linearly to resemble fine lamellas. The thin inter-layers (average thickness 3.5 ± 0.6 µm) featured relatively low concentration of dispersoids.

iii. Macro-mechanical behaviour of the LMD-built $Fe_{82.4}Ti_{17.6}$ alloy can be summarised as brittle under tension and compression at room temperature. It showed a high compressive yield strength ≈ 1800 MPa and almost zero plasticity at room temperature, when loaded uniaxially parallel to the build direction. Onset of plasticity

was observed above 500 °C and the alloy showed very high plasticity at 600 °C (up to 90 % deformation without failure) while always maintaining a yield strength above 1000 MPa. Further, some anisotropy was observed with respect to the loading direction as the compressive yield strength dropped by ≈ 20 % while loading perpendicular to the build direction. Pre-existing thin cracks in tensile specimens resulted in brittle fractures at low loads for all testing temperatures.

iv. LMD-built $Fe_{82.4}Ti_{17.6}$ could be considered an impressive candidate for compression-based applications in the intermediate temperature range. Induction cast Fe-15 wt % Ti or $Fe_{82.9}Ti_{17.1}$ alloy was reported by Barbier et al. [6] as a new candidate for such applications, demonstrating 780 MPa of compressive yield stress at 600 °C and an interlamellar spacing of 600 nm in the eutectic microstructure. However, no comment was made on the plastic behaviour of the alloy in this temperature range. LMD processing produced a much finer microstructure and better mechanical results for our very similar composition.

v. Macro-mechanical behaviour of SLM-built $Ti_{73.5}Fe_{23}Nb_{1.5}Sn_2$ can be summarised as excellent under compression and tension (at temperatures of 450 °C and above). It showed very high compressive yield strength of 1925 MPa at room temperature and up to 20 % deformation before failure. It became completely plastic at 600 °C while maintaining a high yield strength of 660 MPa. Under tension (uniaxial load perpendicular to build direction), the specimens acted brittle at room temperature, however, this issue was resolved at higher temperatures. At 450 °C, the alloy demonstrated high tensile yield strength of ≈ 1200 MPa with elongation up to 40 %. The strength decreased and the elongation increased at higher temperatures with the alloy becoming completely ductile at 550 °C.

vi. SLM-built $Ti_{73.5}Fe_{23}Nb_{1.5}Sn_2$ can be considered as an excellent (α+β) Ti alloy, further strengthened by FeTi dispersoids, for compression and tension-based applications, especially in the intermediate temperature range. The brittle behaviour of tensile specimens at room temperature needs to be addressed by proper heat treatments or other methods. However, the alloy showed higher tensile yield strength and elongation at intermediate temperatures (450 °C to 600 °C) than popular (α+β) aerospace alloys like Ti-6Al-4V. The yield strengths of wrought Ti-6Al-4V have been reported to be always lower than 1100 MPa at temperatures above 400 °C, while SLM-built Ti-6Al-4V have shown maximum yield strength of 892 MPa, ultimate tensile strength of 979 MPa and elongation up to 25 % in the temperature range 350 − 550 °C [7]–[9].

vii. Micro-mechanical characterisation of LMD-built $Fe_{82.4}Ti_{17.6}$ was performed using compression of micro-pillars carved on the microstructure and nanoindentation. An

average compressive yield strength of 2254.3 ± 109.9 MPa was determined by micro-pillar compression, while micro-pillar in the lamellar eutectic `layer´ showed a higher yield strength (2400 MPa) as compared to the globular `inter-layer´ (1560 MPa). Lamellar eutectic `layer´ also showed higher nano-hardness (6.4 – 9.8 GPa) as compared to the globular `inter-layer´ (3 – 6 GPa).

viii. An additional study was performed on the micro-mechanical behaviour of $Fe_{82.4}Ti_{17.6}$ processed by FAHP (solid state sintering) of pre-alloyed powders. The highest compressive yield strength of micro-pillars achieved by FAHP-processed samples was 1933 ± 16.5 MPa and the lowest average λ observed was 377.5 ± 90.1 nm. The LMD-built $Fe_{82.4}Ti_{17.6}$ remained better than FAHP-processed samples in terms of compressive yield strength of micro-pillars and also showed lower λ.

ix. Micro-pillar yield strength was found to decrease linearly with increasing λ for the LMD and dense (10 min sintering time) FAHP-processed samples. However, change in λ did not affect the nano-hardness behaviour of the samples processed by LMD and FAHP.

REFERENCES

[1] G. Requena *et al.*, "Ultrafine Fe-Fe2Ti eutectics by directed energy deposition: Insights into microstructure formation based on experimental techniques and phase field modelling," *Addit. Manuf.*, vol. 33, no. August 2019, p. 101133, 2020, doi: 10.1016/j.addma.2020.101133.

[2] C. Zhao *et al.*, "Real-time monitoring of laser powder bed fusion process using high-speed X-ray imaging and diffraction," *Sci. Rep.*, vol. 7, no. 1, pp. 1–11, 2017, doi: 10.1038/s41598-017-03761-2.

[3] A. Sinha, S. Sanyal, and N. R. Bandyopadhyay, "2.11 Thermal Treatment for Strengthening Titanium Alloys," *Compr. Mater. Finish.*, vol. 2–3, pp. 288–336, Jan. 2017, doi: 10.1016/B978-0-12-803581-8.09193-1.

[4] Y. yan ZHU, B. CHEN, H. bo TANG, X. CHENG, H. ming WANG, and J. LI, "Influence of heat treatments on microstructure and mechanical properties of laser additive manufacturing Ti-5Al-2Sn-2Zr-4Mo-4Cr titanium alloy," *Trans. Nonferrous Met. Soc. China*, vol. 28, no. 1, pp. 36–46, Jan. 2018, doi: 10.1016/S1003-6326(18)64636-9.

[5] Z. Ding and Z. Jiao, "Metallic Materials for Making Multi-Scaled Metallic Parts and Structures," *Encycl. Mater. Met. Alloy.*, pp. 19–36, 2022, doi: 10.1016/B978-0-12-819726-4.00007-7.

[6] D. Barbier, M. X. Huang, and O. Bouaziz, "A novel eutectic Fe-15 wt.% Ti alloy with an ultrafine lamellar structure for high temperature applications," *Intermetallics*, vol. 35, pp. 41–44, 2013, doi: 10.1016/j.intermet.2012.11.016.

[7] A. Popovich, V. Sufiiarov, E. Borisov, and I. Polozov, "Microstructure and mechanical properties of Ti-6AL-4V manufactured by SLM," *Key Eng. Mater.*, vol. 651–653, no. February, pp. 677–682, 2015, doi: 10.4028/www.scientific.net/KEM.651-653.677.

[8] S. Ivanov, M. Gushchina, A. Artinov, M. Khomutov, and E. Zemlyakov, "Effect of Elevated Temperatures on the Mechanical Properties of a Direct Laser Deposited Ti-6Al-4V," *Materials (Basel).*, vol. 14, no. 21, Nov. 2021, doi: 10.3390/MA14216432.

[9] J. Song *et al.*, "Temperature sensitivity of mechanical properties and microstructure during moderate temperature deformation of selective laser melted Ti-6Al-4V alloy," 2020, doi: 10.1016/j.matchar.2020.110342.

Chapter 7

Conclusions

7 Conclusions

This chapter summarises the main conclusions coming out of this thesis which have been grouped into four sections.

7.1 Powder production and characterisation

(i) For the studied Ti-rich compositions $Ti_{66}Fe_{27}Nb_3Sn_4$ (near-eutecic) and $Ti_{73.5}Fe_{23}Nb_{1.5}Sn_2$ (non-eutectic), Arc-Melting Atomisation (AMA) produced powders with the highest purity (≤ 910 pmm of O_2 in the SLM size range) and the best physical properties. They featured Particle Size Distributions (PSDs) slightly shifted towards larger particle sizes when compared to powers produced by Crucible-Free Atomisation (CFA) and Crucible-based Gas Atomisation (CGA).

(ii) CGA powder demonstrated the worst physical properties suggesting the need for further optimisation of the process for Ti-based alloys. The novel methodogy for analysing XCT scan data of powders, developed as part of this thesis, concluded that CGA produced powder featured much higher internal porosity (1.9 vol %) as compared to powders produced by other methods (≤ 0.6 vol %), had a PSD skewed towards lower particle sizes and scored least on the number percent of particles in the SLM size range that qualified for our set 'ideal' morphology standards for SLM processing.

(iii) All produced Ti-rich powders (CFA, CGA, AMA and AMA2) retained compositions very close to the target. Further, Ti-rich powders remained sensitive to Carbon and Oxygen contamination from crucibles used in the overall powder production process. Melting in a graphite crucible led to undesirable carbide phases in CGA $Ti_{66}Fe_{27}Nb_3Sn_4$ powder. The high Oxygen content in cast (using ceramic crucibles) feedstock rods for CFA led to unwanted oxide phase in $Ti_{66}Fe_{27}Nb_3Sn_4$ powder. Fe-rich near-eutectic composition $Fe_{82.4}Ti_{17.6}$ produced by CFA did not face this issue.

(iv) Finally, **the AMA2 powder of target composition $Ti_{73.5}Fe_{23}Nb_{1.5}Sn_2$ was selected for SLM processing.** Trials involving CFA and AMA powders of near-eutectic composition $Ti_{66}Fe_{27}Nb_3Sn_4$ witnessed cracking and demanded serious processing optimisation which did not fit the project's timeline and go beyond the scope of this thesis. Although AMA2 powder composition is non-eutectic, it produced crack-free builds and provided a new design opportunity for a "composite" alloy composed of β-Ti and FeTi, with part of the intermetallic FeTi being lamellar and the rest existing as dispersoids.

(v) For the studied Fe-rich composition $Fe_{82.4}Ti_{17.6}$, CFA produced powders with good physical properties and low contamination (≤ 600 ppm of O_2 in the LMD size range). They contained slightly more than intended Fe content (≈ 17.3 wt % instead of target 15.5 wt %). **They qualified to go forward with LMD processing.**

7.2 Rapid solidification behaviour of powders

(i) Microstructural studies on powders revealed that powder particle size is clearly related to, and can possibly predict, the solidification pathway selected during gas atomisation as well as its degree of completion, i.e. microstructural growth achieved. Further, the different solidification behaviour observed in CFA, CGA and AMA powders of the same target composition $Ti_{66}Fe_{27}Nb_3Sn_4$ was influenced by small constitutional variations in addition to the atomisation method used and their process parameters, which in turn define the solidification rates.

(ii) The binary lamellar eutectics (β-Ti + FeTi) and (α-Fe + Fe_2Ti) observed in powder microstructures were ultrafine featuring inter-lamellar spacing 'λ' between 27.6 – 187.7 nm for $Ti_{66}Fe_{27}Nb_3Sn_4$ and between 60.7 – 172.5 nm for $Fe_{82.4}Ti_{17.6}$ powders. Calculations based on the Jackson-Hunt relation for binary eutectic growth revealed that solidification rates experienced by these powders were similar to those encountered during SLM/LMD processing of the same or similar compositions. This suggests that gas atomisation can be potentially used to study rapid solidification and Laser-AM processing.

(iii) The average λ of observed binary lamellar eutectics increased almost linearly with increasing powder particle size. Going by the Jackson-Hunt relation for binary eutectic growth, this reaffirms the fact that smaller particles solidify faster during atomisation. However, particle size and λ do not strongly affect powder nano-hardness, which lies between 8 to 10 GPa for most powders.

7.3 Advanced image analysis of XCT data for powders

(i) In a novel approach, the trainable machine learning-based tool WEKA of *Fiji* was used in combination with 3D watershed separation tools of Avizo for accurate segmentation and separation of powder particles measured by XCT. The end results provided a reliable and comprehensive set of information for the characterisation of powder volumes, shapes and their respective internal pores.

(ii) Unlike laser diffraction, XCT analysis methodology showed skewed gaussian distributions for CFA and AMA2 powders in the SLM size range (20 – 63 µm). However, both methods revealed CGA to have the smallest particle sizes on average. Although conventional laser diffraction has a statistical advantage over XCT analysis in plotting volume-based size distributions, the latter provides reliable results while addressing the assumptions and shortcomings of Mie theory. Further, the methodology is not limited to measuring volume/size.

(iii) A simplistic model was introduced that quantified the shape distribution of particles based on three parameters: Sphericity, Aspect ratio and Volume3d determined by the proposed XCT image analysis methodology. The user was allowed to choose 'ideal' morphologies

from a visual database (created using AMA2 powder morphologies as reference) and calculate the powder's qualification ratio, i.e., the number percent of 'ideal' particles. The model was proven to work for evaluating differences between atomisation methods.

(iv) AMA2 powder showed high qualification ratios of 63.5 to 65 % with 'ideal' particles distributed uniformly across all volumes/sizes in the SLM size range (20 – 63 µm). Evaluation of Ti-rich compositions produced by CFA and CGA was performed using the same 'ideal' shape standards as for AMA2. CGA showed extremely low qualification ratios (5.4 to 16.4 %) that decreased with increasing particle size/volume. CFA showed high qualification ratios similar to that of AMA2 across most sizes, but with a decline of ≈ 10 % for high volume particles (≥ 125000 μm^3 or Equivalent diameter ≥ 62 µm).

7.4 Characterisation of AM-built alloys

(i) $Fe_{82.4}Ti_{17.6}$ alloy built by LMD using CFA produced pre-alloyed powders featured ultrafine lamellar eutectic microstructure (λ = 206 ± 51 nm). The arc-shaped `inter-layers´, lying between the lamellar eutectic layers, were 12.2 ± 0.8 µm thick and consisted of a globular eutectic morphology.

(ii) $Ti_{73.5}Fe_{23}Nb_{1.5}Sn_2$ alloy built by SLM using AMA produced pre-alloyed powder (named AMA2) featured significant phase fractions of both β-Ti and α-Ti, accompanied by a large fraction of inter-metallic FeTi as dispersoids. In a matrix strengthened by dispersoids, a portion of FeTi further arranged themselves linearly to resemble fine lamellas. The thin inter-layers (average thickness 3.5 ± 0.6 µm) featured relatively low concentration of dispersoids.

(iii) LMD-built $Fe_{82.4}Ti_{17.6}$ showed a high compressive yield strength ≈ 1800 MPa and almost zero plasticity at room temperature, when loaded uniaxially parallel to the build direction. Onset of plasticity was observed above 500 °C and the alloy showed very high plasticity at 600 °C (up to 90 % deformation without failure) while always maintaining a yield strength above 1000 MPa. Further, some anisotropy was observed with respect to the loading direction as the compressive yield strength dropped by ≈ 20 % while loading perpendicular to the build direction. Pre-existing thin cracks in tensile specimens resulted in brittle fractures at low loads for all testing temperatures.

(iv) SLM-built $Ti_{73.5}Fe_{23}Nb_{1.5}Sn_2$ showed very high compressive yield strength of 1925 MPa at room temperature and up to 20 % deformation before failure, when loaded uniaxially parallel to the build direction. It became completely plastic at 600 °C while maintaining a high yield strength of 660 MPa. Under tension (uniaxial load perpendicular to build direction), the specimens acted brittle at room temperature. But, at 450 °C, they showed elongation up to 40 % and high tensile yield strength of ≈ 1200 MPa. The strength

decreased and the elongation increased above 450 °C, with the alloy becoming completely ductile at 550 °C.

(v) Micro-mechanical characterisation of LMD-built $Fe_{82.4}Ti_{17.6}$ was performed using compression of micro-pillars carved on the microstructure which revealed an average compressive yield strength of 2254.3 ± 109.9 MPa. The alloy showed nano-hardness of 6.4 – 9.8 GPa in the lamellar eutectic `layer´, as compared to 3 – 6 GPa in the globular `inter-layer´.

(vi) In a comparative study of micro-pillar compression, LMD-built $Fe_{82.4}Ti_{17.6}$ performed better than FAHP-processed $Fe_{82.4}Ti_{17.6}$ and also featured microstructures with lower λ. The highest micro-pillar yield strength recorded for FAHP-processed samples was 1933 ± 16.5 MPa and the lowest average λ observed was 377.5 ± 90.1 nm. Micro-pillar yield strength was found to decrease linearly with increasing λ for the LMD and dense (10 min sintering time) FAHP-processed samples. However, λ showed no clear correlation to nano-hardness behaviour of any samples processed by LMD and FAHP (or to that of the powders used as raw material).

(vii) LMD-built $Fe_{82.4}Ti_{17.6}$ could be considered an impressive candidate for compression-based applications in the intermediate temperature range. Induction cast Fe-15 wt % Ti or $Fe_{82.9}Ti_{17.1}$ alloy was reported by Barbier et al. [1] as a new candidate for such applications. LMD processing produced a much finer microstructure and better mechanical results for a very similar composition.

(viii) SLM-built $Ti_{73.5}Fe_{23}Nb_{1.5}Sn_2$ can be considered as an excellent (α+β) Ti alloy, further strengthened by FeTi dispersoids, for compression and tension-based applications, especially in the intermediate temperature range. The alloy showed higher tensile yield strength and elongation at intermediate temperatures (450 °C to 600 °C) than popular (α+β) aerospace alloys like Ti-6Al-4V built by laser-AM [2–4].

REFERENCES

[1] D. Barbier, M. X. Huang, and O. Bouaziz, “A novel eutectic Fe-15 wt.% Ti alloy with an ultrafine lamellar structure for high temperature applications,” *Intermetallics*, vol. 35, pp. 41–44, 2013, doi: 10.1016/j.intermet.2012.11.016.

[2] A. Popovich, V. Sufiiarov, E. Borisov, and I. Polozov, “Microstructure and mechanical properties of Ti-6AL-4V manufactured by SLM,” *Key Eng. Mater.*, vol. 651–653, no. February, pp. 677–682, 2015, doi: 10.4028/www.scientific.net/KEM.651-653.677.

[3] S. Ivanov, M. Gushchina, A. Artinov, M. Khomutov, and E. Zemlyakov, “Effect of Elevated Temperatures on the Mechanical Properties of a Direct Laser Deposited Ti-6Al-4V,” *Materials (Basel).*, vol. 14, no. 21, Nov. 2021, doi: 10.3390/MA14216432.

[4] J. Song *et al.*, “Temperature sensitivity of mechanical properties and microstructure during moderate temperature deformation of selective laser melted Ti-6Al-4V alloy,” 2020, doi: 10.1016/j.matchar.2020.110342.

Chapter 8

Future work

8 Future Work

This chapter outlines and anticipates the future work that can be accomplished along the research lines of this thesis, i.e., the development of pre-alloyed powders for laser additive manufacturing of Ti-Fe-based eutectic/near-eutectic alloys. The key objectives and visions for the future are addressed in the following three sections.

8.1 Alloy and powder production

In the near future, advanced characterisation techniques, like Transmission Electron Microscopy (TEM) or nano-X-ray Computed Tomography (nano-XCT), should be used for 3D characterisation of eutectic growth in powders. The occurrence and evolution of metastable phases (like $FeTi_2$, α-Ti) need to be understood under the fast kinetics of gas atomisation. This would expand the solidification knowledge database of the studied alloys and help develop computational models in the long run.

The current popular methods of gas atomisation (i.e. CGA and CFA like set-ups), need to be adapted for very reactive alloys like those used in this thesis. For example, the use of Yttria-stabilised Zirconia crucibles instead of Graphite could reduce the chances of contamination by Carbon. Similarly, the casting conditions of rods for CFA-like set-ups should be improved and standardised for reactive alloys in order to minimise Oxygen contamination. Such knowledge should be shared with and implemented by commercial suppliers in the future for access to bulk production. Alternative cleaner methods like Arc-melting atomisation or plasma spheroidisation are still quite expensive and unpopular for bulk production of powders.

Further, the data analysis tool developed for XCT scans (discussed in chapter 5) could be further improved to deploy additional features and unleash the full potential of the technique. The main objectives would be to improve the watershed separation of particles with open pores (or try other particle separation methods), evaluate open porosity accurately and develop machine learning for classifying or evaluating particle morphologies rather than relying on manually created visual databases. This would lead to the creation of a 'one measurement for all' kind of tool in the field of advanced powder characterisation.

8.2 Processing and post-processing

Laser solidification dynamics and laser-matter interaction during laser melting of Ti-Fe alloys need to be studied in-depth for the future. This will help optimising processing parameters for such alloys which face issues like unwanted brittle phases and internal stresses leading to cracks (like in case of near-eutectic $Ti_{66}Fe_{27}Nb_3Sn_4$). Some plans are already underway in this direction, like performing in-situ fast X-ray Radiography (XRR) using synchrotron radiation

during laser processing of these alloys (examples found in [1]) and using neutron or synchrotron X-ray diffraction for characterising residual stresses. Initiatives like the European project *EASI-stress* aim at developing standardised advanced characterisation tools for the proper residual stress determination of AM components [2].

Further, more knowledge on powder production and processing conditions would allow newer Ti-Fe-based near-eutectic compositions to be produced and evaluated. The aim is to expand into other laser and arc-based AM processing routes for future bulk production.

Besides the fact that additional mechanical characterisation needs to be performed on the SLM-built $Ti_{73.5}Fe_{23}Nb_{1.5}Sn_2$ alloy in the near-future, appropriate post-processing treatments also have to be developed for both AM-built alloys in order to improve their brittle behaviour at/near room temperature. Future research plans include longer annealing times for stress-relieving of LMD-built $Fe_{82.4}Ti_{17.6}$, surface treatments, and annealing followed by water-quenching for SLM-built $Ti_{73.5}Fe_{23}Nb_{1.5}Sn_2$ alloy in order to minimize formation of brittle α-Ti phase. This will be combined with further optimisation of powder bed pre-heating conditions to relieve the residual stress generated during building. In this direction, the high temperature mechanical behaviour (like onset of plasticity above 500 °C in $Fe_{82.4}Ti_{17.6}$) of alloys can serve as a starting point.

8.3 Modelling and simulation

A long-term goal is to build a simulation tool for evaluating the feasibility and performance of binary eutectic alloys processed by laser-AM. Existing AM models can be adapted to these alloys and new models can be created based on in-depth knowledge acquired on rapid solidification behaviour of pre-alloyed powders as well as for solidification dynamics occurring during laser melting. In order to fully describe the AM process, all these models need to be interconnected and share data, i.e. be interoperable. Also, they will require experimental data from advanced characterisation techniques describing the dynamic processes for further validation. For this to happen, sufficient interoperability between characterisation and various modelling tools must be ensured. Experiments, the data formats, their acquisition and analysis software would all have to be standardised. This is a long-term vision and would require the cooperation of several research groups specialised in experiments and modelling.

REFERENCES

[1] C. Zhao *et al.*, “Real-time monitoring of laser powder bed fusion process using high-speed X-ray imaging and diffraction,” *Sci. Rep.*, vol. 7, no. 1, pp. 1–11, 2017, doi: 10.1038/s41598-017-03761-2.

[2] “EASI-STRESS Home.” https://www.easi-stress.eu/ (accessed Apr. 30, 2023).

Appendix A

Appendix A

Image analysis tool in Fiji (ImageJ) for measuring inter-lamellar spacing λ

The methodology implemented in *Fiji* to measure the inter-lamellar spacing λ using SEM images is described in this supplementary material. Operations from step 2 onwards can be performed automatically by a macro, which is mentioned at the end of the document.

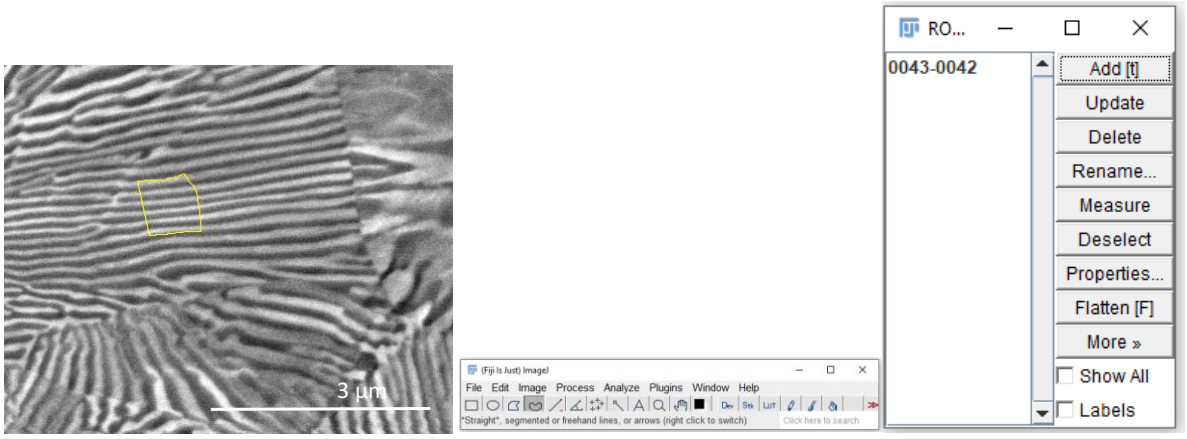

Figure A 1*:* Selection and saving of the ROI in a SEM image for measuring λ

1. The image containing lamellar eutectic to be analysed is loaded into *Fiji*. The freehand selection tool, as highlighted in Figure A 1, is used to draw a Region of Interest (ROI) where the lamellae are to be analysed. The ROI is subsequently saved to the ROI manager, as shown in Figure A 1.
2. Any kind of scale is removed and all the results are measured in pixels. They are converted later into µm based on the image magnification (images of various magnifications were used for analysis). This was carried out for convenience of following image procedures; however, the user has an option to modify the macro in order to retrieve and reset the scale information for every analysed image.
3. A median filter with radius 2 is applied to the ROI in order to slightly reduce the noise.
4. This region is then duplicated and converted into 8-bit. It is auto-thresholded into a black and white image, as shown Figure A 2: Use of median filter on ROI and conversion to 8-bit binary image. This separates lamellas of the two different phases into white (value = 0) and black (value = 255) pixels. Note: colours and values have inverted LUT (algorithm need to be revised if this is changed in *Fiji*).

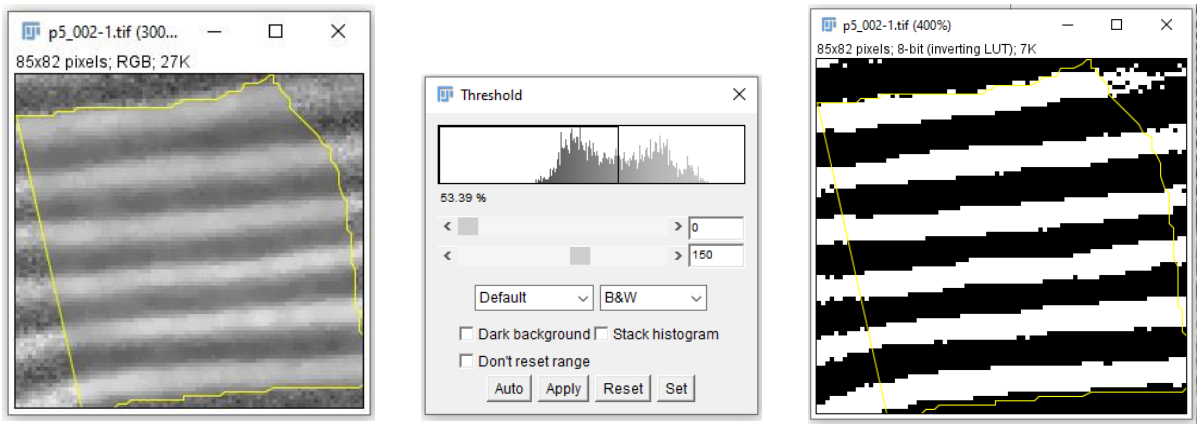

Figure A 2: Use of median filter on ROI and conversion to 8-bit binary image

5. The 8-bit thresholded image is duplicated twice to create 3 copies in total.

For determining λ, the average thickness of the black and white phases needs to be calculated. This is done by determining the medial position of each phase by iterative erosion and knowing the average distance that was eroded to reach the centre. The phase thickness would be double this distance. "Skeletonize" and "distance map" operations were used for these objectives.

6. On one copy, a "skeletonize" (can be found in *Fiji* under the tab Process/binary/skeletonize) operation is performed which determines the centrelines of the black phases by eroding pixels iteratively. Only a skeleton of black phases with pixels = 255 is left, as shown in Figure A 3. Pixels outside the ROI were removed using "Edit/Clear outside" option in order to avoid image border effects.

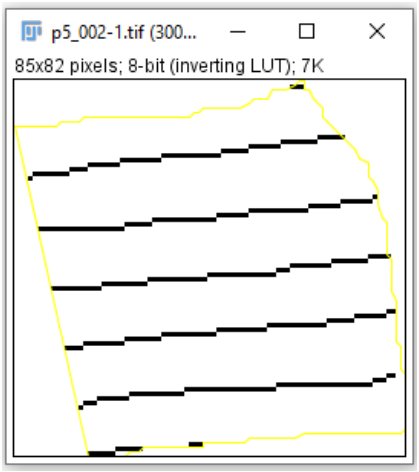

Figure A 3: Result after skeletonization of 8-bit binary ROI

7. On another 8-bit thresholded copy, a "distance map" (can be found in *Fiji* under the tab Process/binary/skeletonize) operation is performed which generates a map of pixels with grayscale value as their distance from the nearest background or white phase (value = 0), as shown in Figure A 4. Pixels outside the ROI were removed using "Edit/Clear outside" option in order to avoid image border effects.

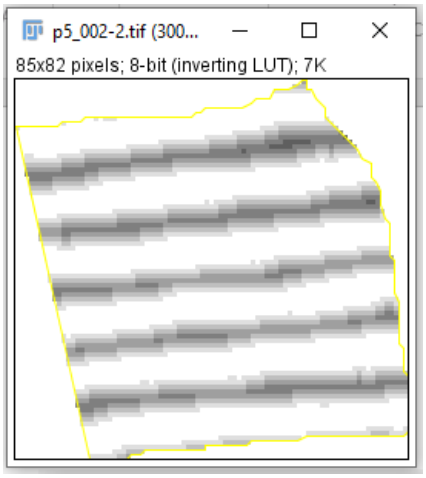

Figure A 4: Result after using distance map on 8-bit binary ROI

The pixels towards the phase centre appear darker in the distance map as they are the farther from the background. We only need the distance from the centreline to determine the half-thickness of the black phase. The skeletonised binary image has all pixels set to 0 except the centrelines of black phase whose values are 255. If we divide all pixels in the image by 255, we will have the centrelines as 1 and all other pixels as 0. Multiplying the resulting image (using Process/Image calculator in Fiji) by the distance map will create in a new image whose only pixels are distance values for the centrelines, as all other distance values will be removed upon multiplication by 0.

8. The skeletonized binary image in is divided by 255 (Process/Math/Divide) and the resulting image is multiplied by the distance map obtained in Figure A 4. The resulting image, shown in Figure A 5: Result after multiplying Skeletonized image (divided by 255) and distance map of 8-bit binary ROI, contains pixels whose values represent distances of the centreline pixels from the white phase, in other words, the half-thicknesses of the black phase.

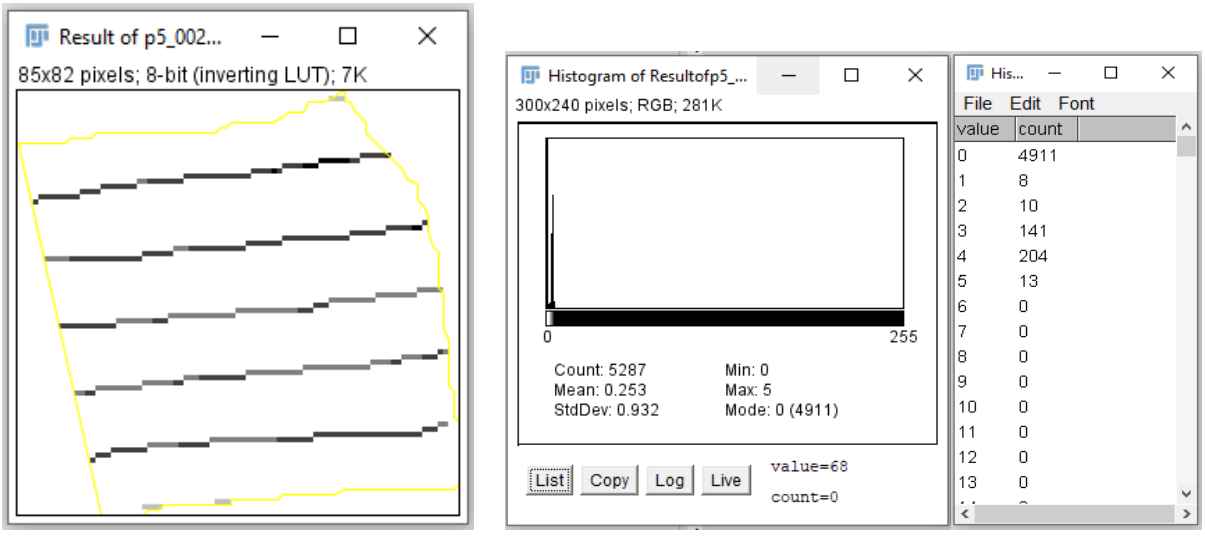

Figure A 5: Result after multiplying Skeletonized image (divided by 255) and distance map of 8-bit binary ROI

9. The pixel values are extracted from the resulting image's histogram. A weighted average gives the mean half-thickness of the black phase, called meanA in the macro.

*meanA = sum of (value*count)/(total counts excluding for ´0´)*

Average thickness of the dark phase= 2*meanA = 7.085 pixels (in this example).

10. The one remaining 8-bit thresholded image after step 5 is inverted (ctrl+shift+I) to reverse the pixel colour and values of the two phases. Then it is duplicated to create another copy.

11. The steps from 6 to 9 are repeated with these two copies of binary images. The result is meanB= average half-thickness of the second phase

Once we have meanA and meanB, we can calculate,

λ= sum of average thicknesses of the two phase lamellas = 2(meanA + meanB) = 13.198 pixels = 13.198 x 10.348 (Scale factor) = 136.57 nm (in this example).*

The macro returns both thicknesses and λ when it is executed after performing step 1, as shown in Figure A 6.

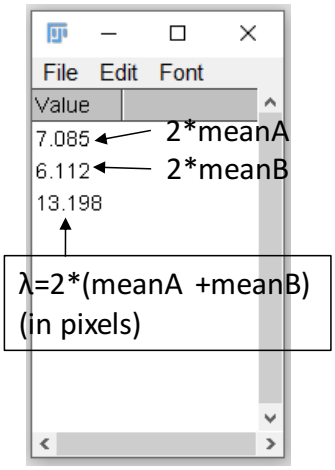

Figure A 6: Final result returned by executing the macro developed

All the steps are summarised into a Flowchart below for easier understanding.

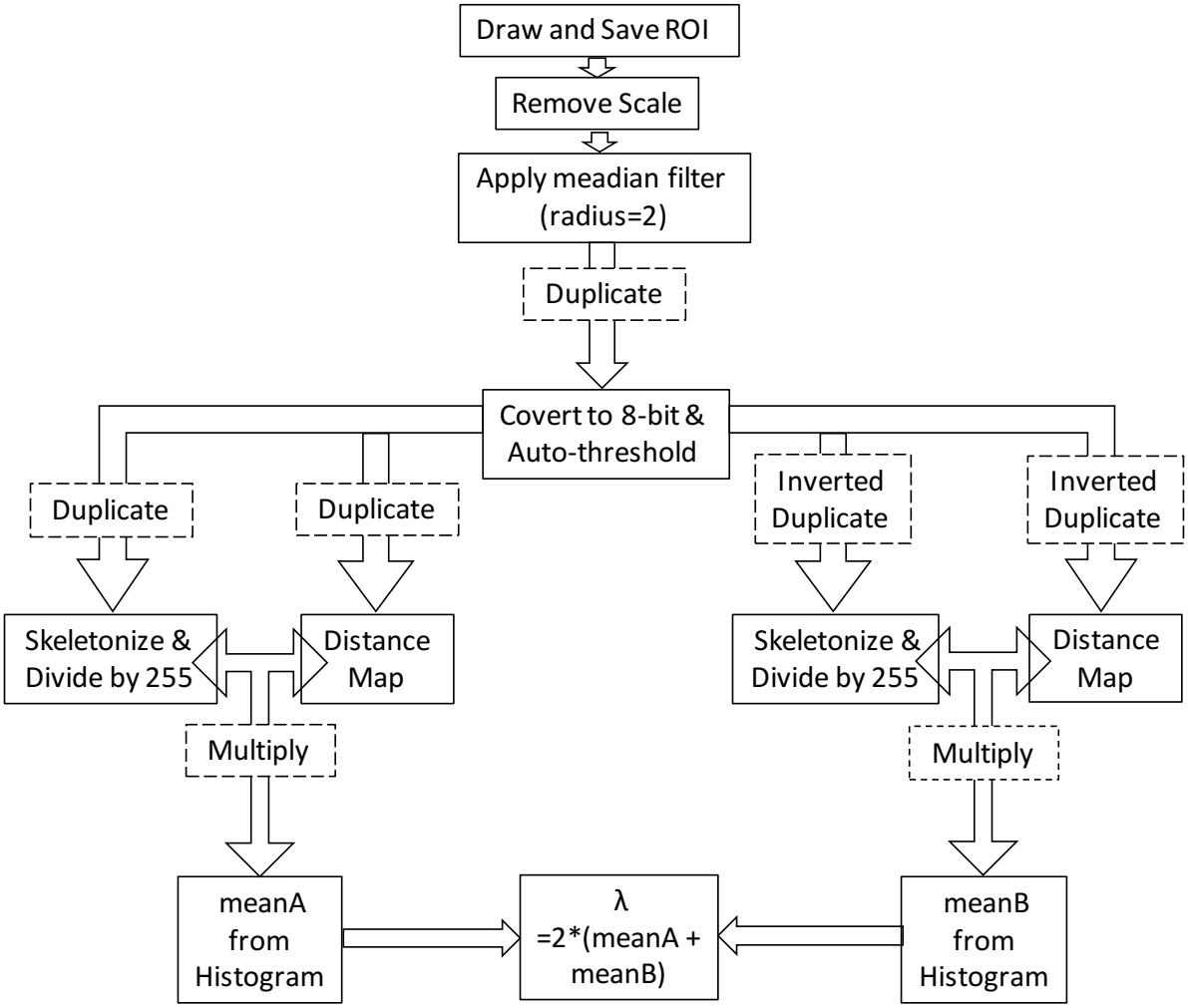

The macro is as following:

```
close("\\Others");                          //close all images except the current one
run("Set Scale...", "distance=0");          //set 1 pixel=1 length unit for simplicity
run("Median...", "radius=2");               //filtering noise in the image ROI
run("Duplicate...", "title=copy-1.tif ");   //make an image copy with the ROI
roiManager("Add");                          //record the ROI
run("8-bit");                               //convert to 8-bit image
setAutoThreshold("Default");
run("Convert to Mask");                     //convert to binary threshold
run("Duplicate...", "title=copy-2.tif ");
selectWindow("copy-2.tif");
run("Duplicate...", "title=copy-3.tif");    //make copies of binary thresholded image
```

```
selectWindow("copy-3.tif");
run("Invert");                          //invert phase colour and values
selectWindow("copy-3.tif");
run("Duplicate...", "title=copy-4.tif ");
selectWindow("copy-1.tif");
count=roiManager("count");
roiManager("select", count-1);          // select latest roi
run("Skeletonize");
run("Clear Outside");                   //skeletonize and clear outside
run("Divide...", "value=255.000");      // Divide Each pixel value by 255 in skeleton
selectWindow("copy-2.tif");
run("Distance Map");
roiManager("Select", count-1);
run("Clear Outside");                   //distance map and clear outside
selectWindow("copy-1.tif");
imageCalculator("Multiply create", "copy-1.tif","copy-2.tif");
//multiply skeleton &distance map
selectWindow("Result of copy-1.tif");
roiManager("Select", count-1);
getHistogram(0,histA,256);                          //get histogram data
histA[0]=0;
sum=0; meanA=0;
for(i=0;i<256;i=i+1){
sum=sum+histA[i];                       //sum of all counts except for value 0 or background
}
for(i=0;i<256;i=i+1){
meanA=meanA+(i*histA[i]/sum);           // calculate meanA
}
selectWindow("copy-3.tif");
```

```
roiManager("Select", count-1);
run("Skeletonize");
run("Clear Outside");
run("Divide...", "value=255.000");
selectWindow("copy-4.tif");
roiManager("Select", count-1);
run("Distance Map");
run("Clear Outside");
imageCalculator("Multiply create", "copy-3.tif","copy-4.tif");
selectWindow("Result of copy-3.tif");
roiManager("Select", count-1);
getHistogram(0,histB,256);
histB[0]=0;
sum=0; meanB=0;
for(i=0;i<256;i=i+1){
sum=sum+histB[i];
}
for(i=0;i<256;i=i+1){
meanB=meanB+(i*histB[i]/sum);                    //calculate meanB
}
meanA=2*meanA;
meanB=2*meanB;
lamda=meanA+meanB;                    // calculate lambda
R=newArray(meanA,meanB,lamda);
Array.show(R);                                  //print Result in array R
print("Mean Grey phase "+meanA);
print("Mean white phase "+meanB);
print("mean Lamda "+lamda);                    //print results in Log
```

Appendix B

Appendix B

Macros to save and load ROIs into WEKA (for training)

For training the 'Trainable WEKA segmentation' plugin in *Fiji (ImageJ)*, 10 equally spaced slices are selected from the volume to be segregated and opened. Before this, all images were converted to 8-bit and their contrast and brightness were homogenised through histogram adjustment (the grey level of the background air was corrected so the mean of all 'background' pixels was 50, while a mean 'particle' grey level of 200 was chosen). After loading the 10 slices, the WEKA plugin is opened (Plugins > Segmentation > Trainable WEKA segmentation). The next step is to create ROIs on the images using a freehand selection tool and add them to defined classes (in our case, 'Particle' and 'Background') in the plugin interface. The problem here is that this is a tedious task and the plugin does not save the manually created ROIs. If the user wants to add more ROIs to a re-train a model later, he cannot retrieve the previously created ROIs. He will end up creating a new classifier model trained only with the new set of ROIs which will replace the old model. Therefore, it is not possible to improve models without finding a way to save and load the ROIs used for training. To solve this issue, we created three keyboard shortcuts by writing macros in *Fiji*.

Shortcut "1" renames the default 'class 1' as 'Particles', adds the drawn ROI into this class and saves it for later use.

Shortcut "2" renames the default 'class 2' as 'Background', adds the drawn ROI into this class and saves it for later use.

Shortcut "q" loads previously saved ROIs from a folder (specified by the user) into the plugin.

The user only needs to press "1" or "2" after drawing ROIs in the particle or background pixels of the image respectively. Then, he/she trains the model. If the user wants to re-train the model later, he/she presses "q" and selects the folder with saved ROIs from previous or any other training, which are loaded into the image stack. He/she then draws and adds more ROIs into the model before training again. The macros behind all three shortcuts are presented (and explained in comments) in the next pages.

1. Creating Keyboard shortcut “1” to save ‘Particle’ ROIs during training of WEKA

```
var defaultPath = getDirectory("Choose a Folder to your Image/volume Data");
//Select the path where you want to save or load the ROIs as a Global variable
macro "TrainWEKA_saveROIs_particles... [&1]" {
// assigns shortcut “1” to the following code to save ROIs inside particles
path=defaultPath;                    //take path input by user
call("trainableSegmentation.Weka_Segmentation.changeClassName", "0", "Particles");
 //change class name to Particles
run("ROI Manager...");               //open ROI manager
roiManager("Add");                   // add selected ROI to ROI manager
var r=roiManager("count");           //count entries in ROI manager
roiManager("select",r-1);            //select first entry in ROI manager
if (r>=1) setKeyDown("alt");         //select latest entry in ROI manager for multiple ROI´s
else roiManager("Select", 0);
var i=1; var j=1;
i=r;                                 //get particle number to ROI
j=getSliceNumber();                  //get slice number to ROI name
roiManager("Rename",i+"Part_z"+j);   // rename with particle and slice number like
2Part_3
call("trainableSegmentation.Weka_Segmentation.addTrace", "0", d2s(j,0));
//add trace of ROI to WEKA plugin


RoiManager.setPosition(j);roiManager("Set Color", "yellow");roiManager("Set Line Width",
0); //add slice position (in var j) to the ROI data for retrieving later
roiManager("deselect");roiManager("Save",path+"ROIs_all.zip");
//saves all rois in ROI manager as zip folder ROIs_all.zip
}
```

2. Creating Keyboard shortcut “2” to save ‘Background’ ROIs during training of WEKA

```
var defaultPath = getDirectory("Choose a Folder to your Image/volume Data");
//Select the path where you want to save or load the ROIs as a Global variable


macro "TrainWEKA_saveROIs_particles... [&2]" {
// assigns shortcut “2” to the following code to save ROIs inside background
path=defaultPath;                          //take path input by user
call("trainableSegmentation.Weka_Segmentation.changeClassName", "1", "Background");
//change class name to Background
run("ROI Manager...");                     //open ROI manager
roiManager("Add");                         // add selected ROI to ROI manager
var r=roiManager("count");                 //count entries in ROI manager
roiManager("select",r-1);                  //select first entry in ROI manager
if (r>=1) setKeyDown("alt");               //select latest entry in ROI manager for multiple ROI´s
else roiManager("Select", 0);
var i=1; var j=1;
i=r;                                       //get background number to ROI
j=getSliceNumber();                        //get slice number to ROI name
roiManager("Rename",i+"Bkg_z"+j);          // rename with background and slice number like
2Bkg_3
call("trainableSegmentation.Weka_Segmentation.addTrace", "0", d2s(j,0));
//add trace of ROI to WEKA plugin
RoiManager.setPosition(j);roiManager("Set Color", "yellow");roiManager("Set Line Width",
0);
//add slice position (in var j) to the ROI data for retrieving later
roiManager("deselect");roiManager("Save",path+"ROIs_all.zip");
//saves all rois in ROI manager as zip folder ROIs_all.zip
}
```

3. Creating Keyboard shortcut “q” to load previously stored ROIs into WEKA

```
macro "TrainWEKA_loadROIs... [q]" {

//assigns shortcut “q” to macro for loading previously stored rois in ROIs_all.zip

defaultPath_load=getDirectory("Load ROIs from");  //take input from user for ROI location

run("ROI Manager...");                          // open ROI manager

call("trainableSegmentation.Weka_Segmentation.changeClassName", "0", "Particles");
//change class name to particles

call("trainableSegmentation.Weka_Segmentation.changeClassName", "1", "Background");
//change class name to background

roiManager("Open", defaultPath_load+"ROIs_all.zip");    //load all ROIs into ROI manager

n = roiManager('count');

for (i = 0; i < n; i++)

{

roiManager('select', i);    //select each ROI one by one

j=getSliceNumber();       // get slice number of each ROI

k=Roi.getGroup();

//get group info stored during saving each ROI: 0 is particles, 1 is background

if(k==0) call("trainableSegmentation.Weka_Segmentation.addTrace", "0", d2s(j,0));

// add trace of ROI to WEKA plugin in class particles

else {

   call("trainableSegmentation.Weka_Segmentation.addTrace", "1", d2s(j,0));

// add trace of ROI to class background

}}

}
```